Rigidized subscale kite wind tunnel test

J.M. van Spronsen

Delft University of Technology & Technical University of Denmark

Rigidized subscale kite wind tunnel test

by

J.M. van Spronsen

to obtain the degrees

Master of Science
in Aerospace Engineering
at Delft University of Technology

&

Master of Science
in Wind Energy
at Technical University of Denmark

to be defended on Thursday October 17, 2024 at 10:45.

Project duration:	November 1, 2023 – July 31, 2024	
Thesis committee:	Dr.ing. R. (Roland) Schmehl,	TU Delft, chair
	J.A.W. (Jelle) Poland MSc,	TU Delft, daily supervisor
	M. (Mac) Gaunaa PhD,	DTU, daily supervisor
	Dr.ir. A.H. (Alexander) van Zuijlen,	TU Delft, external examiner
Master programme:	European Wind Energy Master	
Track and profile:	Rotor Design, Aerodynamics	
Institution:	TU Delft	DTU
Student number:	4866959	s223610
Faculty:	Aerospace Engineering	Wind Energy

An electronic version of this thesis is available at `http://repository.tudelft.nl/`.

Cover:	Kite model and support structure in the OJF by Jelle Poland
Style:	TU Delft Report Style, with modifications by Daan Zwaneveld

TU Delft

DTU

Preface

When I started the European Wind Energy Master in August 2022, by moving to Denmark to pursue a lifelong dream of mine to study abroad, little did I know I would be doing a thesis project in Airborne Wind Energy. In fact, it was completely new to me at that time. As I emailed various contacts in search of thesis topics, I discovered potential projects in this area. One project in particular grabbed my attention—it involved designing and conducting a wind tunnel experiment on a rigidized leading edge inflatable kite, a novel endeavor that had never been attempted before. This made the decision to pursue it an easy one.

I would like to express my gratitude to my daily supervisor Jelle Poland, on the TU Delft side. The weekly progress meetings, the construction of the support structure, the visit to Curve Works, the intensive two weeks of doing the experiment (during which working days of 14 hours were not unheard of) were really enjoyable with him. Furthermore, his input, enthousiasm, and overall company was much appreciated.

In addition, I would like to express my gratitude to Mac Gaunaa, my supervisor on the DTU side. Unfortunately, he was not able to join the meetings in person as I was in the Netherlands most of the time during the thesis project. However, his insights in the weekly progress meetings, his knowledge on wind tunnel testing, and his company were greatly appreciated. I could not have been reminded enough of the importance of doing zero runs.

I am extremely grateful to Roland Schmehl for his guidance throughout the process and his valuable feedback that helped keep the project on course. His enthusiasm was particularly appreciated, as it kept me motivated during the project.

I would also like to thank all the countless people that Jelle and I met during the project because, as Jelle said, it was better to ask questions about subjects we were not familiar with to those who are. Furthermore, I would like to thank my (study-)friends for keeping me sane throughout the whole project. Lastly, I would like to thank my family, in particular my parents and my little brother Niels, for supporting me at all times.

Mark van Spronsen
Monster, October 2024

Abstract

When doing Computational Fluid Dynamics (CFD) simulations on an object, it is necessary to have the right experimental data available to validate these simulations. In case of the Kitepower V3A Leading Edge Inflatable (LEI) Kite, this validation data is scarce, and non-existent if you are doing steady-state simulations. Such LEI kites are soft, and deform continuously during flight. When scaling such a kite down to wind tunnel scale, complex aeroelastic scaling issues present. For these reasons, experiments have been conducted in TU Delft's Open Jet Facility (OJF) on a rigidized model of the V3A kite. This experiment is unprecedented, because a wind tunnel test on a rigid kite has never been conducted before.

In short, the V3A is a highly effective aerodynamic model that can be used to simulate a variety of aerodynamic conditions. The aim of this research was to conduct wind tunnel experiments on a rigid subscale model of Kitepower's LEI V3A Kite. The model was constructed using a carbon fiber reinforced polymer, which was layered in a mold composed of structural foam. During the design phase, a support structure was also created to suspend the kite in the wind tunnel. The support structure could adjust its angle of attack and the angle of side-slip via a motorised mechanism.

The V3A kite model was tested in a controlled, yet confined, environment in order to measure aerodynamic performance. The test consisted of measuring the forces and moments acting on the kite for different combinations of wind speed, angle of attack, and angle of sideslip. The load measurements were performed with and without zigzag tape to determine its impact at low Reynolds numbers. The experimental data were then used to determine the corrections, allowing the experimental data to more accurately reflect true, unbounded aerodynamic characteristics compared to real-world, free-flight conditions. This is particularly crucial for streamlined lifting bodies, where precise aerodynamic features are critical for performance predictions and design optimizations.

The objective of processing the load measurements is to obtain plots of the kite's lift, drag, and side force coefficients, and moment coefficients in the kite's coordinate system. The load measurements of the support structure are used to interpolate the relationships between the aerodynamic coefficients of support structure and the angle of attack.

The aerodynamic performance of a kite is influenced by a variety of factors, including flow disturbances, unsteady aerodynamic forces, higher drag, the influence of surface impurities, and the potential effects of reference point selection at lower Reynolds numbers. In this paper, the aerodynamic characteristics of the kite are analyzed and compared to established literature to evaluate their accuracy and validity. Specifically, the lift coefficient, drag coefficient, lift-to-drag ratio (C_L/C_D) versus angle of attack (α), and C_L versus C_D curves are compared with the 3D steady-state Reynolds-Averaged Navier-Stokes (RANS) simulations of Lebesque [1] and the vortex step method results of Cayon [2]. The comparisons indicate that the experimental results align well with the literature at low Reynolds numbers, validating the experimental setup and measurement techniques.

In conclusion, the research conducted a precise experimental study on a rigid subscale model of the Kitepower V3A Leading Edge Inflatable (LEI) Kite to address the lack of aerodynamic validation data. By overcoming aeroelastic scaling challenges with a rigid model, the study provided essential steady-state validation data through meticulous force balance measurements and a detailed uncertainty analysis. The results, while showing close matches in certain aspects, highlighted notable differences when compared with existing simulations. The study recommends refining the support structure to minimize interference, aligning simulation Reynolds numbers more closely with experimental conditions, and further utilizing Stereoscopic Particle Image Velocimetry (SPIV) for a comprehensive aerodynamic analysis.

Contents

List of Figures

List of Tables

Nomenclature

Abbreviations

Abbreviation	Definition
2D	Two dimensional
3D	Three dimensional
AIC	Aerodynamic Influence Coefficient
AWE	Airborne Wind Energy
AWEC	Airborne Wind Energy Conference
AWES	Airborne Wind Energy Systems
CAD	Computer Aided Design
CG	Center of gravity
CFD	Computational Fluid Dynamics
DNS	Direct Numerical Simulation
FEM	Finite Element Method
HAWT	Horizontal Axis Wind Turbine
KCU	Kite Control Unit
LBM	Lattice-Boltzmann method
LE	Leading Edge
LEI	Leading Edge Inflatable
LES	Large Eddy Simulation
LLM	Lifting Line Method
LLT	Lifting Line Theory
NLR	Nederlands Lucht- en Ruimtevaartcentrum
NS	Navier-Stokes
OJF	Open Jet Facility
PIV	Particle Image Velocimetry
PLA	Polylactic Acid
RANS	Reynolds-Averaged Navier-Stokes
SPIV	Stereoscopic Particle Image Velocimetry
TE	Trailing Edge
URANS	Unsteady Reynolds-Averaged Navier-Stokes
VAWT	Vertical Axis Wind Turbine
VLM	Vortice Lattice Method
VSM	Vortex Step Method

Symbols

Symbol	Definition	Unit
AR	Aspect ratio	-
$A_{f,model}$	Frontal area of the model	m^2
A_{outlet}	Area of the wind tunnel outlet	m^2
a	Semi-major axis	m
B	Wind tunnel blockage factor	-
b	Semi-minor axis	m
b_{max}	Maximum allowable span width	m
b_{proj}	Projected wing span	m

Symbol	Definition	Unit
C	Force and moment coefficient	-
C_D	Drag coefficient	-
$C_{F,support}$	Force coefficient of force balance	-
$C_{F,total}$	Force coefficient of force balance and kite	-
C_{kite}	Force or moment coefficient of kite	-
C_L	Lift coefficient	-
C_l	Airfoil lift coefficient	-
C_L/C_D $(or L/D)$	Lift-to-drag ratio	-
$C_{M,support}$	Moment coefficient of force balance	-
$C_{M,total}$	Moment coefficient of force balance and kite	-
C_mx	Moment coefficient about x-axis of the force balance	-
C_my	Moment coefficient about y-axis of the force balance	-
C_mz	Moment coefficient about z-axis of the force balance	-
C_S	Side force coefficient	-
$C_{support}$	Force or moment coefficient of force balance	-
C_{pitch}	Pitching moment coefficient	-
C_{roll}	Rolling moment coefficient	-
C_x	Force coefficient in x-direction of the force balance	-
C_y	Force coefficient in y-direction of the force balance	-
C_{yaw}	Yawing moment coefficient	-
C_z	Force coefficient in z-direction of the force balance	-
c_{max}	Maximum allowable chord length	m
c_{min}	Minimum allowable chord length	m
c_r	Root chord	m
c_{sym}	Chord length at symmetry plane	m
D	Kite drag force	N
D_{LE}	Diameter of the leading edge	m
d_{cg}	Distance between hinge point and kite center of gravity	m
E	Young's modulus of elasticity	Pa
F_x	Force in x-direction of the force balance	N
F_y	Force in y-direction of the force balance	N
F_z	Force in z-direction of the force balance	N
h	Projected height of the V3A	m
h_{bar}	Height of the bar regulating the angle of attack	m
I	Moment of inertia	m^4
L	Characteristic length	m
L	Kite lift force	N
M_{pitch}	Kite pitching moment about its CG	Nm
M_{roll}	Kite rolling moment about its CG	Nm
M_{symm}	Wing half moment about center chord	Nm
M_x	Moment about x-axis of the force balance	Nm
M_y	Moment about y-axis of the force balance	Nm
M_{yaw}	Kite yawing moment about its CG	Nm
M_z	Moment about z-axis of the force balance	Nm
m_{model}	Mass of the kite model	kg
Re	Reynolds number	-
S	Kite area	m^2
S	Kite side force	N
U_a	Apparent flow speed	m/s
U_∞	Free-stream velocity	m/s
x	x-distance between kite CG and force balance CG	m
x_{cg}	Distance in x-direction between hinge point and kite center of gravity	m
x_{hinge}	Distance in x-direction between hinge point and force balance center of gravity	m

Symbol	Definition	Unit
z	z-distance between kite CG and force balance CG	m
z_{cg}	Distance in z-direction between hinge point and kite center of gravity	m
z_{hinge}	Distance in z-direction between hinge point and force balance center of gravity	m
α	Angle of attack	°
α_{free}	Angle of attack in free-stream conditions	°
α_{stall}	Stall angle of attack	°
α_{kite}	Kite angle of attack	°
$\alpha_{geo,openjet}$	Measured angle of attack in open-jet wind tunnel	°
α_{rod}	Rod angle of attack	°
β	Sideslip angle of the kite	°
$\Delta\alpha openjet$	Difference between measured wind tunnel and free stream angle of attack	°
δ_{max}	Max. tip deflection	m
μ	Dynamic viscosity	Pa·s
π	Ratio between the circumference and the diameter of a circle	-
ρ	Air density	kg/m^3

1

Introduction

"Life on earth is under siege", according to Ripple et al. [3]. For many years, researchers have continuously alerted to a future shaped by severe weather patterns due to rising global temperatures, a consequence of persistent human actions that emit dangerous greenhouse gases into the atmosphere. Renewable sources of energy are needed to combat these emissions. Assessments have been performed on whether power generated by wind energy can supply the whole world with electricity, from which the outcomes are positive, although there are practical barriers to overcome to realize this [4].

Nowadays, horizontal axis wind turbines (HAWTs) are the main machines used to convert the energy present in the wind to electric energy. On the other hand, the use of vertical axis wind turbines (VAWTs) is also rising in recent years [5]. The difference between both of these turbines is that the VAWTs do not need yaw control to align the rotor of the turbine with the wind direction, whereas HAWTs do. This allows for easier control and thus less expensive machines. The challenge for both of these types of machines is scaling: at higher altitudes, there are higher and more constant wind speeds available, which means that there is more power to be harvested. These machines will simply get too large and can therefore not reach these altitudes. A possible solution is the so called airborne wind energy systems (AWESs) [6]. These systems can operate at higher altitudes, allowing for a greater energy yield. An airborne wind energy system is essentially a tethered flying device, connected to a ground station. Through recent years, interest in the airborne wind energy sector has risen substantially. However, there are still plenty of challenges in the sector given its infancy. Examples of these challenges are the safe autonomous operations, and reducing the costs of operation and increasing the energy output of such a system. The last challenge is certainly the biggest one, because a higher energy output of such a system can raise the attractiveness, and thereby raise more funds for research in the field.

A common characteristic of such kites is that they are made of soft fabric, or membrane. It is due to the soft nature that these kites continuously deform during flight: the aerodynamic loads impose deformations on the structure, which in their turn change the aerodynamic characteristics. It is therefore called a fluid-structure interaction between the air and the kite. It therefore should make sense that modelling such interactions is no straightforward task. Many attempts have been made, for example at TU Delft, where a spin-off company called Kitepower develops their own kites. Take for example their Kitepower V3A Leading Edge Inflatable (LEI) kite. Steady-state Reynolds Averaged Navier-Stokes (RANS) simulations have been performed by Demkowicz [7] and Lebesque [1], while a Vortex Step Method has been developed by Cayon [2]. What is missing is reliable aerodynamic validation data that can be used to validate these simulations and models. While Demkowicz' and Lebesque's simulations were steady state, Cayon's model is able to model deformations, but can also model steady-state. This, together with the reason that scaling down such a complex aeroelastic problem, is the reason for the experiment conducted in this thesis.

Therefore, the research objective of this thesis is:

> "To design and conduct an experimental study to obtain steady-state aerodynamic validation data for the Kitepower LEI V3A Kite, rigidized to avoid aeroelastic scaling issues."

This research objective served as a guide for the literature review, which is presented in chapter 2. After that, the methodology of the model and support structure used in the experiment is discussed in chapter 3. Using that information, the experimental setup is outlined in chapter 4. Then, chapter 5 elaborates on the different test cases that were measured during the experiment. Before analyzing the results, a chapter is dedicated to explaining how the data processing took place, in chapter 6. After that, the results of the experiment is explained and discussed in chapter 7. Finally, the conclusions drawn and recommendations for future work are given in chapter 8.

2

Literature review

This chapter focuses on giving an overview of the available literature on Leading Edge Inflatable (LEI) kites, as well as the research objective and research questions. First, the aerodynamics of LEI will be presented in section 2.1. Then, in section 2.2, a discussion of the computational models and studies performed on LEI kites is presented. Furthermore, the results of previous experimental studies on soft-wing kites will be evaluated section 2.3. Lastly, the research gap will be identified and the research objective and questions will be presented in section 2.4.

2.1. LEI kite aerodynamics

In this section, the aerodynamics of a LEI kite will be discussed to gain a better understanding of the whole system. First, the operational cycle will be discussed in subsection 2.1.1. Then, the geometry of the kite studied in this thesis will be given in subsection 2.1.2. Lastly, the flow characteristics will be discussed in subsection 2.1.3.

2.1.1. Operational phase of a LEI kite

To better understand the aerodynamics of a LEI kite, it is essential to examine its behavior during the operational phase. It consists of two main phases: the traction phase and the retraction phase. During the traction phase, the kite is reeled out and energy is generated. This is done by maximizing the traction force on the tether by flying in fast crosswind motions. During the retraction phase, the kite is reeled in by the generator, using a fraction of the energy generated during reel out. The loads should be minimal in this case to minimize energy consumption, which is done by depowering the kite by decreasing its angle of attack [8]. During the reel-in phase, not only do other flow conditions such as the side-slip angle fluctuate, but the inflow also varies. The side-slip angle refers to the angle between the kite's heading and the inflow direction. The flight path during this operational cycle is depicted in Figure 2.1. During a pumping cycle, the overall performance of the system is based on multiple factors, including system control, structural dynamics, aerodynamics, and flight dynamics [8].

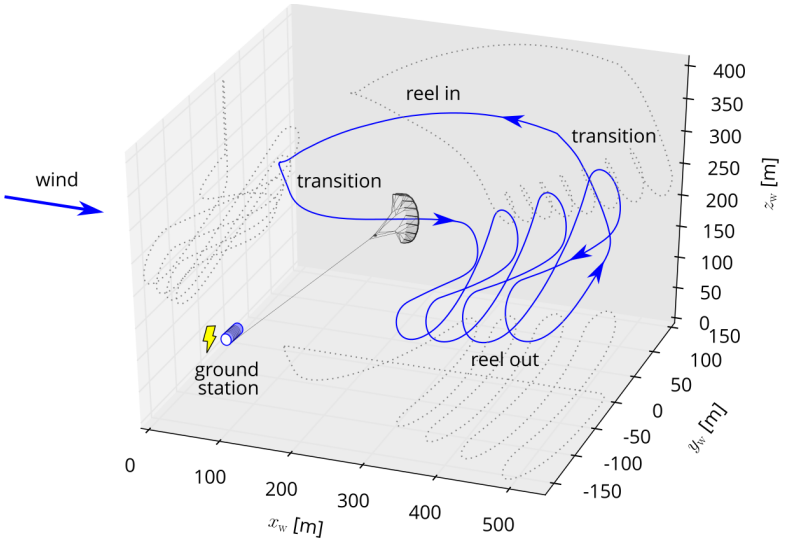

Figure 2.1: Flight path of a pumping kite power system by Fechner [9].

The top-level aerodynamic parameters on which the kites' behavior depends will be briefly mentioned here, while a more detailed analysis will be presented in the following sections. According to Fechner and Schmehl [10], these top-level parameters are the projected surface area of the kite, the lift-to-drag ratio, the maximum wing loading, and the de-power capability (sometimes referred to as the power setting). One should note here that the lift-to-drag ratio also includes the influence of the tether because it certainly influences the kite's overall coefficients. Furthermore, the efficiency of the pumping cycle is most significantly impacted by the de-power capability.

2.1.2. LEI kite components and geometry

Throughout its operational cycle, the LEI wing is subjected to a diverse range of aerodynamic conditions. Before these aerodynamic characteristics can be explained, the components and geometry of the Kitepower LEI V3A kite (the kite on which this thesis is focused) will be elaborated upon.

A photograph of the V3A can be found in Figure 2.2. The V3A consists of a tubular inflatable frame, pressurized with air. The frame consists of a leading edge (LE) tube and strut-wise tubes in the chord-wise direction. The canopy (also called the membrane) is what connects the tubes and forms the LEI kite together with the tubular frame. Furthermore, the rear end of the kite is called the trailing edge (TE). Then, the control pod (also called the Kite Control Unit (KCU)) is connected to the kite by bridle lines, connected to either the LE or TE. The bridle lines connected to the LE are called power lines, whereas the bridle lines connected to the TE are called steering lines. The reason for this name is that the power lines carry the bulk of the force, while the steering lines are responsible for controlling the kite. Lastly, the tether is what connects the kite to the ground station.

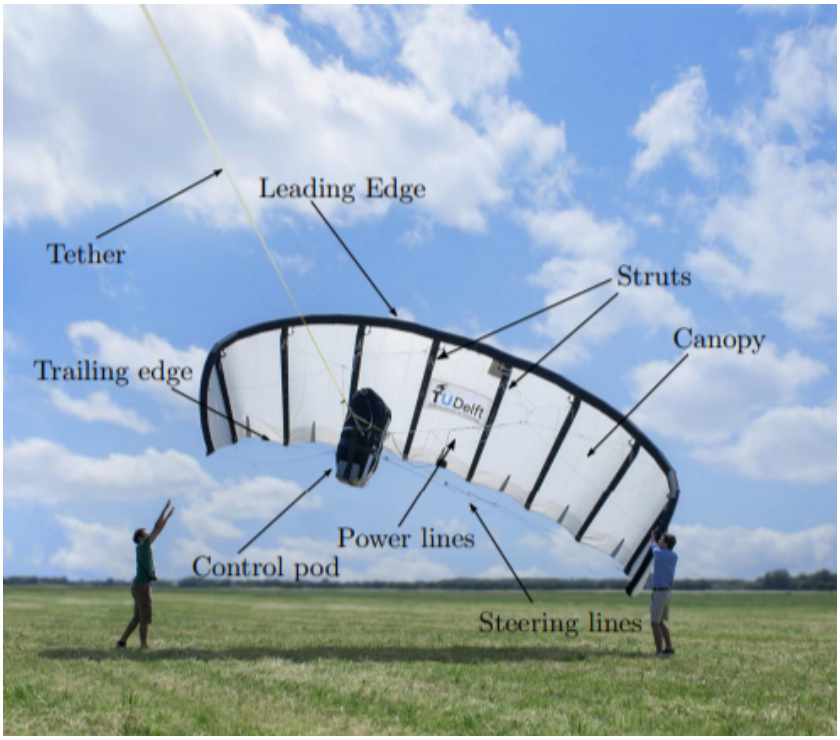

Figure 2.2: Kitepower LEI V3A kite with the different components indicated [11].

A more detailed overview is presented in Figure 2.3, where a graphical representation of the kite is depicted. On the left, a front view of the kite system is shown, with the power and steering lines indicated in different colors. On the right, a side view of the kite is presented. Furthermore, the most important geometric parameters are also presented. The root chord is $c_r = 2.7$ m and the projected wingspan is $b_{proj} = 8.3$ m, resulting in an aspect ratio of $AR = 3.1$.

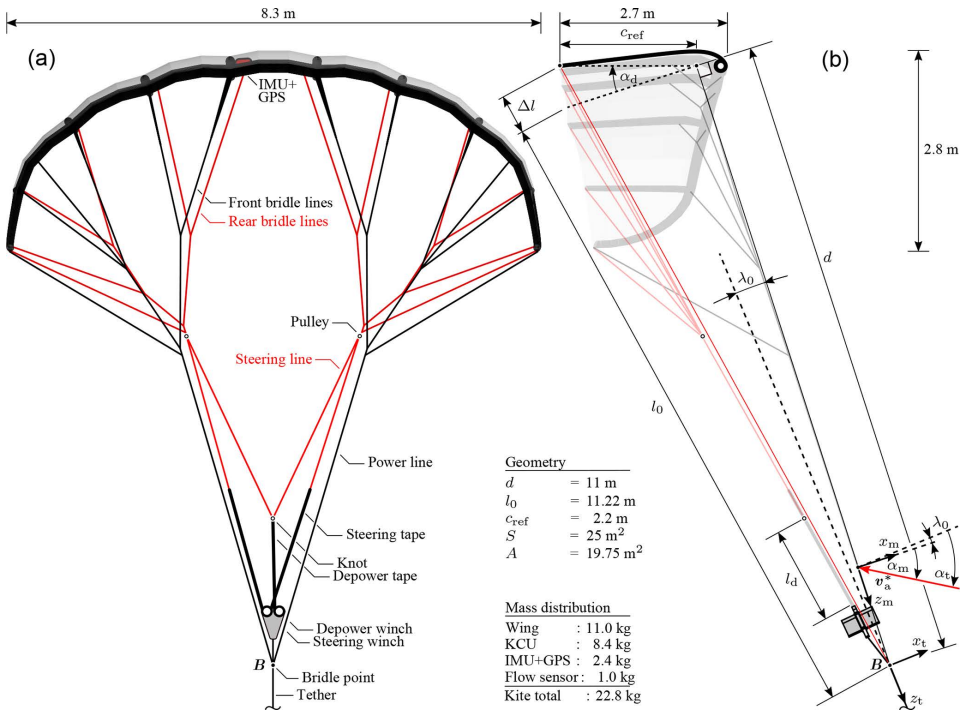

Figure 2.3: Kitepower LEI V3A kite with bridle line system and Kite Control Unit (KCU) [12].

2.1.3. Flow conditions of LEI kite

Now that the components and geometry of the kite have been elaborated upon, the flow conditions can be discussed. Due to their flexible structure, LEI kites exhibit a high uncertainty in flight path data. The orientation of the kite relative to the airflow is influenced by its current deformation state. Oehler et al. [12] made an effort to take flight measurements on the LEI V3A kite by mounting pitot tubes and a wind vane to the bridle line system. In this way, the angle of attack, the angle of side-slip, and the apparent velocity could be deduced.

Throughout the traction phase, the angle of attack varied between $6°$ and $16°$, with an apparent flow speed of approximately $U_a = 18$ m/s. Conversely, in the retraction phase, the angle of attack fluctuated from $-8°$ to $4°$, and U_a was less than 15 m/s. The apparent velocity during the entire flight ranged from 3 m/s to 26 m/s, corresponding to Reynolds numbers of $5 \cdot 10^5$ and $4.5 \cdot 10^6$, respectively. Nevertheless, the side-slip angle remained minimal during straight flight and only increased by about $\pm 10°$ during sharp turns. These measurements have been done using the soft kite itself, meaning that the chord length changes continuously during flight as the kite changes shape. Therefore, a sidenote should be placed here as the chord length can not be measured. Furthermore, the accuracy of the pitot-tube is therefore also questionable.

In Figure 2.4, the flow topology of an airfoil of a LEI kite is presented. The leading edge is a tube with an attached canopy that forms the airfoil, which is often called a sailwing. Extensive research has been done on sailwings, but they will not be included here since they have already been reviewed by Demkowicz [7]. Readers will be referred to his work for further details on sailwings.

The suction side of such airfoils is similar to that of conventional airfoils, whereas the pressure side is not. In Figure 2.4, the first thing that can be observed is the laminar separation bubble. LEI kites experience lower Reynolds numbers during flight compared to, for example, aircraft [13]. The flow around the kite may even be laminar. A laminar boundary layer is known to be less able to resist an adverse pressure gradient compared to a turbulent boundary layer, resulting in laminar flow separation [14]. However, the separated flow has the potential to transition and reattach, creating a laminar separation bubble between the separation and reattachment points. Finally, trailing edge separation on the suction side can happen at high angles of attack.

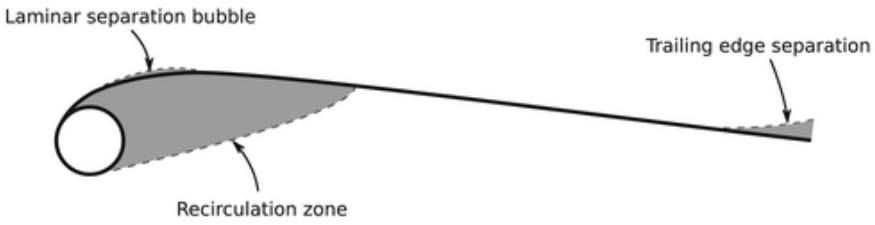

Figure 2.4: Flow topology around a LEI kite airfoil [13].

On the suction side in Figure 2.4, a recirculation zone can be observed, which is formed due to the circular leading edge of the airfoil. The extent of this recirculation zone is influenced by the manner in which separation occurs from the circular leading edge. Given that laminar and turbulent boundary layers exhibit distinct separation characteristics, this can significantly affect the size of the recirculation zone [13]. Another effect caused by the circular leading edge of the airfoil is drag crisis. The drag crisis refers to a phenomenon observed in cylinders, where there is a sudden reduction in drag as the boundary layer flow transitions from laminar to turbulent [15].

2.1.4. Flexible membrane aerodynamics

Flexible membranes have been the subject of extensive research due to their unique aerodynamic properties that are beneficial in various applications [16, 14, 17, 18, 19]. Unlike rigid wings, flexible

membranes adapt their shape in response to aerodynamic loads. This dynamic reshaping allows them to modify their effective camber to reduce boundary layer separation on the suction side, resulting in higher lift coefficients compared to rigid structures [14]. However, this characteristic also introduces more abrupt stall behavior, as can be seen in Figure 2.5. In this figure, the lift coefficients of a rigid wing is compared to the wing coefficients of several flexible wings, with increasing flexibility where the highest Batten is the least flexible.

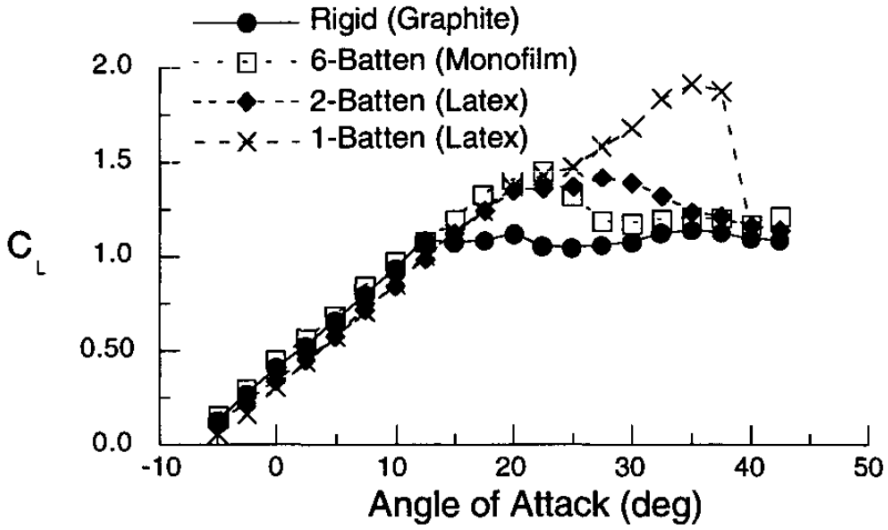

Figure 2.5: Lift curves of rigid versus flexible wings [18].

Several studies, including those of Leuthold [19], have documented the increase in the lift coefficient under attached flow conditions, highlighting two main nonlinear flow phenomena: low-lift hysteresis and separation. Hysteresis is attributed to the membrane's sensitivity to pressure changes, which can lead to significant variations in shape under low lift conditions, potentially causing uncontrollable aerodynamic behavior [20]. Separation will not be discussed here, as was already discussed in subsection 2.1.3.

In the context of LEI kites, the interaction of complex flows involving laminar and turbulent flows, separation, recirculation zones, and fluid-structure interaction presents significant challenges in modeling and experimental validation. Understanding these interactions is crucial for improving the design and performance of LEI kites in Airborne Wind Energy Systems (AWES).

2.2. Computational models of LEI kites

In this section, the existing computational models of LEI kites will be discussed and compared. This is necessary to understand the current state of research, identify knowledge gaps, and provide a foundation for future improvements in the design and performance of LEI kites. Various methods have been formulated over time, each tailored to the desired level of detail. As mentioned previously, the computational models reviewed in this section will not include sailwings.

2.2.1. Simplified aerodynamic models

One of the faster and and lower fidelity aerodynamic models of a LEI kite was developed by Fechner et al. [21]. The goal was to develop an approach that modeled the kite and the tether as a particle system. In this study, two models were developed, namely a one-point model and a four-point model. A representation of both models is shown in Figure 2.6. The difference between the models is that the one-point model represents the kite as a point mass, whereas the four-point model has the mass of the kite distributed over the four points. This meant that the four-point does have rotational inertia and can correctly respond to steering inputs. Each model uses an identical atmospheric model derived from the power law to calculate wind speed at various heights. Then, through state-space parameters, the angle of attack at each point is determined. The lift

and drag forces are calculated by reference data for stalled and attached flow over airfoils, with adjustments made specifically for the LEI wing. The findings of the study were that The one-point model, incorporating the turn-rate correction, more accurately predicts the influence of gravity on the turn rate compared to uncorrected point mass models. Additionally, the four-point model offers a more realistic dynamic response to steering inputs than simpler models while remaining capable of real-time operation. In conclusion, there is no actual LEI kite geometry used in this study, merely airfoil reference data and corrections. In a follow-up study by Roullier, a three-point model was used instead of the one- and four-point models [22].

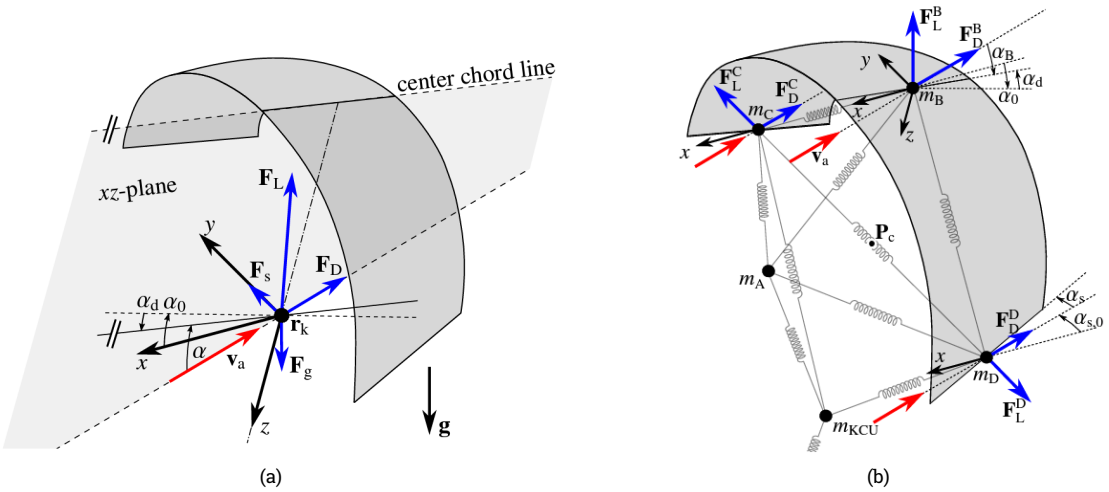

Figure 2.6: One-point (a) and four-point (b) LEI kite models developed by Fechner et al. [21].

Breukels [23] developed a more advanced model for kite aerodynamics. The model used a more parametric based approach, in which the kite is divided in a number of 2D cross-sections. The properties of these cross sections were determined by an algorithm that takes the airfoil thickness, camber, and angle of attack and outputs the lift, drag, and moment coefficient of that cross section. These outputs were determined using lookup tables based on 2D RANS simulations of the different airfoil parameters. The airfoils were divided into 6 nodes, at which the integral forces are determined through arbitrary weighting functions. A representation of this can be found in Figure 2.7. Then, to account for 3D effects, Breukels implemented a correction based on an analysis of a vortice lattice method (VLM) of an arbitrary kite. Nonetheless, Bosch [24] highlighted that Breukels' assumptions are impractical for kites subjected to high angles of attack, near-stall scenarios, and significant deformations. He therefore did not use this correction in his study.

2.2.2. Potential flow methods

Potential flow methods use mathematical techniques to solve fluid flow problems for ideal, incompressible, and inviscid fluids. Assuming irrotational and often incompressible flow, these methods simplify the problem. Flow around an object is represented by vortices, inducing velocity at each point per the Biot-Savart law. Vortices create irrotational flow except at their centers, where velocity singularities occur. The lift generated by a vortex is proportional to its strength, as described by the Kutta-Joukowski theorem [25]. Depending on their arrangement, vortices are called "vortex particles" (discrete positions), "vortex filaments" (continuous loops), or "vortex sheets" (continuous surfaces). Potential flow methods balance speed and accuracy, making them efficient for quick analysis and simulations. They are used in aerodynamics, hydrodynamics, and engineering, including modeling airflow around LEI kites for performance optimization. This section will briefly discuss the different methods available.

Vortex panel methods

The simplest form of potential flow methods is the 2D panel method. This method involves discretizing the surface of an airfoil into panels that can represent sources, doublets, or vortices. By

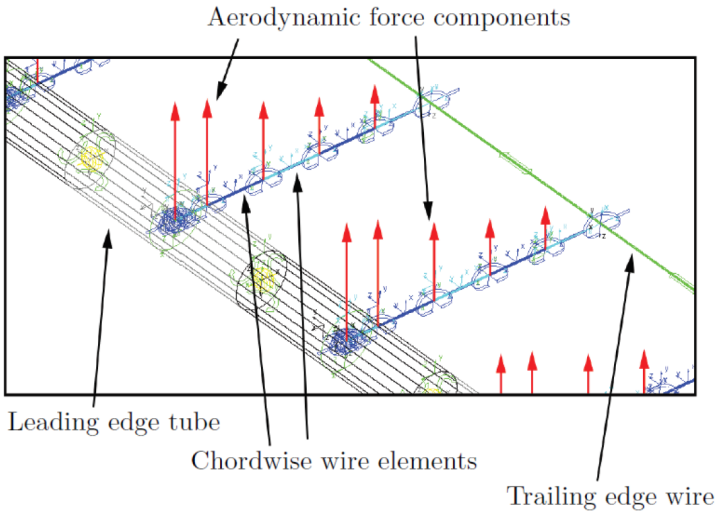

Figure 2.7: Breukels divides the airfoil into 6 nodes [23].

applying boundary conditions such as the non-permeability at the surface and the Kutta condition at the trailing edge, the system of equations can be solved to determine the lift coefficient and pressure distribution over an airfoil [26]. The 2D panel method can be extended to three dimensions using the Lifting Line Method (LLM) or the Vortex Lattice Method (VLM) through the Biot-Savart law.

Gaunaa et al. [27] conducted a study where they developed a technique that integrates VLM with 2D airfoil data using an algorithm designed to adjust for viscous effects and airfoil thickness. In Figure 2.8, the C_L vs. α, the C_L vs. α, and the C_L vs. C_D plot can be found. A comparison is made between the standard VLM, the VLM with the correction algorithm and CFD results obtained by an in-house developed RANS code. The lift coefficients for both the algorithm and CFD cases agree well, showing the viscous correction's effectiveness. However, the VLM with the algorithm shows slightly worse drag performance at higher pitch angles without a specific reason provided. The lift-to-drag coefficient curve correlates significantly better with CFD for the VLM with the algorithm.

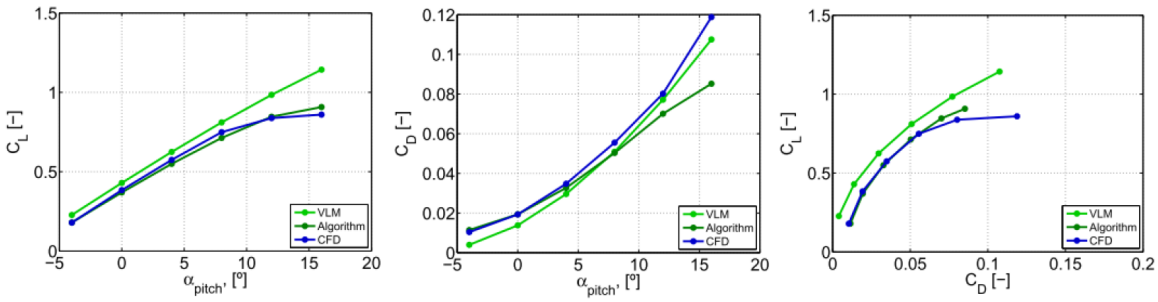

Figure 2.8: Comparison of lift coefficients simulated by regular VLM, 3D CFD, and VLM with viscous correction as obtained by Gaunaa et al. [27].

Vortex particle methods

Vortex particle methods place discrete vortex particles in the flow field to represent vorticity. These particles are often located at the nodes of a uniform grid [28], with the vorticity of each particle distributed over a small finite radius [29]. This method closely represents flow physics and is particularly suitable for modeling flows around morphing bodies, such as soft kites.

Vortex filament methods

In vortex filament methods, point vortices are arranged into deformable lines or filaments. These methods are based on the Helmholtz and Kelvin theorems, which state that vorticity tubes retain their identity and move as material elements in an inviscid flow [29]. A prominent example of this is Prandtl's lifting line theory, which replaces chord-wise circulation with a single concentrated vortex that forms a horseshoe vortex system [30].

Another vortex filament method, called the Vortex Step Method (VSM) or Weissinger Method, is a numerical technique used to model the aerodynamic properties of wings, particularly those with unconventional geometries and low aspect ratios. Based on Prandtl's classic lifting line theory (LLT), VSM involves discretizing the wing into a series of horseshoe vortices and imposing a boundary condition at the three-quarter chord position, as per Pistolesi's theorem [31], to accurately calculate the lift distribution [32]. This method addresses the limitations of LLT, particularly its inaccuracies with non-linear lift slopes near stall conditions and unconventional wing geometries, by iterating the circulation distribution until convergence is achieved.

In a study by Cayon [2], the VSM is implemented to analyze the aerodynamic performance of the Kitepower LEI V3A Kite. The model uses the structural model developed by Poland [33]. The methodology involves creating the wing geometry, setting up the aerodynamic influence coefficient (AIC) matrix, and initializing the circulation distribution. Iterative calculations adjust the circulation to meet the convergence criteria, ensuring accurate force and direction estimations along the wing sections. The process incorporates the Kutta-Joukowski theorem and accounts for the relative velocity at each wing section, iterating until the circulation distribution stabilizes.

The results demonstrate that the VSM can effectively model the aerodynamic behavior of LEI kites, providing accurate predictions for both low- and high-aspect ratio wings. Comparisons with computational fluid dynamics (see Figure 2.9) show that the VSM achieves high accuracy in predicting lift and drag coefficients under various flight conditions, confirming its suitability for unconventional wing designs used in kites [2].

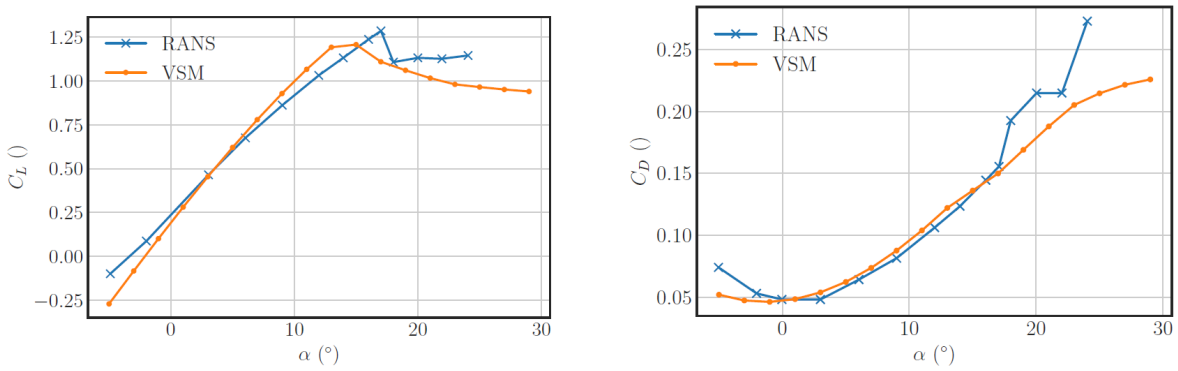

Figure 2.9: Lift and drag curve comparison between VSM and CFD (reproduced from Cayon [2]).

Applications and Enhancements

Potential flow methods have been extensively used in various applications, including the aerodynamic analysis of yacht sails and kites. Early yacht sail theories used irrotational inviscid flow assumptions combined with thin airfoil theory [34]. These methods have been enhanced to account for some viscous effects through viscous corrections, integral boundary layer methods, and thick wake models. For example, Fiddes and Gaydon [35] combined a 3D free-wake vortex lattice method with an integral boundary layer method to correct for viscous effects on yacht sails. Similarly, Lorillu et al. [36] developed a potential flow method with a Helmholtz thick wake model to predict flow separation on 2D yacht sails.

Despite their computational efficiency, potential flow methods have significant limitations. They struggle with accurately predicting flow separation and the presence of boundary layers. For example, studies on parawings and kites using potential flow methods have shown difficulties

in representing three-dimensional effects and accurately predicting performance at high angles of attack [37].

2.2.3. Computational Fluid Dynamics

Since the LEI wing operates under a wide range of flow conditions, it is crucial to evaluate its performance in this spectrum. As discussed previously, potential flow methods struggle with separation, reattachment, and side-slip. Furthermore, they do not account for the transition from laminar to turbulent flow, which significantly affects flow behavior, as highlighted in subsection 2.1.3. Computational Fluid Dynamics (CFD) offers a better approach to handling these aspects. Different CFD models exist, and each model has their own assumptions and complexity. The most widely used methods are presented in Figure 2.10, with increasing complexity ascending the pyramid.

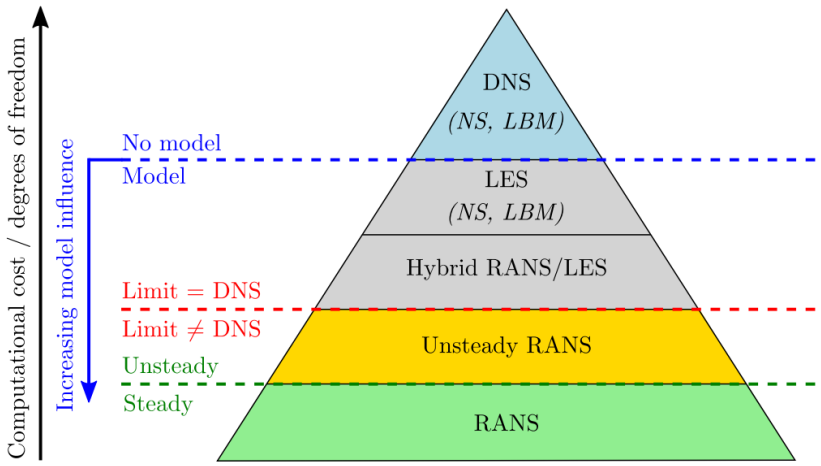

Figure 2.10: Hierarchy of most commonly used CFD methods with different levels of complexity [38].

A list with descriptions is provided below, based on the work of Versteegh and Malalasekera [39].,

- **Direct Numerical Simulation (DNS)** represents the pinnacle of turbulence modeling, capturing all turbulent scales with precision that depends entirely on numerical settings, such as discretization methods and boundary conditions. DNS employs either the Navier-Stokes (NS) equations, which govern Newtonian fluid dynamics, or the Boltzmann equation, which, based on the kinetic theory of gases, can be simplified to derive the NS equations through perturbation.
- Just below DNS is **Large Eddy Simulation (LES)**, which resolves larger turbulent scales while modeling the smaller ones. LES can use both NS equations and the Lattice-Boltzmann method (LBM). While LES can approximate DNS when fully resolving turbulence, it is often combined with Reynolds-Averaged Navier-Stokes (RANS) equations in a hybrid approach to lower computational costs by averaging the largest turbulence scales and solving the fluctuations with LES.
- **RANS equations**, which can be used independently or with LES, model all turbulence scales by separating the mean flow from its fluctuations through Reynolds or Favre decomposition. RANS describes the statistically averaged flow but may face convergence issues in unsteady flows.
- The **Unsteady-RANS (URANS)** method addresses this by considering periodic and deterministic phenomena, recovering periodic fluctuations, and statistically modeling chaotic turbulence.

Having outlined various CFD methods, the existing literature on CFD studies specifically focused on the Kitepower LEI V3A Kite will now be reviewed. This section will not provide a review of the CFD methods applied to various flexible membranes and kite geometries. The reader is referred

to the literature reviews by Deaves [40], Demkowicz [7] and Lebesque [1], where these methods have been systematically reviewed. For an LEI kite like the V3A , CFD methods are feasible only when the kite is in steady state, or, in other words, when it does not deform. This is because a soft kite constantly changes shape while flying. Each deformation requires the creation of a new mesh, which is extremely time consuming. This is why the methods described next all have made the same steady-state assumption.

Folkersma et al. [13] performed a 2D steady-state RANS simulation with transition modeling on a sailwing and on a LEI kite. Thus, it posed as a validation study. In this review, only the simulation on the LEI kite will be reviewed as previously mentioned. The Reynolds numbers simulated by Folkersma et al. [13] ranged from 10^5 to $5 \cdot 10^7$. This has been chosen purposefully as it encompasses the full operational range of the kite. The lift curve and drag polars of the LEI kite without transition modeling are presented in Figure 2.11. The general patterns are consistent with those observed in conventional airfoils [41]. As the Reynolds number increases, the lift coefficient increases while the drag decreases, resulting in enhanced aerodynamic performance. In addition, the critical stall angle increases, leading to higher maximum lift coefficients.

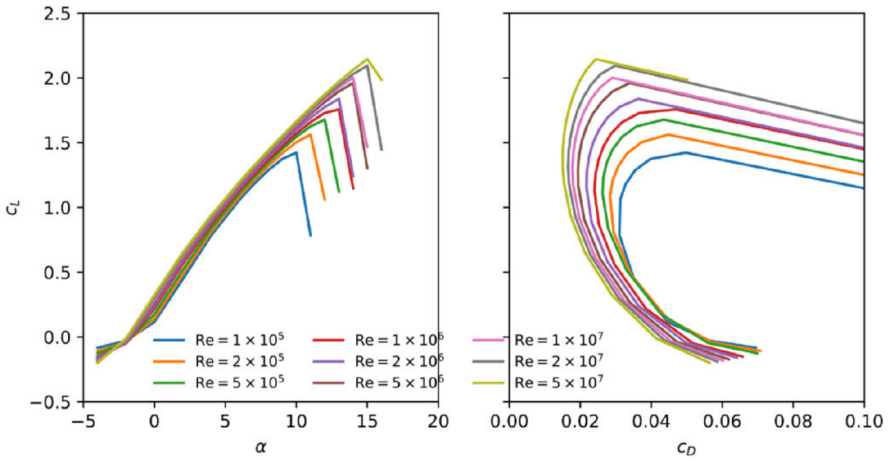

Figure 2.11: Lift curves (left) and drag polars (right) for several Reynolds numbers without transition modeling [13].

The same plots for the model with transition modeling are presented in Figure 2.12. Compared to Figure 2.11, there are several differences. There is a larger spread in both lift and drag coefficients in the simulations with transition modeling. This change comes from the laminar separation bubble disappearing at higher Reynolds numbers, as explained by Folkersma et al. [13].

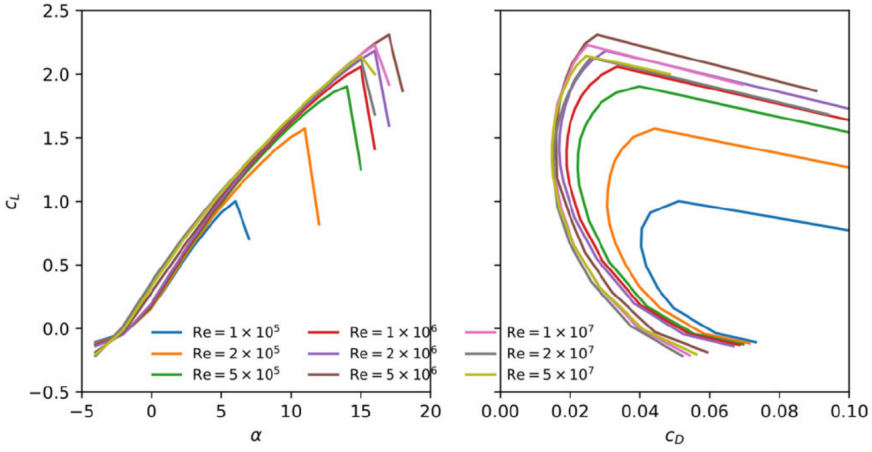

Figure 2.12: Lift curves (left) and drag polars (right) for several Reynolds numbers with transition modeling [13].

Demkowicz [7] performed a study on the Kitepower LEI V3A Kite, using the same setup as Folkersma et al. [13] and extending it to 3D. In this study, the aerodynamic performance of the V3A without struts has been analyzed. Demkowicz developed a novel mesh for the kite, which is more suitable for CFD simulations. Shortly after, Lebesque [1] built upon this work by studying the effect of adding chordwise struts in the kite model. In this study, the same simulation setup as in Demkowicz' work [7] was utilized. Both studies included transition modeling in their simulations, and only included a half-wing simulation because symmetry was assumed. A comparison between the lift and drag curves at zero sideslip angle ($\beta = 0°$) is presented in Figure 2.13. As can be seen in the figure, the differences are minimal. However, for $Re = 3 \cdot 10^6$ and $Re = 15 \cdot 10^6$, there is a slight difference in drag after reaching the stall angle. Lebesque explains these variations as being due to the differences in lift, which subsequently cause changes in lift-induced drag [1]. Furthermore, for $Re = 0.1 \cdot 10^6$, the drag is slightly higher for the study with struts. This is likely due to laminar flow at lower Reynolds numbers [1].

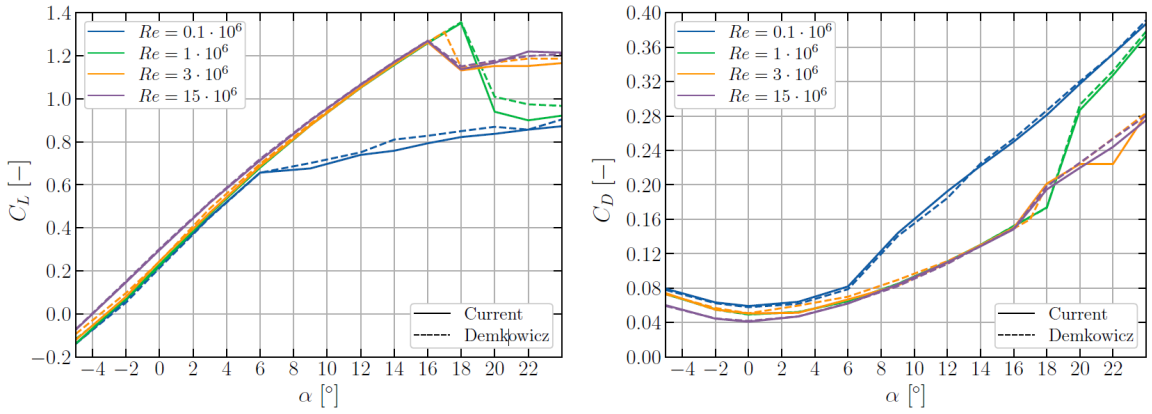

Figure 2.13: Comparison between lift and drag curves of Lebesque [1] and Demkowicz [7] for zero sideslip. Lebesque included chordwise struts, while Demkowicz did not.

Lebesque also investigated the effect of the struts for cases with non-zero sideslip angles. A comparison with Demkowicz' work is presented in Figure 2.14. In this figure, the lift coefficient, drag coefficient, side-force coefficient and lift-to-drag ratio have been plotted versus the sideslip angle β. The flow conditions are $\alpha = 12°$ and $Re = 3 \cdot 10^6$. Again, there are minimal differences between the simulations with and without struts, with no differences in side-force. Lebesque attributes these slight differences to the marginal differences in the lift and drag coefficients, as presented in Figure 2.13.

2.3. Experimental methods

RANS CFD simulations have proven to be a valuable asset in simulating aerodynamic models over the years. However, at this point in time, there is simply not enough computational power to fully solve a flowfield using a higher fidelity method such as DNS. Therefore, researchers must resort to experimental testing to obtain physically accurate data. However, there will always be certain challenges to overcome in these experiments.

Wind tunnel testing is a common type of experiment that is used to gain aerodynamic insights. Large amounts of data can be collected in a wind tunnel test. Over the years, methodologies have been developed to aid in this process, for example, by Rae and Pope [42]. The test sections of these wind tunnels are often not large enough to fit full-scale models, which is why these models should be scaled down. This is a manageable problem for rigid models, as only aerodynamic scaling needs to be considered. However, for flexible models like the V3A, it is nearly impossible because the structural properties do not scale down the same as the aerodynamic properties due to the flexible membrane [12]. For this reason, De Wachter [43] took a full-scale model of a ram-air kite into a wind tunnel to study its aerodynamic and structural behavior. Under certain loading conditions, a CAD model was generated using photogrammetry on which several CFD studies

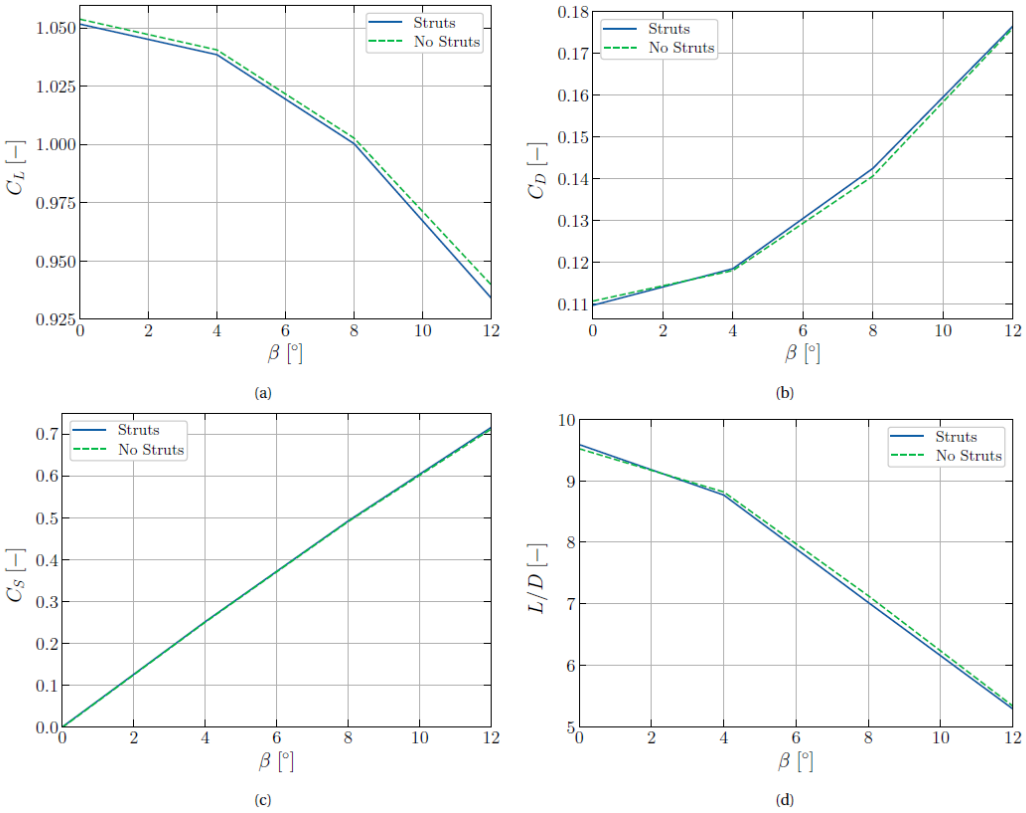

Figure 2.14: Comparison between lift and drag curves of Lebesque [1] and Demkowicz [7] for non-zero sideslip. The plots have been generated for $\alpha = 12°$ and $Re = 3 \cdot 10^6$. Lebesque included chordwise struts, while Demkowicz did not.

have been performed. The findings from these studies significantly deviated from De Wachter's experiment due to the influence of wind tunnel wall effects and the fact that the CFD studies were conducted outside of a wind tunnel environment. It was evident that full-scale wind tunnel tests was unfeasible, and that other methods should be utilized.

Due to the aforementioned reasons, researchers started to investigate the possibilities of field and in situ measurements. Hummel et al. [44] developed a highly repeatable test apparatus for flexible membrane wings, as presented in Figure 2.15. The same setup was then used by Python [45] to test three different membrane wings to improve the model by Hummels et al. [44]. However, this testing method faces several challenges, including the physical limit of the traction force, measurement uncertainty caused by wind variations, and the inability to measure the lift-to-drag ratio during dynamic maneuvers [46].

Oehler et al. [12] introduced a novel approach to circumvent the previously mentioned issues. Instead of having the measurement equipment on the ground, an approach to use on-board equipment was used. The kite was then performing routine flight manouvres, during which the flow conditions and kite attitude could be measured. This way, the apparent velocity, angle of attack, lift coefficient and lift-to-drag ratio could be measured for any kite. In Figure 2.16, the lift-to-drag ratio of Kitepower's LEI Kite during the tests of Oehler et al. [12] is compared to the existing models at that time, of Ruppert [47] and Fechner et al. [21]. There is a satisfactory correlation between the models and the experimental data in the figure.

Alongside research on LEI kites, several experimental investigations have been conducted on inflatable wings. The key distinction between these inflatable wings and LEI kites is the airfoil: inflatable wings incorporate a complete airfoil design, whereas LEI kites feature only an inflated leading edge. An overview of all these experimental studies can be found in **??**, where all important technical details are presented. This overview was taken from Desai et al. [48].

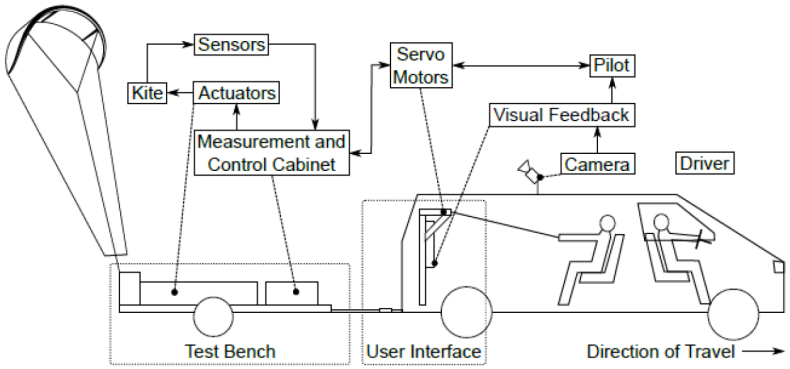

Figure 2.15: Towing test rig developed by Hummels et al. [44].

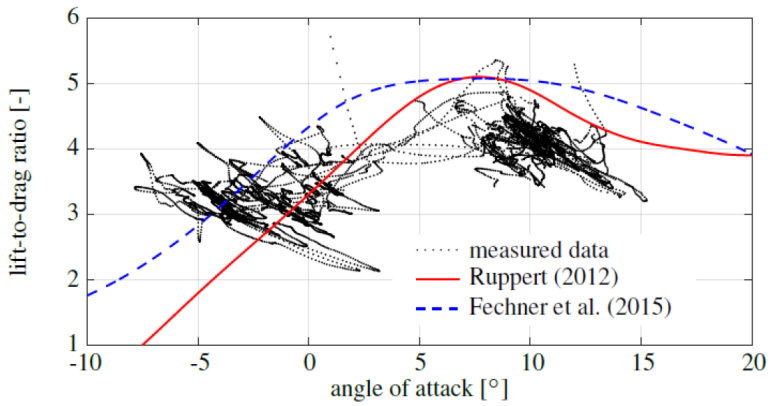

Figure 2.16: Lift-to-drag ratio comparison as measured by Oehler et al. [12] against the results from Ruppert [47] and Fechner et al. [21].

Desai et al. [48] executed wind tunnel tests on two tethered inflatable wings constructed from different fabrics, investigating how material properties and tether setups affect aerodynamic performance. Although the study offered an extensive database for validating aeroelastic models, it was confined to static conditions with a constant angle of attack, thereby neglecting dynamic phenomena such as gust responses and material endurance under prolonged cyclic loads. Likewise, Okda et al. [49] assessed an inflatable airfoil to determine lift and drag coefficients but did not account for three-dimensional deformation effects, nor did they collect displacement data that would have aided in comprehending structural distortions during the experiments. Simpson et al. [50] expanded this research by studying the aeroelastic characteristics of inflatable wings through both wind tunnel and flight testing, albeit primarily concentrating on static conditions without an in-depth examination of flow structures and dynamic behavior. The NASA investigation [51] on the Goodyear Inflatoplane also emphasized the link between inflation pressure and aerodynamic performance in wind tunnel scenarios, but it too did not address the long-term operational robustness of the inflatable design under varying environmental conditions.

Although there have been several experimental studies on flexible membrane kites and inflatable wings as mentioned before, there has never been a wind tunnel test on a rigid kite. However, there exists one particular experimental investigation conducted on a rigid paraglider model. In this study, Belloc [52] performed a wind tunnel experiment on a rigid paraglider wing. A front and top view of the wing used in this experiment can be found in Figure 2.18. As can be seen, the wing is elliptical. Additionally, the kite employs a NACA23015 airfoil, which is typical of the common aerodynamic selections for paragliders.

	Okda et al. [49]	Cocke [51]	Simpson et al. [50]	Desai et al. [48]
Wind Tunnel	Chalmers Low Speed Tunnel	Langley Full-Scale Tunnel	Eiffel Type Low Speed Tunnel	VT Stability Wind Tunnel
Wind Tunnel Cross-Section	1.25 m × 1.80 m (4.1 ft. × 6 ft.)	9.14 m × 18.28 m (30 ft. × 60 ft.)	0.61 m × 0.61 m (2 ft. × 2 ft.)	1.85 m × 1.85 m (6 ft. × 6 ft.)
Wind Tunnel Turbulence	~ 0.15%	0.14% – 1.05%	~ 0.25%	0.016% – 0.033%
Model Geometry	b = 1.00 m c = 1.00 m AR = 1.0	b = 6.70 m c = 1.52 m AR = 4.4	b = 0.45 m c = 0.33 m AR = 1.36	b = 1.17 m c = 0.31 m AR = 3.8
Base Airfoil	NACA 0021	NACA 0015	NACA 4318	NACA 0015
Test Article Configuration	Straight Rectangular	Complete Aircraft	Straight Rectangular	30° Swept Rectangular
Tethers/Cables	No	With Guy Cables	No	LE and TE Tethers
Inflation Pressure, kPa (psig)	50 (7.3), 100 (14.5), 150 (21.7)	20.7 (3)–48.3 (7)	13.8 (2), 27.5 (4), 41.4 (6)	13.79 (2.5)
Test Velocity, m/s	10	16.1 – 31.7	12.8 – 25.6	15 – 32.5
Angle of Attack	−20° to +20°	−12° to +8°	−4° to +16°	2.5°
Re_c	651k	1136 – 1941k	300 – 600k	268 – 634k

Figure 2.17: Overview of experimental studies on inflatable wings.

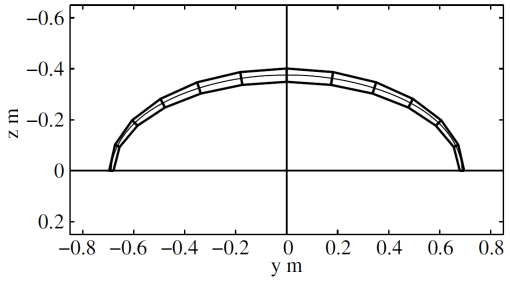

(a) Front view of the kite used in Belloc's experiment [52].

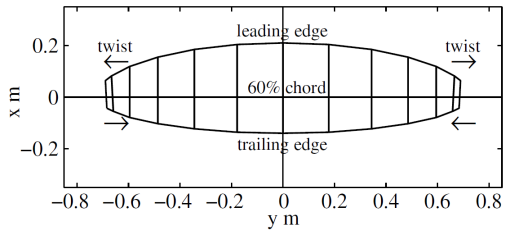

(b) Top view of the kite used in Belloc's experiment [52].

Figure 2.18: Dimensions of the kite used in Belloc's experiment [52].

The experimental configuration is described as follows. The kite model features a spar made of a wood-carbon composite sandwich, designed in the form of an elliptical arch. The volume of the wing comprises 12 panels constructed from polyurethane foam, with a fiberglass coating on the surface. A cylindrical metal mast supports the wing on its lower surface, secured at 60% of the center chord. The wind tunnel has a turbulence intensity of 0.5% and a maximum velocity of 40 m/s. A motorized two-axis device (positioned outside of the flow) controls the angle of attack and the angle of sidelip. A picture of the experimental setup can be found in Figure 2.19. The model is scaled down to a scale of 1:8. The Reynolds number in the experiment $Re = 0.92 \cdot 10^6$, which is high enough to expect similar boundary layer behaviour without risking local laminar flow. [52]

In the experiment, longitudinal and lateral tests were performed. The longitudinal tests were performed by varying the angle of attack from $-5°$ to $22°$ for fixed sideslip angles, while the lateral tests were performed by varying the sideslip angle from $-15°$ to $15°$ for fixed angles of attack.

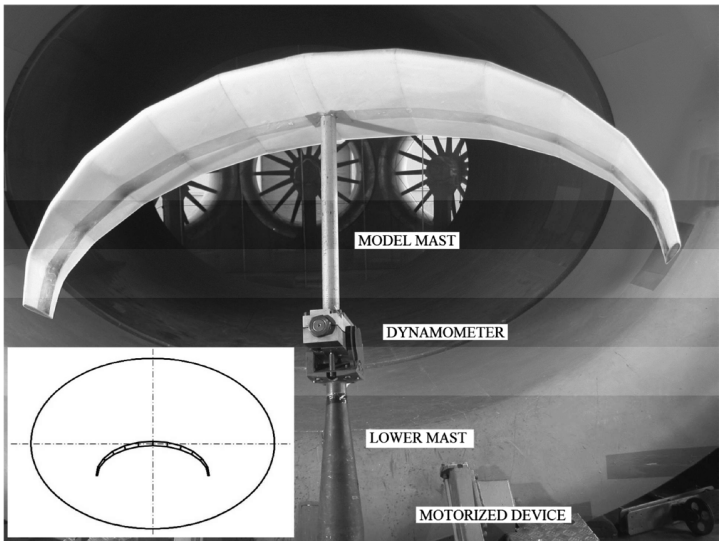

Figure 2.19: Experimental setup of the experiment by Belloc [52].

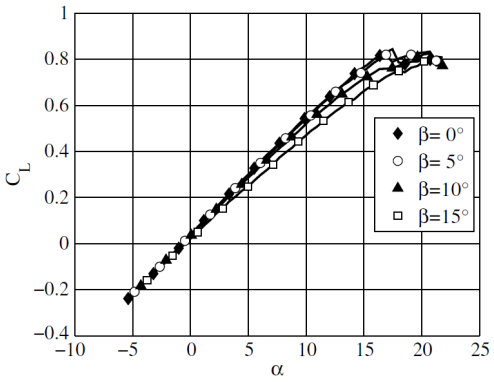

Figure 2.20: Lift curve for different sideslip angles [52].

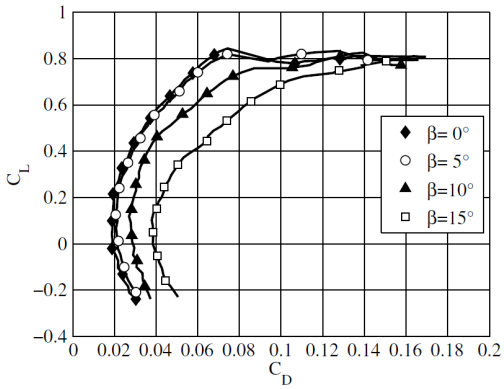

Figure 2.21: Lift-drag polar for different sideslip angles [52].

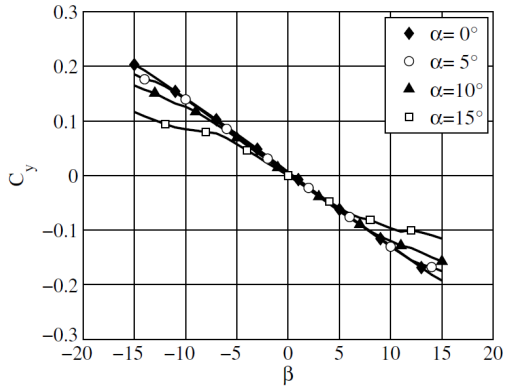

Figure 2.22: Sideforce versus sideslip angle for different angles of attack [52].

In Figure 2.20-Figure 2.22 the different force coefficient curves are presented. It can be seen that, for increasing side-slip angle, the slope of the lift curve is reduced for higher angles of attack. Furthermore, in Figure 2.21, the drag increases as expected for higher sideslip angles. Lastly, the side-force does not depend on angle of attack for lower absolute angles of sideslip, but the

effect grows more prominent for higher absolute angles, which Belloc found is due to a local flow separation near the tip of the kite [52].

2.4. Research questions

The literature review involved an examination of pertinent studies on LEI kites, particularly focusing on the Kitepower LEI V3A kite, its aerodynamics, existing computational models, and experimental results. It was generally found that experimental validation data are limited due to the challenges in scaling down a flexible structure. Additionally, the model by Lebesque [1] also lacks these experimental data. Considering these findings, it would be beneficial to have experimental data for a steady-state scenario. Thus, the author identifies an opportunity to contribute to the scientific community by designing an experiment to obtain these data for the Kitepower LEI V3A Kite. The V3A should be made rigid to achieve a steady-state condition, allowing it to be scaled down without encountering aeroelastic scaling issues. According to the literature, such an experiment on a rigidized LEI kite has not been conducted before. The data from such an experiment could also be used to validate other models that assume or can assume a steady-state, such as the Vortex Step Method developed by Cayon [2]. Belloc's work [52] is regarded as the current state of the art, being the only wind tunnel experiment on a rigid paraglider, which is related to a kite but different as it is not connected to the ground.

Based on the previously identified research gap, the following research objective is formulated:

> **To design and conduct an experimental study to obtain steady-state aerodynamic validation data for the Kitepower LEI V3A Kite, rigidized to avoid aeroelastic scaling issues.**

Based on the research objective, two research questions containing several sub-questions were drawn up.

(i) **How can an experiment be designed such that reliable experimental data for the rigidized Kitepower LEI V3A kite is obtained?**

- How can the kite be rigidized such that it does not deform during the experiment?
- How can a support structure for the kite be designed such that the kite can be tested in a wind tunnel?
- Given the constraints of the wind tunnel, can the Reynolds number match the results in literature, and if not, how does it affect the results?

(ii) **What is the aerodynamic performance of the rigidized Kitepower LEI V3A Kite?**

- What are the lift and drag coefficients of the kite?
- How do the aerodynamic properties change with angle of attack and sideslip angle?
- What is the uncertainty in the data and how can it be quantified?
- To what extent does the data measured in the experiment match the already performed simulations?

3

Methodology

In this chapter, the model and support structure design of the Kitepower LEI V3A Kite wind tunnel test is presented. First, in section 3.1, the wind tunnel used in the experiment is described. Subsequently, in section 3.2, the steps taken in designing the kite model are discussed. Finally, the design of the support structure is explained in section 3.3.

3.1. Wind tunnel

The wind tunnel in which the experiments took place was the Open Jet Facility (OJF) of Delft University of Technology, located at the High Speed Lab. The OJF is a closed-loop wind tunnel capable of reaching a free stream velocity of $U_\infty = 35$ m/s, but in reality this is normally $U_\infty = 25$ - 30 m/s due to high turbulence intensity at high velocities and due to the drag cause by dirty vanes. The wind tunnel test section is located in a large room with a width of 13 m and a height of 8 m. Furthermore, the wind tunnel has an octagonal outlet of 2.85 m by 2.85 m.

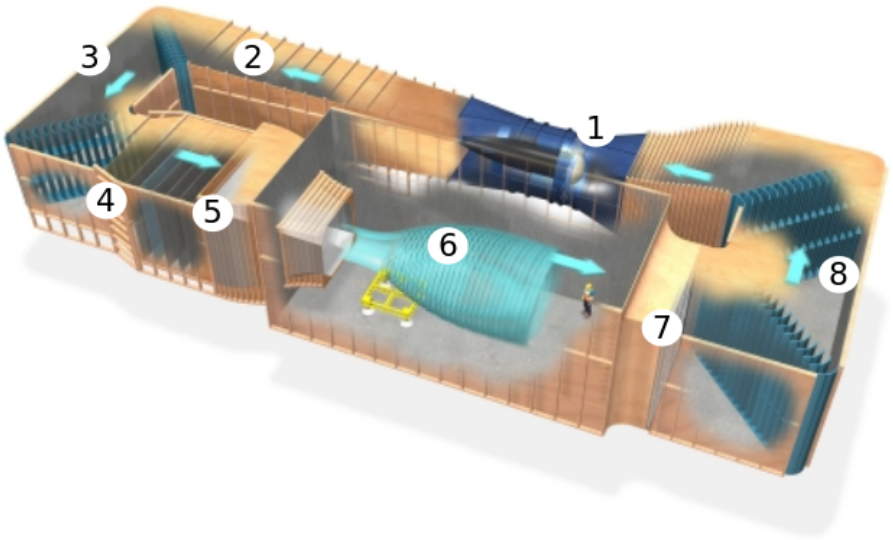

Figure 3.1: Circuit layout of the Open Jet Facility (OJF).

In Figure 3.1, a schematic of the wind tunnel layout is shown. The flow is driven by a large fan (1) powered by a 500 kW electric engine. After this large fan, the flow passes a long diffusor (2), after which it is guided by two rows of corner vanes (3) to rotate the flow 180 degrees. The flow then enters a second short diffusor (4) in which a wire mesh prevents flow separation. In the settling chamber (5) after this, the velocity deviations and turbulence in the flow are reduced to about 1% turbulence intensity [53]. The flow is then blown into the open test section (6). At the end of the test section, the flow is cooled by a 350 kW radiator system (7) to compensate for the added heat in the flow. Unfortunately, during the experiments, this system did not work, resulting in a continuous increase in the flow temperature during the operation of the wind tunnel. Finally, the flow is redirected again by two rows of corner vanes (8) to blow the flow back into the fan.

3.2. Model design

The model to be tested in this wind tunnel is the Kitepower LEI V3A Kite. As mentioned in chapter 2, research on this kite has already been done, namely field experiments by Oehler et al. [12], 3D CFD RANS simulations by Demkowicz [7] and Lebesque [1] and the potential flow model developed by Poland [33] and Cayon [2]. The potential flow model uses 2D airfoil data generated by Breukels' regression model [23], while the CFD simulations by Lebesque and Demkowicz used a high-quality volume mesh of the V3A specifically developed for these simulations. Demkowicz used the original geometry as specified in Figure 2.3, and made several alterations to it. The alterations relevant to this study are mentioned in the following.

- Removal of bridle line system and chordwise struts
- Specification of finite thickness of the canopy.
- Rounded trailing edge connecting upper and lower surface of the canopy
- Filling in behind the LE tube
- Recreation of kite tips

These alterations lead to the airfoil as presented in Figure 3.2. As can be seen, the leading edge has been connected to the canopy. The chordwise position at which it connects is about 25% of the chord. According to Deaves [40], the impact on the flow is negligible since a separation bubble already exists at that location.

Figure 3.2: Comparison of original airfoil (dashed) and airfoil recreated by Demkowicz (solid) at kite symmetry plane [7].

The resulting CAD model of Demkowicz is presented in Figure 3.3. Then, in the study by Lebesque [1], chordwise struts were added to Demkowicz model. A comparison between both CAD models is presented in Figure 3.4, where the lower side is shown.

Lebesque's implementation of the struts was complex due to their typically sharp attachment to the canopy. This posed significant challenges for the CFD meshing software, necessitating the creation of fillets around the edges of the strut, as illustrated in Figure 3.5. Furthermore, the trailing edge was sealed to achieve a closed geometry, as the original design featured open trailing edges (refer to Figure 3.6).

The study by Lebesque [1] found that the inclusion of chordwise struts did not significantly affect the aerodynamic performance of the kite, although there were minor local differences in the flow field. To remain consistent with the original kite design (which includes the struts), this study also opted to include the struts and therefore uses the same model as Lebesque [1].

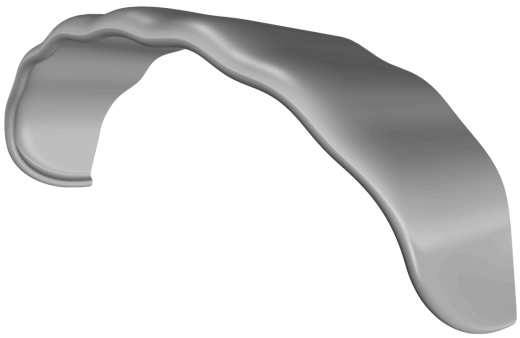

Figure 3.3: Perspective view of the V3A Kite CAD model developed by Demkowicz [7].

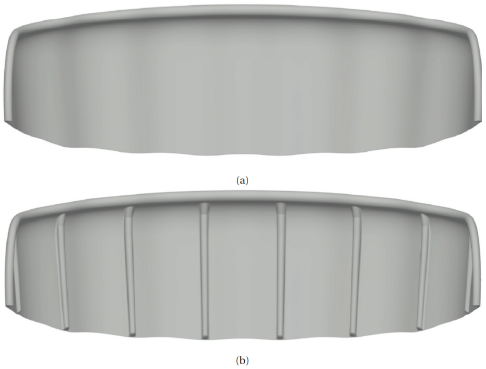

Figure 3.4: Lower side of CAD model used in the study Demkowicz [7] (a) and Lebesque [1] (b).

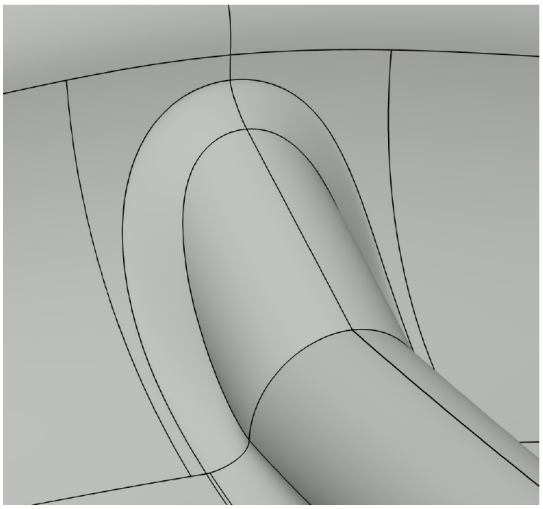

Figure 3.5: Strut integration visualized around the leading edge [1].

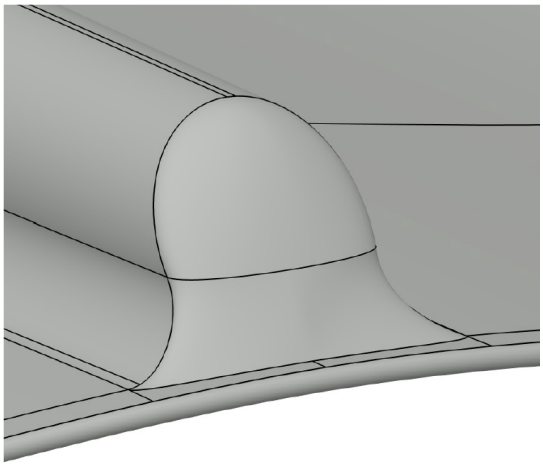

Figure 3.6: Strut integration visualized at the trailing edge [1].

3.2.1. Coordinate system definition

To effectively analyze the aerodynamic performance of the rigidized LEI kite, a coordinate system is defined that facilitates the description of the orientation of the kite and the forces acting on it during the wind tunnel tests. The right-handed coordinate system is defined as follows:

- The x-axis runs along the longitudinal direction of the wind tunnel, pointing downstream.
- The y-axis is oriented laterally, pointing to the left when facing downstream.
- The z-axis is vertical, pointing upwards.

Figure 3.7a illustrates the xz-symmetry-plane, capturing the longitudinal and vertical dimensions of the kite. The chord line c_{sym} is also drawn. This plane is crucial for analyzing pitch moments and vertical aerodynamic forces. Similarly, Figure 3.7b depicts the yz-plane, representing the lateral and vertical dimensions of the kite, which is essential for examining yaw moments and side forces. The projected wing span b_{proj} and height h are also defined.

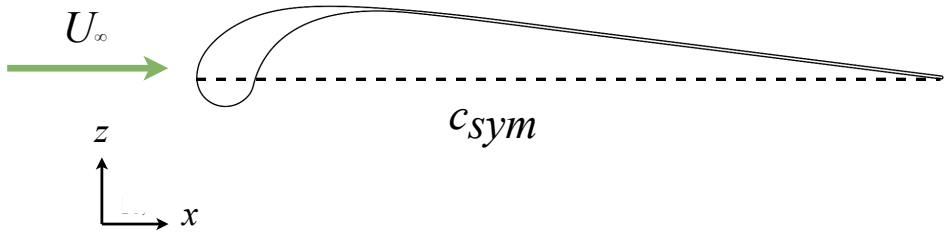

(a) xz-symmetry-plane of the kite.

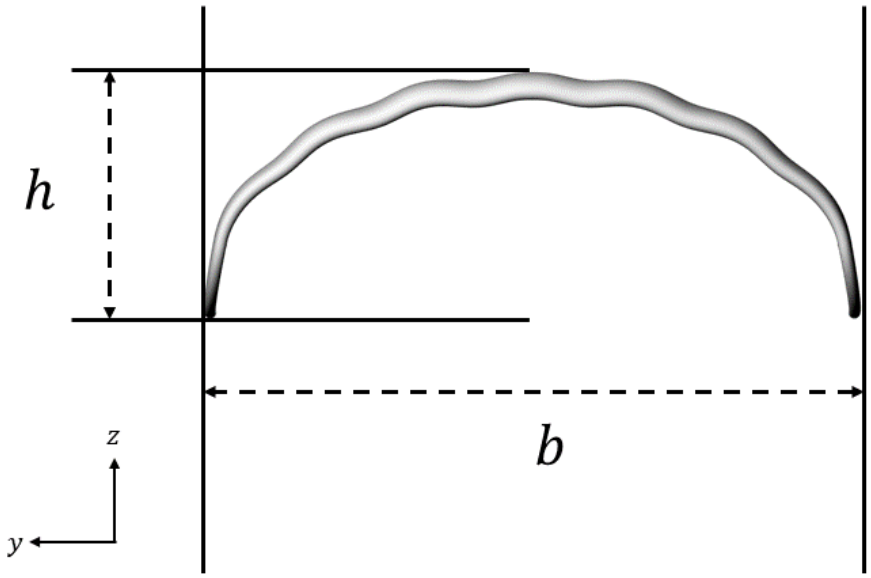

(b) yz-plane of the kite.

Figure 3.7: Coordinate system and geometry of the kite model.

By setting up this coordinate system, the aerodynamic properties of the LEI kite can be methodically assessed under various scales and wind conditions. The xz-plane and the yz-plane offer distinct references for examining the kite's performance and the forces acting on it during wind tunnel experiments.

3.2.2. Scale selection

The selection of the wind tunnel model scale is a critical aspect of conducting accurate wind tunnel tests, especially for the Leading Edge Inflatable (LEI) kite experiment discussed in this thesis. This section will discuss the constraints and considerations for scaling, including wind tunnel size, Reynolds number similarity, and tunnel blockage. Proper scale selection is vital for minimizing discrepancies and ensuring that the collected data is reliable and applicable to full-scale scenarios. However, note that it is impossible to impose hard limits on the scales. Therefore,

this section was merely written to give some directions in the scale selection.

Wind tunnel size

The initial limitation to consider is the wind tunnel's dimensions. Naturally, the scale model must fit inside the wind tunnel. As stated in section 3.1, the wind tunnel features an octagonal outlet measuring 2.85 m in both width and height. Consequently, the model's span must not surpass this measurement and, ideally, should be slightly smaller to ensure the entire model remains within the streamtube. Therefore, the value for the maximum wing span is to selected to be a slightly conservative value of $b_{max} = 2.5$ m. To determine the scale limit this imposes, the full scale dimensions of the V3A are presented below. Based on the full-scale wing span, the upper limit of the scale model is 1:3.32. As a result, the maximum chord length is determined to be $c_{max} = 0.78$ m. Furthermore, a visualization of the dimensions is shown in Figure 3.8.

- Projected span b_{proj}: 8.3 m
- Center chord length c_{sym}: 2.6 m
- Height h: 3.7 m

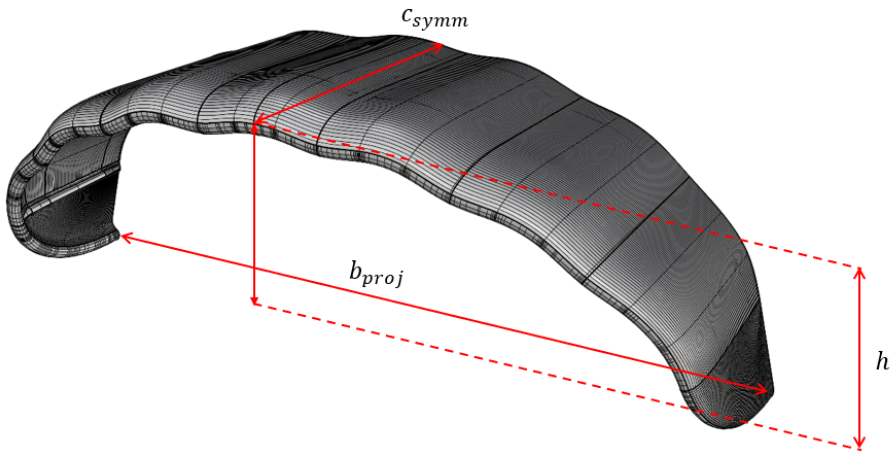

Figure 3.8: Dimensions of the V3A Kite model.

PIV measurements

The model utilized in this study was scaled considering that stereoscopic particle image velocimetry (SPIV) could be performed on it. Specifically, to capture chordwise flowfields at specific points of interest along the kite's span. This topic will not be discussed in this thesis report, but the information in this paragraph is adequate. These SPIV measurements also set a limit on the maximum chord length, as the cameras used in SPIV have a restricted field of view. In practice, the low-speed cameras employed in the OJF have a maximum field of view of approximately 20x20 cm, but 30x30 cm can also be reached if the resolution of the flow field is desired not too high. When this limit is exceeded, the flow information that can be extracted is minimal. The objective of these SPIV measurements also includes obtaining flow-field data in front of the leading edge and behind the trailing edge of the model. The maximum chord length imposed by the SPIV measurements is $c_{max} = 0.4$ m, or an upper scale limit of 1:6.5.

Reynolds number

The Reynolds number is a vital parameter in wind tunnel experiments, indicating the ratio of inertial forces to viscous forces in a fluid flow. Essentially, it determines the flow nature, laminar or turbulent, around a test model, thereby impacting aerodynamic properties such as lift, drag, and boundary layer behavior. Accurately replicating the Reynolds number encountered by full-scale

models is crucial to ensure that wind tunnel tests produce data that are relevant and applicable to real-world scenarios [54, 55]. The Reynolds number equation can be found in Equation 3.1.

$$Re = \frac{\rho U L}{\mu} \tag{3.1}$$

In this equation, ρ is the air density in m^3, U is the wind speed in m/s, L is the characteristic length in m, and μ is the dynamic viscosity in Pa·s. Practically, achieving high Reynolds numbers in wind tunnel tests, typically between 1 million and 10 million for general aerodynamic tests, is ideal to closely simulate the actual performance of full-scale vehicles or structures. However, lower Reynolds numbers, such as 200,000, can still offer valuable insights, especially for smaller-scale models and specific applications such as vertical axis wind turbines (VAWTs) and other low-speed aerodynamic studies [55].

Applying these findings to the experiment of this thesis means that during the testing, the Reynolds number should ideally be higher than $Re = 2 \cdot 10^5$ to obtain reliable results. The study by Lebesque uses a range of Reynolds numbers between $0.1 \cdot 10^6$ and $15 \cdot 10^6$, meaning that it is also preferable to choose a Reynolds number that falls within that range to allow data validation. However, one should also look at the tunnel limits when selecting this. The wind tunnel namely has a maximum speed of $U_\infty = 35$ m/s, but in reality it is better to assume that it can reach $U_\infty = 25 - 30$ m/s because of the high levels of turbulence intensity at high wind speeds. Then, assuming sea level conditions, the minimum chord length of the model (the characteristic length L in this case) can be calculated for various Reynolds numbers. The results can be found in Table 3.1. Here, the Reynolds numbers used by Lebesque [1] have been used.

Re [-]	c_{min} [m] for $U_\infty = 25$ m/s	c_{min} [m] for $U_\infty = 30$ m/s
$0.1 \cdot 10^6$	0.059	0.049
$0.2 \cdot 10^6$	0.12	0.099
$0.5 \cdot 10^6$	0.30	0.24
$1 \cdot 10^6$	0.59	0.49
$3 \cdot 10^6$	1.8	1.5
$15 \cdot 10^6$	8.9	7.4

Table 3.1: Reynolds number and wind tunnel speed combinations yielding different minimum chord lengths.

The chord lengths, as shown in Table 3.1, have a wide range of values, ranging from about 0.05 m to almost 9 m. It should be highlighted in the table that chord lengths associated with higher Reynolds numbers can also correspond to lower Reynolds numbers, as the wind speed in the wind tunnel can simply be reduced. However, when looking at the results from earlier in this section regarding wind tunnel size and SPIV measurements constraints, the maximum chord length is 0.4 m. This automatically excludes the three lowest rows of Reynolds numbers because they lead to a higher minimum chord length. Furthermore, as mentioned before, the Reynolds number should ideally be higher than $0.2 \cdot 10^6$. This gives a range of chord lengths of 0.099 m to 0.4 m, or in other words, a scale of lower scale limit of 1:26 and an upper scale limit of 1:6.5.

Blockage factor

The blockage factor is an essential parameter in wind tunnel experiments, described as the ratio between the frontal area of the test model and the cross-sectional area of the wind tunnel's test section. To obtain precise aerodynamic measurements, it is advised that the blockage factor should not surpass 5% (0.05) [56, 57]. This limit ensures minimal interference effects while preserving the accuracy of the test data.

The wind tunnel used for this test has an octagonal exit opening with an area of 7.4727 m^2. The blockage factor B is calculated as follows:

$$B = \frac{A_{f,model}}{A_{outlet}} \tag{3.2}$$

In this equation, $A_{f,model}$ is the frontal area of the model and A_{outlet} is the cross-sectional area of the wind tunnel outlet. Given the cross-sectional area of the OJF $A_{outlet} = 7.4727$ m^2, the maximum frontal area allowed for the model is $A_{f,max} = 7.4727 \cdot 0.05 = 0.3736$ m^2. For the V3A model, approximating the frontal area of the kite is not straightforward due to the complex shape. Furthermore, one should also take into account the maximum angle of attack during testing, because the kite has the least frontal area when the angle of attack is 0 (see Figure 3.7b). According to Lebesque's study [1], the maximum angle of attack is $\alpha_{max} = 24°$, indicating that this angle must be considered when estimating the frontal area of the kite. A visualization of this is presented in Figure 3.9. It can be seen that the frontal area of the kite is approximately half the area of the larger ellipse subtracted by half the area of the smaller ellipse. A formula for this approximation can be found in Equation 3.3.

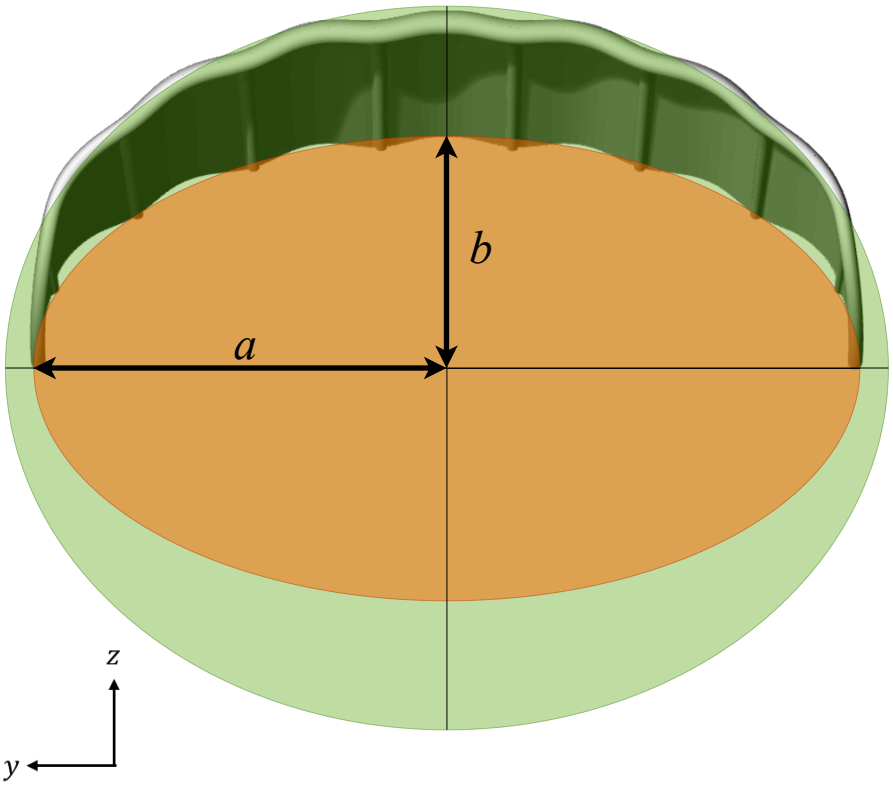

Figure 3.9: Front view of the V3A model at $\alpha = 24°$. Ellipses have been drawn to aid in calculating the frontal area.

$$A_f = 0.5\,(A_{gr} - A_{or}) = 0.5\pi\,(a_{gr}b_{gr} - a_{or}b_{or}) \tag{3.3}$$

In Equation 3.3, A_{gr} is the area of the larger ellipse while A_{or} is the area of the smaller ellipse, both in m^2, and a and b are the semi-major and semi-minor axes, respectively, in m. The semi-major and semi-minor axes a and b can be expressed in terms of the span. For the orange ellipse, the semi-major axis a is obviously half the projected span b_{proj}, but for the green ellipse this is approximately $0.537b_{proj}$ after verifying with the CAD model. For both ellipses, the semi-minor axis b is not that straightforward. This has been determined after verifying the CAD model of the V3A. The values for both ellipses can be found in Table 3.2. Keep in mind that this likely represents a minor overestimation of the frontal area, but it is preferable to overestimate rather than underestimate.

At this point, the blockage factor B can be calculated for each limit using the present scale limits of 1:26 and 1:6.5. The results of this can be found in Table 3.3.

	a/b_{proj} [-]	b/b_{proj} [-]
Green ellipse	0.537	0.407
Orange ellipse	0.5	0.262

Table 3.2: Semi-major and semi-minor axes values divided by the projected wing span.

Scale	Projected span b_{proj} [m]	Frontal area A_f [m^2]	Blockage factor B [%]
1:26	0.319	0.0139	0.19
1:6.5	1.27	0.224	3.0

Table 3.3: Frontal area and blockage factors for the upper and lower scale limit.

As shown in Table 3.3, the blockage factors for both limits remain below the recommended threshold of 5% for wind tunnel tests. Thus, the blockage factor does not restrict the choice of the model scale, and the limits remain at 1:26 and 1:6.5.

Conclusion
In conclusion, the scale of the model must be anywhere within 1:6.5 and 1:26. At this stage of the design, no final decisions can be made on the basis of the constraints discussed in this section. However, something that can be said is that the bigger the model, the better the Reynolds number similarity. To reach a Reynolds number of $0.5 \cdot 10^6$, a chord length of 0.24 is needed at $U_\infty = 30$ m/s. This is approximately equal to a scale of 1:10. Therefore, at this point in the model design stage, two different scales within the range have been selected for further investigation. These scales are the upper limit of 1:6.5 and the aforementioned 1:10.

3.2.3. Material selection

The aim of this research was to conduct wind tunnel experiments on a rigid subscale model of Kitepower's LEI V3A Kite. Consequently, part of the project involved rigidizing the model to ensure minimal to no deformation. This proved to be quite challenging, as the kite's canopy is only a few millimeters thick. Locally increasing the kite's thickness could be a solution due to the separation bubble behind the leading edge on the pressure side. The flow is separated there, so it is expected that increasing the canopy thickness would have little to no impact. However, due to the difficulty in quantifying this effect, it was decided not to pursue this option. The next topic of discussion will be the reinforcement of the tubular structure, as it is easier to quantify.

The V3A model features a complicated design, characterized by a zigzagging front edge and a double-curved canopy. Consequently, deformation calculations are intricate and require the use of a Finite Element Method (FEM) for accurate determination. However, it was concluded that these calculations are beyond the scope of this project, leading to the decision to perform only simplified calculations.

The main form of deformation is expected to be the tip deformation. Therefore, it has been chosen to calculate the tip deformation based on several assumptions presented below.

- The lift force acting on the kite is a distributed force directed perpendicular to the kite's surface. This distributed lift can be represented by two half-wing moments of equal magnitude but opposite direction around the x-axis that passes through the plane of symmetry. In reality, this was not the case because the forces on the kite would have been translated through two steel rods to the support structure, changing the distributed lift force. However, during the design, this was sufficient, as it probably would have overestimated the tip deflection due to higher tip loads that would have been lower in reality.
- The leading edge tube of the kite bears the entire lift force, as the chordwise struts do not contribute stiffness in this direction, and the canopy is too thin to withstand forces.
- The leading edge tube will be modelled as a solid cylinder. According to Figure 3.7b, the diameter of the leading edge in the z-direction remains constant along the entire span. Ver-

ification of this in the CAD model of the V3A led to the conclusion that this diameter is $D_{LE} = 0.0417 b_{proj}$.

The above assumptions are visualized in Figure 3.10. In the figure, it can be seen that the distributed lift is replaced by two symmetric moments M_{sym} and the leading edge is replaced by a solid cylinder.

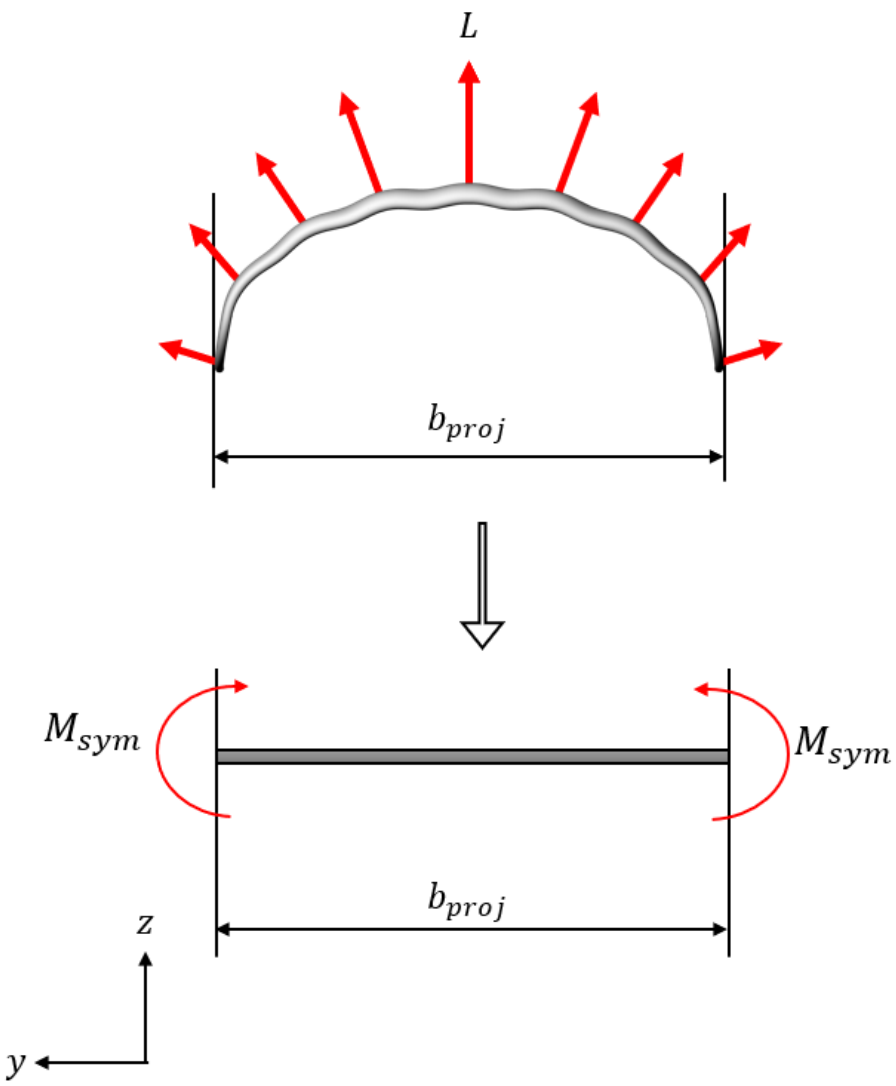

Figure 3.10: Simplification of the kite for deformation calculations

The maximum tip deflection δ_{max} of the simplified kite can be approximated by Equation 3.4 [58].

$$\delta_{max} = \frac{M_{sym} b_{proj}^2}{8EI} \tag{3.4}$$

In Equation 3.4, M_{sym} is the moment about half the span in Nm, b_{proj} is the projected span of the cylinder in m, E is Young's modulus of elasticity in Pa and I is the moment of inertia in m^4. For a cylinder, $I = (\pi/64)D^4$ with D the diameter of the cylinder in m. For the scales 1:6.5 and 1:10, M_{sym} has been approximated using the Vortex Step Method (VSM) solver by Cayon [2] and Poland [33]. The solver was executed under conditions of the tunnel's maximum wind speed ($U_\infty = 30$ m/s) and the stall angle of attack of the V3A ($\alpha_{stall} = 15.33°$) to guarantee the extreme load scenario and

consequently the maximum tip deflection. Then, using Young's moduli for relevant materials[1], the maximum tip deflection normalised by the span for the scales 1:6.5 and 1:10 have been plotted for each material. The resulting plot can be found in Figure 3.11. As a sidenote, for materials like glass fiber and carbon fiber composites, a thin walled cylinder of 2 mm thickness has been assumed as this is more realistic than a solid composite cylinder. The moment of inertia has been changed accordingly.

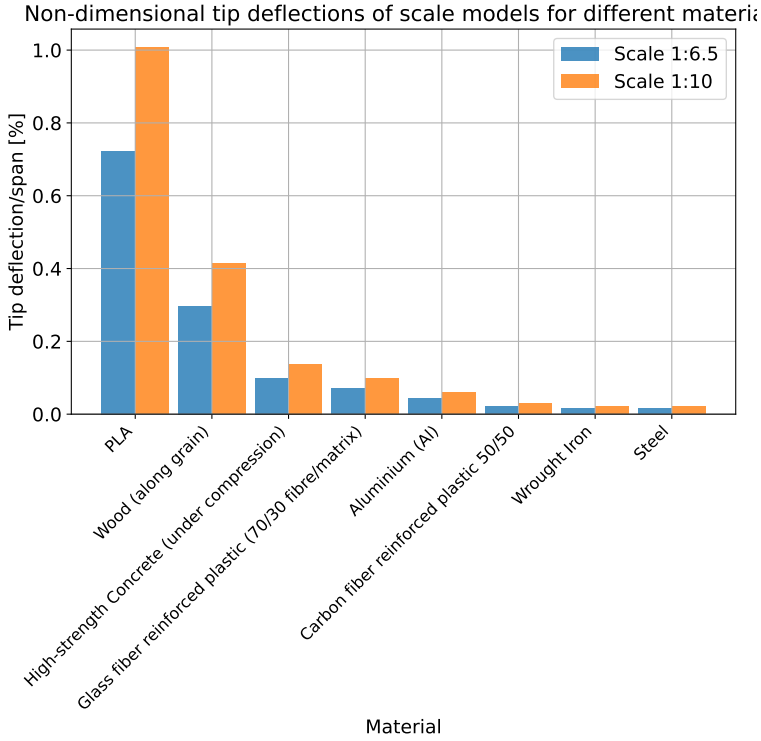

Figure 3.11: Maximum tip deflection normalized by the span for scales 1:6.5 and 1:10 for various materials.

According to the plot, PLA and wood, which are 3D print materials, exhibited the greatest deflection. Among the metals, steel displayed the least deflection, while carbon fiber reinforced plastic showed the minimal deflection among the composites. Additionally, it is observed that the larger scale model experienced less deflection compared to the smaller scale model, indicating that the larger model is preferable in terms of deflection.

During the design phase, various methods for building the model were evaluated. According to Figure 3.11, 3D printing was less appealing compared to constructing the model from carbon fiber composite or steel. Steel was too heavy for the wind tunnel measurement devices and needed a larger support structure. Although a carbon fiber composite would be much lighter than metal, it wouldn't significantly reduce deflections. Additionally, a carbon fiber composite was initially considered more expensive than a metal model. However, milling a metal model was complicated and costly due to the thin canopy. The thin canopy posed fewer challenges for a carbon fiber composite model, as the carbon fiber layup can be several millimeters thin [59]. Consequently, a carbon fiber reinforced polymer model was chosen. The model's scale was set at 1:6.5, which is optimal for Reynolds number similarity and minimal deformations.

3.2.4. Model construction

The model was manufactured by Curve Works[2], an expert on manufacturing such complex and intricate structures. The model was constructed using a carbon fiber reinforced polymer, which

[1] `https://www.je-depa.com/Training/Tutorial/Appendix/YMforcommonmaterials.html`
[2] `https://curveworks.nl/`

was layered in a mold composed of structural foam. After discussions with Curve Works, it was decided that the canopy thickness would be 3 mm across the entire kite. However, for the two central panels, a thickness of 4 mm was selected to provide additional reinforcement needed for attaching to the support structure, which will be discussed in the next section. The outer 2 mm consisted of carbon fiber, while the inner 1 or 2 mm was constructed from glass fiber reinforced polymer to enhance stiffness and reduce costs compared to carbon fiber. The leading edge and the chordwise struts were made from structural foam.

Pictures of the resulting model can be found in Figure 3.12, Figure 3.13 and Figure 3.14. The chordwise struts made from the structural foam are clearly visible in Figure 3.12. The model has a smooth surface finish which is visible in Figure 3.14. This was done to ensure that there were no irregularities on the surface that could cause unwanted disturbances in the wind tunnel tests. Any holes were filled up with paste and sanded down to a smooth surface. Dark pigment was mixed into the epoxy to reduce the model's reflectivity. This proved useful for the PIV tests. Finally, two steel cylinders with a diameter of 20 mm were inserted into the central two struts, serving as the connection points to the support structure discussed in the following section. The mass of the model including the steel rods is $m_{model} = 7.965$ kg.

Figure 3.12: V3A kite model being manufactured in its mold.

Figure 3.13: Rear of the finished V3A Kite model.

Figure 3.14: Front of the finished V3A Kite model.

3.2.5. Model shape

To account for any differences between the final model, as it was delivered by CurveWorks, and the CAD model, which is used by Lebesque in his simulations [1], an attempt was made to map the model using a laser. A laser measurement system normally used to measure space related things, produced by FARO[3], was utilised. A picture made during the laser can be found in Figure 3.15,

[3] `https://faro.com/en/`

where the different parts of the system are highlighted.

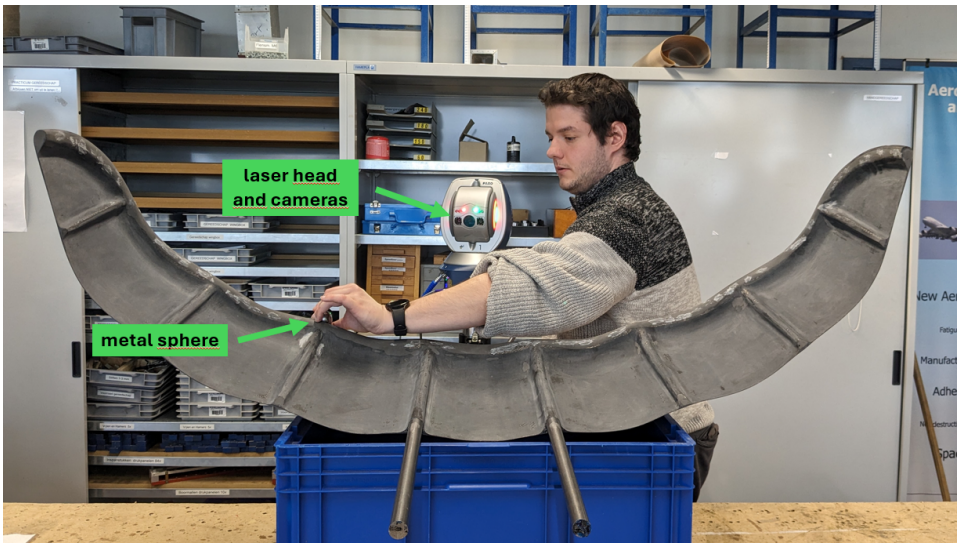

Figure 3.15: FARO laser system and its components.

The system operates as follows. The laser head is equipped with two cameras and follows the metal sphere in space continuously, provided the sphere remains within its field of view. For the kite, the sphere needs to touch the kite, and as the sphere moves along the kite, the laser head tracks it. The FARO software includes sophisticated features capable of generating the entire curvature of the kite, though this feature unfortunately failed to function. Nevertheless, points could be created in space. Consequently, points were positioned at various crucial spots on the kite, such as the outer tips, the center chord, the spanwise strut positions, and the model's highest and lowest points, and a `.stp` file was produced. The CAD model of the kite was then inserted into this file and aligned with the points as accurately as possible. A visualization of the CAD model and the FARO point clouds is found in Figure 3.16, for several different views.

In general, Figure 3.16 shows good correspondance between the laser measurements and the original CAD file. It seems that the span is equal, however, the chord length of the model seems a tiny bit larger than the CAD file's chord. Furthermore, the height is about the same for the CAD file and the model. Therefore, based on the comparison, it seems that the model produced by Curve Works is within the said manufacturing allowance. While there are differences, they are minimal and can also be attributed to the complexity of the laser system and the difficulty in lining up the model with the point cloud produced by the FARO measurements.

3.3. Support structure design

In addition to designing and building the model, a support structure was also created to suspend the V3A model in the wind tunnel. Various concepts for the support structure were explored during the design phase. The support structure from Belloc's rigid paraglider experiment [52] was taken into account. Briefly, Belloc used a cylindrical metal mast fixed at 60% of the central chord (refer to Figure 2.19). The model could adjust its angle of attack and the angle of side-slip using a motorised mechanism. However, for the experiment in this study, such motorised mechanisms were not available; only a rotary table was used on which the force balance was mounted, which will be discussed in more detail in chapter 4. If the kite were to be mounted sideways (with the lift thus pointing to the side), the angle of attack change could be performed by the rotary table. This approach complicated the variation of the side-slip angle, leading to the decision to suspend the kite in its normal orientation. In this orientation, the rotary table would be used to change the side-slip angle. However, a way to change the angle of attack would have to be designed.

In order to keep the flow disturbance caused by the support structure around the kite at a minimum, it was decided that the kite would be suspended in front of the support structure. To ac-

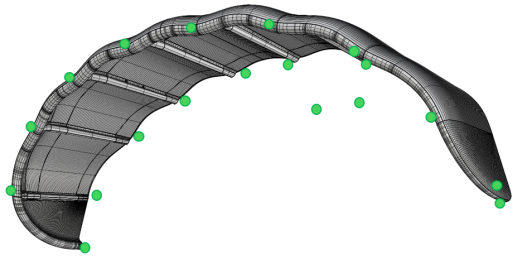

(a) Isometric view of the original CAD model with the point cloud generated by FARO measurements.

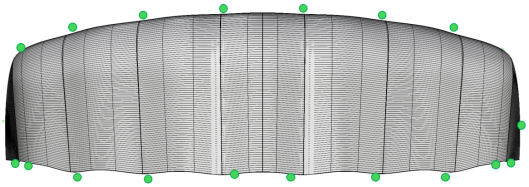

(b) Top view of the original CAD model with the point cloud generated by FARO measurements.

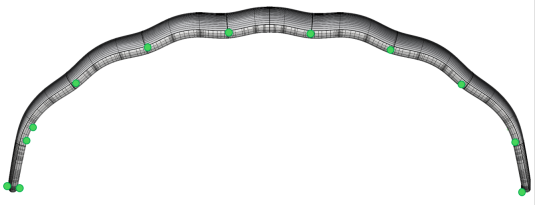

(c) Front view of the original CAD model with the point cloud generated by FARO measurements.

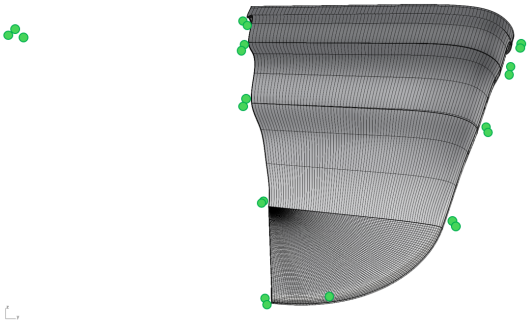

(d) Side view of the original CAD model with the point cloud generated by FARO measurements.

Figure 3.16: Different views of the original CAD model with the FARO point cloud.

complish this, two 20mm diameter steel rods were manufactured inside of the middle two struts (see Figure 3.13), which could then be clamped to a support structure. The reason these rods were made out of steel is that after calculations performed by Curve Works, it was concluded that on the basis of the maximum wing loading determined by the VSM solver of Cayon and Poland, aluminium would deform too much.

In Figure 3.17, the CAD representation of the support structure is shown. It is evident that the support framework is a truss structure. The support structure consists of aluminium beams manufactured by Item[4]. This selection was made because the support framework would be simpler to assemble, as Item offers aluminium profiles that are straightforward to put together using their fasteners, while also offering excellent structural rigidity. When deciding the width of the support structure, the tip vortices shedding from the kite have been taken into account [1] such that the structure does not disturb this. The truss structure was mounted on an aluminium plate, which was necessary to bolt the whole structure to the force balance.

The rotation mechanism for the angle of attack change is also shown in Figure 3.17 in green. The green bar is a horizontal bar, fastened in between the two vertical beams. This horizontal bar can be easily loosened, allowing it to move in a vertical direction. This movement in the vertical direction then creates a rotation of the steel tube in between the two pillow block bearings mounted to the vertical beams. Two steel tubes were connected to the rotating steel tube using tube connectors. Aluminium profiles connecting the adjustable horizontal bar to these two tubes were also connected on the hinges by tube connectors. A visualisation of this can be found in Figure 3.18. The kite can be easily mounted to the support structure, by sliding the steel rods of the kite into the steel tubes of the support structure and fastening this connection using adjustment bolts screwed into the tubes (one of which is indicated by the green arrow).

In Figure 3.19, a picture is presented in which the kite is attached to the support structure as it would look during the wind tunnel testing campaign. There are slight differences compared to the CAD model in Figure 3.17. The angled beam is connected using two heavy duty hinges instead

[4] `https://nl.item24.com/nl/`

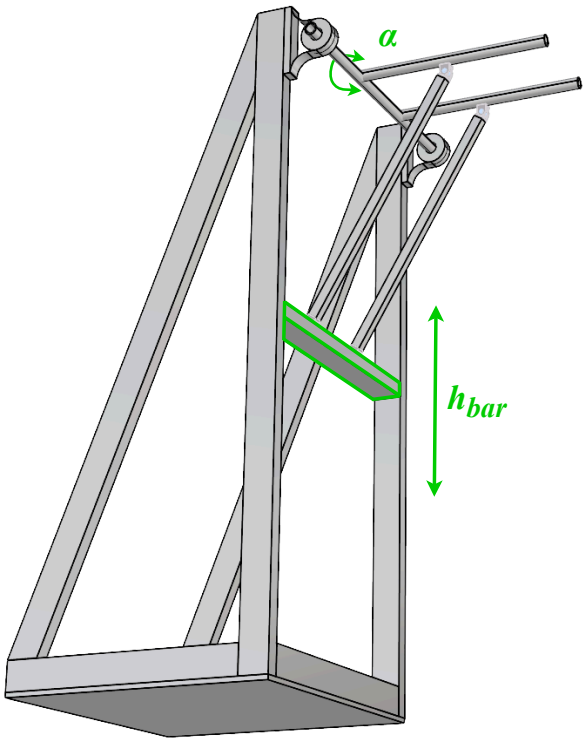

Figure 3.17: CAD model of the support structure.

of bolted to the other beams. This connection is easier to assemble, cheaper, and is also stronger than the proposed bolted connection.

Figure 3.18: Picture of the structure that connects the tubes. The green arrow indicates an adjustment bolt used to fasten the kite to the support structure.

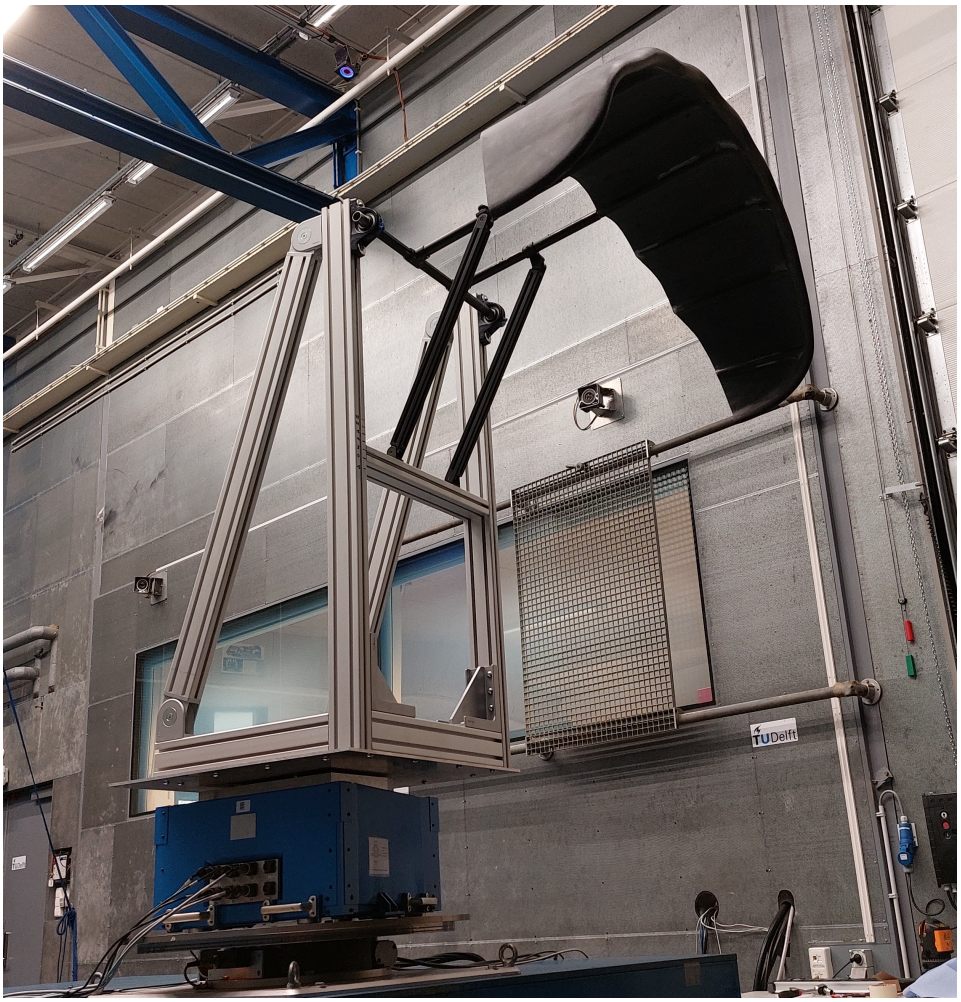

Figure 3.19: Actual model and support structure.

4

Experimental setup

The experiment was divided into two parts, namely aerodynamic load measurements and PIV measurements. The first part consisted of measuring the forces and moments acting on the kite for different combinations of wind speed, angle of attack, and angle of sideslip. The second part consisted of PIV measurements for two different configurations of wind speed, angle of attack, and angle of sideslip. The first part was considered the core part of the thesis project, while the PIV measurements were regarded as a bonus (which is why it will not be part of this thesis report), as these usually take a long time to set up and measure. This chapter presents the experimental setup for the load measurements.

4.1. Force balance

The objective of this project was to acquire steady-state aerodynamic data for the V3A kite model. This data included, for example, the lift, drag, side force, and moment coefficients of the model under various flow conditions. The forces were recorded with a force balance, specifically the NLR force balance commonly employed in the OJF for this experiment. This force balance was a six-axis device, capable of detecting all forces and moments around its principal axes. The balance operated at an acquisition frequency of 2000 Hz. Furthermore, the balance was mounted on top of a rotary table, which was used to easily modify the side slip angle of the model during the experiment. The rotary table had a precision of $0.01°$ in adjusting its angle of incidence. A schematic representation of the force balance and the rotary table is presented in Figure 4.1. Furthermore, the dimensions of the force balance and its coordinate system can be found in Figure 4.2.

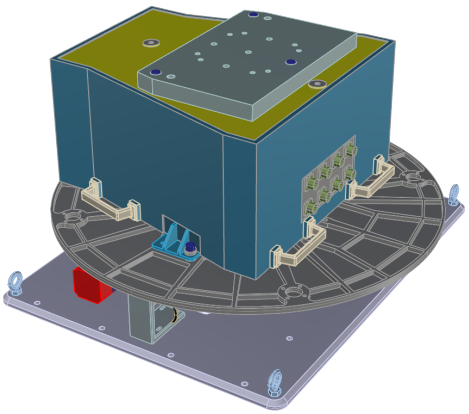

Figure 4.1: Schematic of the force balance on top of the rotary table.

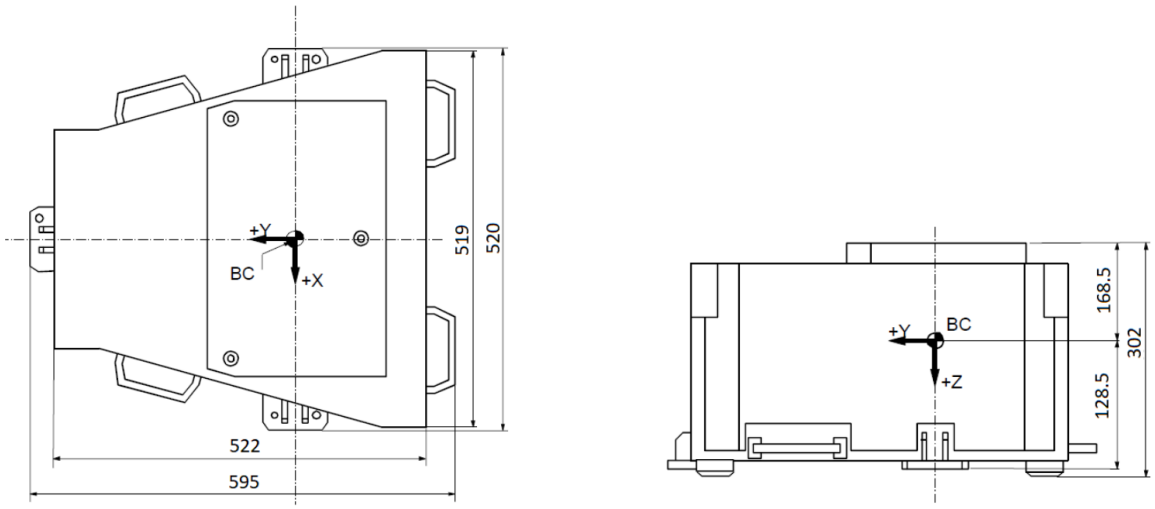

(a) Top view of the force balance.

(b) Side view of the force balance.

Figure 4.2: Dimensions and coordinate system of the OJF NLR force balance.

The highest nominal ranges for simultaneous load measurements and single load measurements of the NLR force balance are provided in Table 4.1. However, the latter is not relevant to this study, as only simultaneous measurements of six components were taken into account.

	Simultaneous measurements	Single measurements
Axial force (F_x)	±250 N	±250 N
Side force (F_y)	±500 N	±600 N
Vertical force (F_z)	±500 N	±3500 N
Rolling moment (M_x)	±500 Nm	±550 Nm
Pitching moment (M_y)	±250 Nm	±500 Nm
Yawing moment (M_z)	±50 Nm	±125 Nm

Table 4.1: Force balance load and moment ranges.

4.2. Model alignment

The kite model and its support structure were installed on the force balance and rotary table as previously described. This entire assembly was then secured to the blue table in the OJF. The blue table is a hydraulic system that can be raised and lowered. However, the entire setup needed to be aligned with the tunnel outlet. This alignment was achieved using a 3-plane leveling laser and by verifying the table's alignment with the floor tiles in the test section. These tiles were correctly oriented, making them suitable for this purpose. A picture of this alignment process is shown in Figure 4.3.

4.3. Rotation mechanisms

In section 3.3, the mechanism responsible for changing the angle of attack was already briefly mentioned, but in this section a more detailed explanation of it will be presented. It was already explained that the horizontal bar in between the vertical beams can be moved up or down, changing the tubes of the support structure and with that the angle of attack of the kite.

The angle of attack of the kite was not easy to measure because of the shape of the kite. However, the angle of the protruding rods of the kite could be measured. This angle was not equal to the angle of attack, but had a 7.25° difference between the centre chord line and the angle of the tubes, which was verified using the V3A CAD model. Measurement of tube angle was done by placing a flat plate with two digital inclinometers on top and placing it against the tube connectors that

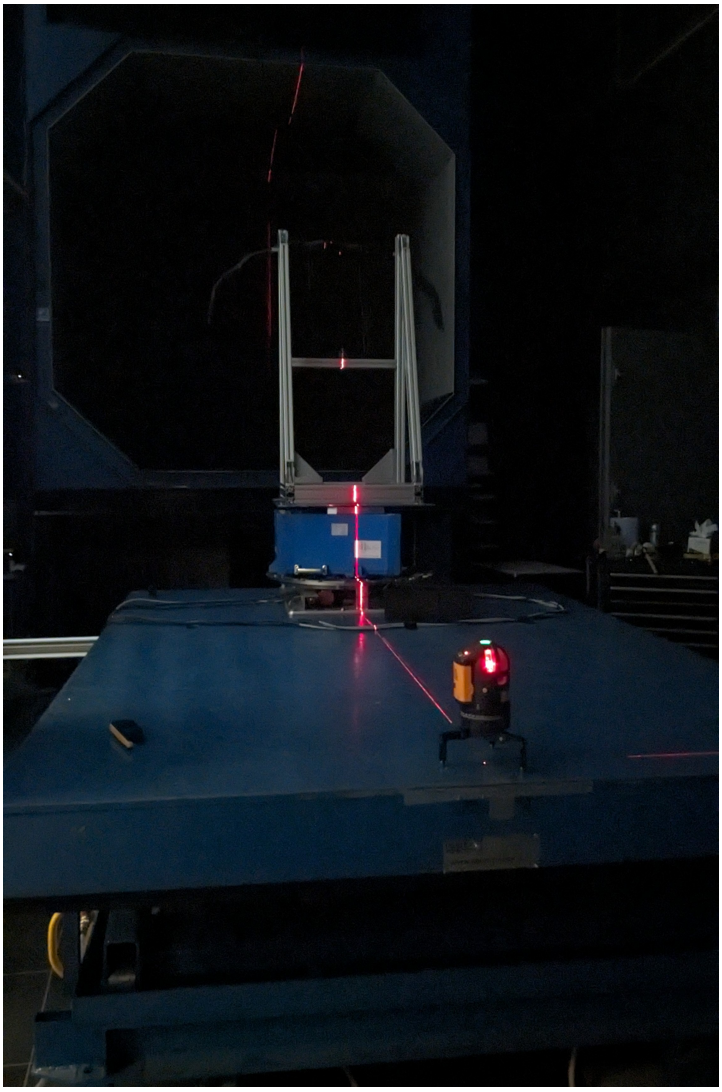

Figure 4.3: Kite model alignment process.

connect the horizontal bar to the tubes. The inclinometers had an accuracy of $0.01°$. A visualisation of this process can be seen in Figure 4.4. Each time the angle of attack changed during the experiment, these inclinometers were recalibrated using the floor of the test section and the side of the wind tunnel outlet to minimise the angle of attack error.

The other rotation mechanism was also mentioned earlier and was used to change the angle of sideslip of the kite. This was done using the rotary table. The rotary table was controlled using the PC in the OJF control room and also had an accuracy of $0.01°$. A picture of the interface of the rotary table control can be found in Figure 4.5. As can be seen, the rotational speed could also be adjusted.

4.4. Zigzag tape

At lower Reynolds numbers, zigzag tape can be used on a wind tunnel model to induce turbulent flow around the object [60]. Turbulent flow maintains higher momentum near the object's surface compared to laminar flow, reducing the likelihood of boundary layer separation and thus performing better than a laminar boundary layer. The V3A kite operates at a Reynolds number of approximately $3 \cdot 10^6$ [46], placing it within the turbulent flow regime. Furthermore, the full-scale V3A kite features protruding stitched seams where the canopy is attached to the leading edge, as illustrated in Figure 4.6. Watchorn [61] anticipated that these seams would naturally trigger the

Figure 4.4: Digital inclinometers used to determine the angle of attack of the kite.

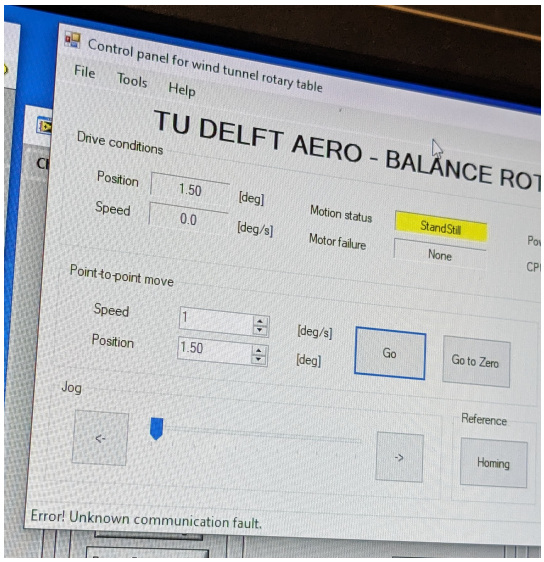

Figure 4.5: Interface of the rotary table control panel.

transition from laminar to turbulent flow [62]. Consequently, load measurements were performed with and without zigzag tape to determine its impact at low Reynolds numbers.

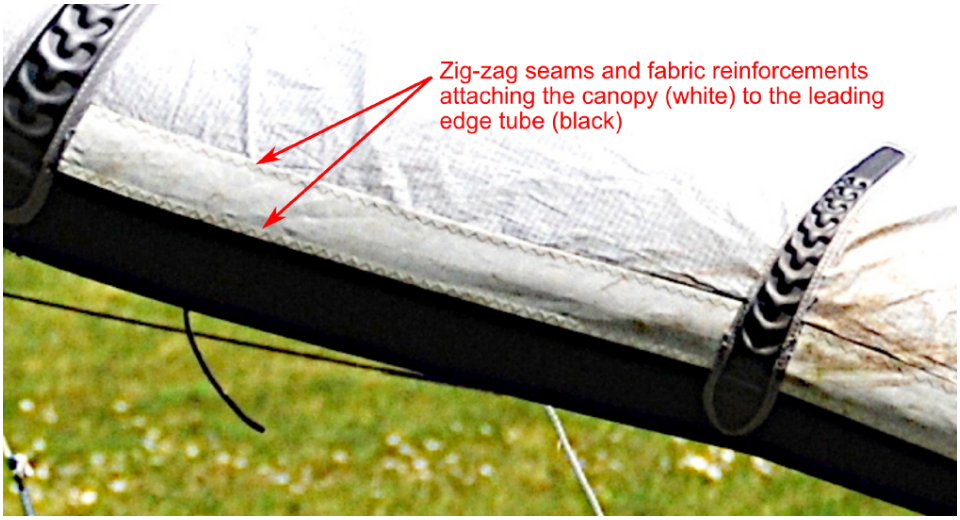

Figure 4.6: Protruding stitched seams near the leading edge of the V3A kite [61].

The thickness of the zigzag tape was selected as follows. Typically, for conventional airfoils, the thickness of the zigzag tape should be between 0. 5% and 1% of the chord length [63]. In the case of this experiment, this would be within 4 mm and 2 mm. Therefore, a thickness of 2 mm has been selected for this experiment. The chordwise position of the tape is usually at 5% chord on the suction side and at 10% chord on the pressure side of the airfoil [64]. However, due to the unconventional airfoil with the separation bubble on the pressure side behind the leading edge, it was deemed that a zigzag tape there would not have any benefit. Therefore, only a zigzag tape has been applied at 5% chord on the suction side. A visualisation of this is presented in Figure 4.7.

4.5. Load measurement setup

Images of the final experimental setup are available in chapter 4 and Figure 4.9. chapter 4 shows that the support structure, including the kite, is installed on the force balance and rotary table, which are placed on the blue table. Figure 4.9 clearly displays that the kite is positioned well

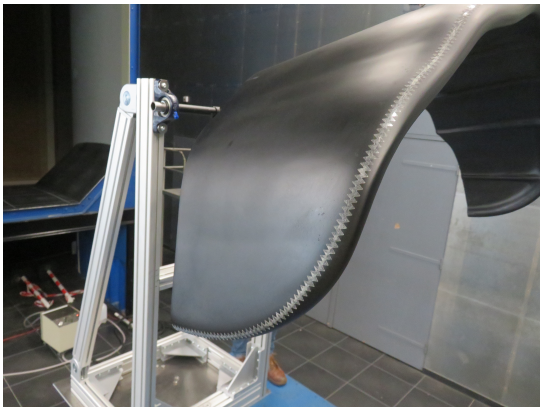

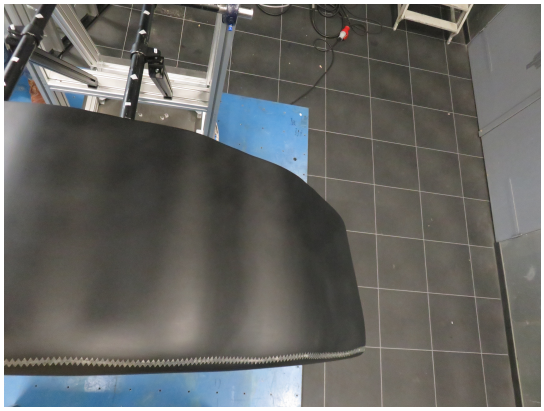

Figure 4.7: Zigzag tape applied to the suction side of the V3A kite model.

within the wind tunnel outlet and therefore within the airflow. Furthermore, a CAD drawing of the experimental setup is presented in Figure 4.10. This drawing and more pictures taken during the experiment were already published in the Book of Abstracts of the 2024 Airborne Wind Energy Conference (AWEC) in Madrid [65].

Figure 4.8: Experimental setup for the load measurements.

Figure 4.9: Rear view of the experimental setup for the load measurements.

4.6. Uncertainty and vibrations

During the testing campaign it became clear that the support structure with the kite showed vibrations at larger angles of attack, where the kite could possibly be stalled. Other instances of vibrations were, for example, when the kite was not mounted, and only the support structure was measured. For this reason, attempts were made to track the shape of the kite and support structure during the tests.

In the OJF, there is a camera system that is normally used to track drone positions using reflective stickers that are stuck to the drone. Although these stickers could not be stuck to the kite's

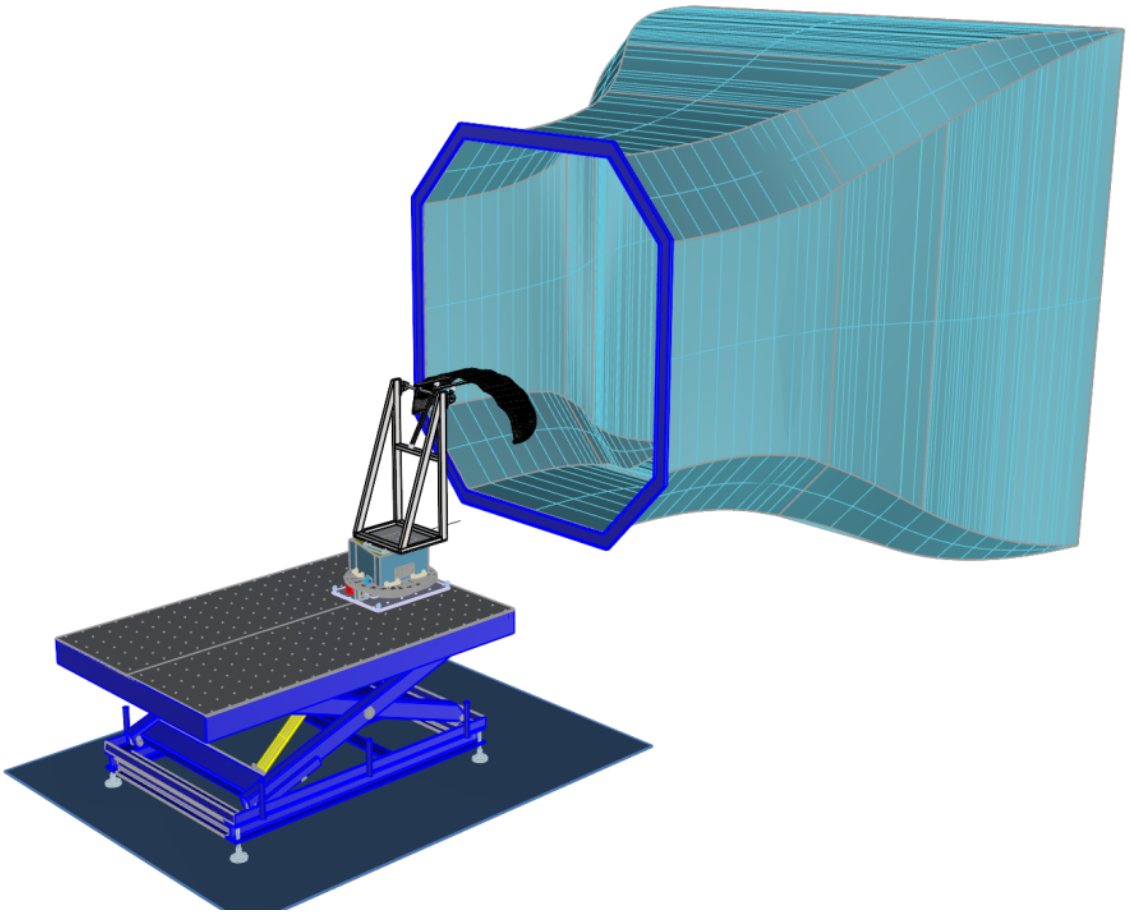

Figure 4.10: Isometric view of the experimental setup as drawn in a CAD file.

surface as they would have interfered too much, they could be stuck on the support structure, and more specifically the rods supporting the kite. If more than two stickers are stuck at different longitudinal locations, in theory the angle of the rods could be determined. However, in practice, the angle of the rods determined using this approach was not consistent with the angle of the rods determined using the digital inclinometer, and therefore it was decided not to use this camera system.

However, vibrations and deflections during the measurements still needed to be tracked. Instead of the aforementioned camera system, a GoPro camera was pointed at the kite, and the kite was recorded during the measurements. Unfortunately, there was no quantitative way to determine the kite's attitude, but it was better than not having any way of determining vibrations.

4.7. Wind tunnel corrections

Wind tunnel corrections are essential in aerodynamic testing to ensure the accuracy and relevance of the results obtained in a controlled, yet confined, environment compared to real-world, free-flight conditions. Wind tunnels, whether open-jet or with hard walls, introduce boundary effects that alter the natural flow behavior around the test model. These disturbances can lead to significant discrepancies in measurements of lift, drag, and other aerodynamic forces. Consequently, corrections are applied to account for these effects, allowing the experimental data to more accurately reflect true, unbounded aerodynamic performance. This is particularly crucial for streamlined lifting bodies, where precise aerodynamic characteristics are critical for performance predictions and design optimizations. In this section, one method of determining the corrections will be presented, namely an angle of attack correction. This method was explained to the author by Mac Gaunaa, who is an expert in the field of 2D wind tunnel testing.

The objective is to measure the free, unbounded behavior of the flow around a lifting body. For simplicity, a 2D case is used as an example. For a 3D case, the corrections will always be lower. In short, there is a disturbance effect at the centerline where the airfoil is, resulting in a curvature of the onset flow streamliens. This is also known as the "streamline curvature effect". This effect corresponds to an increased lift due to the tunnel disturbance. This increased lift can be interpreted as an additional angle of attack due to the tunnel, defined in the equation below.

$$\alpha_{\text{free}} = \alpha_{\text{geo,openjet}} - \Delta\alpha_{\text{openjet}} \tag{4.1}$$

In Equation 4.1, α_{free} is the angle of attack in free-stream conditions, $\alpha_{\text{geo,openjet}}$ is the geometric angle of attack as it is set in the wind tunnel and $\Delta\alpha_{\text{openjet}}$ is the angle of attack correction. Please note that for hardwall experiments, the minus sign should be a plus sign as the tunnel effects are different. Then, an expression for the angle of attack correction is derived as formulated in Equation 4.2.

$$\Delta\alpha_{\text{openjet,deg}} \approx 7.5\frac{c}{h^2}C_l \quad \text{[deg]} \tag{4.2}$$

In Equation 4.2, c is the chord length, h is the maximum height of the airfoil and C_l is the lift coefficient of the 2D airfoil. When filling in the values of the V3A kite model, with $c = 0.4$ m, $h = 0.57$ m and using the C_l values simulated by Lebesque [1], for $Re = 1 \cdot 10^5$ and $Re = 1 \cdot 10^6$ and for both a scale of 1:6.5 and 1:10, Figure 4.11 is created. In the plot, the angle of attack correction is plotted versus the lift coefficient. As can be seen in the plot, the angle of attack correction is higher for the biggest scale, which is expected. However, it is only 0.25 degrees, and this is of course the 2D case meaning that the 3D case will be even less. Therefore, it has been decided not to use tunnel corrections after considering the correction discussed in this section.

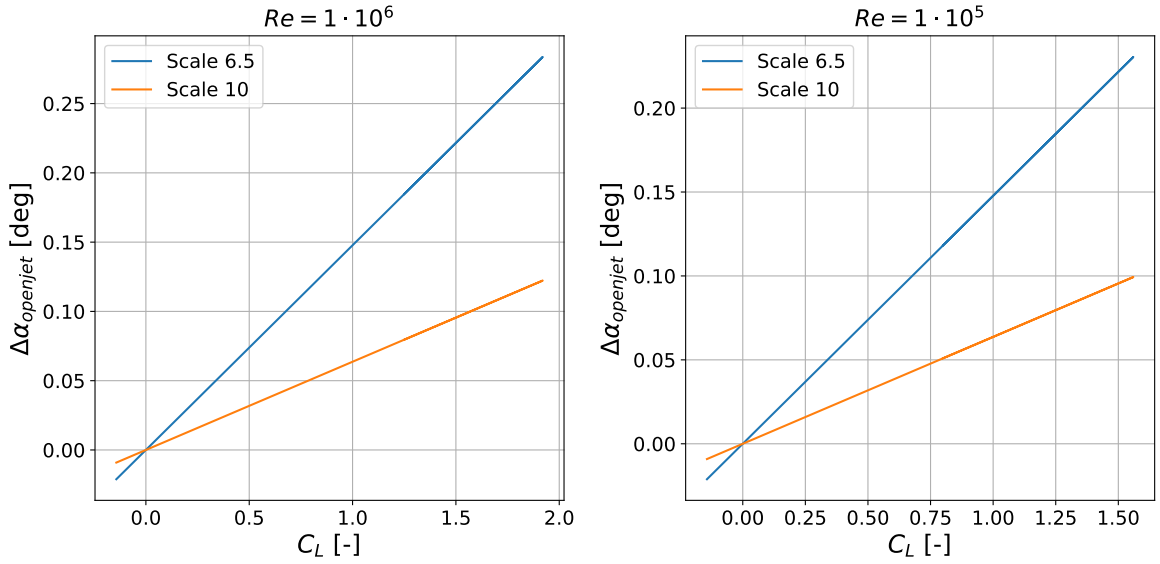

Figure 4.11: Angle of attack correction plotted versus lift coefficient for different Reynolds numbers and model scales.

5

Test cases

In this chapter, the test cases for both the load measurements and the PIV measurements will be given. Furthermore, for the load measurements, it will also be explained how the influence of the support structure will be mitigated.

5.1. Load measurements

In this section, the test cases for the load measurements will be explained, starting with the normal load measurements.

5.2. Normal load cases

This section explains the different test cases measured during the experimental campaign. The load measurements were performed for several configurations, following the ranges established in studies by Lebesque [1], Demkowicz [7], and Folkersma [13]. These studies used an angle of attack ranging between $-5°$ and $24°$, and sideslip angles ranging from $0°$ to $12°$. To obtain validation data for these simulations, the same ranges were used in the experiment. An overview of each measured angle of attack is shown in Table 5.1.

For each angle of attack, the table indicates whether all sideslip values have been measured or just at zero sideslip. "All sideslip values" refer to a range of sideslips between $-14°$ to $14°$ in steps of $2°$, plus $\beta = \pm 20°$.

This table shows that the measured angles of attack exceed the predefined range, and some angles of attack are atypical. Midway through the measurement campaign, it was noted that there was a $7.25°$ discrepancy between the angle of the rod and the angle of attack of the kite. For example, if the angle of the rod was measured at $10°$, the actual angle of attack was $2.75°$. Due to time constraints, it was decided that only several more angles of attack would be measured to complete the angle of attack range.

Moreover, $\alpha = 12°$ is the angle of attack most commonly used during the operation of the V3A [12]. Therefore, all sideslip angles were measured for this angle of attack. Originally, this was the plan for $\alpha = 10°, 12°, 14°$, but due to the angle of attack discrepancy and time constraints, it was only done for $\alpha = 12°$.

The wind speeds at which the measurements were performed were $U_\infty = 5, 10, 15, 20, 25$ m/s. This resulted in a Reynolds number range of 1.2×10^5 to 7.0×10^5.

Now that the flow conditions and angle configurations have been explained, the steps in which the tests were performed can be outlined. Note that for all the force balance measurements, the recording time was 10 seconds, and the balance operated at a sampling frequency of 2000 Hz. Adjusting the angle of attack took the longest as it had to be done manually. Wind speed was regulated from the control room, requiring less time but with some delay for stabilization. Adjusting

Angle of attack α [°]	Sideslip angles β [°]
-12.65	0
-7.15	0
-3	0
-2.25	0
2.35	all
4.75	all
6.75	all
8.8	0
10.95	0
11.95	all
12.8	0
14	0
15.75	0
17.85	all
19.75	0
22.55	no
24	no

Table 5.1: Measured angles of attack and sideslip angles for test cases with kite.

the sideslip angle was the quickest. Hence, the sequence of configuration changes was: first, the angle of attack, followed by the wind speed, and finally, the sideslip angle. The following steps outline the measurement campaign process:

1. Set angle of attack using the horizontal bar and the digital inclinometers.
2. Record data without wind speed for $\beta = 0$.
3. Increase tunnel speed to 5 m/s.
4. Record all required sideslip angles. When a measurement is recording, note down the air density, temperature, actual wind speed, pressure, and dynamic pressure for the desired data points.
5. Repeat steps 1-4 for other wind speeds.
6. Once steps 1-5 have been performed, repeat the same steps for all angles of attack.

5.2.1. Runs without kite

In addition to the measurements mentioned above, tests were conducted at three angles of attack without the kite attached to the support structure. This was done to obtain to obtain interpolation relationships between angle of attack and force and moment coefficients to save valuable measurement time. These coefficients could then be subtracted from the measurements taken with the kite, isolating the forces and moments acting solely on the kite. These measurements have been performed for angles of attack and sideslip angles as found in Table 5.2. These angles of attack were chosen because they initially represented the extreme and middle angles of attack. However, due to the aforementioned angle discrepancy of $7.25°$, the actual angles of attack were lower.

Angle of attack α [°]	Sideslip angles β [°]
-12.25	all
2.6	all
17.85	all

Table 5.2: Measured angles of attack and sideslip angles for test cases without kite.

5.2.2. Zigzag tape

Another test case is the comparison between a case with and without zigzag tape. For this case, an angle of attack of $\alpha = 8.75°$ has been selected. For this angle of attack, only one sideslip angle has been measured, namely zero sideslip. The measured wind speeds are 0, 5, 10, 15 and 20 m/s. Reasons for choosing this are to check whether the zigzag tape causes the flow over the kite to transition earlier for low Reynolds numbers. Furthermore, the kite itself has a stitched seam near the leading edge, as discussed in section 4.4.

5.2.3. Flipped configuration

In order to do the PIV measurements on the pressure side, the kite had to be flipped for these measurements. During these measurements, load measurements were also performed. The angles of attack for these cases were $\alpha = 6°$ and $\alpha = 16°$. These measurements can be used to check whether the flipped kite produces the same lift as the kite in normal configuration. Unfortunately, the necessary runs without wind speed were not performed, leading to not being able to subtract the influence of steady forces and moments from the aerodynamic forces and moments. Therefore, no comparison between the flipped and normal configuration could be made.

5.2.4. Double measurements

In wind tunnel testing, it is important to check whether the things you are measuring are not arbitrary and can be reproduced. In order to check this, double measurements were performed for some test cases at different times during the testing campaign. An angle of attack of 4.75 was selected for this purpose, as it was expected to be in the linear region of the lift curve. For this angle of attack, double measurements were done for a wind speed of 20 m/s and for sideslip angles of -20, 0 and 20 degrees. In total, these measurements were done at three different times.

5.2.5. Signal drift

A not so common phenomenon in wind tunnel testing is signal drift. Signal drift refers to the gradual change or deviation of the recorded signal of a measurement device over time. This drift is independent of the actual forces that are being measured. If not taken into account, this can significantly affect the accuracy and reliability of the measurement data. For this reason, at the beginning and the end of each testing day, 30 second measurements with zero wind speed were taken to check whether signal drift occurs.

6

Data processing

This chapter details the methods employed to process the data gathered from the experiment. Initially, the focus is on the load measurements. Subsequently, the PIV measurements are addressed.

6.1. Procedure for determining aerodynamic coefficients of the kite

This section covers the processing of load measurement data. From the force balance measurements, two files were acquired: one containing the mean values of forces and moments for the 10-second measurements, and another with the unsteady data for these measurements sampled at 2000 Hz. The objective of processing the load measurements is to obtain plots of the kite's lift, drag, and side force coefficients, and moment coefficients in the kite's coordinate system.

6.1.1. Support structure data processing

First, the aerodynamic coefficients of the support structure were determined. Recall subsection 5.2.1, where it was stated that three angles of attack were measured for the support structure to save measurement time. The measurements of these three angles of attack were used to interpolate the relationships between angle of attack and force and moment coefficients. To obtain these relationships, the following steps were employed.

1. **Aerodynamic forces on support structure:** For each angle of attack, the steady force readings obtained from zero-wind runs were subtracted from the measurements with non-zero wind speed to obtain the aerodynamic forces on the support structure.
2. **Non-dimensionalization:** The aerodynamic forces were non-dimensionalized to obtain the aerodynamic coefficients:
$$C_{F,\text{support}} = \frac{F}{0.5\rho V^2 S} \tag{6.1}$$
where F is the aerodynamic force, ρ is the air density, V is the wind speed, and S is the kite reference area. Similarly, the moment coefficients were non-dimensionalized as follows:
$$C_{M,\text{support}} = \frac{M}{0.5\rho V^2 S c} \tag{6.2}$$
where c is the centre chord length of the airfoil.
3. **Interpolation:** Least square regression was used to approximate the relationship between the aerodynamic coefficients of the support structure and the angle of attack, to fit a line through the three datapoints:
$$C_{\text{support}}(\alpha) = a\alpha + b \tag{6.3}$$
where α is the angle of attack, and a and b are interpolation coefficients. This regression was done for each wind speed and sideslip angle combination. An alternative approach

of fitting a quadratic polynomial through the three datapoints was considered. Nevertheless, the regression method was chosen because the quadratic fit might result in significant deviations at the boundaries of the angle of attack range based on the values of the three measured datapoints. Thus, using a linear regression provided a safer assumption.

6.1.2. Kite data processing

In a manner similar to the processing of the support structure, the kite measurements required comparable steps. They are detailed as follows.

1. **Steady force correction:** For each angle of attack, the steady forces obtained from zero-wind runs were subtracted from the readings with non-zero wind speed to obtain the aerodynamic forces for the kite and support structure together. However, during the tests in the wind tunnel it became apparent that the wind speed was never equal to 0, but more often equal to approximately 0.5 m/s, even though it was set to zero in the control room. Therefore, the steady forces were taken from a single reading where the wind speed was known to be zero, namely where $\alpha = 2.75°$. These steady readings were then subtracted from all angles of attack, instead of using the zero readings for each respective angle of attack.
2. **Non-dimensionalization:** The aerodynamic forces were non-dimensionalized in the same way as the support structure to obtain aerodynamic coefficients:

$$C_{F,\text{total}} = \frac{F_{\text{total}}}{0.5\rho V^2 S} \tag{6.4}$$

   where F_{total} is the aerodynamic force measured with both the kite and the support structure. Similarly, the moment coefficients were non-dimensionalized as follows:

$$C_{M,\text{total}} = \frac{M_{\text{total}}}{0.5\rho V^2 S c} \tag{6.5}$$

3. **Isolation of kite aerodynamic coefficients:** For each angle of attack, the interpolated support structure coefficients were used to calculate the contribution of the support structure at the corresponding Reynolds number.
   The support structure coefficients were subtracted from the combined coefficients to isolate the kite aerodynamic coefficients:

$$C_{\text{kite}} = C_{\text{total}} - C_{\text{support}} \tag{6.6}$$

6.1.3. Coordinate system translation

The force and moment coefficients, as they are now, are in the coordinate system of the force balance, as defined in Figure 4.2. However, these should be translated to the coordinate system of the kite, located at its centre of gravity. A sketch of the cross-section of the kite and its support structure in the centre chord, mounted onto the force balance is presented in Figure 6.1. In the sketch, it can be seen that the kite's coordinate system is translated to the kite's centre of gravity, and rotated 180 degrees about the x-axis. Therefore, to obtain the lift, drag and side-force acting on the kite, the following equations are used.

$$\begin{aligned} D &= F_x \\ S &= -F_y \\ L &= -F_z \end{aligned} \tag{6.7}$$

where D is the drag of the kite, S is the side force of the kite, L is the lift of the kite and F_x, F_y and F_z are the output forces of the force balance.

The translation of the moments were slightly more complex, as the position of the centre of gravity changes with angle of attack. Using Figure 6.1, the following relations of the moments can be derived. It should first be noted that the distance between the coordinate systems is defined as

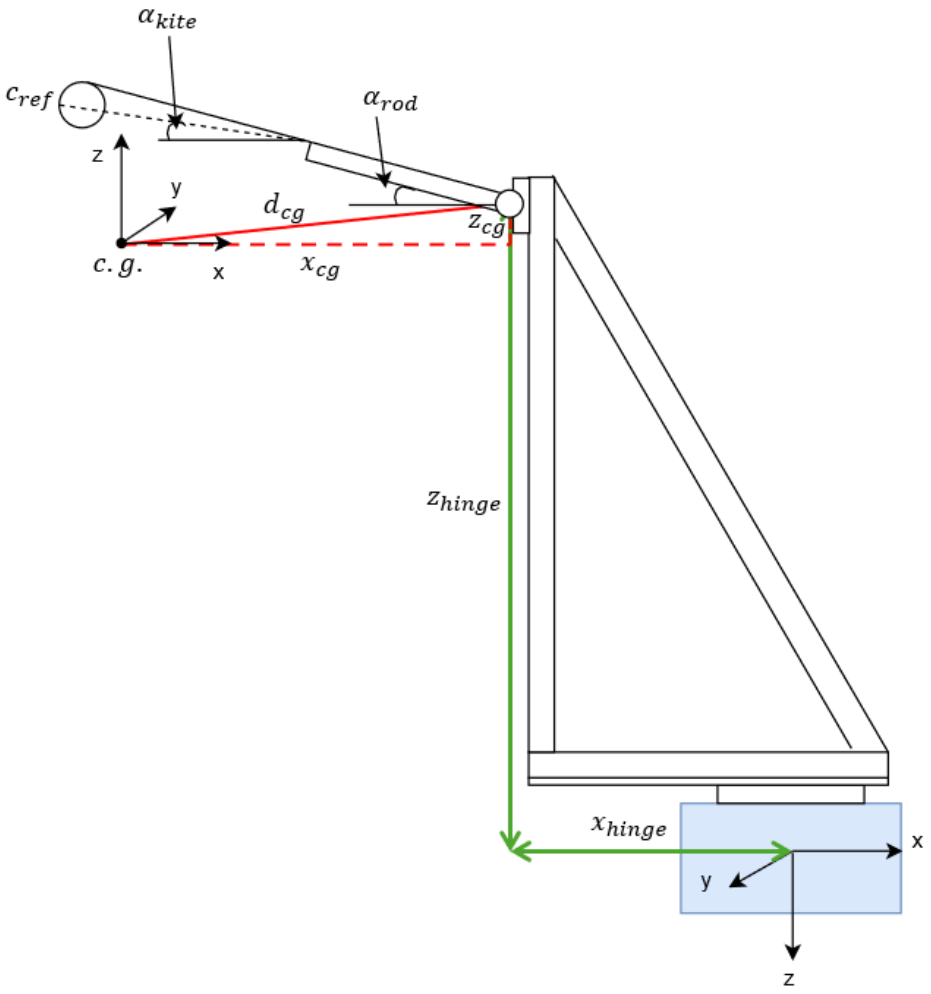

Figure 6.1: Cross-section of the kite and support structure in the centre chord, with both the kite and force balance coordinate system.

$x = x_{hinge} + x_{cg}$ and similarly $z = z_{hinge} + z_{cg}$ (as z_{cg} would be negative for a negative angle between d_{cg} and the horizontal), where x_{cg} and z_{cg} are functions of angle of attack. Furthermore, M_{pitch} is the moment about the y-axis, M_{roll} is the moment about the x-axis and M_{yaw} is the moment about the z-axis, all in the coordinate system of the kite.

$$\begin{aligned} M_{pitch} &= -M_y + F_z x - F_x z \\ M_{roll} &= M_x - F_y z \\ M_{yaw} &= -M_z - F_y x \end{aligned} \tag{6.8}$$

The above steps used to translate the forces and moments to the correct coordinate system were for the forces and moments, in Newton. Nevertheless, these procedures can also be adapted for application to force and moment coefficients, which are the primary focus of this project. Forces and moments could simply be replaced by the corresponding coefficients, while distances x and z should be divided by the reference length c, which is the length of the central chord.

7

Analysis of the load measurement data

In this chapter, the analysis of the load measurement data is presented. The data collected during measurements of only the support structure is analysed in section 7.1. Similarly, the data collected during the measurements with the kite mounted is discussed in section 7.2. Special test cases are analysed in section 7.3, followed by an analysis of the unsteady data gathered during the experiments in section 7.4. Finally, a comparison with literature is presented in section 7.5.

7.1. Support structure aerodynamics

As discussed in chapter 5, measurements have been made on the support structure only to obtain interpolation relationships for the aerodynamic force and moment coefficients of the support structure. These coefficients, as explained in chapter 6, would then be used to subtract the aerodynamic influence of the support structure by subtracting them from the coefficients determined in the experiments with the kite mounted on the support structure. The interpolation relationships are plotted together with the actual measured quantities for the five different measured Reynolds numbers in Figure 7.1, Figure 7.2 and Figure 7.3 for sideslip angles 0, 6 and 12 degrees. Note that these coefficients are in the force balance coordinate system, not in the kite coordinate system. The plots for all other sideslip angles are presented in section A.1.

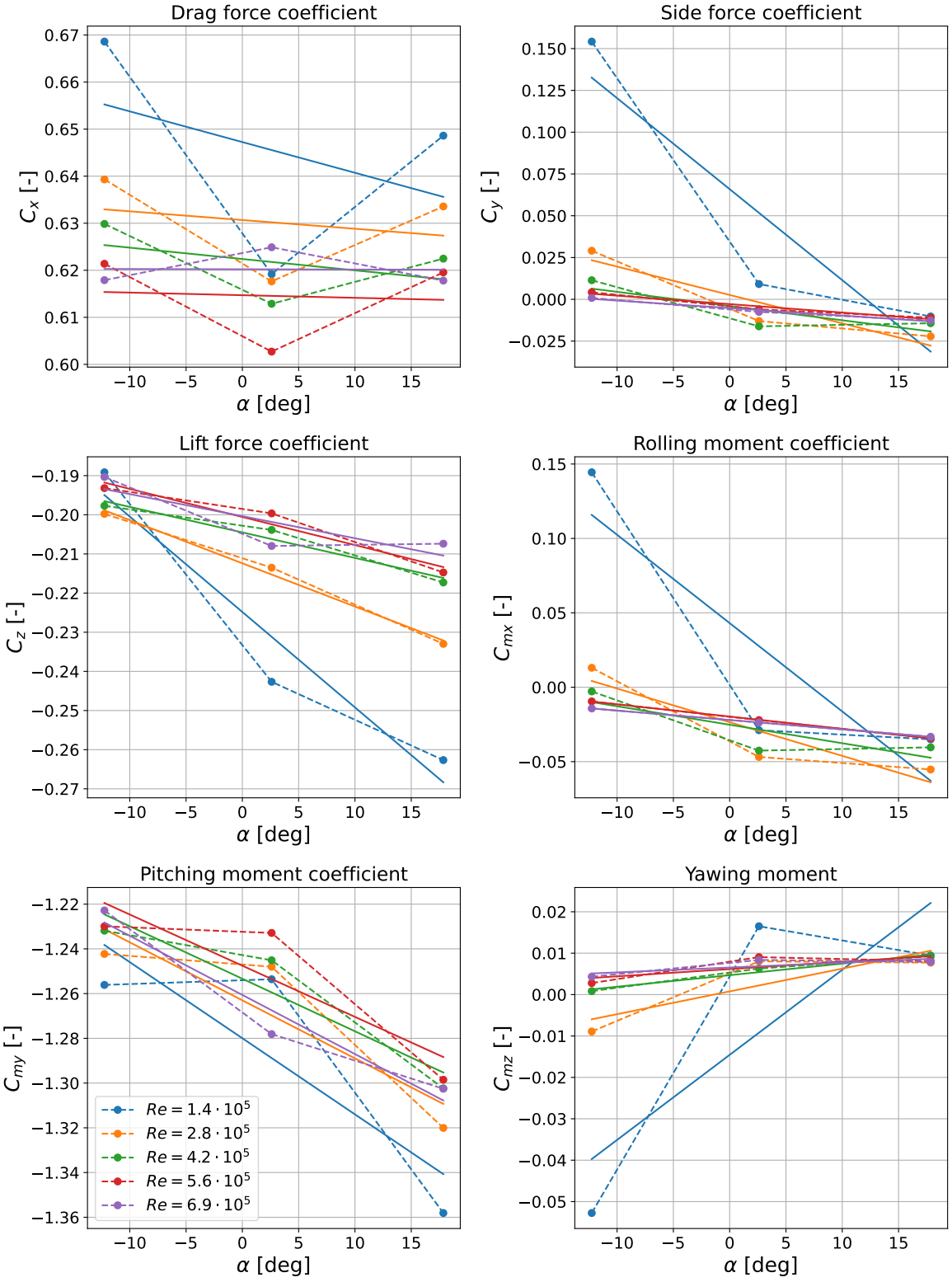

Figure 7.1: Force and moment coefficient plots of the support structure for $\beta = 0$ deg.

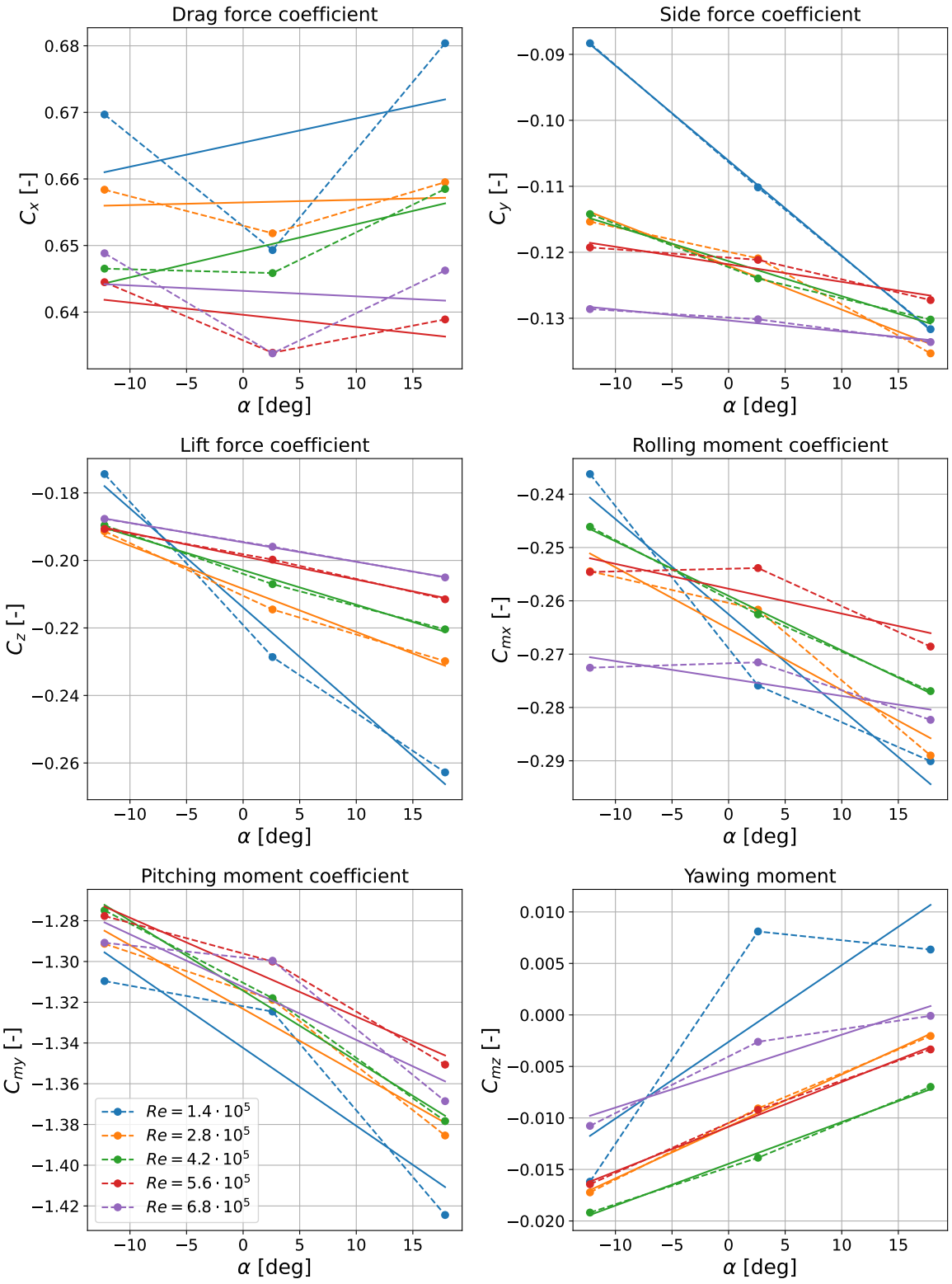

Figure 7.2: Force and moment coefficient plots of the support structure for $\beta = 6$ deg.

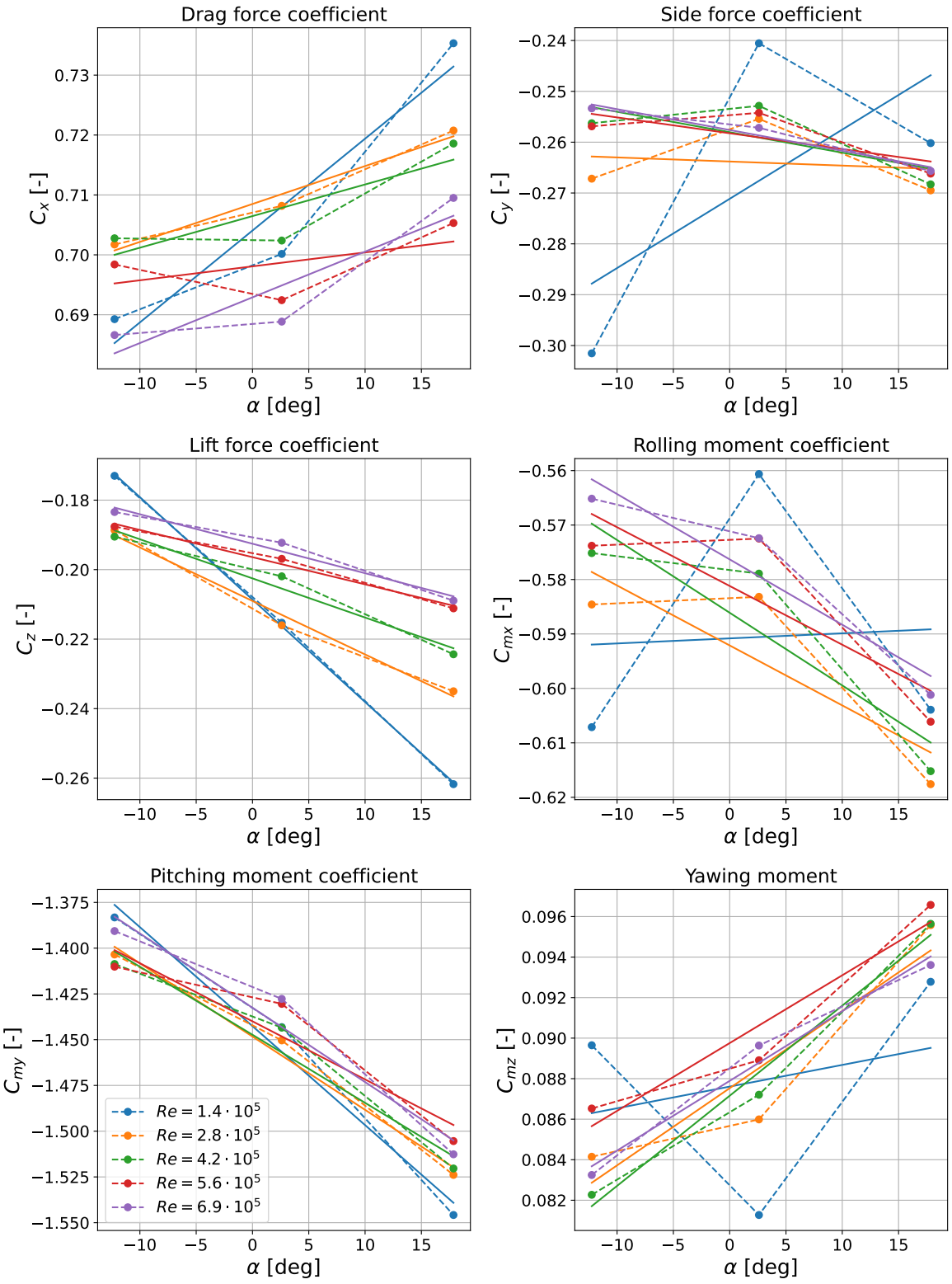

Figure 7.3: Force and moment coefficient plots of the support structure for $\beta = 12$ deg.

In the plots, the points are the measured values, connected by the dashed line, whereas the solid curves through these points are the fitted regression curves. When investigating Figure 7.1, Figure 7.2 and Figure 7.3, it can immediately be seen that the lines for $Re = 1.4 \cdot 10^5$ deviate from

the other Reynolds numbers. This was already expected to happen, as stated in , where it was explained that for reliable results, the Reynolds number should ideally be above $Re = 2.0 \cdot 10^5$. The reasons for its deviation can be attributed to several possible factors. First, flow separation and vortex shedding are more prominent at lower Reynolds numbers [66]. The protruding cylinders (as shown in Figure 3.17) could cause this vortex shedding, as the cylinders are pointing into the flow, at a certain angle of attack. Furthermore, airflow is more likely to be laminar over certain portions of the support structure, introducing more unsteadiness.

What is also noticeable in the plots, more especially in the top right plot, is that the support structure produces a certain amount of lift, increasing with angle of attack. In the plots, the lift force is negative, but because the z-axis is pointing downward for the force balance coordinate system, the lift is positive. Nonetheless, this lift must be generated by some part of the structure. A portion of this lift can be attributed to the protruding rods. However, the majority of the lift must originate from another component of the system. Analyzing the support structure reveals that other angled beams are present in the airflow, specifically the beams supporting the rods bearing the weight of the kite. Given the absence of other apparent lifting surfaces on the structure, it can be concluded that these beams, along with the protruding rods, are responsible for the observed lift.

It can also be observed from Figure 7.1 that the side force, rolling moment and yawing moment are close to zero for all angles of attack, but are not always equal zero for every angle. This is unusual as the structure is expected to be symmetrical, meaning that there are no side forces when the structure is not subject to a sideslip angle. This suggests that minor errors were introduced during the construction phase of the support structure. These discrepancies are minor and are anticipated when assembling such a structure in-house. Importantly, these errors remain minimal.

The symmetry of the support structure can be even better analysed by plotting the forces and moment coefficients for a certain angle of attack versus the sideslip angle. Such a plot for $\alpha = 2.6$ degrees is shown in Figure 7.4. Again, plots for the other angles of attack can be found in section A.1.

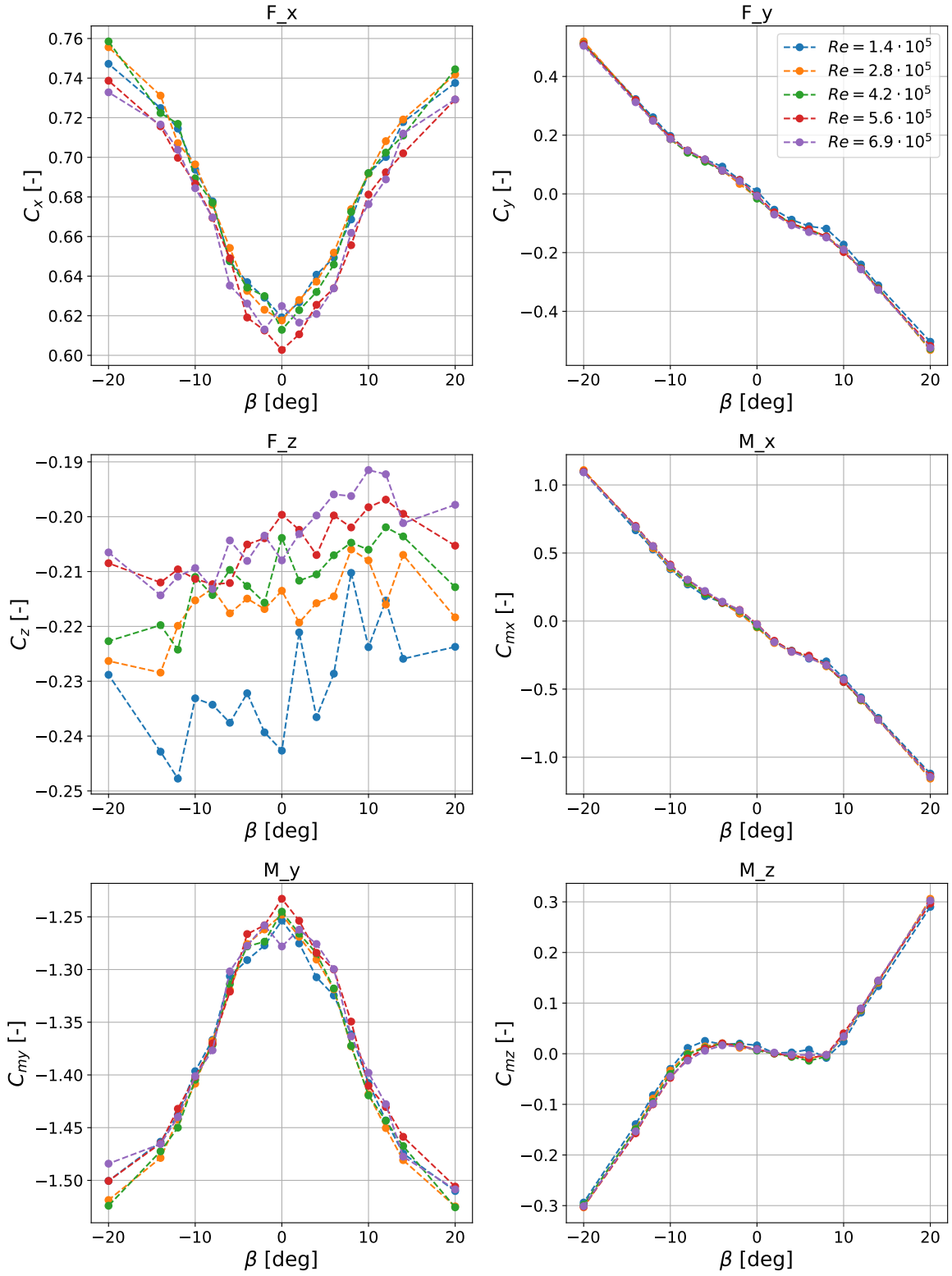

Figure 7.4: Force and moment coefficient plots of the support structure for $\alpha = 2.6$ deg.

In Figure 7.4, it can be seen that there is a near perfect symmetry for all plots except the lift force plot. For example, for $\beta = 0$, the drag coefficient and pitching moment coefficient all have their extremes. Furthermore, the side force, rolling moment and yawing moment plots all are near

zero for $\beta = 0$, and the negative and positive extreme sideslip angles are about equal but opposite in sign. Looking at the outer β values for the drag and pitching moment coefficients, only a slight difference is observed.

When observing the lift force coefficient plot in the top right of Figure 7.4, no real patterns can be observed because the plot looks quite spiky on first impression. However, when looking at the range on the y-axis, the difference between the maximum and minimum measured lift coefficient is only 0.02-0.03, and slightly higher for the lowest Reynolds number. Therefore, it can be concluded that the lift remains almost constant for all sideslip angles.

7.2. Kite aerodynamics

Similarly to the plots of the support structure in section 7.1, force and moment coefficients were created for the kite only. These coefficients were calculated using the interpolation relationships of the support structure coefficients, which have been analysed in section 7.1. The outcome of this analysis did not show large irregularities that allowed them to not be used for this purpose, except for the Reynolds number $Re = 1.4 \cdot 10^5$. However, it was decided to use the interpolation relationships for this low Reynolds number in the processing of the measurement data, where the kite was mounted on the support structure to remain consistent in processing the data. The aerodynamic coefficients plotted versus the angle of attack of the kite for $\beta = 0$ are shown in Figure 7.5. The same plots for other sideslip angles are shown in section A.2.

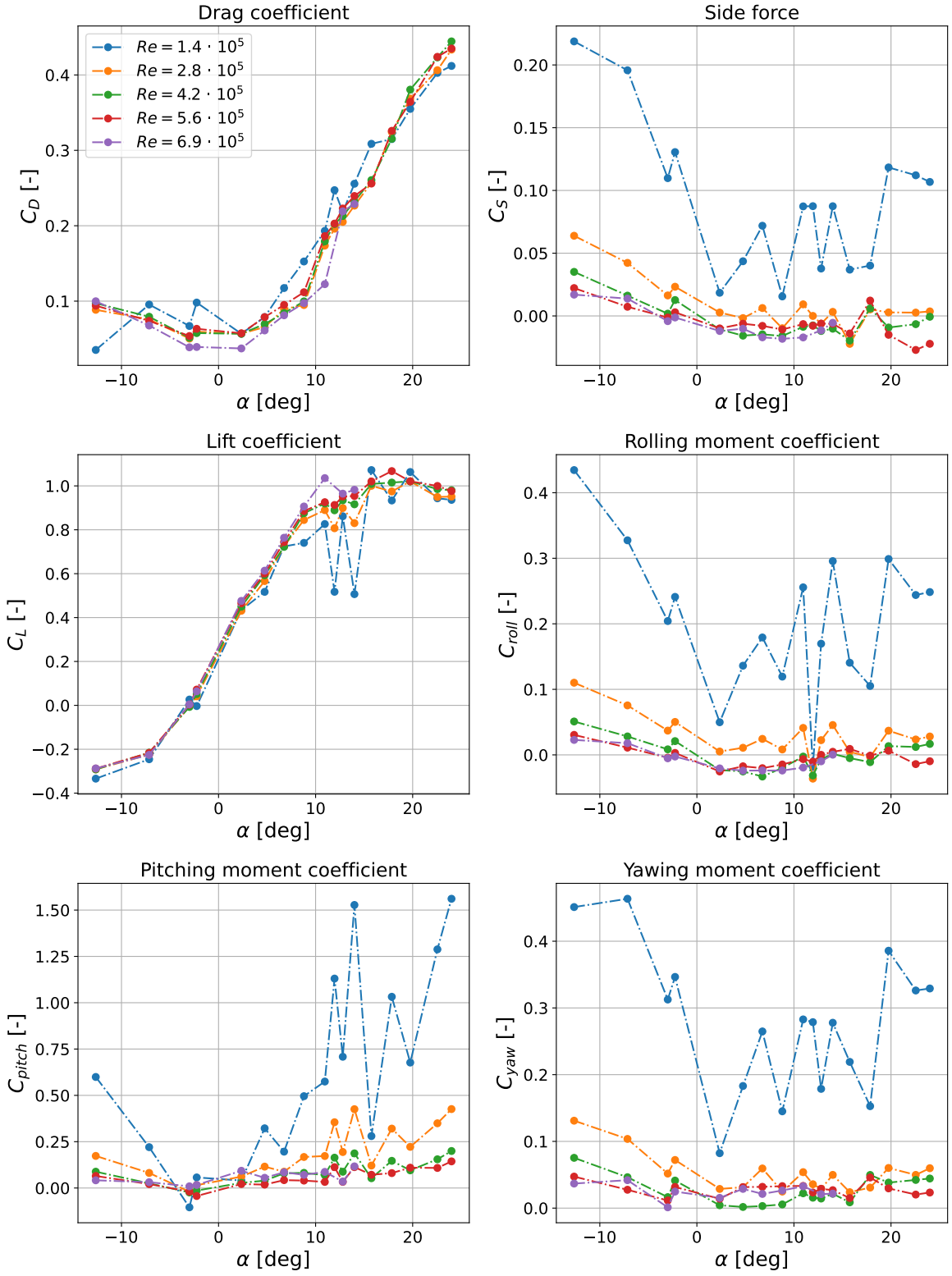

Figure 7.5: Force and moment coefficient plots of the kite for $\beta = 0$ deg.

Upon examination of Figure 7.5, it is evident that the curves corresponding to $Re = 1.4 \cdot 10^5$ exhibit inconsistencies compared to the results obtained in other Reynolds numbers. This can again be attributed to the fact that reliable results are usually obtained above a Reynolds number of $2.0 \cdot 10^5$,

as explained in section 7.1. However, the lift and drag coefficient plots show smaller deviations between the lowest Reynolds number and the other ones.

The smaller deviations in the lift and drag coefficients, particularly in the linear part of the lift curve, can be attributed to the nature of these forces. In the linear region, the lift coefficient is primarily a function of the angle of attack and is less sensitive to flow separation and transition effects. At low Reynolds numbers, while there may be laminar separation, it is often not severe enough to significantly disrupt the linear relationship between lift and angle of attack [67]. Similarly, the drag coefficient in this region is dominated by skin friction drag, which remains relatively stable even at lower Reynolds numbers. The pressure drag component, which can be more sensitive to flow separation, is smaller in the linear part of the lift curve [25].

In contrast, the side force, rolling moment, pitching moment, and yawing moment coefficients show larger deviations at $Re = 1.4 \cdot 10^5$. These coefficients are highly dependent on the asymmetry and unsteadiness in the flow around the kite. At lower Reynolds numbers, the flow is more prone to laminar-turbulent transition and unsteady flow separation. Such irregularities can lead to significant variations in pressure distribution, resulting in larger deviations in side force and moment coefficients [68].

The boundary layer behavior at lower Reynolds numbers is another contributing factor. At $Re = 1.4 \cdot 10^5$, the boundary layer is expected to be thinner and more susceptible to disturbances [42], affecting the side force and moments more than the lift and drag in the linear region. The transition from laminar to turbulent flow along the kite's surface can cause fluctuations in the aerodynamic forces, leading to the observed inconsistencies.

Surface impurities and roughness also play a significant role at lower Reynolds numbers. Imperfections on the kite's surface can lead to premature boundary layer transition from laminar to turbulent flow, thereby affecting the aerodynamic performance. These surface impurities can exacerbate the irregularities in the flow, causing further deviations in the side force, rolling moment, pitching moment, and yawing moment coefficients. At higher Reynolds numbers, the effect of surface roughness is less pronounced as the flow is already more turbulent and less sensitive to such imperfections [67].

Additionally, the deviations in the lift coefficient at lower Reynolds numbers become more pronounced when the kite is in the stalled regime compared to the linear regime. In the stalled regime, the flow is characterized by large-scale separation and unsteady reattachment, leading to highly irregular and unstable aerodynamic forces. At lower Reynolds numbers, the laminar flow is less capable of handling adverse pressure gradients, resulting in earlier and more severe flow separation. This contributes to greater variability and larger deviations in the lift coefficient in the stalled regime compared to the more stable and predictable linear regime [25].

The pitching moment coefficient also shows unusual behavior, with a negative slope from $\alpha = -12$ degrees until $\alpha = -3$ degrees, and then becoming slightly positive. This behavior could be related to the point around which the moments are taken. In this experiment, the moments are referenced to the center of gravity. The choice of reference point can significantly affect the moment coefficients. If the center of pressure shifts with angle of attack, it can cause variations in the pitching moment slope. When the center of pressure moves aft of the center of gravity, it results in a nose-down pitching moment (negative slope). Conversely, if it moves forward, it results in a nose-up pitching moment (positive slope). This shift can explain the change from a negative to a slightly positive slope around $\alpha = -3$ degrees [69].

Overall, the increased sensitivity to flow disturbances, unsteady aerodynamic forces, higher drag, the influence of surface impurities, and the potential effects of reference point selection at lower Reynolds numbers contribute to the larger deviations in the side force, rolling moment, pitching moment, and yawing moment coefficients, as compared to the lift and drag coefficients in the linear part of the lift curve.

Again, the symmetry of the kite can be better analysed by looking at the coefficients plotted versus the sideslip angle. The choice of angle of attack here is $\alpha = 6.75$ degrees, as it falls within the linear part of the lift curve, and $\alpha = 11.95$ degrees, as it is one of the angles of attack most fre-

quently seen in operation of the V3A kite. These plots can be found in Figure 7.6 for the first case and Figure 7.7 for the latter. Again, plots for other angles of attack can be found in section A.2.

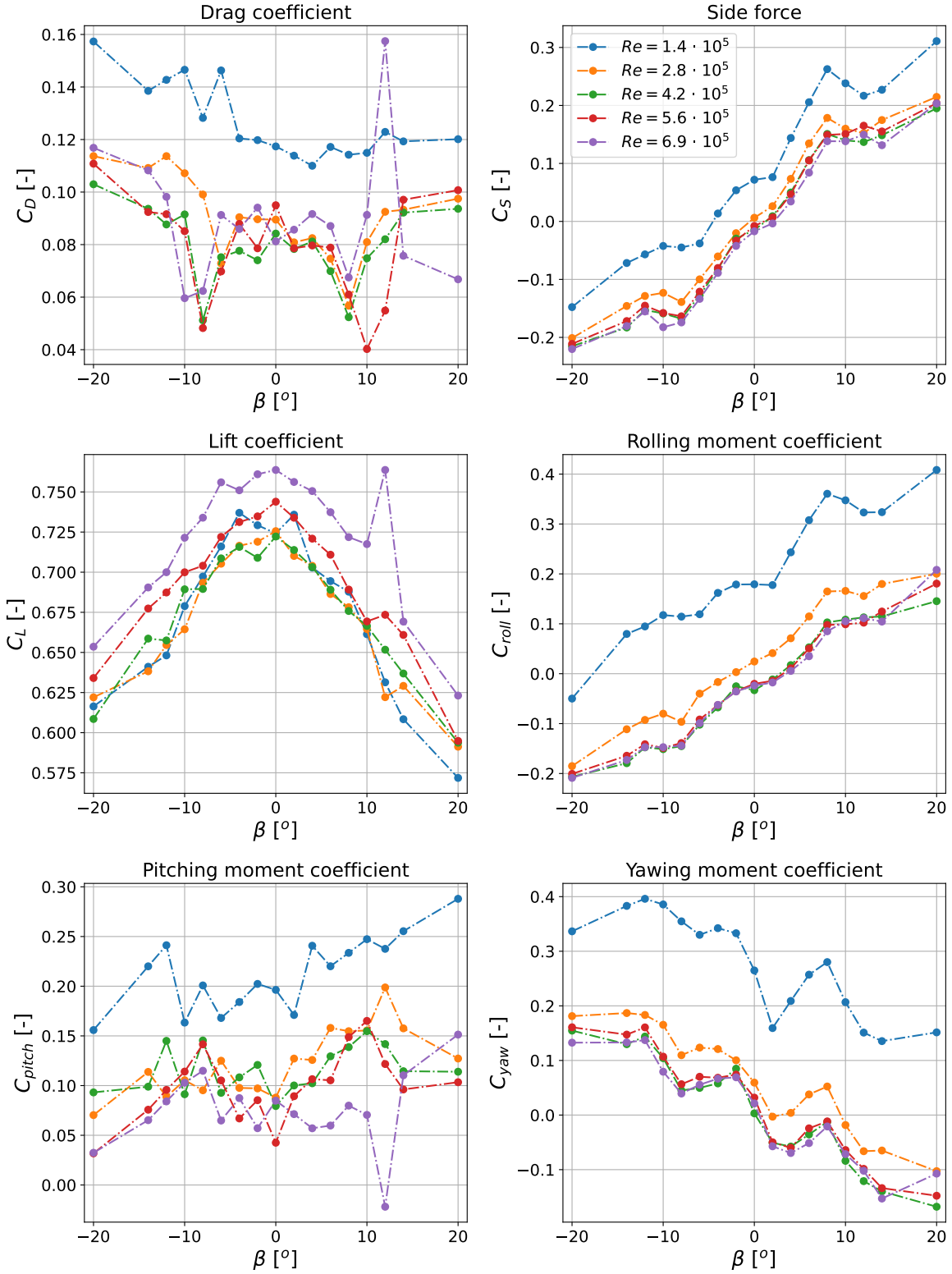

Figure 7.6: Force and moment coefficient plots of the kite for $\beta = 6.75$ deg.

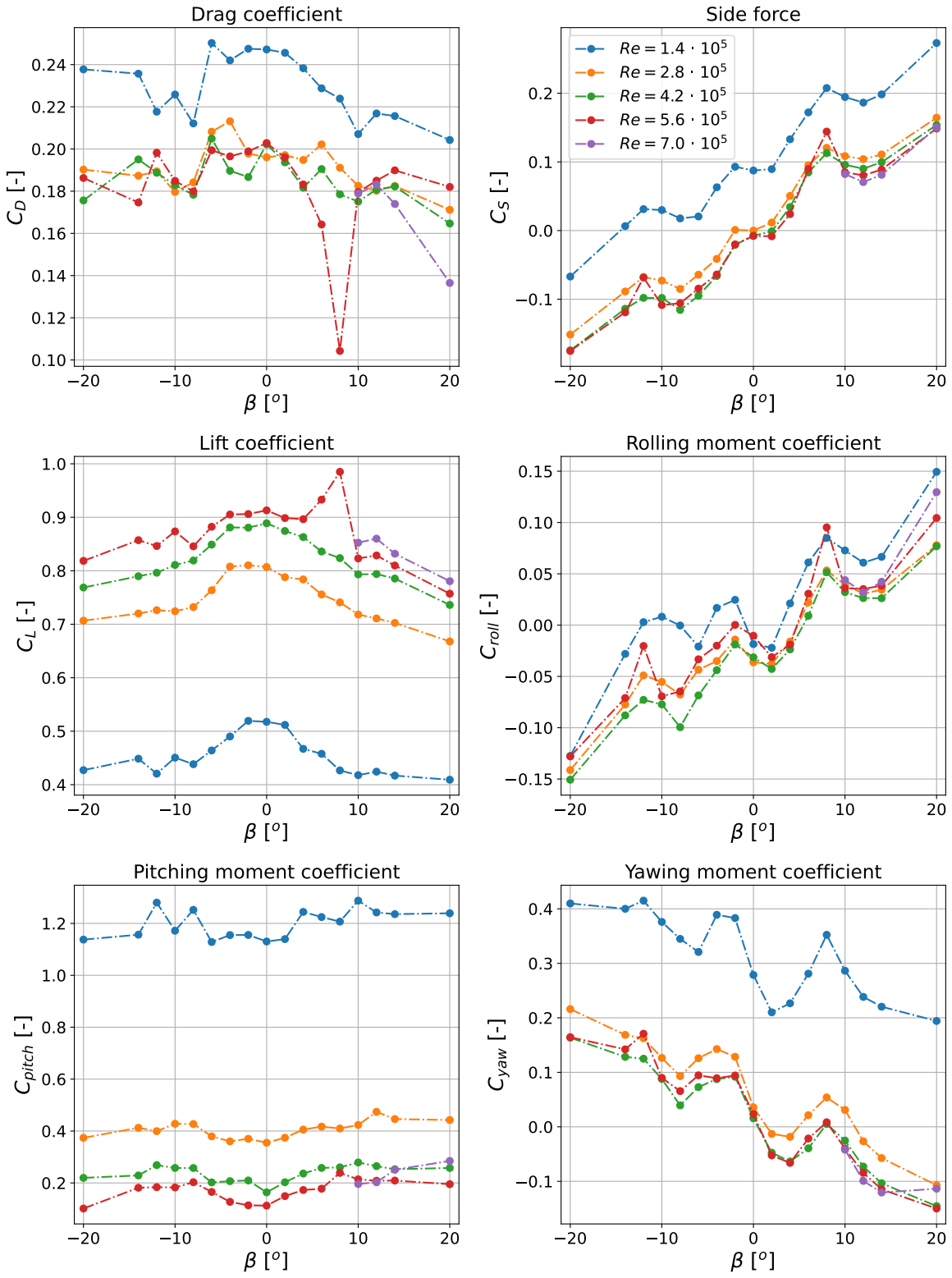

Figure 7.7: Force and moment coefficient plots of the kite for $\alpha = 11.95$ deg.

Observations for the non-stalled case ($\alpha = 6.75$ degrees) reveal that the lowest Reynolds number has higher drag and side force coefficients. This can be attributed to the fact that at lower Reynolds numbers, the boundary layer is thinner and more prone to separation, resulting in

higher pressure drag and increased side force due to more prominent flow asymmetries [67]. Additionally, the higher roll, pitch, and yawing moment coefficients observed at the lowest Reynolds number are indicative of more significant flow separation and unsteady aerodynamic effects, which can induce larger moments due to asymmetric pressure distributions [25].

Interestingly, the lift coefficient at the lowest Reynolds number is similar to those at higher Reynolds numbers in the non-stalled case. This suggests that while the lower Reynolds number affects drag and side forces significantly, it does not drastically alter the lift in the linear part of the lift curve. This behavior is consistent with the understanding that lift in the linear regime is primarily a function of angle of attack and less influenced by Reynolds number [68].

Some outliers are observed at a sideslip angle of 12 degrees, which might be due to experimental anomalies or specific flow disturbances at that particular angle. These outliers can affect the perceived symmetry of the force and moment coefficients, especially in terms of drag and moments [42]. For higher Reynolds numbers, the side force shows good symmetry around zero sideslip, indicating that the kite maintains a balanced aerodynamic behavior at these conditions. However, the rolling moment and yawing moment coefficients are not entirely symmetric, which could be due to minor asymmetries in the kite's design or mounting imperfections that become more noticeable at higher angles of sideslip [69].

The lift force is nearly symmetric, with the maximum lift occurring at zero sideslip, but there are slight differences in the extremes, indicating minor asymmetries in the flow or kite geometry. Drag shows a somewhat symmetric pattern for higher Reynolds numbers, but the highest Reynolds number displays less symmetry, potentially due to the outlier mentioned earlier [67].

In the stalled case ($\alpha = 11.95$ degrees), similar observations are made with higher drag and side force coefficients at the lowest Reynolds number. However, the lift coefficient for the lowest Reynolds number is significantly lower compared to higher Reynolds numbers. This can be explained by the nature of stalled flow, where large-scale separation and unsteady reattachment occur. At lower Reynolds numbers, the flow is less capable of maintaining attachment in adverse pressure gradients, leading to earlier and more severe stall, which drastically reduces lift [25].

Overall, the increased sensitivity to flow disturbances, unsteady aerodynamic forces, and higher drag at lower Reynolds numbers contribute to the larger deviations in the force and moment coefficients. The symmetry analysis reinforces the understanding that the kite's aerodynamic performance is more predictable at higher Reynolds numbers, where the flow is more stable and less prone to separation and other irregularities.

7.3. Special cases

As stated in chapter 5, several special test cases have been measured, namely a test case with zigzag tape applied to the kite, a test case where a certain data point is measured multiple times, a test case where the kite is flipped upside down, and a test case to measure possible sensor drift. Unfortunately, the test case for the flipped kite could not be processed due to the absence of the necessary zero-run data. However, the other test cases have been processed and are analysed and discussed in this section.

7.3.1. Zigzag tape

To investigate the impact of zigzag tape on the leading edge of the kite, measurements were performed at a fixed angle of attack $\alpha = 6.75$ degrees and sideslip angle $\beta = 0$ degrees. The zigzag tape was applied to the leading edge on the suction side. The force and moment coefficients were plotted against Reynolds number for both the zigzag tape case and the non-zigzag tape case. These results are shown in Figure 7.8.

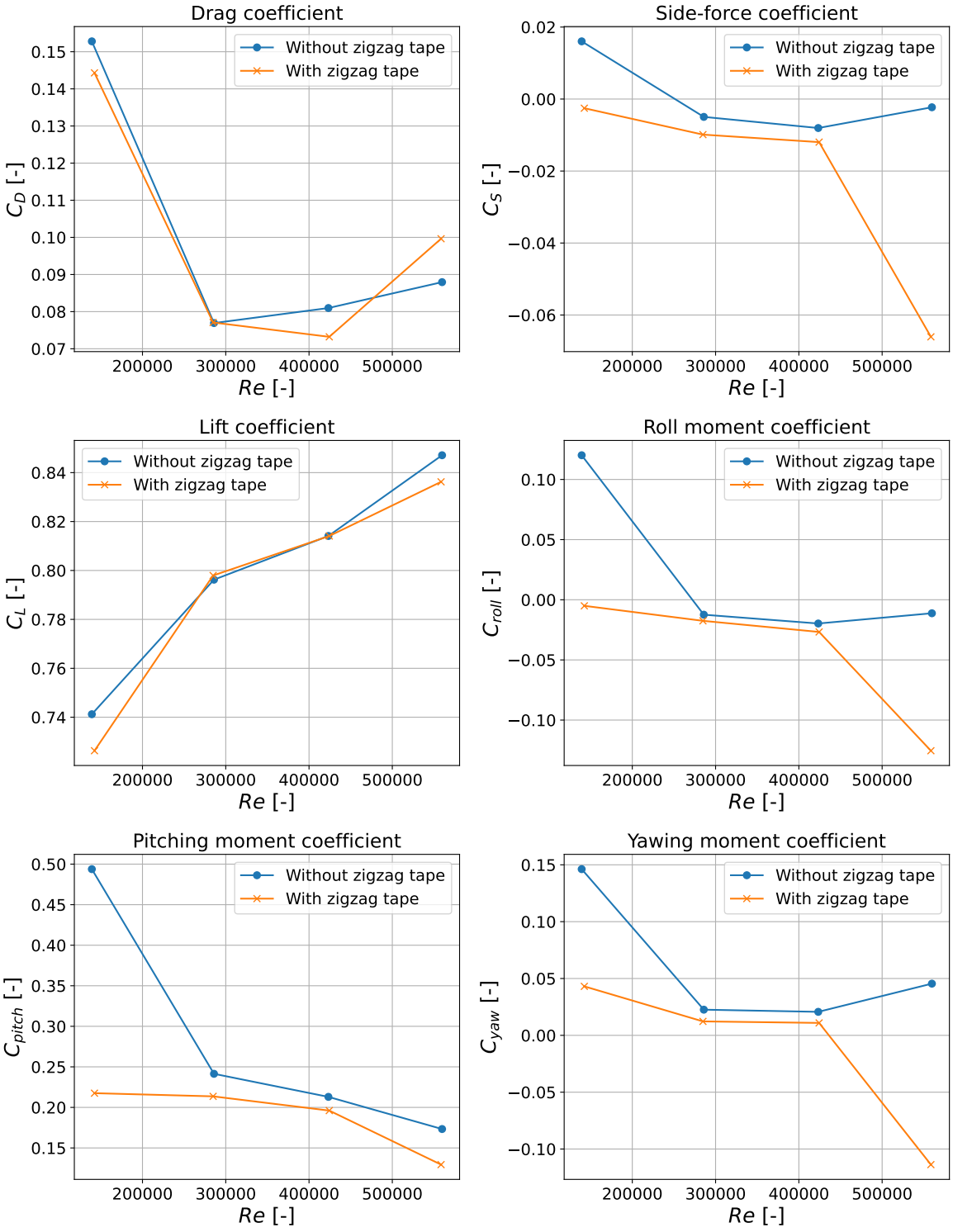

Figure 7.8: Comparison of force and moment coefficients plotted against Reynolds number for the zigzag tape and non-zigzag tape cases at $\alpha = 6.75$ deg and $\beta = 0$ deg.

The drag coefficient shows an interesting trend where the case without zigzag tape exhibits slightly lower drag at the lowest Reynolds number. As the Reynolds number increases, the drag

coefficients for both cases become similar, with minor variations. At intermediate Reynolds numbers, the case without zigzag tape shows slightly higher drag, which then becomes slightly lower again at the highest Reynolds number. This variation can be attributed to the complex interaction between the boundary layer and the surface irregularities introduced by the zigzag tape. Zigzag tape is known to induce early transition from laminar to turbulent flow, reducing drag by delaying separation at lower Reynolds numbers but potentially increasing drag slightly as Reynolds numbers increase due to higher skin friction [70].

The side force coefficient remains close to zero for both cases, as expected for a zero sideslip angle. However, there is a slightly higher side force in the zigzag tape case, especially at higher Reynolds numbers, where an anomalous larger negative side force is observed. This might be due to an erroneous data point or an unsteady aerodynamic effect introduced by the zigzag tape, causing asymmetry in the flow [71].

The lift coefficient for the zigzag tape case is almost equal to the case without zigzag tape, showing only slightly lower values at both the highest and lowest Reynolds numbers. This suggests that the zigzag tape does not significantly affect the overall lift generation in the linear part of the lift curve. However, the minor reduction in lift at the extreme Reynolds numbers could be due to the altered boundary layer characteristics and early transition induced by the tape, affecting the pressure distribution on the airfoil surface [72].

In terms of rolling moment, the case without zigzag tape generally shows slightly higher values. At the lowest Reynolds number, the rolling moment is non-zero for the no zigzag tape case, indicating some asymmetry or unsteady aerodynamic effect. Conversely, at the highest Reynolds number, the zigzag tape case exhibits a non-zero rolling moment, possibly influenced by the aforementioned large negative side force. This behavior highlights the sensitivity of rolling moments to slight changes in flow conditions and boundary layer characteristics [42].

The pitching moment coefficient is slightly higher for the no zigzag tape case across most Reynolds numbers. However, at the lowest Reynolds number, the pitching moment is significantly higher for the no zigzag tape case compared to the zigzag tape case. This could be due to the stabilizing effect of the zigzag tape, which promotes earlier transition to turbulence, thereby reducing the pitching moment by stabilizing the flow over the airfoil [73].

The yawing moment shows behavior similar to the rolling moment, with the no zigzag tape case generally having slightly higher values. The observed non-zero yawing moment at the lowest Reynolds number for the no zigzag tape case and at the highest Reynolds number for the zigzag tape case indicates potential asymmetries introduced by the zigzag tape at specific Reynolds numbers. This reinforces the idea that the zigzag tape influences the overall aerodynamic balance of the kite, potentially by modifying the flow separation characteristics and promoting symmetry in some conditions while introducing asymmetries in others [42].

Overall, the application of zigzag tape on the leading edge appears to affect the aerodynamic coefficients in a nuanced manner. While it primarily aims to stabilize the flow by inducing early transition to turbulence, its effects on drag, lift, and moment coefficients vary with Reynolds number. These variations highlight the complex interplay between flow transition, separation, and surface modifications, emphasizing the need for careful consideration when implementing such modifications in aerodynamic designs.

7.3.2. Double cases

In wind tunnel testing, it is important to check whether the things you are measuring are not arbitrary and can be reproduced. In order to check this, double measurements were performed for some test cases at different times during the testing campaign. An angle of attack of 4.75 was selected for this purpose, as it was expected to be in the linear region of the lift curve. For this angle of attack, double measurements were made for a wind speed of 20 m/s and for sideslip angles of -20, 0, and 20 degrees. In total, these measurements were performed three different times. Figure 7.9 shows the box plots of the force and moment coefficients for these double measurements for $\beta = 0$ deg, allowing for an easier comparison between the different test times. The other two box plots can be found in section A.3.

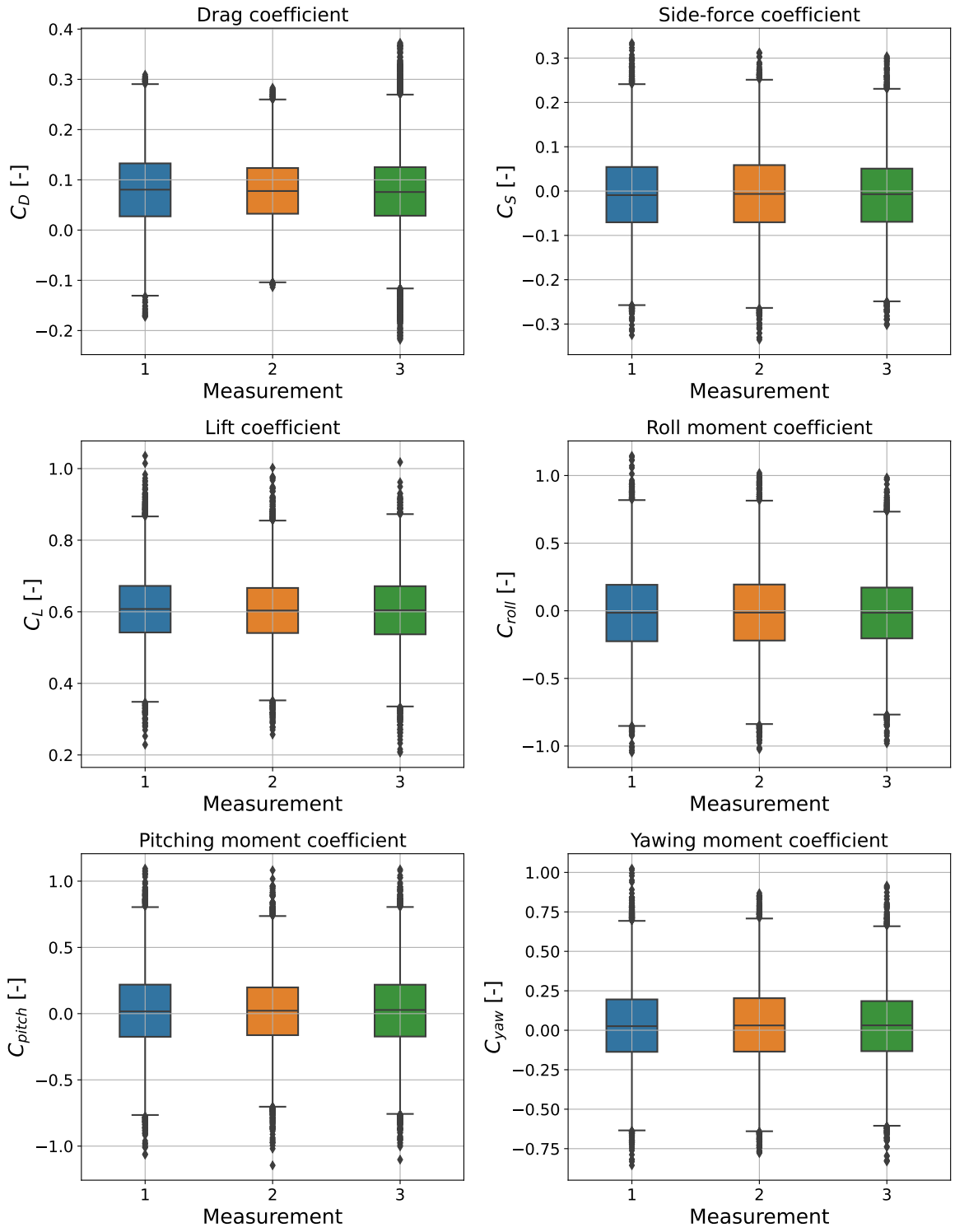

Figure 7.9: Boxplots of force and moment coefficients for double measurements at $\alpha = 4.75$ deg, $\beta = 0$ deg, and wind speed of 20 m/s.

The box plots for all force and moment coefficients show that the boxes are nearly equal in size, and the medians align well across the different measurements. This indicates good repeatabil-

ity and consistency in the measurements, suggesting that the experimental setup and conditions were well controlled. The primary differences observed are in the whiskers for some data points, which show slightly more variation, though still relatively small. This variation could be attributed to minor fluctuations in wind tunnel conditions or slight variations in the setup during the different test times. Furthermore, vibrations could also cause these differences, as slight vibrations were seen in some measurements.

In addition, there are several outliers outside the whiskers in the boxplots. The presence of outliers suggests that while the bulk of the data is consistent, there are occasional deviations that could be due to transient effects, measurement errors, or minor inconsistencies in the kite's positioning or condition. These outliers, although they do not significantly affect the overall trend, highlight the importance of considering potential sources of variability in wind tunnel experiments.

Overall, the observations from the boxplots indicate that the double measurements are reproducible and reliable, with only minor variations and some outliers that do not substantially affect the general consistency of the data. This repeatability is crucial to ensure that the aerodynamic characteristics measured in the wind tunnel are reliable and can be used confidently for further analysis and design considerations.

7.3.3. Sensor drift

To ensure the accuracy and reliability of the force balance measurements, it is crucial to monitor potential sensor drift over time. For this purpose, sensor drift measurements were conducted at the start and end of each testing day, before touching anything in the test chamber of the tunnel. During these measurements, the force balance readings were recorded for 30 seconds without wind. This procedure was repeated across multiple days to identify any drift in the sensors. The barcharts in Figure 7.10 compare the force and moment coefficients at the beginning and end of each day, providing a visual representation of potential sensor drift.

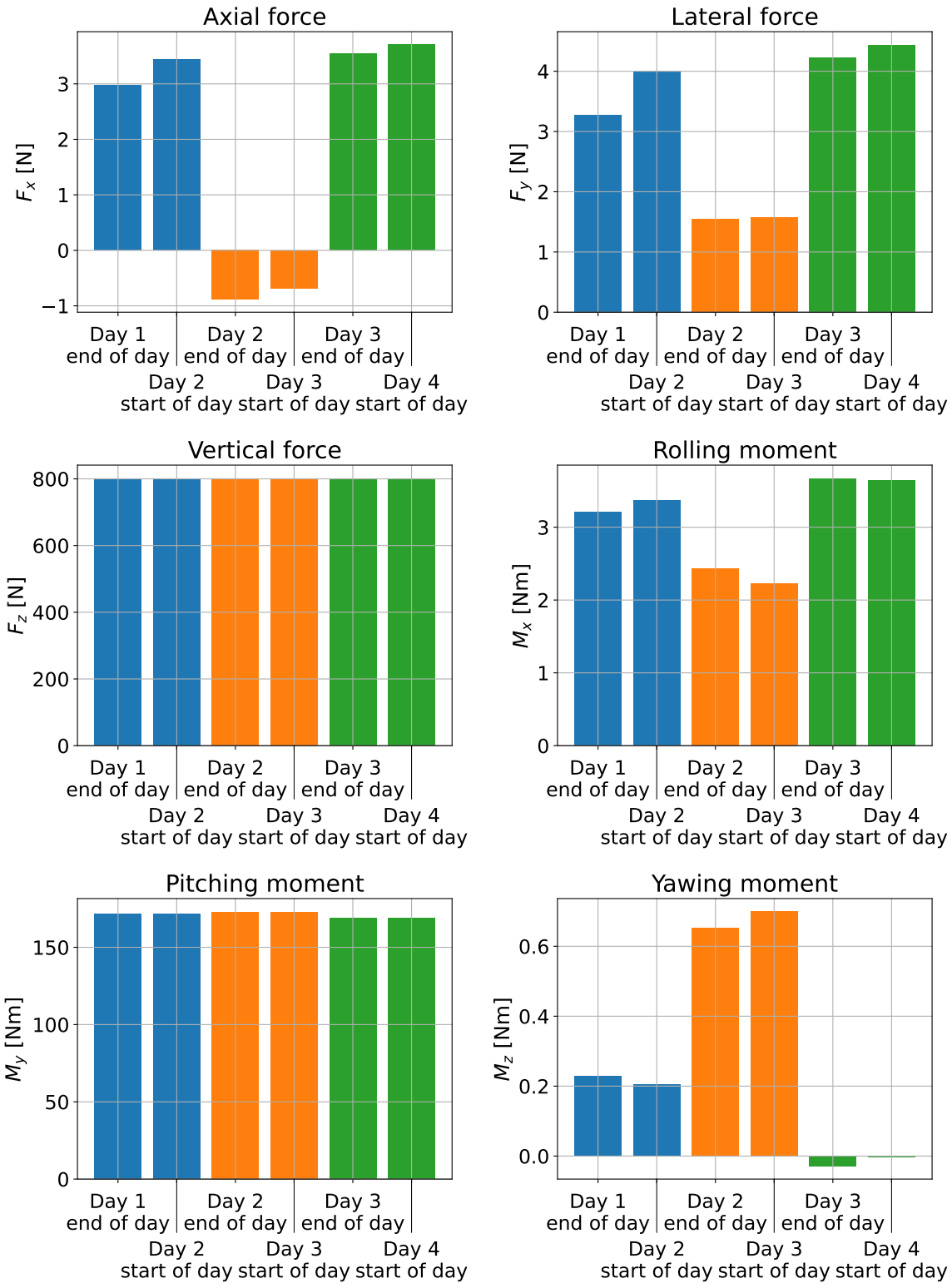

Figure 7.10: Comparison of force and moment coefficient readings at the start and end of each testing day to assess sensor drift.

In Figure 7.10, the bars of the end and beginning of the consecutive days are plotted in the same colour, as comparisons should be made for the same colours. For example, the end of day 1 must

be compared to the beginning of day 2, and so on. As can be observed, there are almost no differences between the end and beginning of the days, for all loads. This indicates that no sensor drift occurs and that it does not have to be taken into account when processing the data.

However, for F_x, F_y, M_x and M_z there are noticeable differences between the different colours. This difference could be attributed to the fact that there might have been objects on the blue table in the test chamber, interfering with the orientation of the table causing it to not be entirely level anymore. Another reason could be that the kite and support structure were left at 90 degrees sideslip, because the angle of attack changes were easier this way. This could have also caused the blue table to not be level anymore.

7.4. Uncertainty analysis

In wind tunnel testing, understanding and quantifying the uncertainty in the measurements is crucial to ensure the reliability and accuracy of the results. This section presents the uncertainty analysis conducted for the steady-state aerodynamic coefficients obtained from the experiments.

7.4.1. Boxplot analysis

To assess the uncertainty in the aerodynamic coefficients, boxplots were generated for each Reynolds number separately, plotting the coefficients versus angle of attack. This section focuses on the zero sideslip case, with wind speeds of 5, 15, and 25 m/s. The boxplots provide a visual representation of the variability in the data, with the mean value overlaid on top of each boxplot for clarity. These plots help in understanding the spread and central tendency of the measurements, highlighting any significant uncertainties.

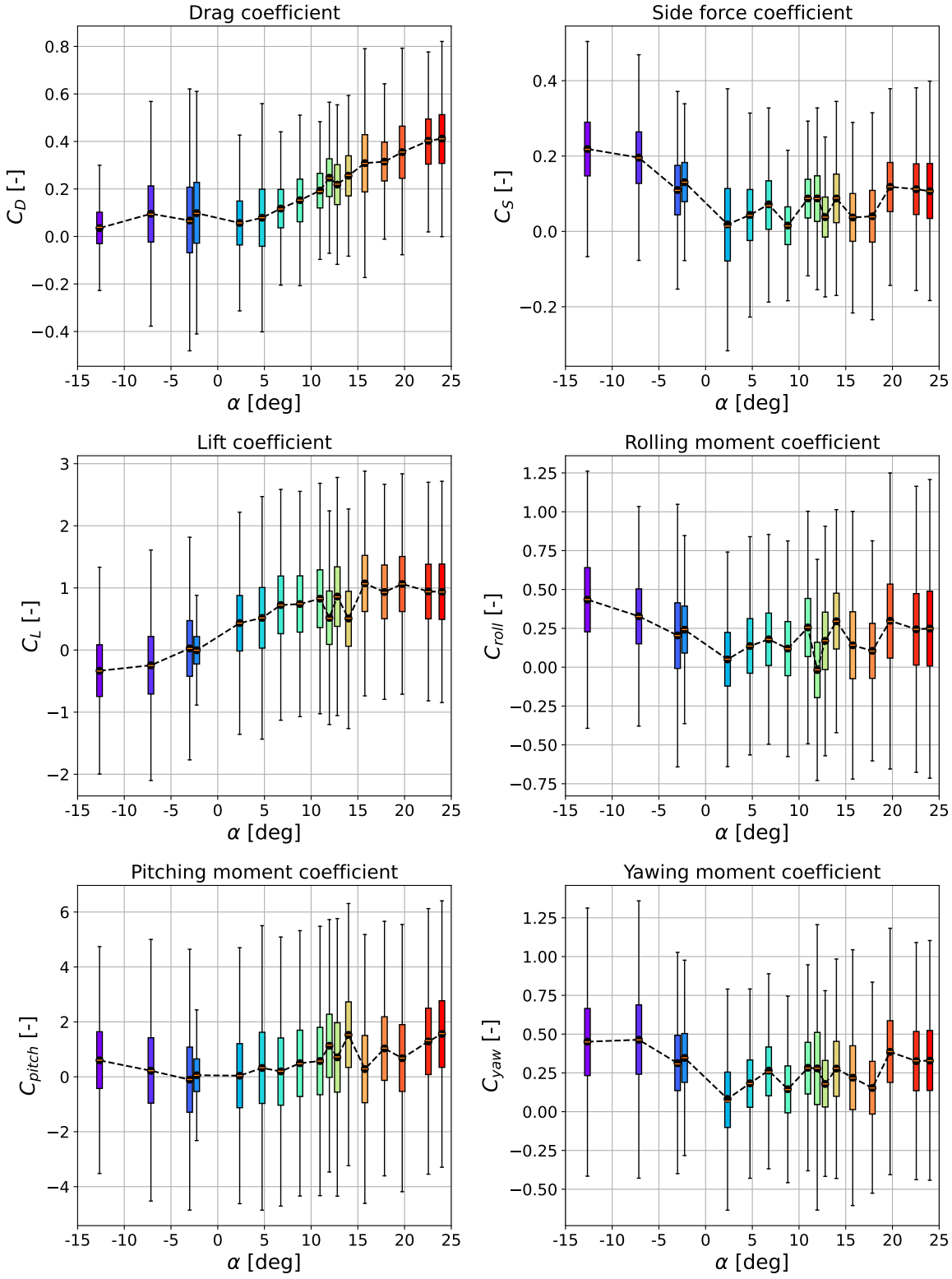

Figure 7.11: Boxplots of aerodynamic coefficients versus angle of attack for $Re = 1.4 \cdot 10^5$ at zero sideslip. The mean values are indicated by the black curve.

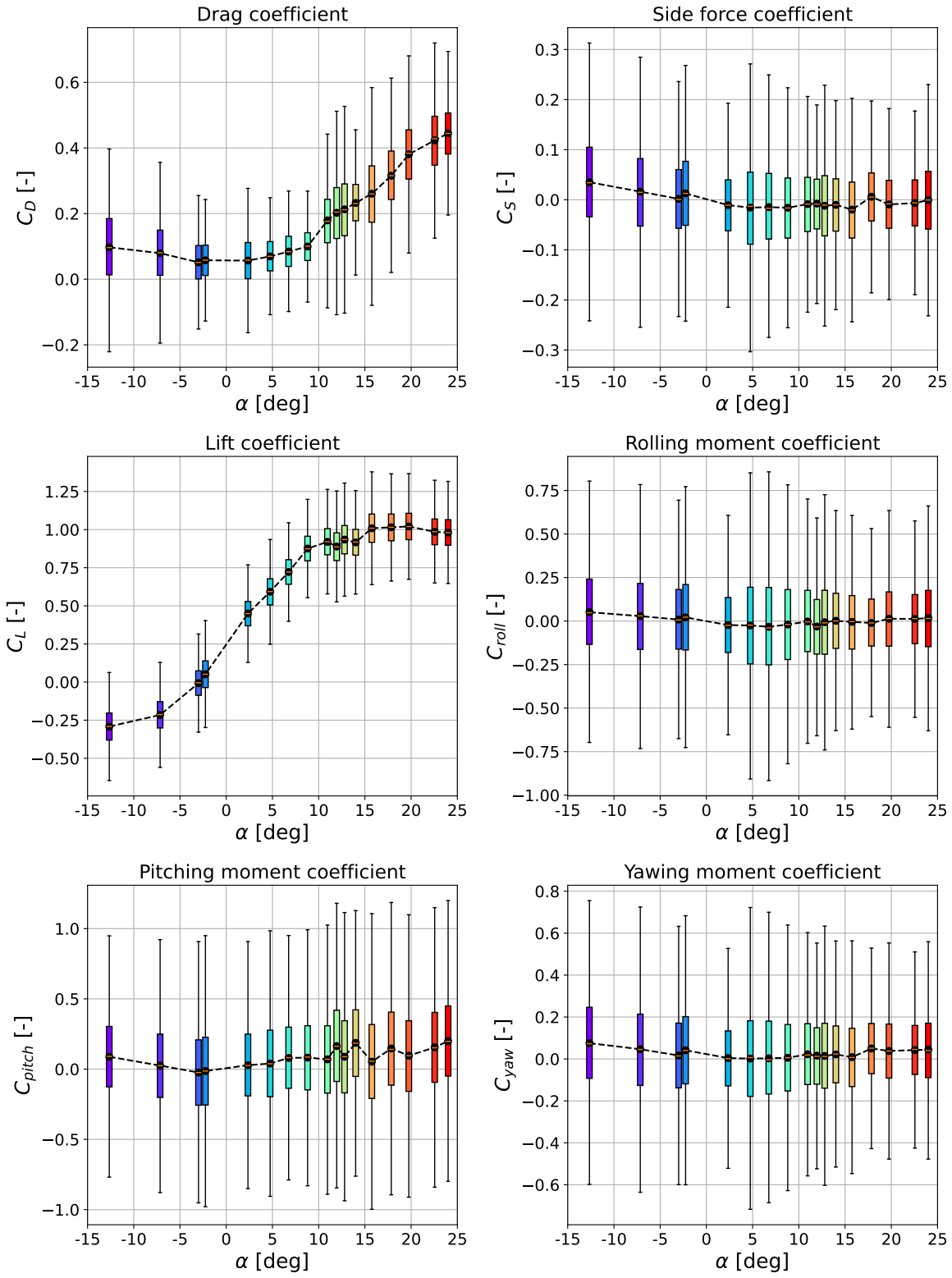

Figure 7.12: Boxplots of aerodynamic coefficients versus angle of attack for $Re = 2.8 \cdot 10^5$ at zero sideslip. The mean values are indicated by the black curve.

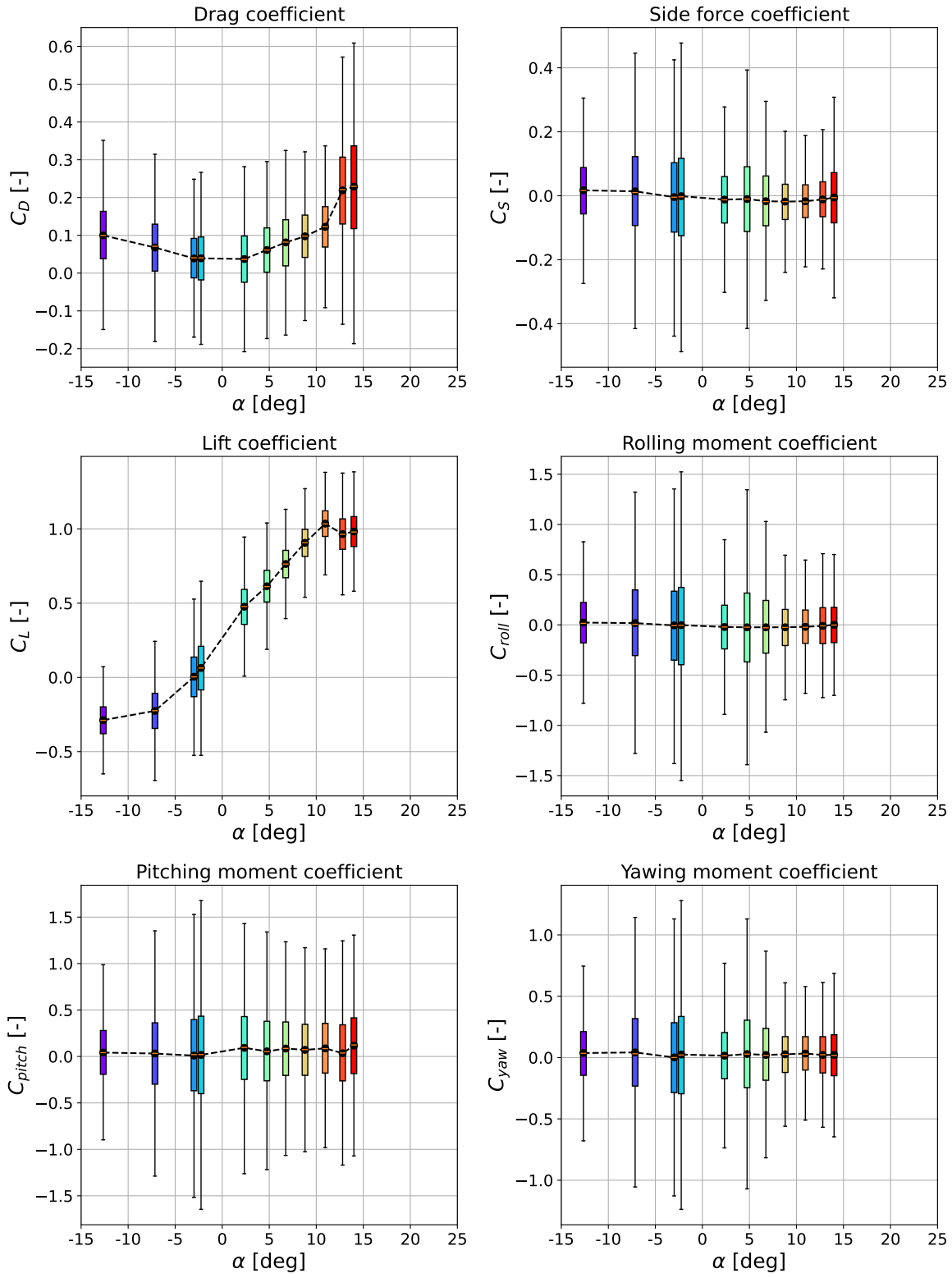

Figure 7.13: Boxplots of aerodynamic coefficients versus angle of attack for $Re = 4.2 \cdot 10^5$ at zero sideslip. The mean values are indicated by the black curve.

The analysis of the boxplots for Reynolds numbers (Re) $1.4{\cdot}10^5$, $2.8{\cdot}10^5$, and $4.2{\cdot}10^5$ reveals several important trends and insights into the behavior of the aerodynamic coefficients and their associ-

ated uncertainties. For the lowest Reynolds number ($Re = 1.4 \cdot 10^5$), the interquartile ranges (IQR) of the boxplots for all forces and moment coefficients are approximately the same, with min/max values also showing minimal variation. This consistency suggests that the measurement variability is relatively uniform across different angles of attack, with some isolated outliers, such as at $\alpha = 2.5$ degrees. These observations align with findings in the literature that indicate lower Reynolds numbers typically exhibit more stable and predictable aerodynamic characteristics due to reduced turbulent flow effects [66].

For the middle Reynolds number ($Re = 2.8 \cdot 10^5$), a similar trend is observed, where the IQRs and min/max values remain relatively consistent across different angles of attack. This suggests that the flow characteristics are stable and the measurement uncertainties are not significantly affected by changes in the angle of attack. Studies have shown that at intermediate Reynolds numbers, the flow transitions start to stabilize, leading to more predictable aerodynamic performance [67].

At the highest Reynolds number ($Re = 4.2 \cdot 10^5$), the general trend of consistent IQRs and min/-max values persists; however, there are more outliers, particularly at $\alpha = 13$ degrees and $\alpha = 14$ degrees in the drag coefficient plot, where the IQR is about 0.2 compared to 0.1 for other angles. These outliers can be attributed to the increased vibrational effects at higher angles of attack, which led to the termination of measurements beyond $\alpha = 14$ degrees. This phenomenon is well-documented in aerodynamic studies, where higher Reynolds numbers and increased angles of attack can lead to flow separation and unsteady aerodynamic forces, resulting in higher measurement uncertainties [74]. Additionally, at $\alpha = -2$ degrees, outliers are observed in the side force, rolling moment, pitching moment, and yawing moment coefficient plots, indicating potential anomalies in the flow behavior or measurement system at this specific angle.

When comparing the different Reynolds numbers, distinct patterns emerge. For the drag coefficient, the IQR for the lowest Re is about 0.2, while for higher Re, it reduces to about 0.1, and the min/max range also decreases from 0.6-0.8 to 0.5-0.6. This reduction in variability with increasing Reynolds number is consistent with the findings that higher Reynolds numbers typically lead to more turbulent but stable boundary layers, reducing overall measurement uncertainty [75]. Similarly, for the side force coefficient, the IQR at low Re is about 0.15 with a min/max range of 0.6, whereas for higher Re, the IQR is below 0.1, and the min/max range is about 0.5-0.6, indicating improved measurement consistency.

For the lift coefficient, the lowest Re shows an IQR of about 1 and a min/max range of 3-3.5, while for higher Re, the IQR significantly reduces to 0.12-0.13 and the min/max range to 0.7. This dramatic reduction in variability is indicative of the stabilizing effects of increased Reynolds number on lift forces, which is corroborated by aerodynamic theories and experimental data [76]. The rolling moment coefficient follows a similar trend, with the lowest Re showing an IQR of 0.5 and a min/max range of 1.25, while higher Re show an IQR of about 0.4 and min/max range of 1.3-1.4.

For the pitching moment coefficient, the IQR for the lowest Re is about 1 with a min/max range of 9-10, while for higher Re, the IQR reduces to about 0.4 and the min/max range to approximately 2-2.5. This reduction is consistent with increased flow stability at higher Reynolds numbers, leading to more predictable pitching moments [25]. Similarly, for the yawing moment coefficient, the lowest Re shows an IQR of 0.3-0.4 and a min/max range of 1.5-1.7, while higher Re show an IQR of about 0.3 and a min/max range of 1.3-1.4.

Overall, the analysis indicates that higher Reynolds numbers generally result in reduced variability and uncertainty in aerodynamic measurements, consistent with established aerodynamic principles and experimental observations. The presence of outliers at specific angles of attack and Reynolds numbers highlights the importance of considering flow instability and measurement system limitations in aerodynamic testing.

To further investigate the uncertainty in the aerodynamic coefficients, additional boxplots were generated by plotting the force and moment coefficients versus the sideslip angle. This way, it can be checked whether there were sideslip angles that systematically show more uncertainty than others. This analysis was conducted at a Reynolds number of $Re = 5.6 \cdot 10^5$, focusing on two

distinct cases: a non-stalled condition at $\alpha = 5$ degrees and a stalled condition at $\alpha = 18$ degrees. Figure 7.14 and Figure 7.15 present the boxplots for the non-stalled and stalled case, respectively.

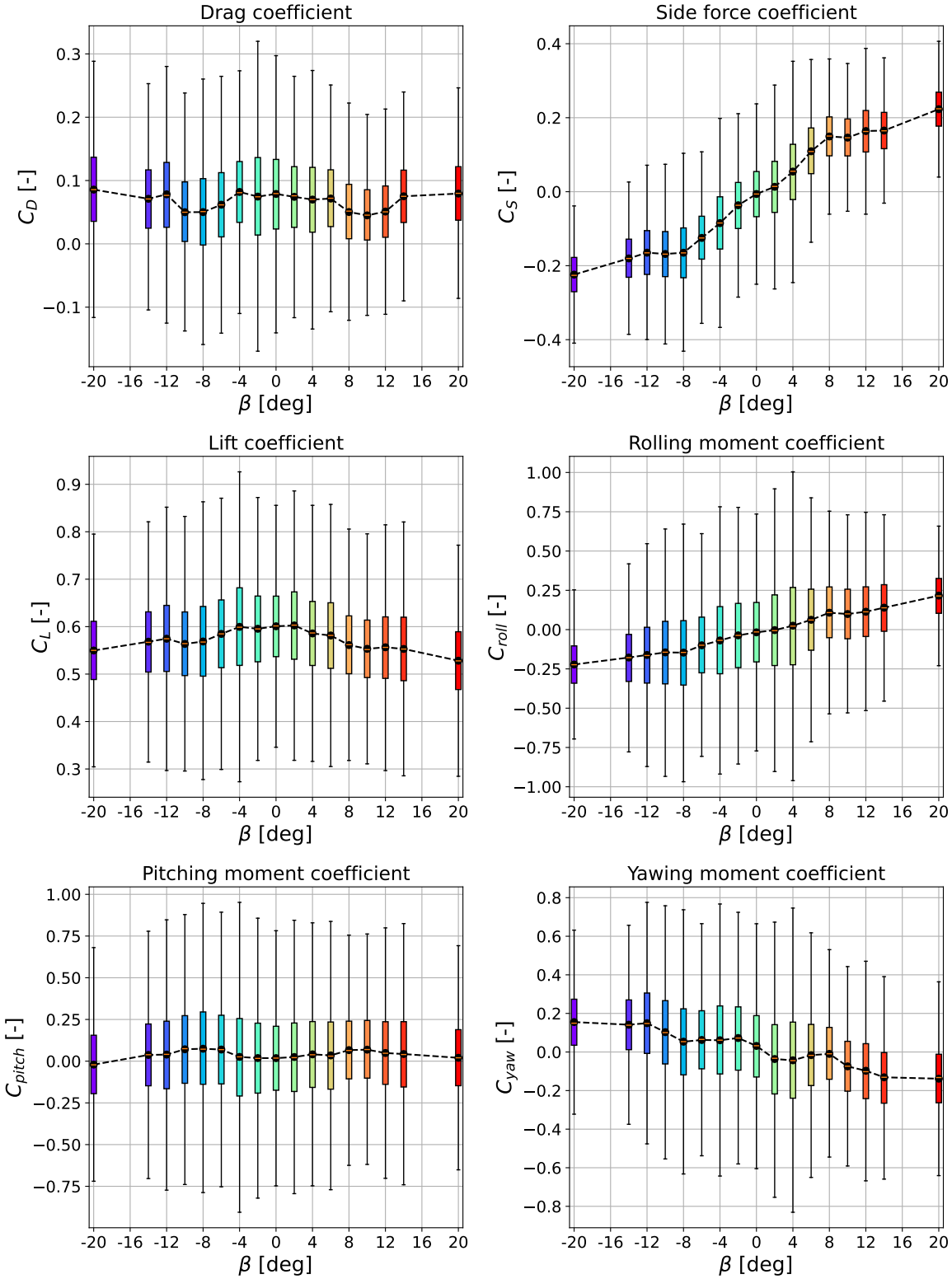

Figure 7.14: Boxplots of aerodynamic coefficients versus sideslip angle for $Re = 5.6 \cdot 10^5$ at $\alpha = 5$ degrees. The mean values are indicated by the black curve.

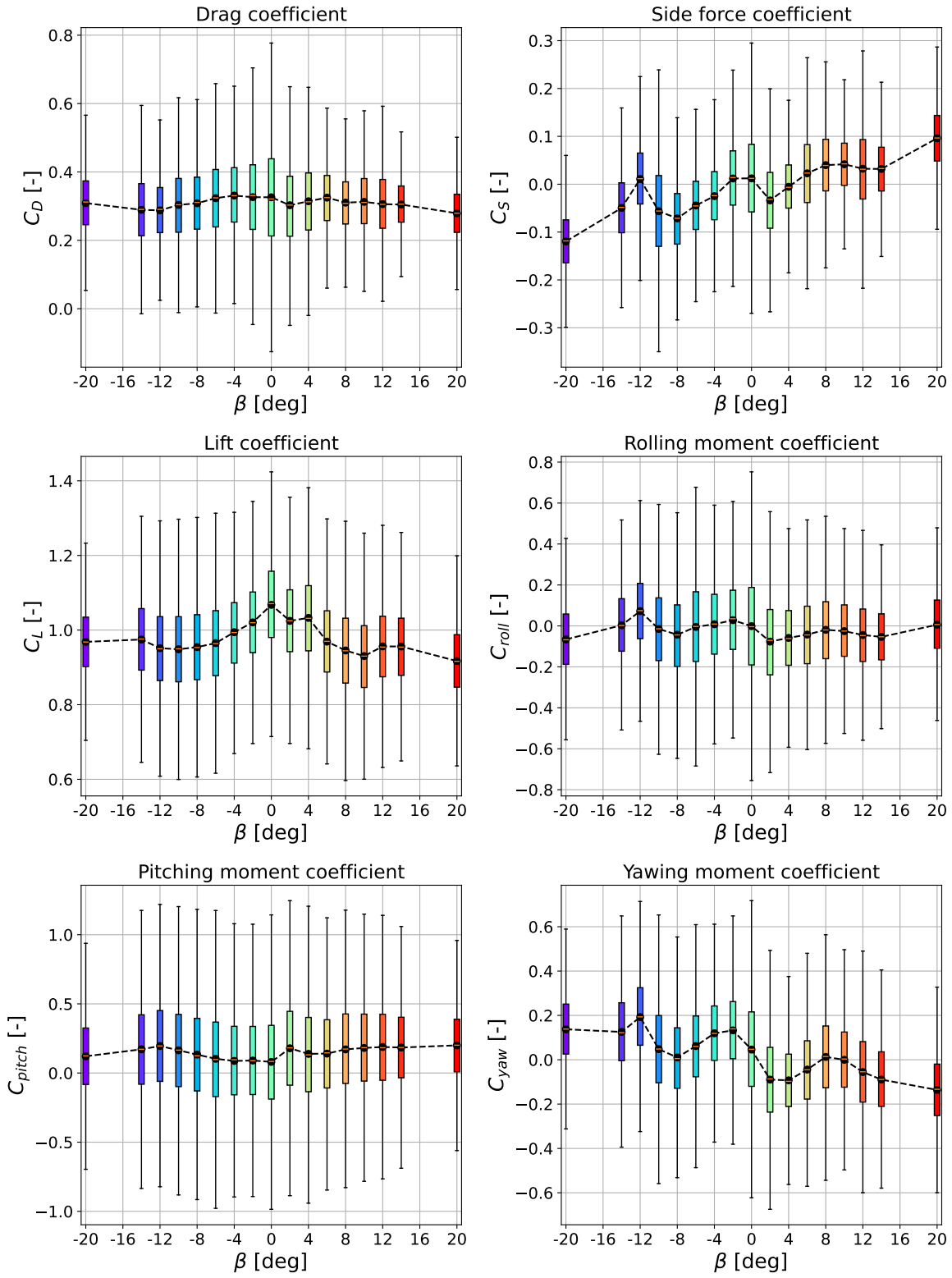

Figure 7.15: Boxplots of aerodynamic coefficients versus sideslip angle for $Re = 5.6 \cdot 10^5$ at $\alpha = 18$ degrees. The mean values are indicated by the black curve.

For the non-stalled case at $\alpha = 5$ degrees shown in Figure 7.14, the interquartile ranges (IQRs) for all force and moment plots are generally equal when examined individually. This consistency

suggests that the measurement variability is relatively uniform across different sideslip angles. Although a few outliers are present, they do not deviate significantly from the rest of the data. This observation indicates that, in a non-stalled condition, there is no evident relationship between uncertainty and sideslip values. This stability in aerodynamic coefficients under varying sideslip angles for non-stalled conditions aligns with findings in the literature that suggest more predictable aerodynamic behavior in linear flow regimes [76].

In contrast, for the stalled case at $\alpha = 18$ degrees shown in Figure 7.15, the IQRs and min/max ranges exhibit different behaviors across the various sideslip angles. For the lift coefficient and pitching moment coefficient plots, the IQRs and min/max ranges remain approximately the same for all sideslip values, indicating consistent measurement uncertainty. However, for the drag, side force, rolling moment, and yawing moment coefficients, there is noticeable deviation in the IQRs and min/max ranges along the sideslip values. Specifically, the drag coefficient shows the highest uncertainty at $\beta = 0$ degrees, which decreases as the sideslip angle increases or decreases. This trend suggests a potential sensitivity of drag forces to sideslip angles around 0 degrees in stalled conditions, likely due to the complex flow separation phenomena occurring at these angles [74].

For the side force coefficient, the highest uncertainty is observed at sideslip angles of -10, 0, and 12 degrees. This increased variability translates into the rolling moment and yawing moment coefficients, which depend on the side force. These observations suggest that in stalled conditions, the side force and its resultant moments are more susceptible to variations in sideslip angles, possibly due to the asymmetric flow behavior and vortex shedding effects associated with stall [67]. Understanding these dependencies is crucial for predicting the aerodynamic performance and stability of kites under different operating conditions. The findings underscore the importance of accounting for sideslip angle effects in the design and simulation of kite-based systems, particularly in stalled flight regimes.

7.4.2. Frequency analysis

In this section, examples of time series measurements are presented to illustrate the varying degrees of vibration present in the data. The purpose of examining the time series data is to identify whether the experimental setup, mounted on a blue table with a known natural frequency of approximately 4-5 Hz [77], experiences resonance issues at higher Reynolds numbers. By understanding the vibration characteristics, it can be determined if these frequencies are causing significant resonance, which would necessitate filtering the data to reduce measurement uncertainty. The following plots showcase two time series measurements: one exhibiting minimal to no vibrations in Figure 7.16, and the other demonstrating significant vibrations in Figure 7.17. In the plots, the whole time series is shown, as well as zoomed in subplots showing the shape of the vibrations. Note the difference in Reynolds number, meaning that the vibrations get worse with increasing wind tunnel speed. The same conclusion was drawn after reviewing the GoPro-footage of the measurements.

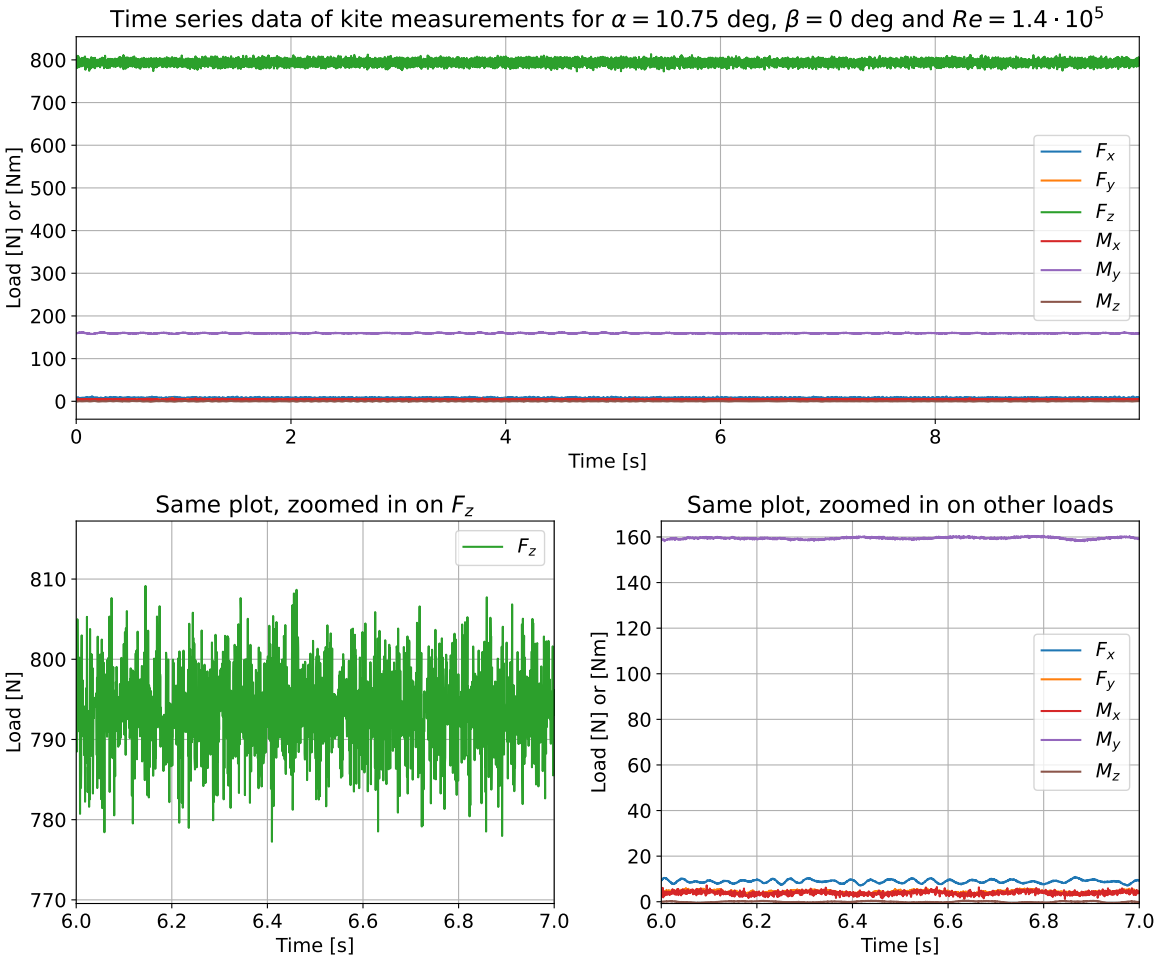

Figure 7.16: Time series data of the kite measurements for $\alpha = 10.75$ deg, $\beta = 0$ deg and $Re = 1.4 \cdot 10^5$.

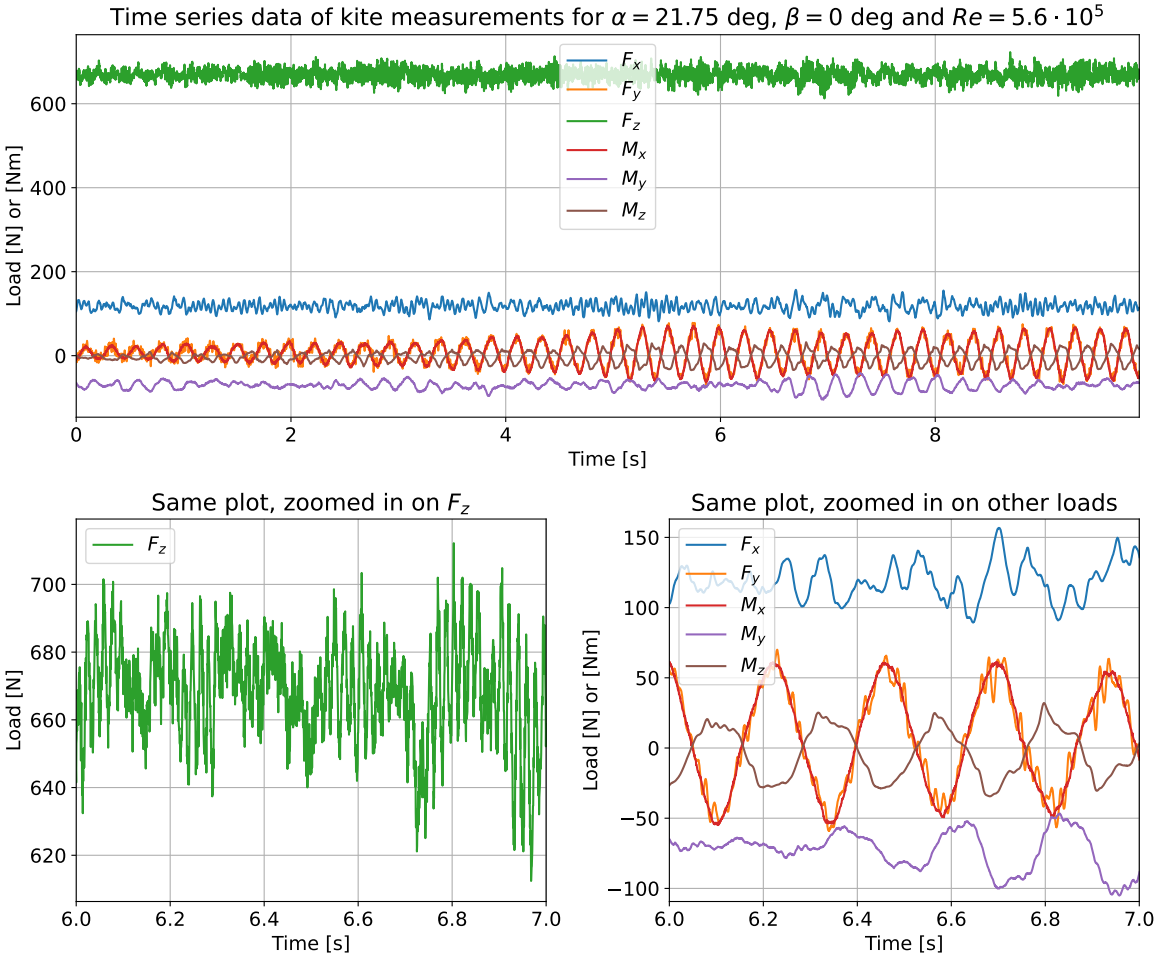

Figure 7.17: Time series data of the kite measurements for $\alpha = 21.75$ deg, $\beta = 0$ deg and $Re = 5.6 \cdot 10^5$.

In Figure 7.16, the time series data shows relatively stable measurements with minimal fluctuations, indicating that the system is not significantly affected by vibrations. The consistency in the data suggests that any inherent noise is low, and the measurements can be considered reliable without the need for extensive filtering.

Conversely, Figure 7.17 reveals considerable fluctuations, and in particular for F_y and M_x, indicative of significant vibrations within the system. These variations in the time series data could be symptomatic of resonance effects due to the natural frequency of the blue table. The pronounced oscillations suggest that at higher Reynolds numbers, the setup might be experiencing resonance, thereby affecting the accuracy of the measurements.

To further investigate the presence of resonance frequencies, a Fast Fourier Transform (FFT) was performed on the time series data. The FFT is a mathematical technique that transforms a time-domain signal into its constituent frequencies, providing a spectrum that shows the amplitude of each frequency component present in the original signal. This analysis aimed to identify any clear frequency peaks at 4-5 Hz, which could confirm the presence of resonance issues due to the natural frequency of the blue table. If these peaks were consistently observed, appropriate filters could be applied to mitigate the vibrations and reduce uncertainty in the measurements. Conversely, if the frequency peaks were not consistent, filtering might not be a viable solution. It was chosen to plot three examples that were known to have shown large vibrations. These can be found in Figure 7.18, Figure 7.19 and Figure 7.20. Please note that only the first 100 Hz are plotted. The FFTs went up to 1000 Hz, but after the 100 Hz shown in the figures there were no distinguishable peaks at all. The reason for this 1000 Hz number is because according to the

Nyquist-Shannon sampling theorem, an FFT can only be accurate up to half of the sampling frequency [78]. The sampling frequency in this experiment was 2000 Hz, therefore the FFTs are only accurate until 1000 Hz.

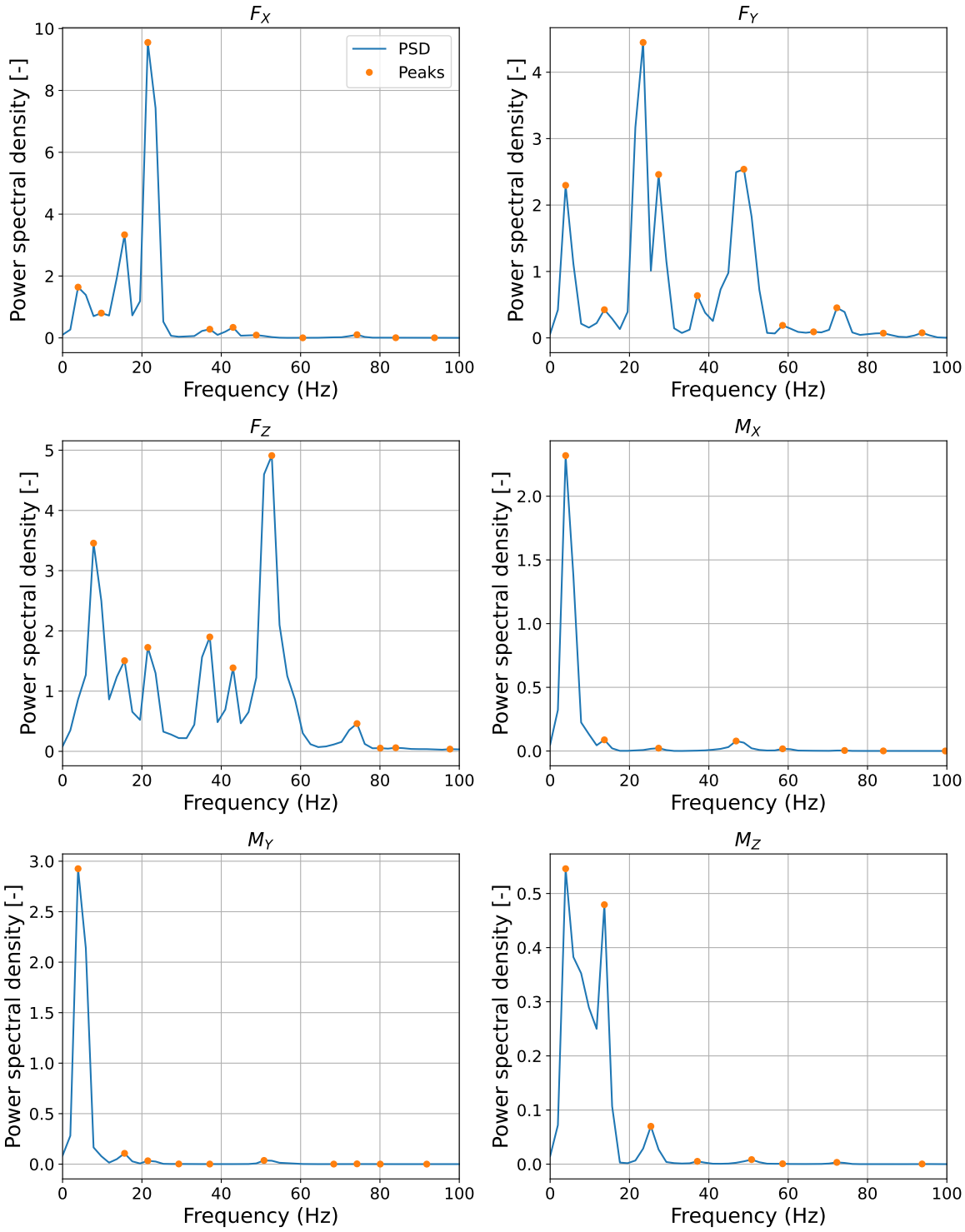

Figure 7.18: Frequency peaks of the force balance signals for $\alpha = 2.4$ deg, $\beta = 0$ deg and $Re = 5.6 \cdot 10^5$.

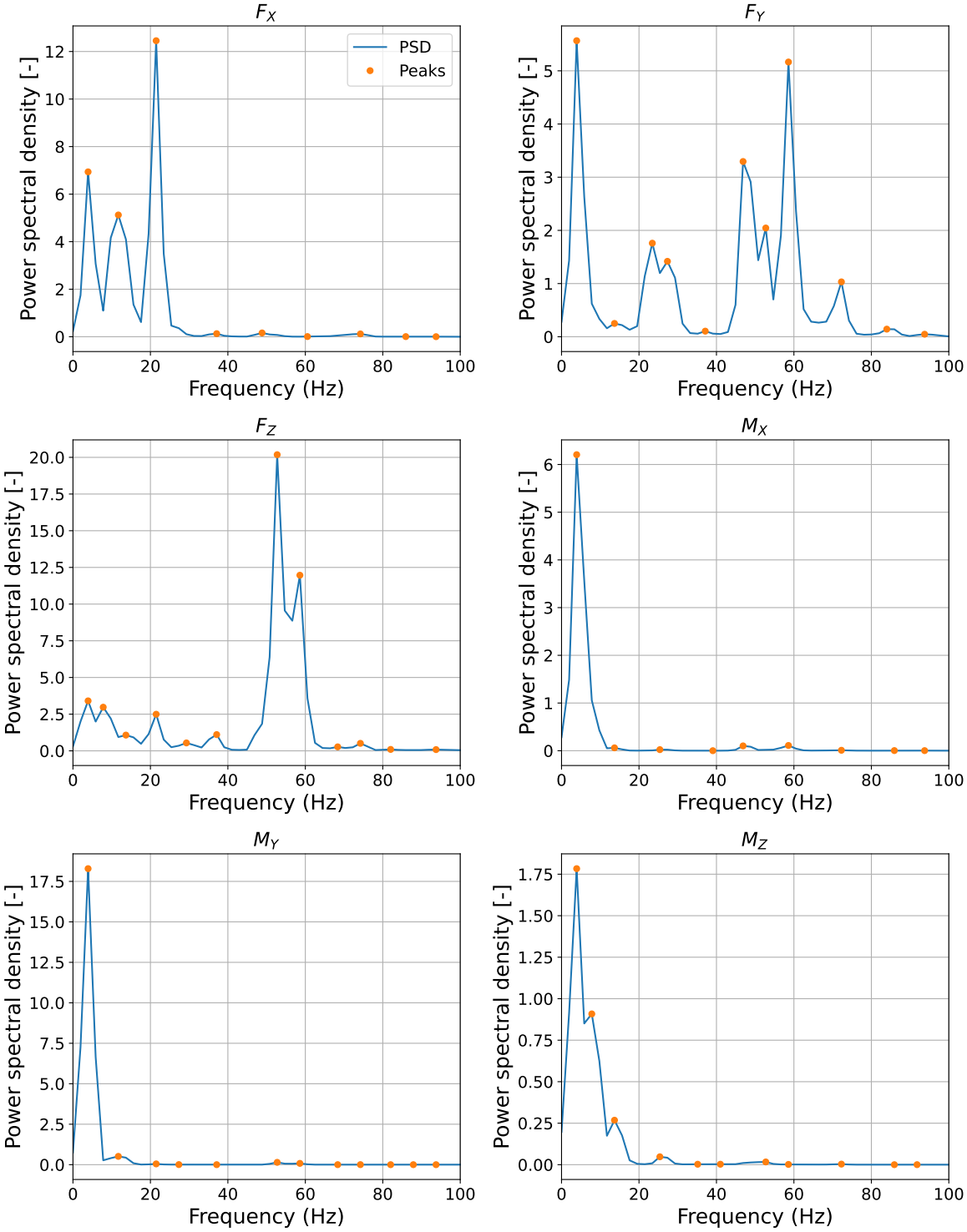

Figure 7.19: Frequency peaks of the force balance signals for $\alpha = 24$ deg, $\beta = 0$ deg and $Re = 5.6 \cdot 10^5$.

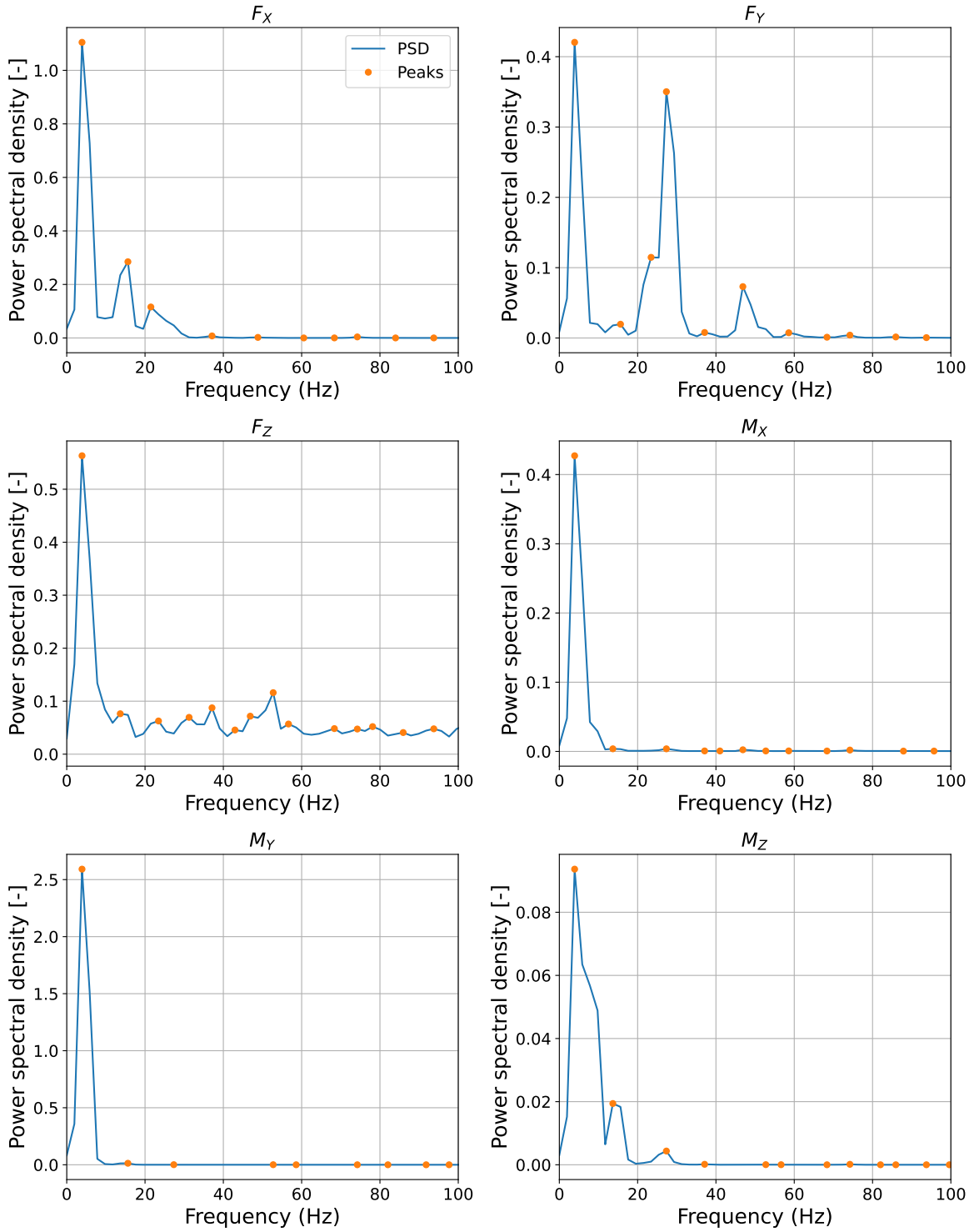

Figure 7.20: Frequency peaks of the force balance signals for $\alpha = 16$ deg, $\beta = 0$ deg and $Re = 2.8 \cdot 10^5$.

When examining Figure 7.18, Figure 7.19, and Figure 7.20, it becomes evident that there are frequency peaks at the lower frequencies, approximately around 5 Hz. However, as illustrated in the top left plot of Figure 7.18 and the middle left plot of Figure 7.20, these peaks are not consistent

across all loads. This pattern was also noticed in other frequency peak plots, which are not included here for conciseness, given that there are several hundred of them. Therefore, despite the presence of peaks near the expected frequencies, it is not advisable to eliminate this frequency because it is not certain that the vibrational cause is due to the blue table's natural frequency. Filtering it out might also remove crucial aerodynamic features.

7.5. Comparison to literature

In this section, the experimental results are compared to established literature to evaluate their accuracy and validity. Specifically, the lift coefficient (C_L), drag coefficient (C_D), lift-to-drag ratio (C_L/C_D) versus angle of attack (α), and C_L versus C_D curves are compared to the 3D steady-state Reynolds-Averaged Navier-Stokes (RANS) simulations of Lebesque [1] and the vortex step method results of Cayon [2]. Additionally, the C_L, C_D, C_L/C_D, and side force coefficient (C_S) versus sideslip angle (β) curves are analyzed in relation to these simulation results. These comparisons are crucial for validating the experimental data and ensuring consistency with theoretical models and numerical simulations.

The Reynolds numbers used in Figure 7.21 for the experimental data are the lowest ($Re = 1.4 \cdot 10^5$), which is approximately the same as the lowest Reynolds number used by Lebesque, and therefore includes that data for comparison. Additionally, the experimental data for the highest Reynolds number that has a full range of α ($Re = 5.6 \cdot 10^5$) was plotted. For comparison, Lebesque's second lowest simulated Reynolds number of $Re = 1 \cdot 10^6$ was also included. Furthermore, the data from Cayon's results, which do not go lower than $Re = 3 \cdot 10^6$, were incorporated into the analysis.

For Figure 7.22, the lowest simulated Reynolds number for Lebesque was $Re = 1 \cdot 10^6$ and for Cayon it was $Re = 3 \cdot 10^6$. The highest Reynolds number achieved in the experiments was only $Re = 5.6 \cdot 10^5$, so this was plotted against the aforementioned Reynolds numbers from Cayon and Lebesque. Please note that the original C_S values generated by Lebesque and Cayon have been divided by $\frac{A_{proj}}{A_{side}}$, because they multiplied them by this ratio in their results.

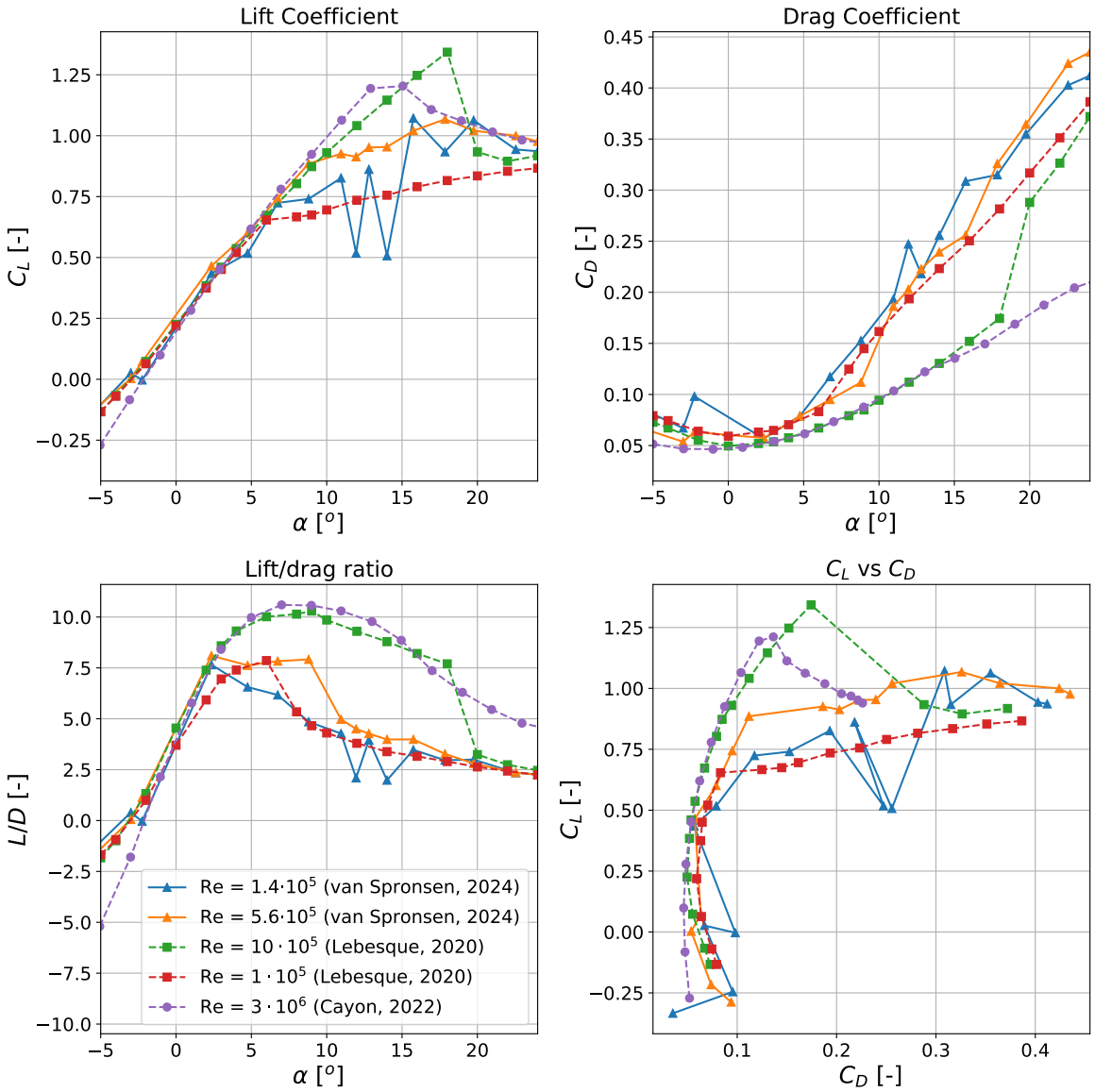

Figure 7.21: Comparison of experimental results to literature: $C_L, C_D, C_L/C_D$ versus α and C_L versus C_D curves.

he comparison of experimental results to literature revealed several important insights regarding the aerodynamic performance of the kite. The $C_L - \alpha$ curve in Figure 7.21 showed that the linear regimes from -5 to approximately 7 degrees were nearly identical for all curves. The Reynolds number (Re) of $1 \cdot 10^5$ from Lebesque's simulations stalled first at $\alpha = 6$ degrees, and from there, the lift coefficient (C_L) gradually increased from 0.65 to 0.85 as α ranged from 6 to 24 degrees. The experimental $Re = 1.4 \cdot 10^5$ also stalled around $\alpha = 7$ degrees, and excluding outliers, C_L gradually increased from 0.75 to 0.9 between $\alpha = 7$ degrees and 24 degrees. The experimental $Re = 5.6 \cdot 10^5$ stalled at around $\alpha = 9$ degrees, and C_L remained relatively constant at 0.95. In contrast, higher Reynolds numbers from Lebesque ($Re = 1 \cdot 10^6$) and Cayon ($Re = 3 \cdot 10^6$) stalled at $\alpha = 13$ degrees and $\alpha = 18$ degrees respectively, after which a noticeable drop in C_L was observed.

The observed trends in the $C_L - \alpha$ curve can be attributed to the effects of Reynolds number on boundary layer behavior and flow separation. At lower Reynolds numbers, the boundary layer transitions to turbulence at lower angles of attack, leading to earlier stall. The gradual increase in C_L after stall in Lebesque's $Re = 1 \cdot 10^5$ and the experimental $Re = 1.4 \cdot 10^5$ can be attributed to the reattachment of the flow, forming a bubble that stabilizes the lift increase. This behavior is

consistent with findings in the literature, which show that at lower Reynolds numbers, the flow is more prone to separation and reattachment cycles, leading to increased lift post-stall [66, 67].

The $C_D - \alpha$ curve showed that the experimental curves (both Reynolds numbers) and Lebesque's $Re = 1 \cdot 10^5$ followed similar patterns, indicating comparable drag characteristics. In contrast, Cayon's $Re = 3 \cdot 10^6$ and Lebesque's $Re = 1 \cdot 10^6$ exhibited lower drag coefficients (C_D) across all angles of attack. This trend indicates that higher Reynolds numbers generally result in reduced drag due to the delayed onset of flow separation and the transition to a turbulent boundary layer, which enhances flow attachment and reduces pressure drag [76, 75].

The $L/D - \alpha$ curve further confirmed this pattern, as the experimental curves (both Reynolds numbers) and Lebesque's $Re = 1 \cdot 10^5$ again followed similar trajectories. Conversely, Cayon's $Re = 3 \cdot 10^6$ and Lebesque's $Re = 1 \cdot 10^6$ showed higher lift-to-drag ratios (L/D) due to the lower drag observed in the $C_D - \alpha$ plot. This higher L/D ratio at higher Reynolds numbers is indicative of more efficient aerodynamic performance, which is crucial for applications requiring optimal lift with minimal drag, such as in kite-based energy systems [76].

The C_L versus C_D curve illustrated that the experimental data (both Reynolds numbers) and Lebesque's $Re = 1 \cdot 10^5$ followed a similar pattern, with Cayon's $Re = 3 \cdot 10^6$ and Lebesque's $Re = 1 \cdot 10^6$ exhibiting higher lift for lower drag values. This observation is consistent with the general understanding that higher Reynolds numbers result in improved aerodynamic efficiency due to delayed flow separation and more stable boundary layer behavior [79]. At higher Reynolds numbers, the turbulent boundary layer remains attached to the surface for a longer portion of the airfoil, reducing drag and allowing for higher lift coefficients at a given drag level.

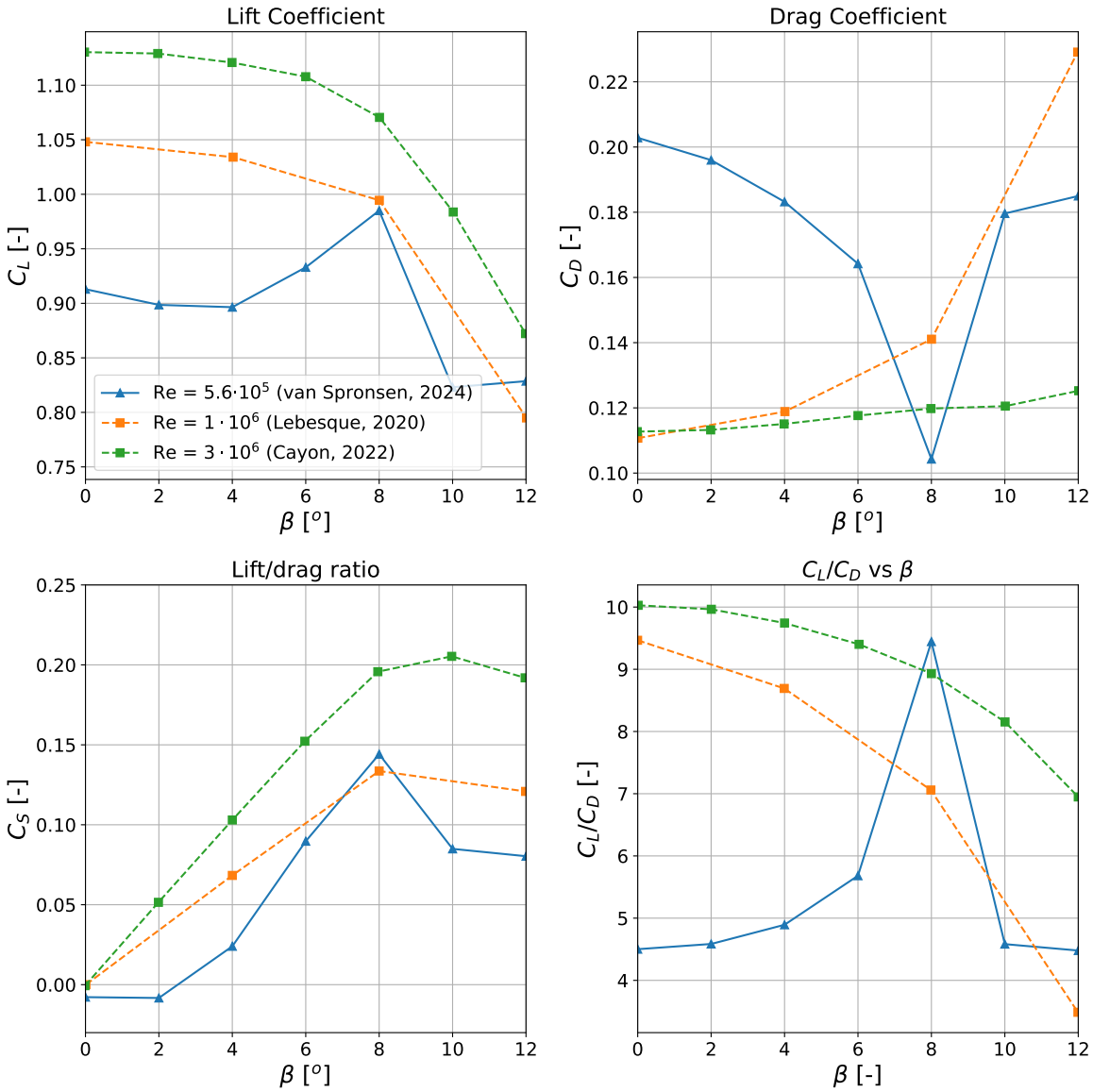

Figure 7.22: Comparison of experimental results to literature: $C_L, C_D, C_L/C_D, C_S$ versus β curves.

For the $C_L - \beta$ curve in Figure 7.22, the experimental data showed that C_L was lower than both Lebesque and Cayon between $\beta = 0$ degrees and 8 degrees, where it increased before decreasing again from $\beta = 8$ degrees to $\beta = 12$ degrees. This could be attributed to differences in flow separation and reattachment behavior influenced by sideslip angles. Lebesque and Cayon's data, representing higher Reynolds numbers, showed a more stable and gradual decrease in C_L, which is indicative of more stable aerodynamic performance at higher Reynolds numbers [67].

In the $C_D - \beta$ curve, the experimental data had higher C_D between $\beta = 0$ degrees and 8 degrees, decreasing during this range and then increasing rapidly. In contrast, Lebesque and Cayon's data started low and increased gradually with increasing β, although Lebesque's slope was higher. This suggests that at higher Reynolds numbers, drag is more predictable and increases steadily with sideslip angle due to more stable flow patterns [75].

The $C_S - \beta$ curve showed that the experimental side force matched Lebesque's data, increasing until $\beta = 8$ degrees and decreasing slightly thereafter until $\beta = 12$ degrees. Cayon's data, while not far off, increased more quickly and started decreasing at $\beta = 10$ degrees. This indicates that side force behavior at higher Reynolds numbers is more pronounced and consistent with theoretical

predictions of vortex dynamics and flow separation [25].

For the $C_L/C_D - \beta$ curve, the experimental data started low, increased exponentially until $\beta = 8$ degrees, and then sharply decreased back to its original value at $\beta = 0$ degrees. In contrast, Lebesque and Cayon's data started high and decreased along the β range, reflecting higher aerodynamic efficiency at higher Reynolds numbers due to lower drag and more stable lift characteristics [76].

Overall, the comparisons indicate that the experimental results align well with the literature at lower Reynolds numbers, validating the experimental setup and measurement techniques. The higher Reynolds number data from Lebesque and Cayon might not have been the most ideal data to compare to the experiments, because they could not be matched. However, there was no better data available at the time of writing this report, meaning no other comparisons could have taken place.

8

Conclusions and recommendations

In the absence of aerodynamic validation data for a rigid model of the Kitepower V3A Leading Edge Inflatable (LEI) Kite, it is essential that the experimental setup is conducted with high precision. The challenge of scaling down such a soft membrane kite is compounded by intricate aeroelastic scaling considerations, leaving little alternative but to opt for a rigid model over a soft one. Furthermore, the novelty of such an experiment underscores its potential significance as a noteworthy contribution to the field. Steady-state 3D RANS simulations were performed by Demkowicz [7] and Lebesque [1], while a Vortex Step Method has been developed by Cayon [2] which could, among other things, be used to investigate the aerodynamic performance of a rigid kite. Both the simulations and model lack validation data, which this thesis project aimed to provide.

The research objective was to conduct an experimental study to obtain steady-state validation data of the Kitepower V3A, rigidized to avoid aeroelastic scaling issues. In this thesis, all the steps taken in designing (see chapter 3 and chapter 4) and conducting the experiment (see chapter 5) were outlined. Furthermore, the way the data is processed was also explained, see chapter 6. Lastly, the results and discussion of these results were presented in chapter 7. In this chapter, the main conclusions from this research are highlighted by answering the research questions that were drawn up in chapter 2. Furthermore, recommendations for future work will be given.

8.1. Conclusions

An experiment on a rigid subscale model of Kitepower's V3A Kite was conducted in the Open Jet Facility (OJF) at TU Delft. The kite was rigidized by making it out of a carbon fiber reinforced polymer, as this was the best option. It was the best option because it was lighter than metals, as weight was something to take into account for the force balance limits. Furthermore, it is more stiff than 3D printed plastic. The support structure was made out of lightweight aluminium beams and included a hinging mechanism to change the angle of attack of the kite. The kite was connected to the support structure by extending the two center struts and shoving these extensions into pipes that exactly fitted around them. The cylinders were made of solid steel to be able to not deflect due to the forces on the kite.

The scale of the kite was chosen such that it could be used for comparison with already done simulations, for example by Lebesque [1]. Lebesque lowest Reynolds number was $Re = 1 \cdot 10^5$, which is the lowest Reynolds number measured in the experiment, and the second lowest in the simulations was $Re = 1 \cdot 10^6$. This Reynolds number could not be reached given the constraints of the tunnel and the other constraints on the scale of the kite model. However, comparison was still possible, as the linear regime of the lift curve showed to be a great match between the experimental data and simulation data. However, after the kite has stalled, comparing the different Reynolds numbers could cause for differences, as the stall characteristics change with Reynolds number. It can thus be said that comparison is still valuable, even though the Reynolds numbers

may not match exactly.

In this experiment, force balance measurements have been done, measuring all three forces and three moments acting on the kite. The kite was mounted on the support structure. This construction was mounted on top of the OJF NLR Force Balance, which was in its turn mounted on a turntable that was used to change the sideslip angle of the kite. When measuring the forces and moments during this experiment, it was clear that a strategy should be devised that subtracts the influence of the support structure on the measurements. This was done by dismounting the kite from the force balance, and doing measurements in the wind tunnel on the support structure alone for several data points. Using these datapoints, interpolation relationships were derived that could be used to determine the aerodynamic coefficients of the support structure for any sideslip, angle of attack and Reynolds number combination. In the literature review it was shown that the Reynolds number should be at least above $Re = 2{\cdot}10^5$ to obtain reliable results, which was confirmed in the plots of the aerodynamic coefficients of the support structure. Namely, that for the lowest Reynolds number ($< 2 \cdot 10^5$), the data was off quite a bit compared to higher Reynolds numbers ($> 2 \cdot 10^5$), which was concluded to be the best data. Furthermore, when looking at the coefficients plotted against sideslip angle β, it was concluded that the support structure showed symmetry.

After determining the aerodynamic coefficients of the support structure, the same was done for the kite. Measurements were done in the OJF with the kite mounted to the support structure. These measurements were processed, and the aerodynamic coefficients of the support structure were subtracted to remove the influence of the support structure as much as possible. The results were plots of the aerodynamic coefficients of the kite versus both angle of attack and sideslip angle. Again, in the plots versus α it was observed that the lowest Reynolds number ($1.4 \cdot 10^5$) was off quite a bit compared to the higher ones, which was in line with expectations. However, for the drag and lift curve, this deviation was smaller than expected. Although there were some outliers, it can be concluded that for this Reynolds number, the results are usable. This however needed further investigation by performing uncertainty analysis.

Aiding in the uncertainty analysis, special test cases were done. The first one being if the addition of zigzag tape, for low Reynolds numbers, increases the aerodynamic performance of the kite. The expectations were that for the lowest Reynolds number, the lift would increase, because the zigzag tape causes the flow to transition to turbulent instead of it being laminar and having a possible laminar separation bubble, reducing the lift. However, in the comparison between the measurements with zigzag tape and without zigzag tape, it was concluded that at the zigzag tape made a minimal difference with respect to the measurements without zigzag tape. This meant that the flow was already turbulent for the low Reynolds number, possibly caused by the roughness of the model to be adequately high for this. It was therefore concluded that using a zigzag tape is obsolete for this specific kite model.

Furthermore, double measurements were conducted to check the repeatability of the experiment. By double measurements is meant that a data point was measured multiple times. These measurements were then compared to each other using boxplots capturing the uncertainty of the measurements. It was concluded that the different measurements were very close to each other, meaning that the repeatability of the experiment is high. Next to this, measurements were done to check for possible sensor drift of the force balance. Comparisons were made between measurements at the end of a day with measurements at the beginning of the next day. These comparisons showed no real deviation, after which it was concluded that no sensor drift occured.

Even more uncertainty analysis was conducted, namely by plotting the boxplots of the generated force and moment coefficient curves versus angle of attack and sideslip angle. This was done to check whether there is a higher degree of uncertainty for certain Reynolds numbers or when the wing stalls. In general, it was concluded that for higher Reynolds numbers, the uncertainty decreased, and that the uncertainty was quite large for the lowest Reynolds number with respect to the measured higher ones, which was also in line with expectations. Furthermore, it was concluded that the uncertainty did not increase when the wing was stalled. When plotting versus sideslip angle, it was observed that some sideslip angles showed higher uncertainty than the rest, namely $\beta = 0$, $\beta = 12$ and $\beta = 20$. Unfortunately no conclusion could be drawn where this

uncertainty comes from, however, the uncertainty was not that high to disregard the datapoints completely.

To minimize the measurement errors, a check was performed to identify a consistent frequency peak between 4-5 Hz across all signals, due to the known natural frequency of the blue hydraulic table, which was around this range. Unfortunately, some signals did show peaks around these frequencies, but it was not consistent along all signals. Therefore, it was concluded that filtering out the data for these frequencies was not advisable. The reason for this is that one can not be completely sure to not filter out any desired aerodynamic data this way.

Finally, the results were compared to the 3D RANS simulations of Lebesque [1] and the Vortex Step Method results of Cayon [2]. The Reynolds numbers of the experiment were matched to those of the simulations as close as possible. From comparing the lift and drag curves plotted versus angle of attack, it was observed that there is a very close match during the linear regime of the curve. However, differences occurs when comparing the stall characteristics of the curves. While the lowest Reynolds number of the experiment matched the lowest Reynolds number simulated by Lebesque up to a certain amount, the other plots had completely different stall characteristics. This could be attributed to the fact that there was no close Reynolds number match between the experiment and simulations.

Furthermore, the lift, drag and side force coefficients were plotted versus the sideslip angle and also compared to results by Lebesque and Cayon. However, the Reynolds numbers got not be matched that well, which meant that the lift and the drag curves were largely different for the experimental result. However, it could be observed that the side force curves were a rather close match. This was deemed a coincidence given the earlier observed trends in the lift and drag curves.

In conclusion, an experiment was designed in order to gain reliable aerodynamic validation data for the Kitepower LEI V3A Kite, which was rigidized to avoid any aeroelastic scaling issues. The aerodynamic performance of the kite model was quantified for various Reynolds numbers, sideslip angles and angle of attack combinations. Furthermore, the uncertainty of these measurements was analysed and an attempt was made to reduce this uncertainty. Lastly, the experimental results were compared to the results of the simulations by Lebesque [1] and the model by Cayon [2], showing close matches at some instances but larger differences at others.

8.2. Recommendations

Based on these findings, several recommendations for future research can be identified. For example, the current support system attached to the kite may notably impact the kite's aerodynamic performance. Although it was accounted for in the measurement data, there might have been interactions between the kite and the support structure that couldn't be completely captured by this subtraction. During the design of the support structure, care was taken to avoid obstructing the tip vortices by maintaining a relatively small spanwise dimension, but it was challenging to fully consider the wakes generated by the kite. Consequently, designing a smaller and more streamlined support structure for future experiments could further minimize this interference. Also, if more force balance measurements will be done on this model, one could opt to do more measurements for the support structure alone, as in this case, only three data points were measured and then interpolated.

In the context of kite measurements, particularly when obtaining zero-run data, which refers to measurements taken without activating the wind, it is essential to ensure the wind speed is completely zero. Even a minimal, non-zero wind speed would be unacceptable. Therefore, in this experiment, zero-run data at a specific angle of attack was employed to eliminate the steady forces from the measurements.

What is also interesting is to use the simulation settings of Lebesque, and to simulate for the Reynolds numbers that were measured in this experiment. This way, a better Reynolds match is obtained, leading to a more reliable comparison. For example, the highest Reynolds number measured in this experiment is $Re = 7.0 \cdot 10^5$, while this only comes close to Lebesque's $Re = 1 \cdot 10^5$

and $Re = 1 \cdot 10^6$. This holds also for the simulations ran by Cayon, as it would be more beneficial to re-run them using the right Reynolds numbers.

Lastly, the model and experiment was designed with keeping in mind the possibility to do Stereoscopic Particle Image Velocimetry (SPIV) on the kite. Some SPIV measurements have already been done, of which some provisional results are found in Figure 8.1 and Figure 8.2. In these plots, the velocity field around the kite can be seen for some spanwise positions, in this case near a struts (Y2) and on a strut (Y3). The stagnation point can be seen by the darker red area near the leading edge of the airfoil, while the wake is also dark red, but at the trailing edge. Furthermore, the flow is shown to speed up over suction side of the airfoil. For future work, more of the already gathered SPIV data can be processed and analysed, while also more SPIV measurements can be done on for example the wake of the kite, or on different chordwise coordinates spanning the whole span of the kite. However, the support structure does need to be altered in case the wake is desired to be measured.

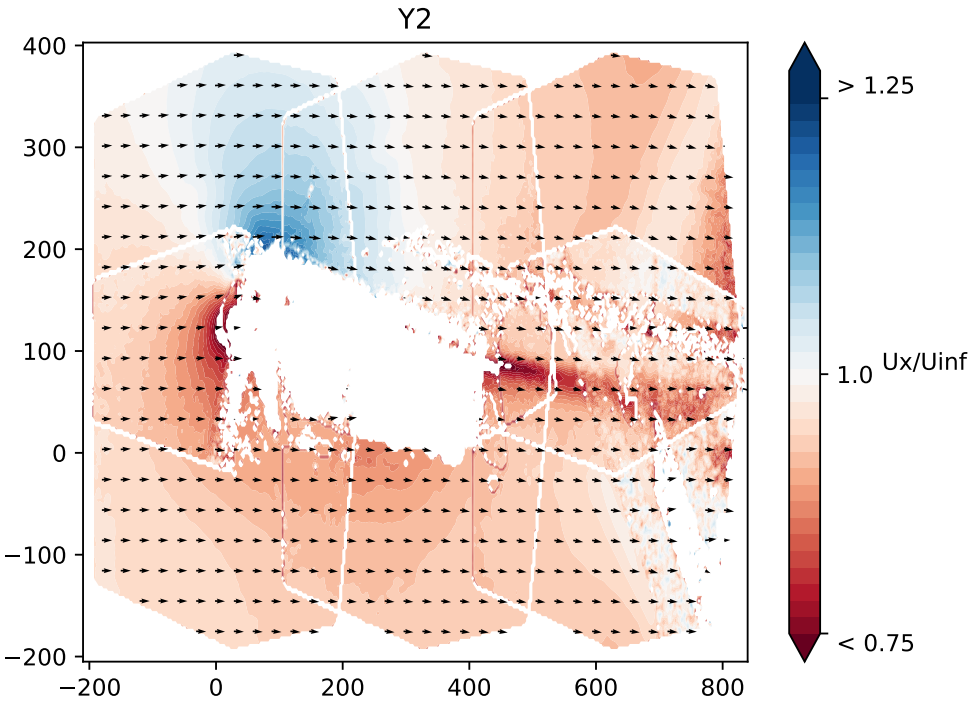

Figure 8.1: Chordwise plane of the V3A near a strut, for $\alpha = 6$ deg, $\beta = 0$ deg and $Re = 4.2 \cdot 10^5$, showing the velocity field around the kite.

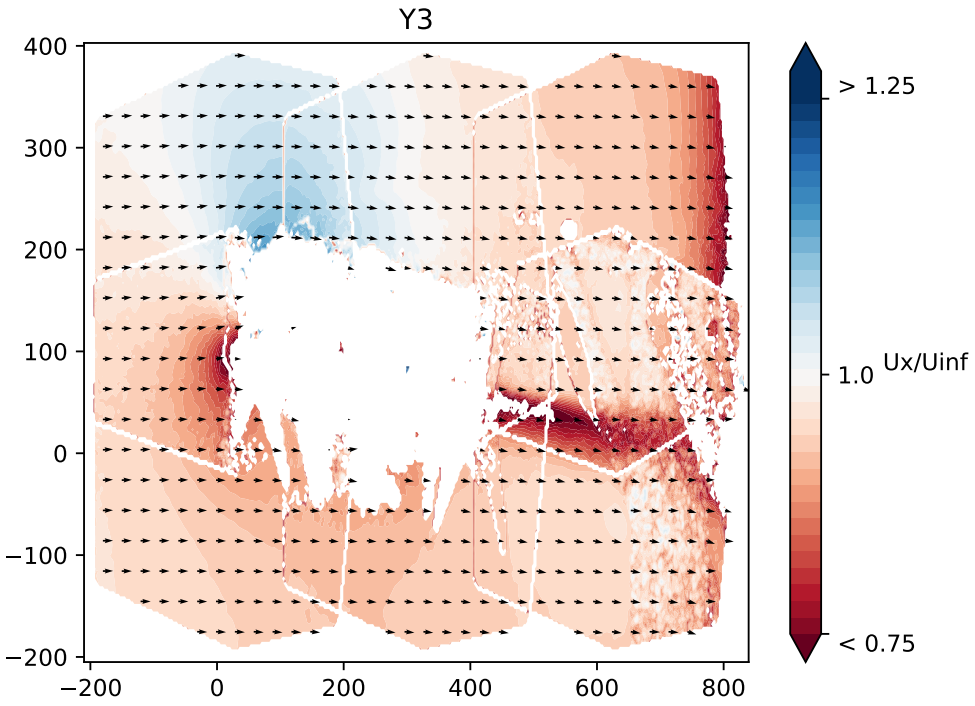

Figure 8.2: Chordwise plane of the V3A on a strut, for $\alpha = 6$ deg, $\beta = 0$ deg and $Re = 4.2 \cdot 10^5$, showing the velocity field around the kite.

References

[1] G.H.M. Lebesque. "Steady-state RANS simulation of a leading edge inflatable wing with chordwise struts". MA thesis. Delft University of Technology, 2020.

[2] O. Cayon. "Fast aeroelastic model of a leading-edge inflatable kite". MA thesis. Delft University of Technology Technical University of Denmark, 2022.

[3] W. J. Ripple et al. "The 2023 state of the climate report: Entering uncharted territory". In: Bioscience (Print) 73.12 (Oct. 2023), pp. 841–850.

[4] C. L. Archer. "Evaluation of global wind power". In: Journal of Geophysical Research 110.D12 (June 2005).

[5] S. Apelfröjd, S. Eriksson, and H. Bernhoff. "A review of research on large scale modern vertical axis wind turbines at Uppsala University". In: Energies 9.7 (July 2016), p. 570.

[6] A. F. C. Pereira and J. M. M. Sousa. "A review on Crosswind Airborne wind Energy Systems: Key factors for a design choice". In: Energies (Basel) 16.1 (Dec. 2022), p. 351.

[7] P. Demkowicz. "Numerical analysis of the flow past a leading edge inflatable kite wing using a correlation-based transition model". MA thesis. Delft University of Technology, 2019.

[8] R. van der Vlugt, J. Peschel, and R. Schmehl. "Design and experimental characterization of a pumping kite power system". English. In: Airborne wind energy. Ed. by U. Ahrens, D. Moritz, and R. Schmehl. Springer, 2013, pp. 403–425.

[9] U. Fechner. "A Methodology for the Design of Kite-Power Control Systems." PhD thesis. Delft University of Technology, 2016.

[10] U. Fechner and R. Schmehl. Model-Based efficiency analysis of wind power conversion by a pumping KITE power system. Jan. 2013, pp. 249–269.

[11] J. Berens. "Dynamic Nonlinear Aeroelastic Behaviour of Flexible Wings in an Airflow". MA thesis. Delft University of Technology, 2015.

[12] J. Oehler and R. Schmehl. "Aerodynamic characterization of a soft kite by in situ flow measurement". In: Wind energy science 4.1 (Jan. 2019), pp. 1–21.

[13] M. Folkersma, R. Schmehl, and A. Viré. "Boundary layer transition modeling on leading edge inflatable kite airfoils". In: Wind energy 22.7 (Mar. 2019), pp. 908–921.

[14] H. Hu and Z. Yang. "An experimental study of the laminar flow separation on a Low-Reynolds-Number airfoil". In: Journal of fluids engineering 130.5 (Apr. 2008).

[15] S. P. Singh and S. Mittal. "Flow past a cylinder: shear layer instability and drag crisis". In: International journal for numerical methods in fluids 47.1 (Nov. 2004), pp. 75–98.

[16] G. Li et al. "Aeroelastic characteristics of flexible membrane wings with ceiling effect". In: Physics of fluids 36.3 (Mar. 2024).

[17] R.G. den Boer. "Low speed aerodynamic characteristics of a two-dimensional sail wing with adjustable slack of the sail". In: Technische Hogeschool Delft, Luchtvaart- en Ruimtevaarttechniek, Report LR-307 (1980).

[18] P. Ifju, M. Waszak, and L. Jenkins. "Stability and control properties of an aeroelastic fixed wing micro aerial vehicle". In: AIAA Atmospheric Flight Mechanics Conference and Exhibit (Aug. 2001).

[19] R.C. Leuthold. "Multiple-Wake Vortex Lattice Method for Membrane Wing Kites". MA thesis. Delft University of Technology, 2015.

[20] S. Tiomkin and J.W. Jaworski. "Unsteady aerodynamic theory for membrane wings". In: Journal of fluid mechanics 948 (Sept. 2022).

[21] U. Fechner et al. “Dynamic model of a pumping kite power system”. In: Renewable energy 83 (Nov. 2015), pp. 705–716.

[22] A. Roullier. “Experimental analysis of a kite system’s dynamics”. MA thesis. Delft University of Technology, 2020.

[23] J. Breukels. “An engineering methodology for kite design”. PhD thesis. Delft University of Technology, 2011.

[24] H.A. Bosch. “Finite element analysis of a kite for power generation”. MA thesis. Delft University of Technology, 2012.

[25] J.D. Anderson. Fundamentals of Aerodynamics. 6th ed. McGraw-Hill Education, Mar. 2016.

[26] A. M. Kuethe and C. Chow. Foundations of aerodynamics: bases of aerodynamic design. 1. Jan. 1976.

[27] M. Gaunaa et al. “A computationally efficient method for determining the aerodynamic performance of kites for wind energy applications”. In: Jan. 2011.

[28] G. Cottet and P. D. Koumoutsakos. Vortex Methods. Cambridge University Press, Mar. 2000.

[29] C. Mimeau and I. Mortazavi. “A review of Vortex methods and their applications: from creation to recent advances”. In: Fluids 6.2 (Feb. 2021), p. 68.

[30] R. E. Spall, W. F. Phillips, and B. B. Pincock. “Numerical analysis of multiple, thin-sail geometries based on Prandtl’s lifting-line theory”. In: Computers fluids 82 (Aug. 2013), pp. 29–37.

[31] E. Pistolesi. Alcune considerazioni sul problema del biplano indefinito. Tech. rep. Pisa R. Scuola d’ingegneria, 1929.

[32] S.T. Piszkin and E.S. Levinsky. Nonlinear lifting line theory for predicting stalling instabilities on wings of moderate aspect ratio. Tech. rep. San Diego, California, USA, 1976.

[33] J.A.W. Poland. “Modelling aeroelastic deformation of soft wing membrane kites”. MA thesis. Delft University of Technology, 2022.

[34] B. Thwaites. “The aerodynamic theory of sails. I. Two-dimensional sails”. In: Proceedings of the Royal Society of London. Series A, Mathematical and physical sciences 261.1306 (May 1961), pp. 402–422.

[35] S.P. Fiddes and J.H. Gaydon. “A new vortex lattice method for calculating the flow past yacht sails”. In: Journal of wind engineering and industrial aerodynamics 63.1-3 (Oct. 1996), pp. 35–59.

[36] O. Lorillu, R. Weber, and J. Hureau. “Numerical and experimental analysis of two-dimensional separated flows over a flexible sail”. In: Journal of fluid mechanics 466 (Sept. 2002), pp. 319–341.

[37] M. R. Mendenhall, S. B. Spangler, and J. N. Nielsen. “Review of methods for predicting the aerodynamic characteristics of parawings.” In: Journal of aircraft 5.6 (Nov. 1968), pp. 597–605.

[38] P. Sagaut, S. Deck, and M. Terracol. Multiscale and multiresolution approaches in turbulence. June 2012.

[39] H. K. Versteeg and W. Malalasekera. An introduction to computational fluid dynamics. Pearson Education, Jan. 2007.

[40] M.E. Deaves. “An Investigation of the Non-Linear 3D Flow Effects Relevant for Leading Edge Inflatable Kites”. MA thesis. Delft University of Technology, 2015.

[41] S. Jain, N. Sitaram, and S. Krishnaswamy. “Effect of Reynolds Number on Aerodynamics of Airfoil with Gurney Flap”. In: International journal of rotating machinery 2015 (Jan. 2015), pp. 1–10.

[42] W. H. Rae and A. Pope. Low-Speed wind tunnel testing. Jan. 1966.

[43] A. De Wachter. “Deformation and aerodynamic performance of a ram-air wing”. MA thesis. Delft University of Technology, 2008.

[44] J. Hummel, D. Göhlich, and R. Schmehl. "Automatic measurement and characterization of the dynamic properties of tethered membrane wings". In: Wind energy science 4.1 (Jan. 2019), pp. 41–55.

[45] B. Python. "Methodology improvement for performance assessment of pumping kite power wing". MA thesis. École polytechnique fédérale de Lausanne, 2017.

[46] J. Oehler, M. Van Reijen, and R. Schmehl. "Experimental investigation of soft kite performance during turning maneuvers". In: Journal of physics. Conference series 1037:052004 (June 2018).

[47] M.B. Ruppert. "Development and validation of a real time pumping kite model". MA thesis. Delft University of Technology, 2012.

[48] S. Desai et al. "Wind Tunnel Testing of Tethered Inflatable Wings". In: Journal of Aircraft 0.0 (July 2024), pp. 1–18.

[49] S. Okda et al. "Testing of the aerodynamic characteristics of an inflatable airfoil section". In: Journal of Aerospace Engineering 33.5 (Sept. 2020).

[50] S. Smith A. Simpson and J. Jacob. "Aeroelastic Behavior of Inflatable Wings: Wind Tunnel and Flight Testing". In: 45th AIAA Aerospace Sciences Meeting and Exhibit. 2007, p. 1069.

[51] B. W. Cocke. Wind-tunnel Investigation of the Aerodynamic and Structural Deflection Characteristics of the Goodyear Inflatoplane. Tech. rep. 19930090147. National Advisory Committee for Aeronautics, 1958.

[52] H. Belloc. "Wind tunnel investigation of a rigid paraglider reference wing". In: Journal of aircraft 52.2 (Mar. 2015), pp. 703–708.

[53] L.E.M. Lignarolo et al. "Experimental analysis of the wake of a horizontal-axis wind-turbine model". In: Renewable energy 70 (Oct. 2014), pp. 31–46.

[54] M. Selig, R. Deters, and R. Williamson. "Low Reynolds Number Airfoil Wind Tunnel Testing". In: AIAA Journal (2011).

[55] L. Santamaría et al. "Aerodynamic Performance of VAWT Airfoils: Comparison between Wind Tunnel Testing Using a New Three-Component Strain Gauge Balance and CFD Modelling". In: Energies 15.24 (Dec. 2022), p. 9351.

[56] E. Mercker, G. Wickern, and J. Weidemann. "Contemplation of Nozzle Blockage in Open Jet Wind-Tunnels in View of Different 'Q' Determination Techniques". In: SAE Technical Paper 970136 (1997).

[57] G. Wickern. "A Theoretical Approach towards the Self-Correcting Open Jet Wind Tunnel". In: SAE Technical Paper 2014-01-0579 (2014).

[58] R. C. Hibbeler. Mechanics of materials. Jan. 2016.

[59] M. A. Karataş and H. Gökkaya. "A review on machinability of carbon fiber reinforced polymer (CFRP) and glass fiber reinforced polymer (GFRP) composite materials". In: Defence technology 14.4 (Aug. 2018), pp. 318–326.

[60] S. R. J. Gahraz, T. M. Lazim, and M. Darbandi. "Wind tunnel study of the effect zigzag tape on aerodynamics performance of a wind turbine airfoil". In: Journal of Advanced Research in Fluid Mechanics and Thermal Sciences 41.1 (2018), pp. 1–9.

[61] J.P. Watchorn. "Aerodynamic Load Modelling for Leading Edge Inflatable Kites". MA thesis. Delft University of Technology, 2023.

[62] M. Folkersma. "Aeroelasticity of Membrane Kites - Airborne Wind Energy Applications". PhD thesis. Delft University of Technology, 2022.

[63] A. Viré et al. "Experimental study of the effect of a slat on the aerodynamic performance of a thick base airfoil". In: Wind energy science 7.2 (Mar. 2022), pp. 573–584.

[64] Z. Pei et al. "Influence of the blunt Trailing-Edge thickness on the aerodynamic characteristics of the very thick airfoil". In: Wind 3.4 (Oct. 2023), pp. 439–458.

[65] G. Sànchez-Arriaga, R. Schmehl, and S Thoms. "10th International Airborne Wind Energy Conference (AWEC 2024) | TU Delft Repository". In: 2024.

[66] S. F. Hoerner. Fluid Dynamic Drag: Practical information on aerodynamic drag and hydrodynamic resistance. June 1965.

[67] H. Schlichting and K. Gersten. Boundary-layer theory. Springer, 2016.

[68] T. J. Mueller. Aerodynamics of Low Reynolds Number Flyers. Springer, 2001.

[69] B. Etkin. Dynamics of Atmospheric Flight. Wiley, 1959.

[70] J. Pearson et al. "The Influence of Zigzag Tape on Boundary Layer Transition and Airfoil Performance". In: Journal of Fluid Mechanics 800 (2016), pp. 1–28.

[71] D. Greenblatt and I. Wygnanski. "The Control of Flow Separation by Periodic Excitation". In: Progress in Aerospace Sciences 36 (2000), pp. 487–545.

[72] J. W. Gregory, M. S. Selig, and T. J. Mueller. "Boundary Layer Transition and Separation on a High-Lift Airfoil at Low Reynolds Numbers". In: AIAA Journal 53 (2015), pp. 1389–1401.

[73] R. C. Nelson. Flight Stability and Automatic Control. McGraw-Hill, 1998.

[74] J. J. Bertin and M. L. Smith. Aerodynamics for engineers. Prentice Hall, 1998.

[75] A. Pope and K. L. Goin. High-speed wind tunnel testing. Wiley, 1978.

[76] I. H. Abbott and A. E. Von Doenhoff. Theory of wing sections, including a summary of airfoil data. Dover Publications, 1959.

[77] B. P. LeBlanc and C. S. Ferreira. "Experimental determination of thrust loading of a 2-Bladed vertical axis wind turbine". In: Journal of Physics Conference Series 1037 (June 2018), p. 022043.

[78] C.E. Shannon. "Communication in the presence of noise". In: Proceedings of the IRE 37.1 (Jan. 1949), pp. 10–21.

[79] John D. Anderson. Fundamentals of aerodynamics. McGraw-Hill, 2010.

A

Additional plots

A.1. Force and moment coefficient plots of support structure

A.1.1. Plots versus α

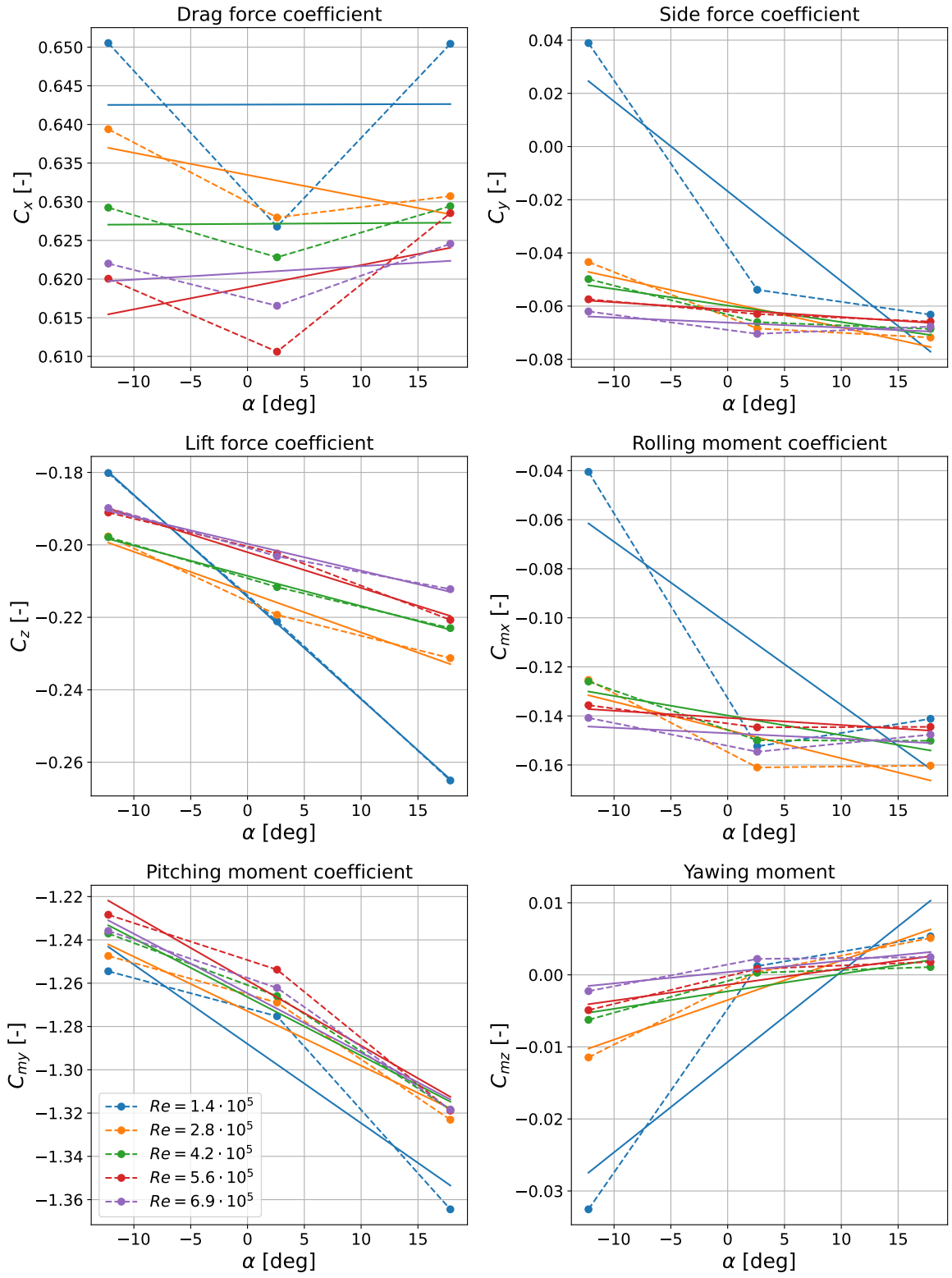

Figure A.1: Force and moment coefficient plots of the support structure for $\beta = 2$ deg.

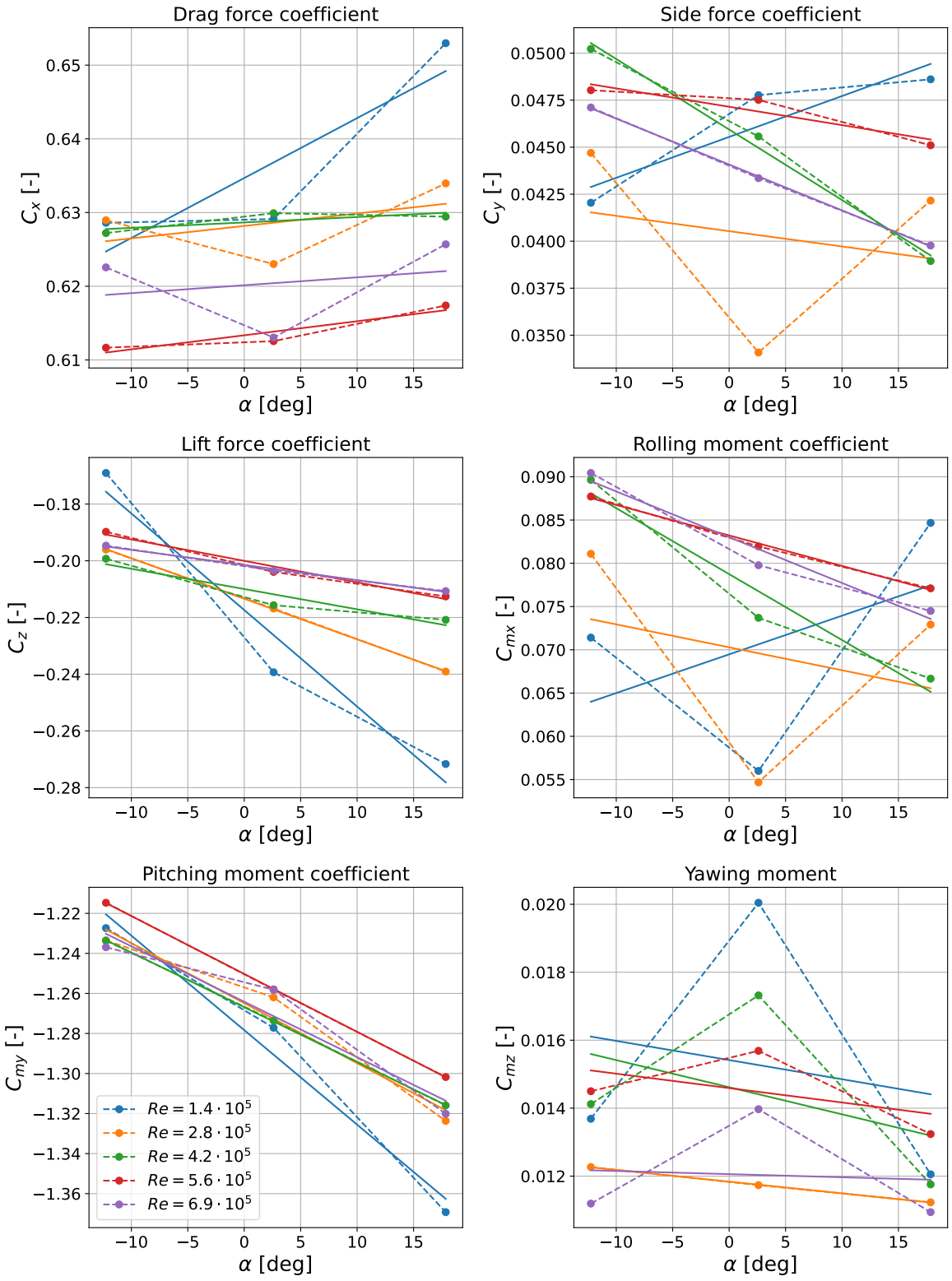

Figure A.2: Force and moment coefficient plots of the support structure for $\beta = -2$ deg.

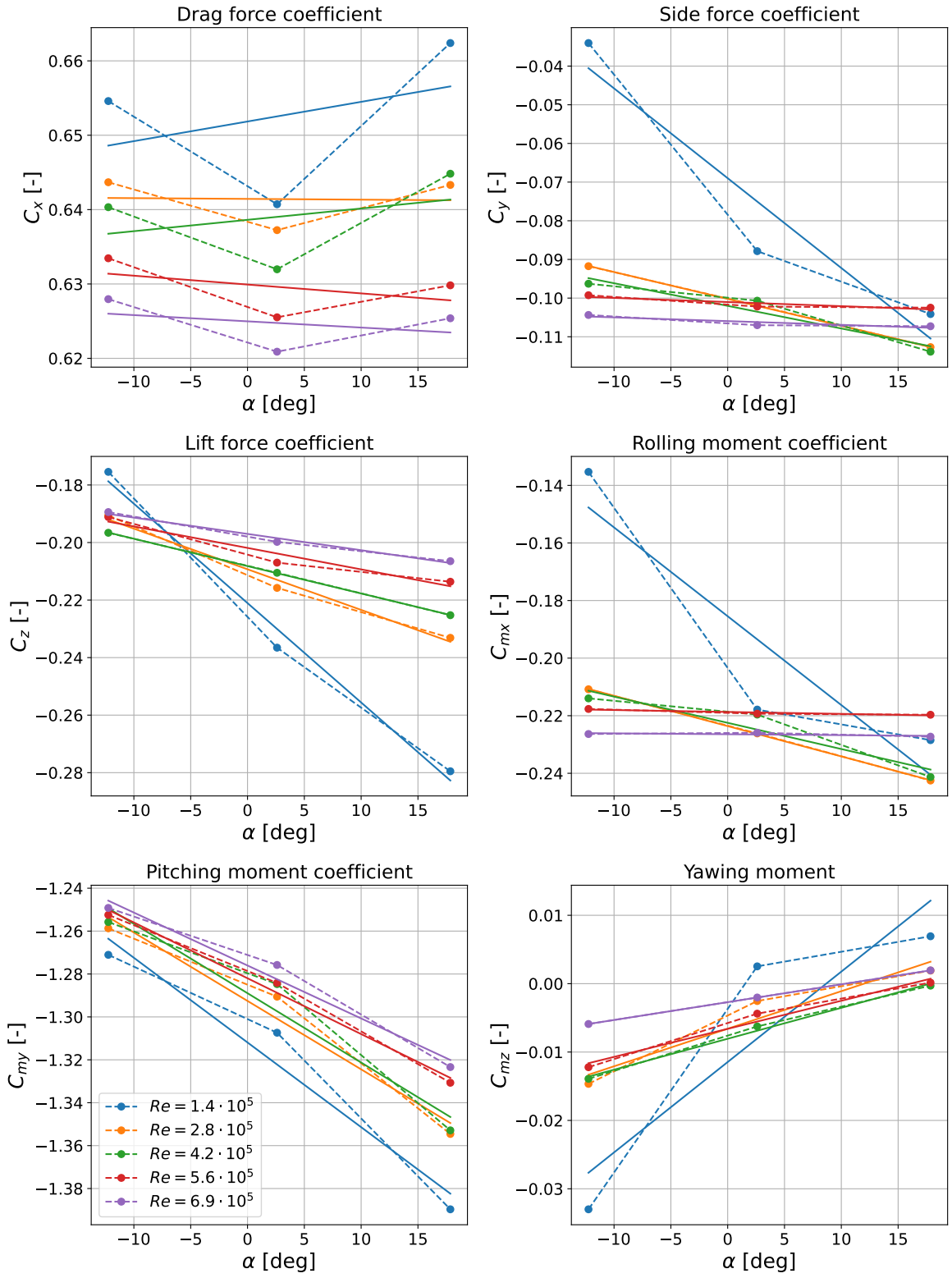

Figure A.3: Force and moment coefficient plots of the support structure for $\beta = 4$ deg.

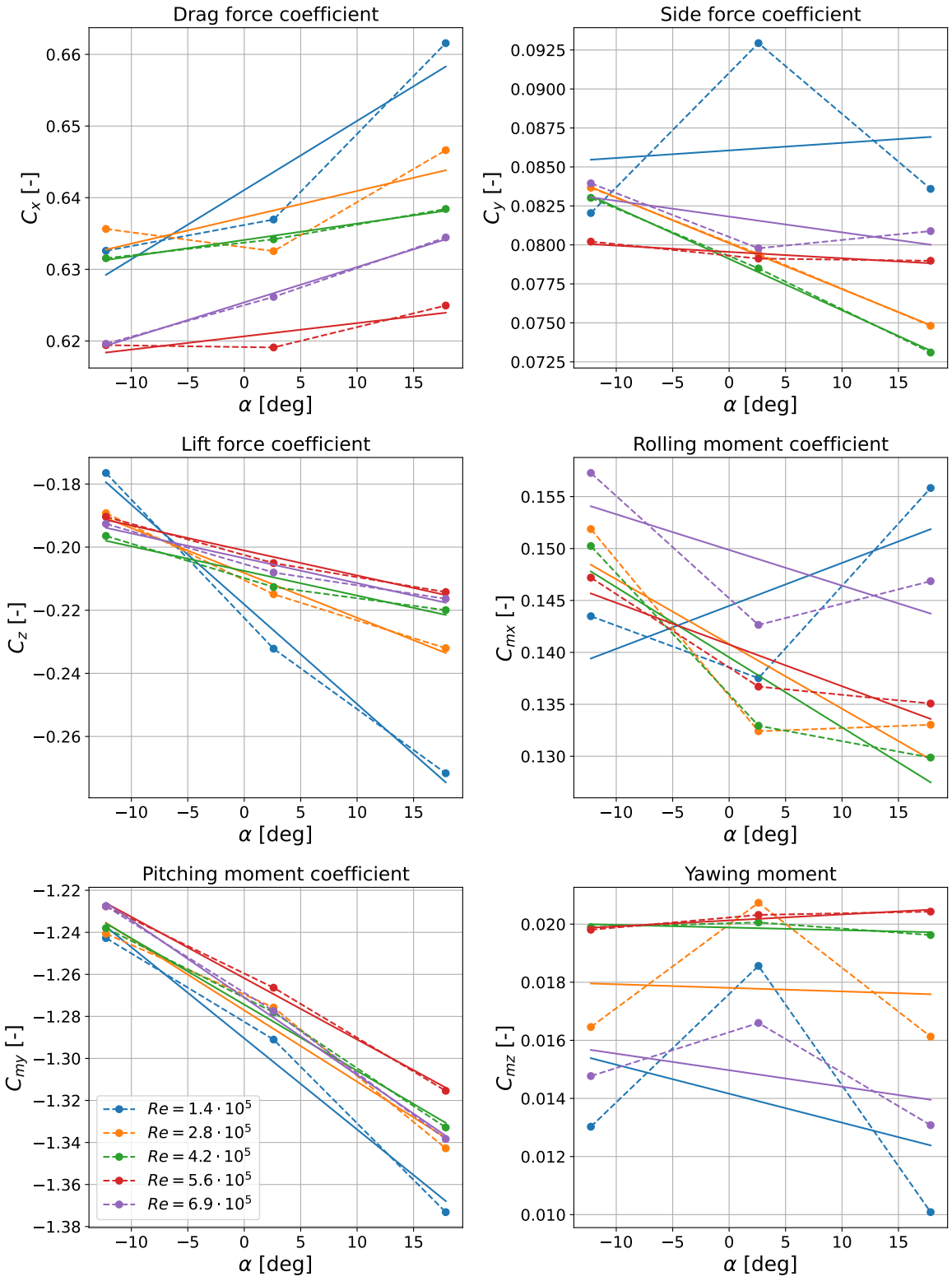

Figure A.4: Force and moment coefficient plots of the support structure for $\beta = -4$ deg.

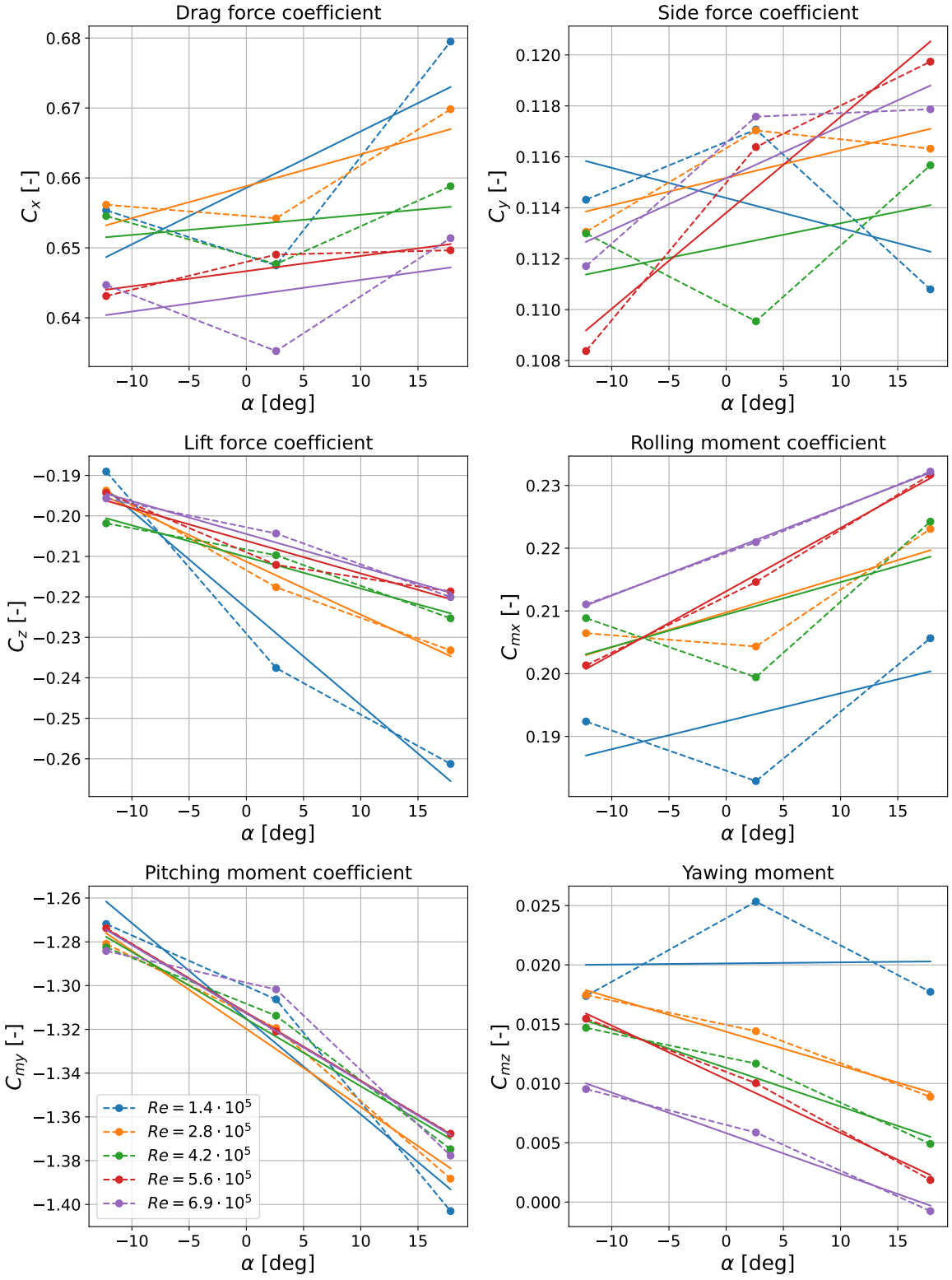

Figure A.5: Force and moment coefficient plots of the support structure for $\beta = -6$ deg.

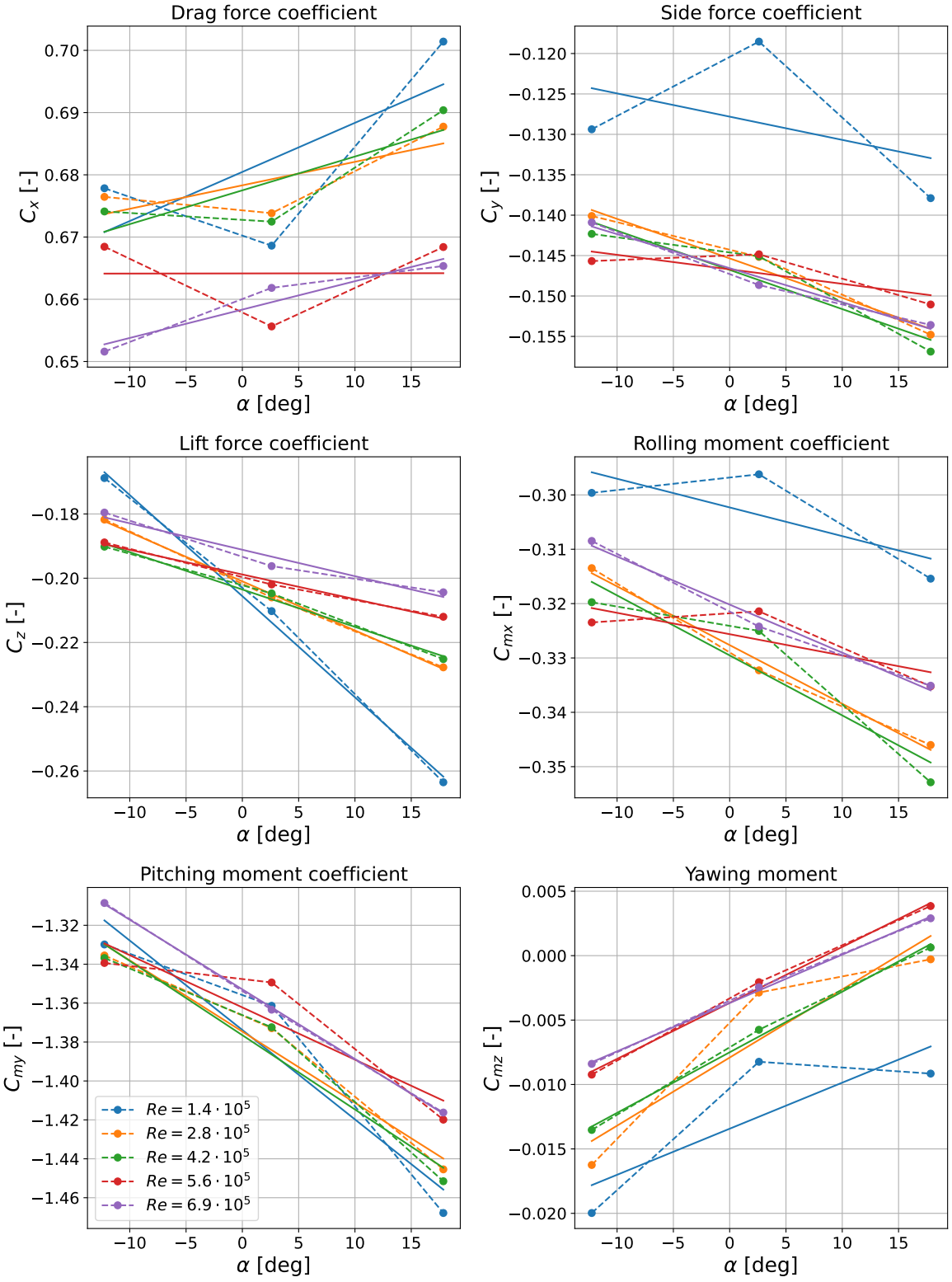

Figure A.6: Force and moment coefficient plots of the support structure for $\beta = 8$ deg.

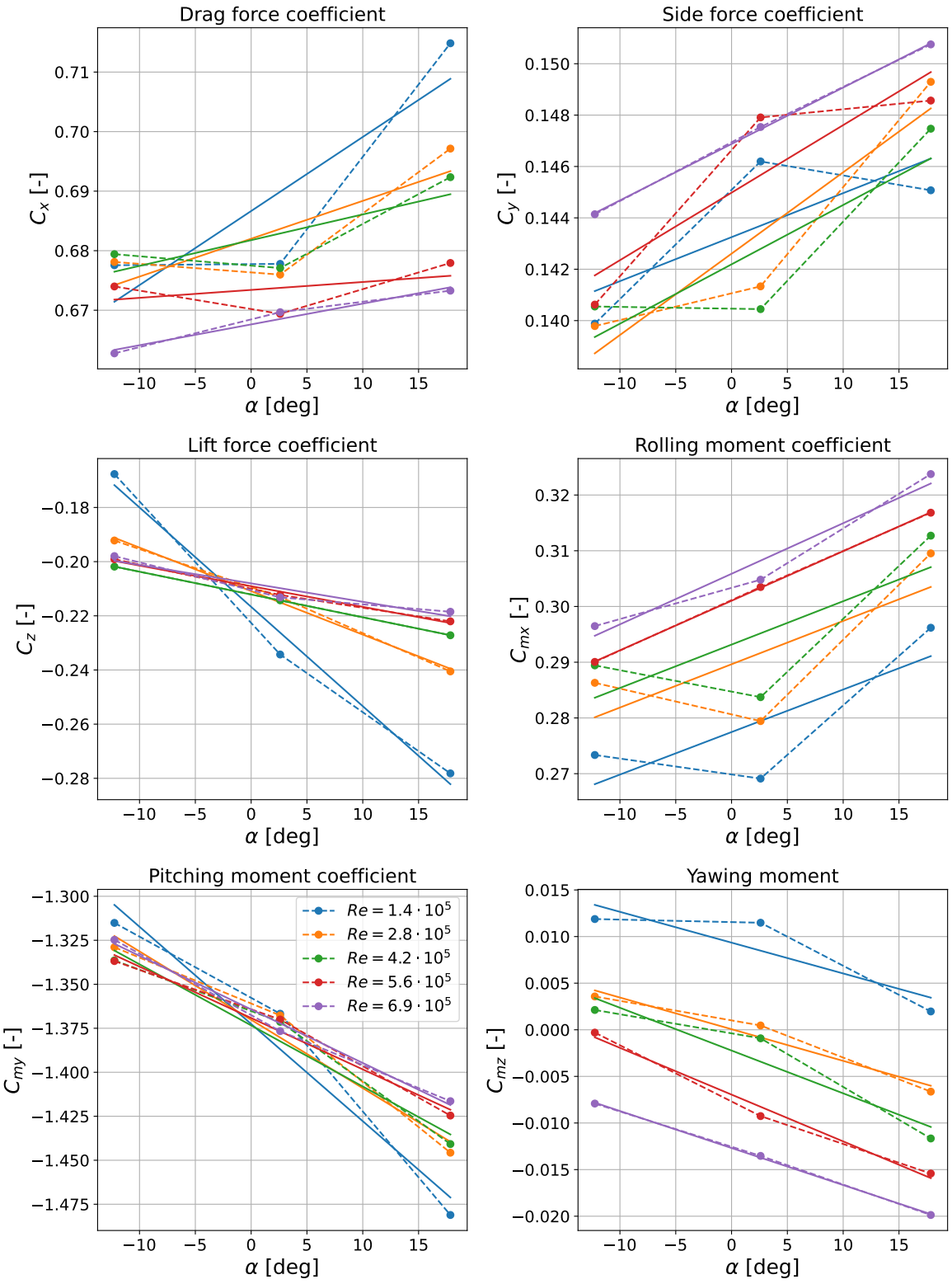

Figure A.7: Force and moment coefficient plots of the support structure for $\beta = -8$ deg.

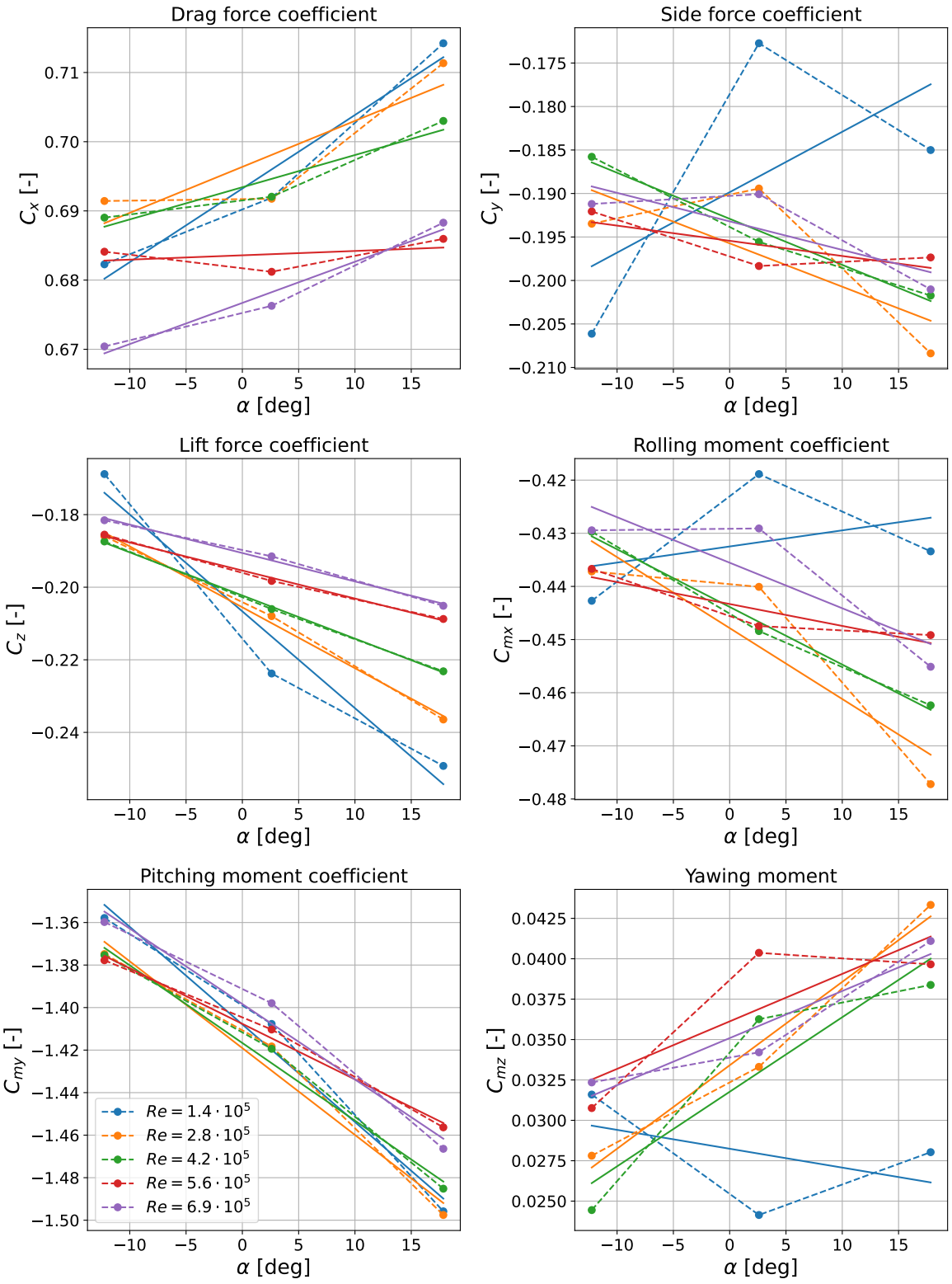

Figure A.8: Force and moment coefficient plots of the support structure for $\beta = 10$ deg.

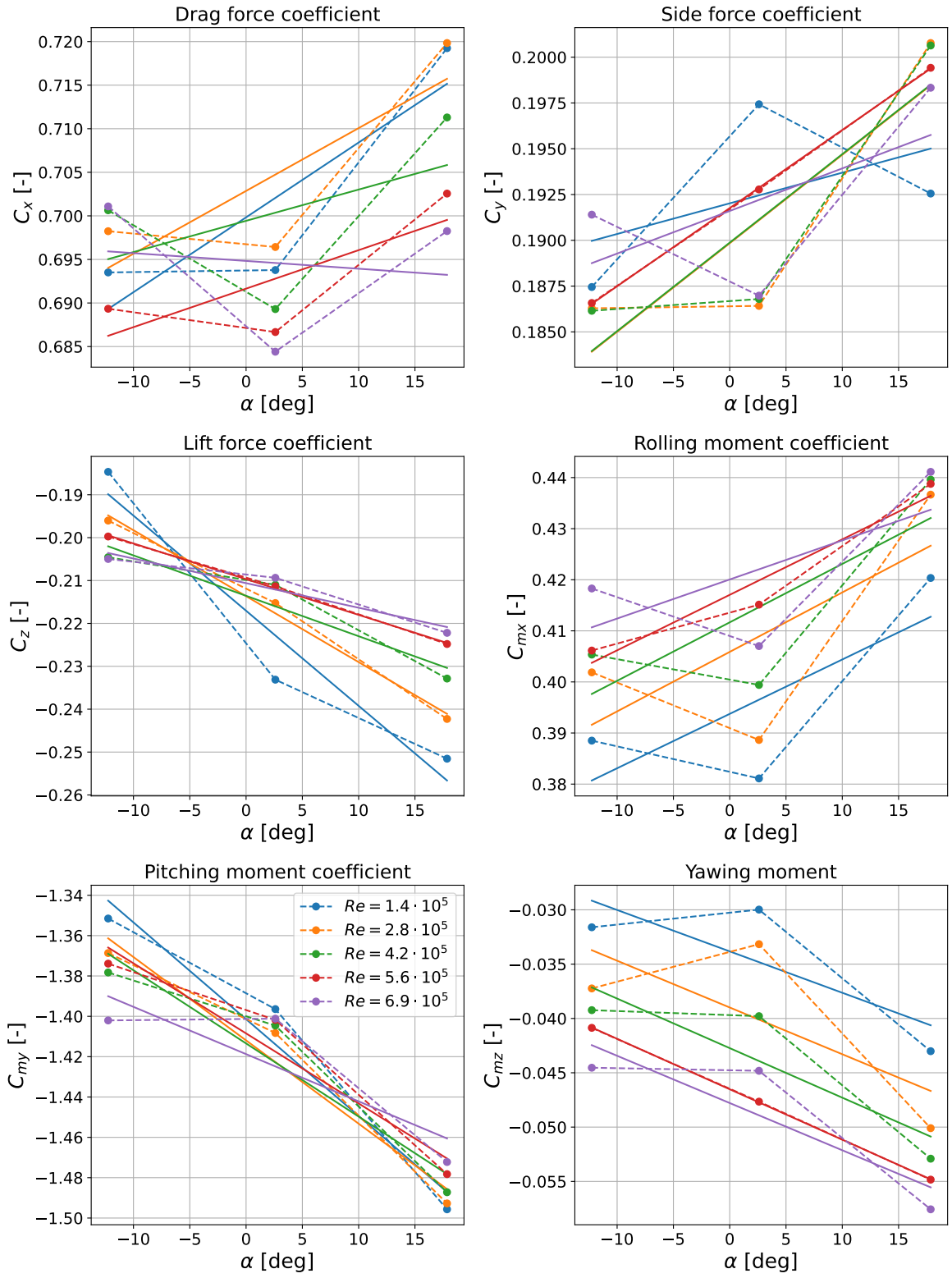

Figure A.9: Force and moment coefficient plots of the support structure for $\beta = -10$ deg.

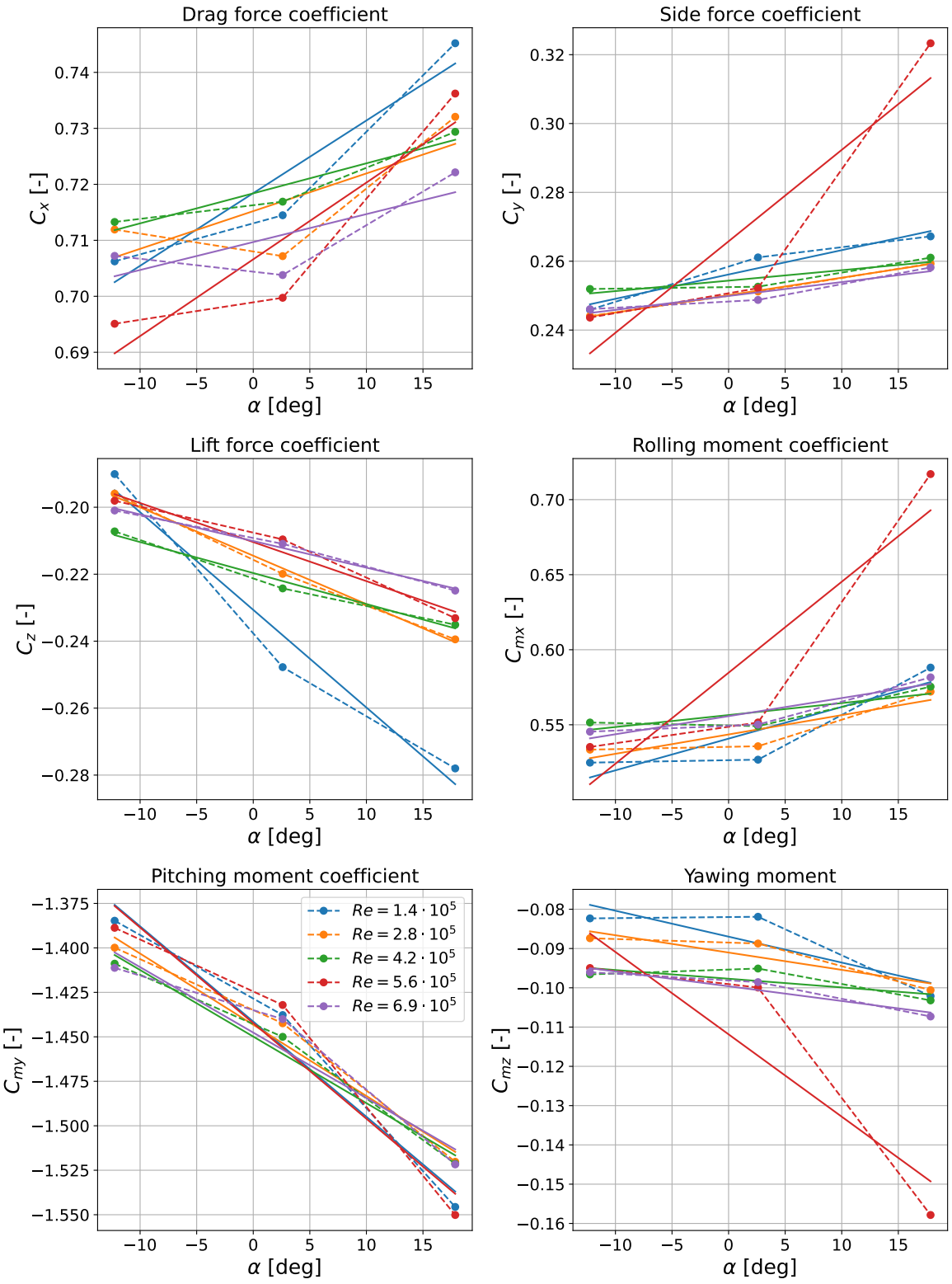

Figure A.10: Force and moment coefficient plots of the support structure for $\beta = -12$ deg.

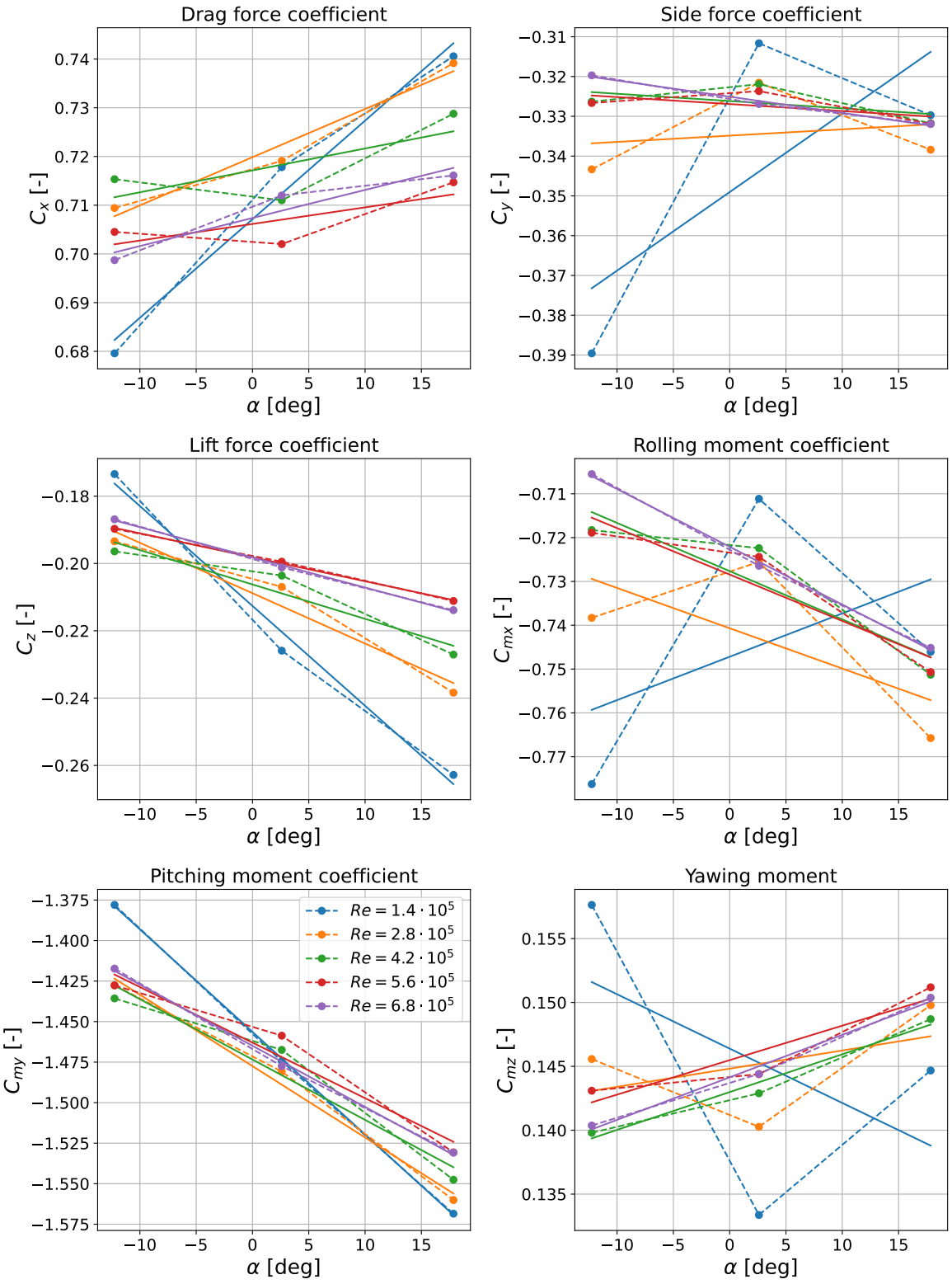

Figure A.11: Force and moment coefficient plots of the support structure for $\beta = 14$ deg.

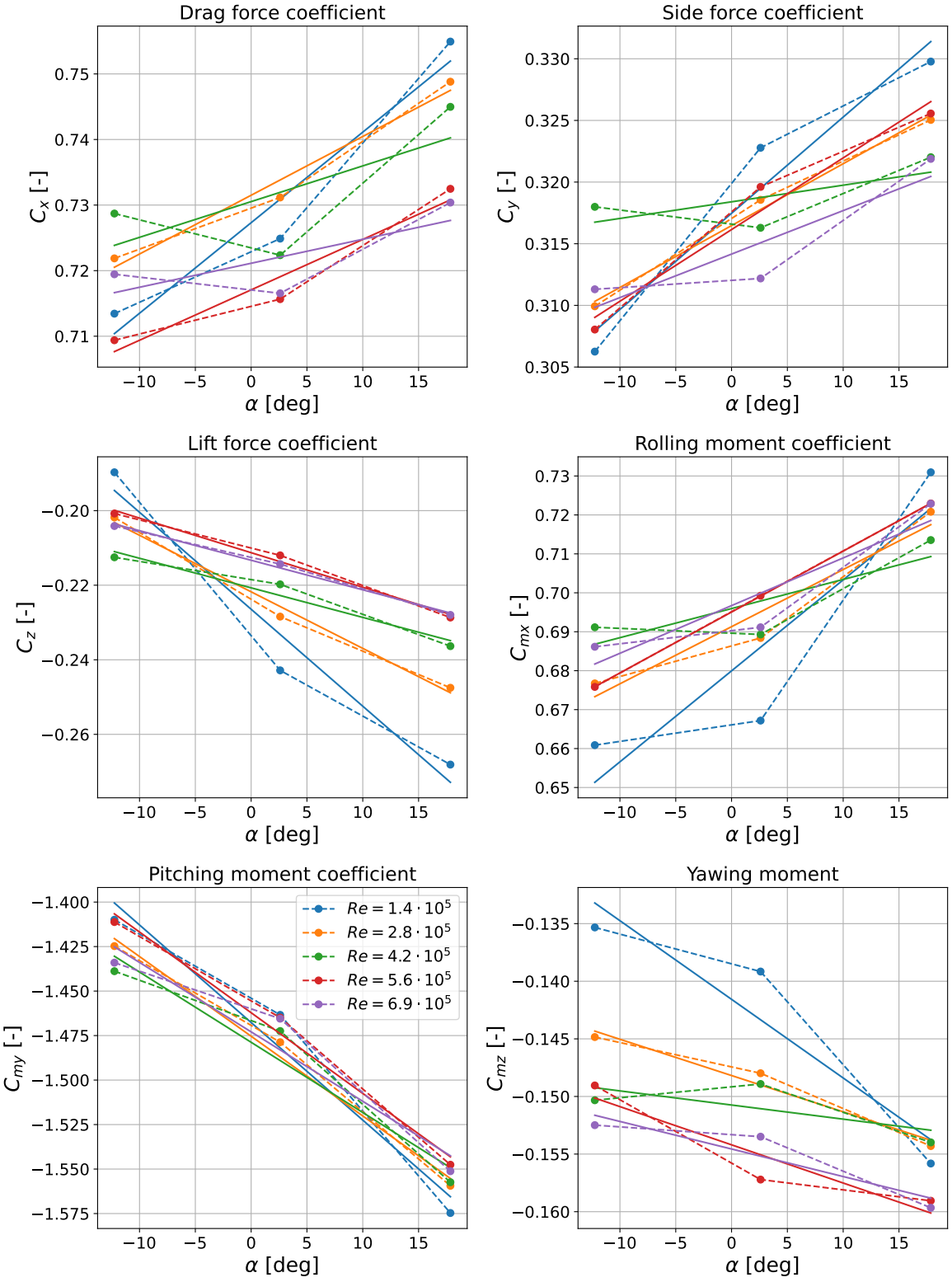

Figure A.12: Force and moment coefficient plots of the support structure for $\beta = -14$ deg.

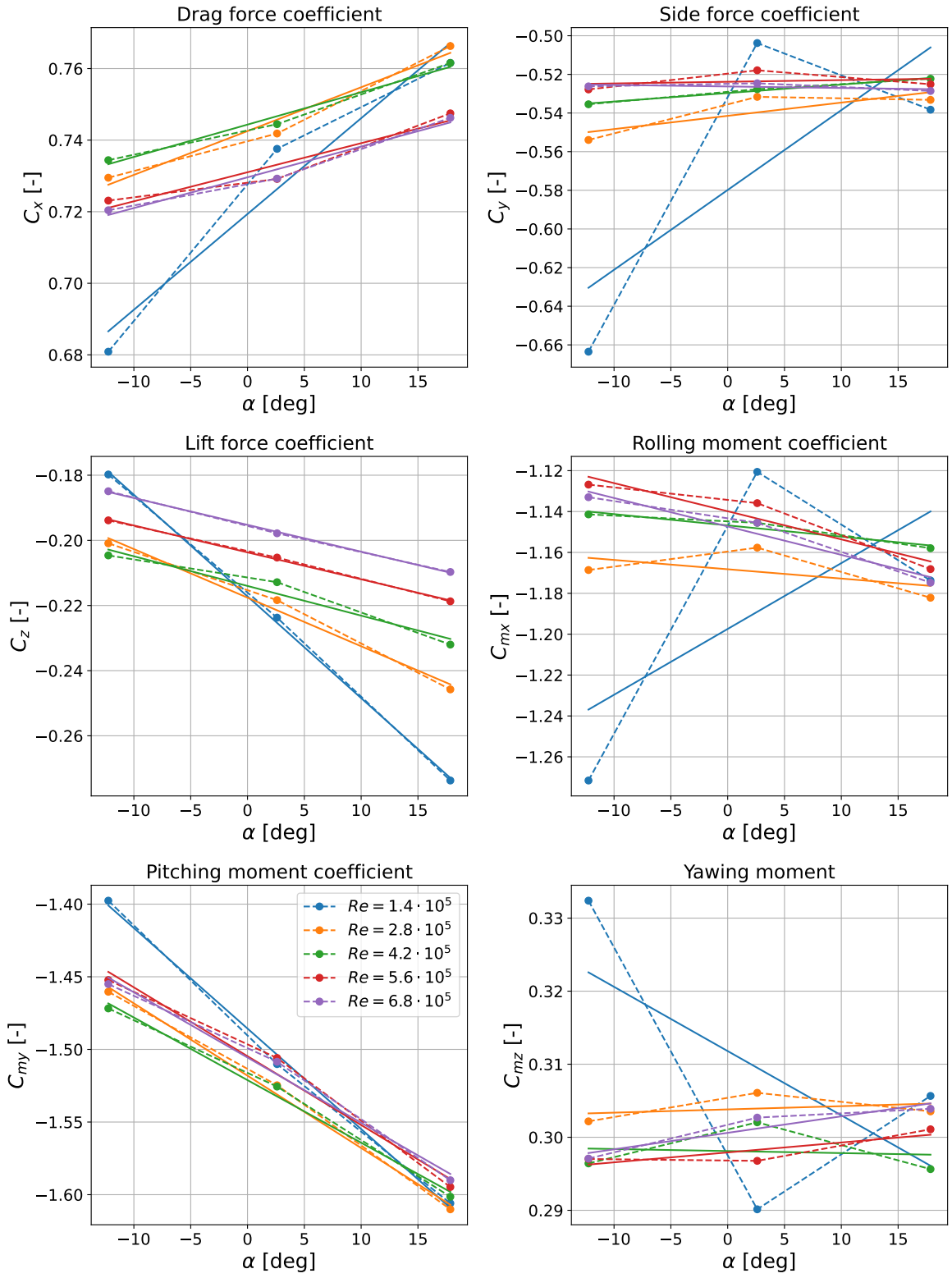

Figure A.13: Force and moment coefficient plots of the support structure for $\beta = 20$ deg.

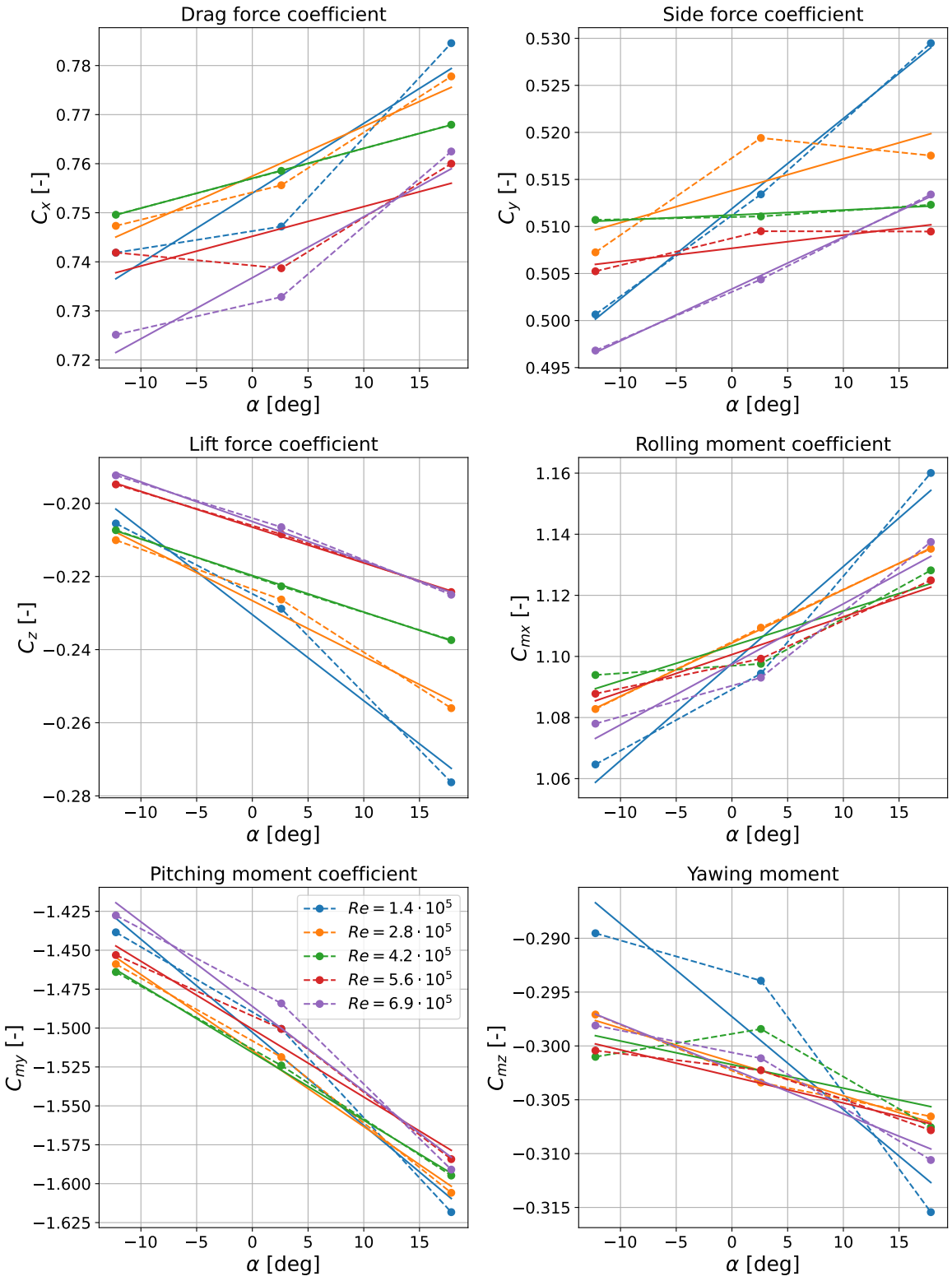

Figure A.14: Force and moment coefficient plots of the support structure for $\beta = -20$ deg.

A.1.2. Plots versus β

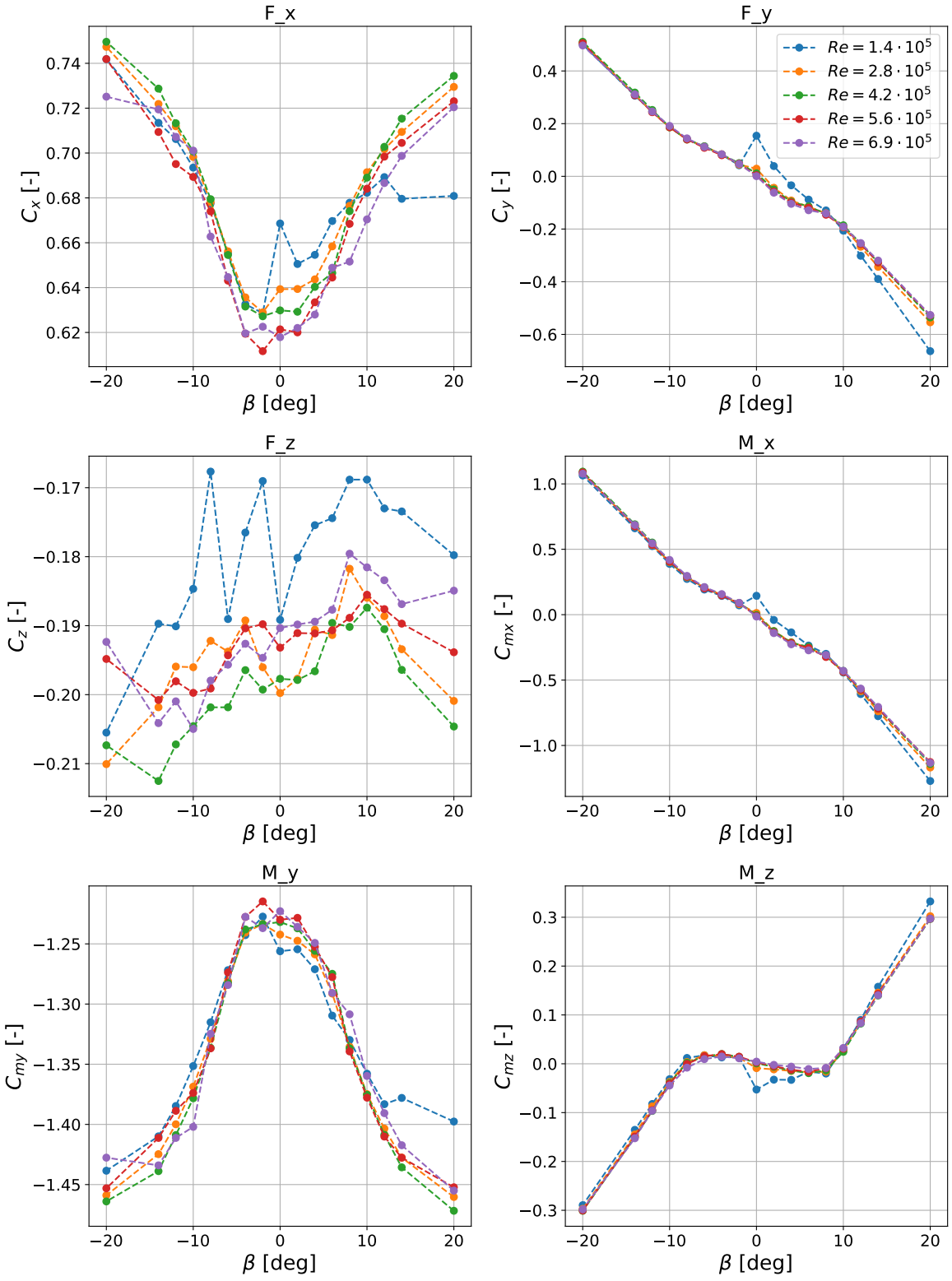

Figure A.15: Force and moment coefficient plots of the support structure for $\alpha = -12.25$ deg.

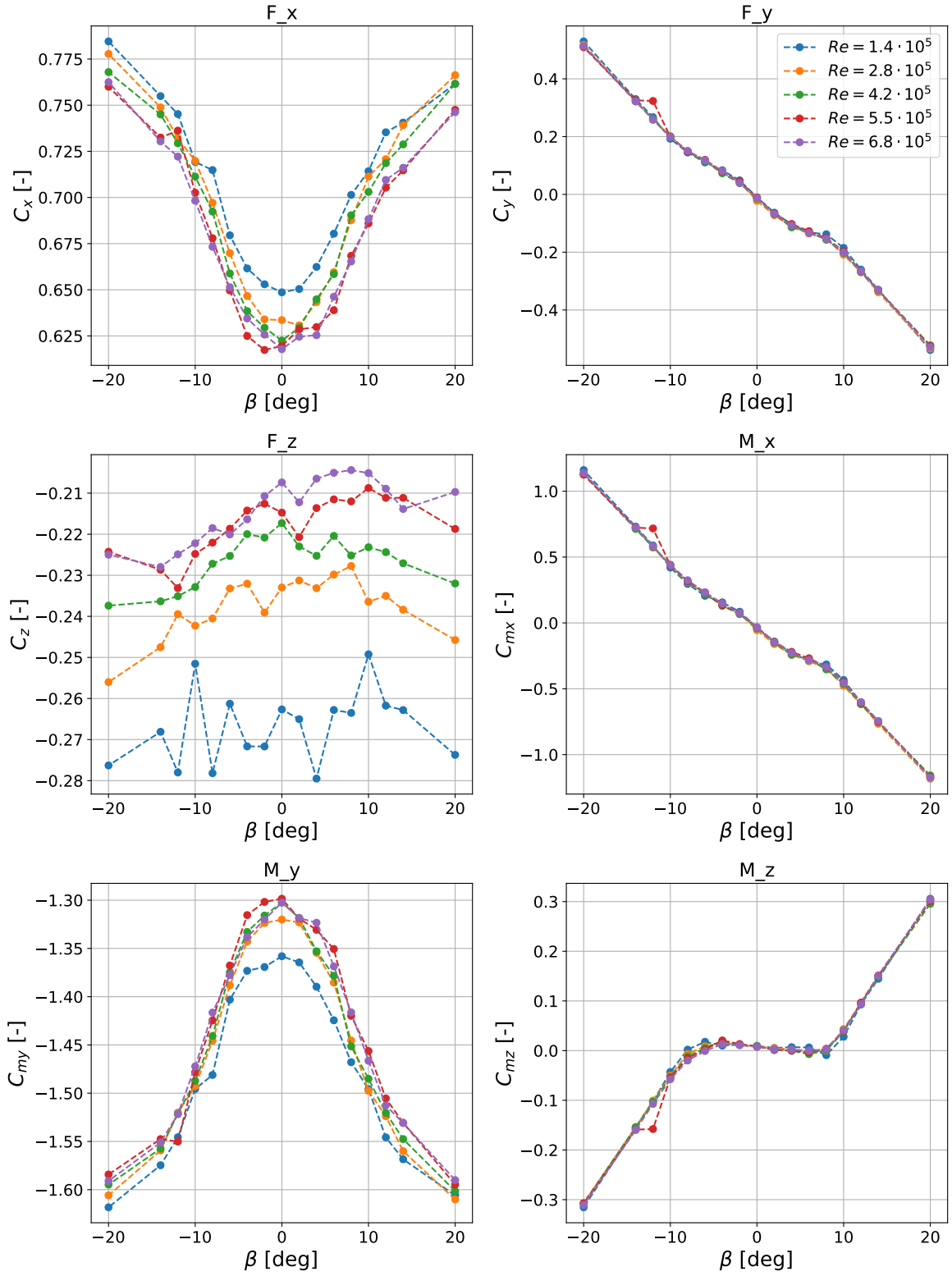

Figure A.16: Force and moment coefficient plots of the support structure for $\alpha = 17.85$ deg.

A.2. Force and moment coefficient plots of the kite

A.2.1. Plots versus α

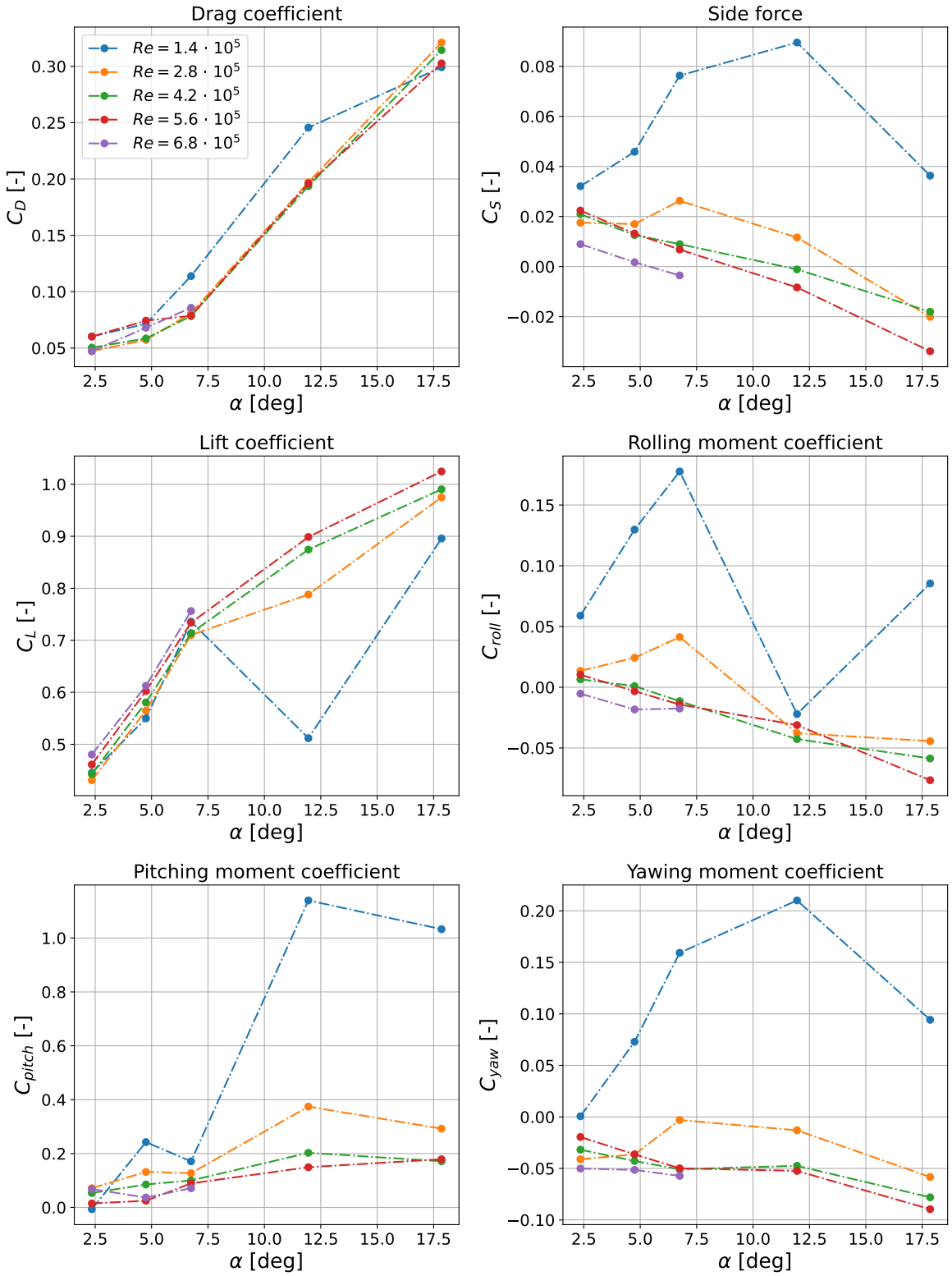

Figure A.17: Force and moment coefficient plots of the kite for $\beta = 2$ deg.

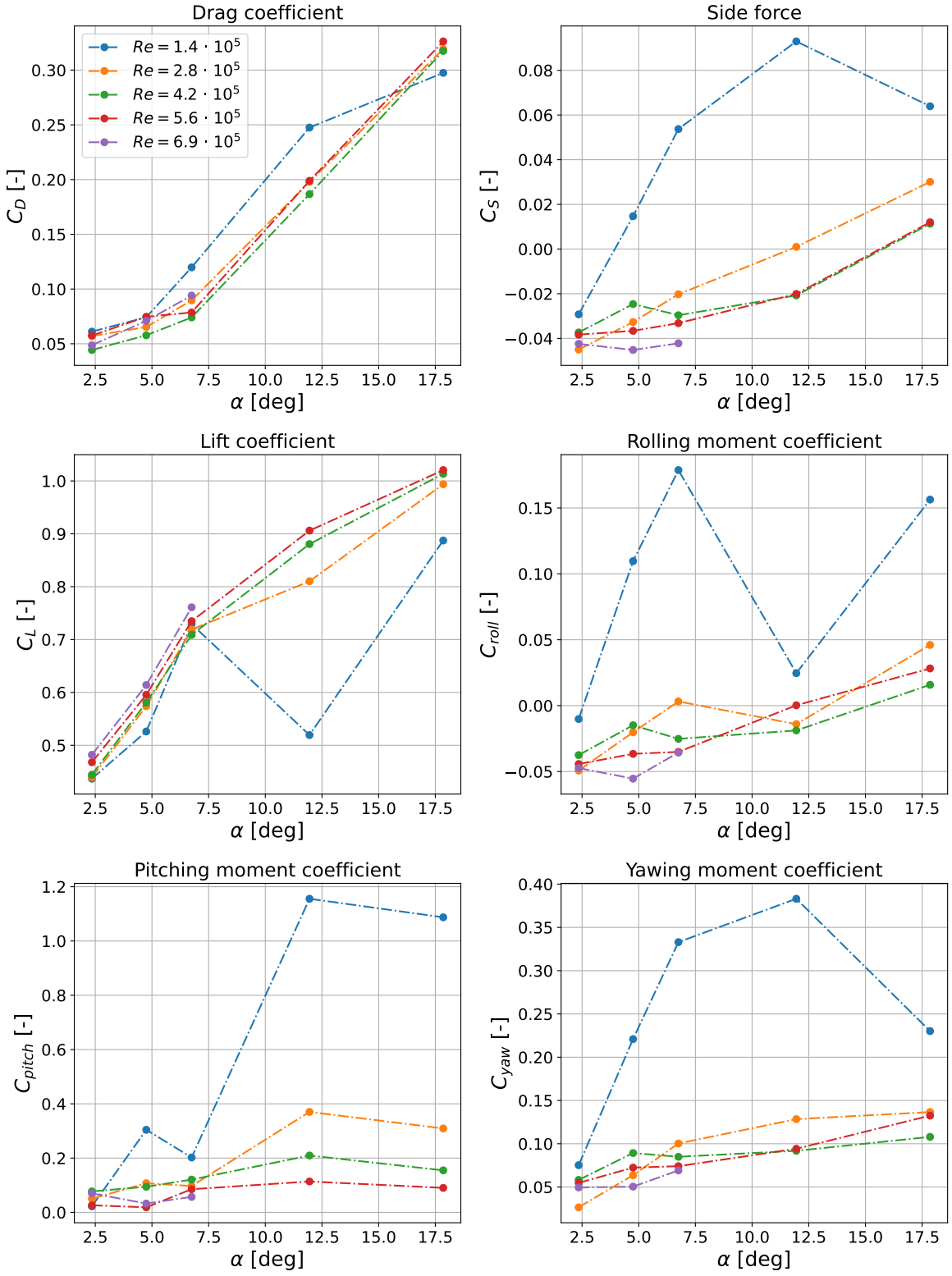

Figure A.18: Force and moment coefficient plots of the kite for $\beta = -2$ deg.

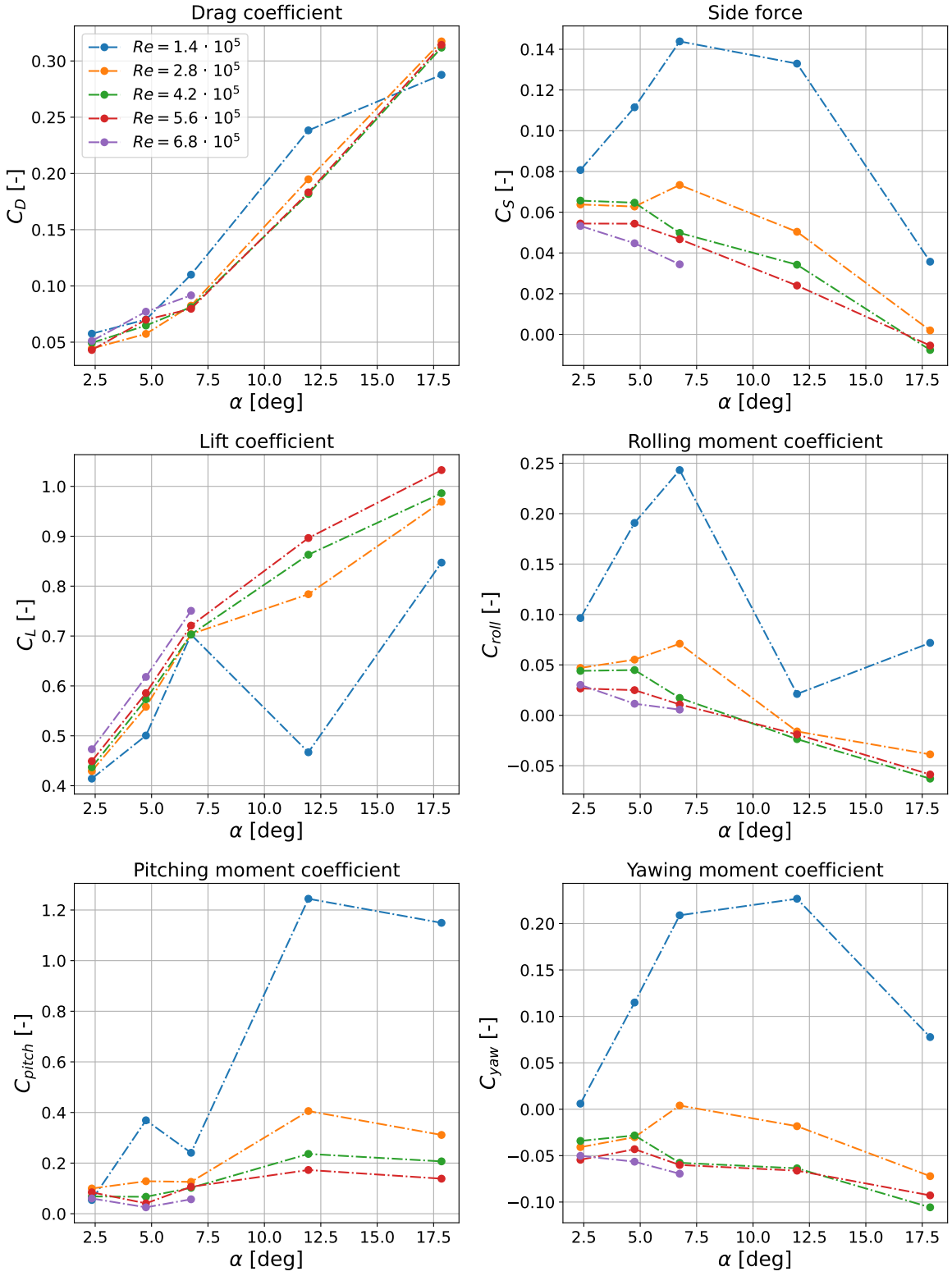

Figure A.19: Force and moment coefficient plots of the kite for $\beta = 4$ deg.

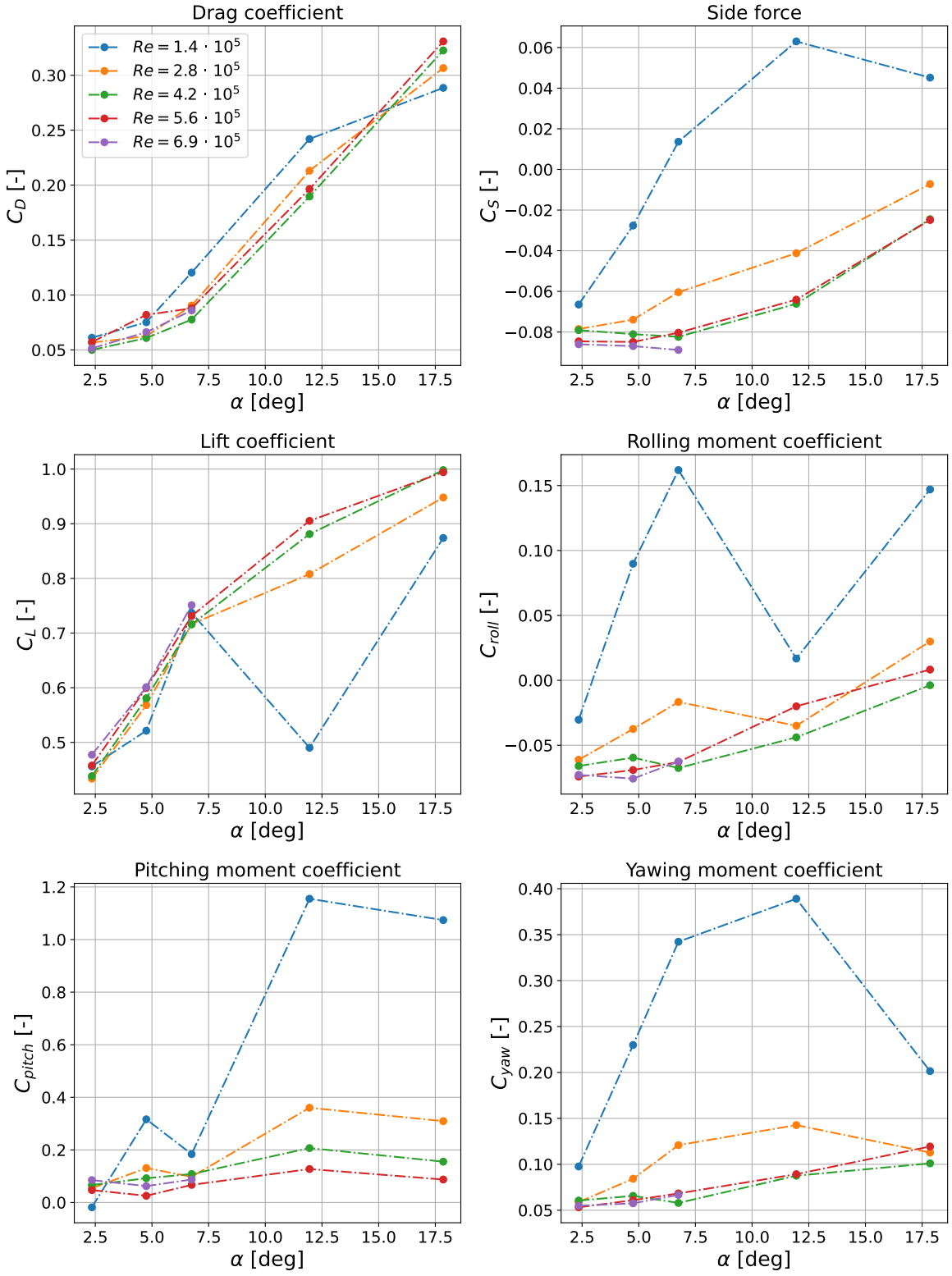

Figure A.20: Force and moment coefficient plots of the kite for $\beta = -4$ deg.

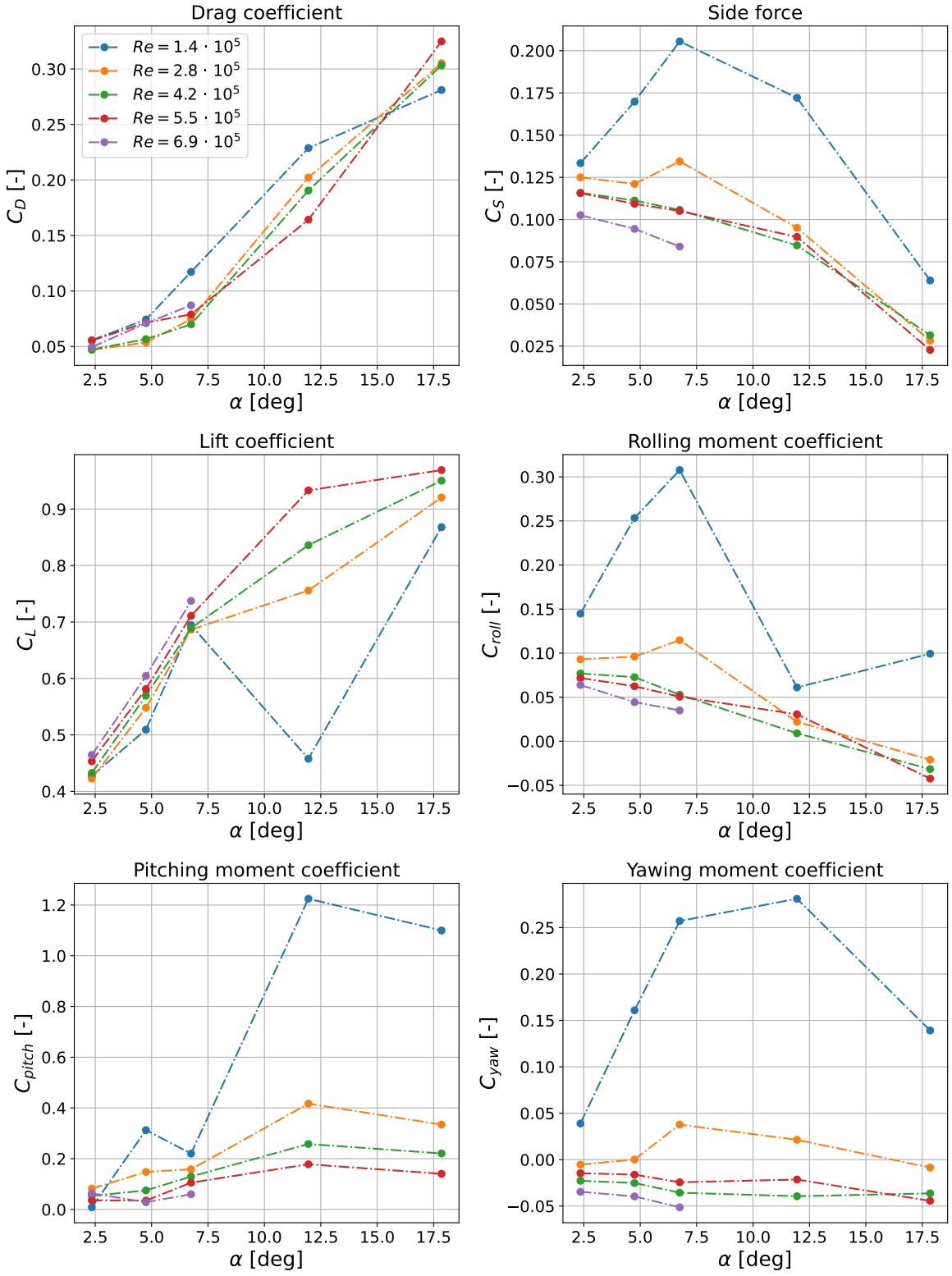

Figure A.21: Force and moment coefficient plots of the kite for $\beta = 6$ deg.

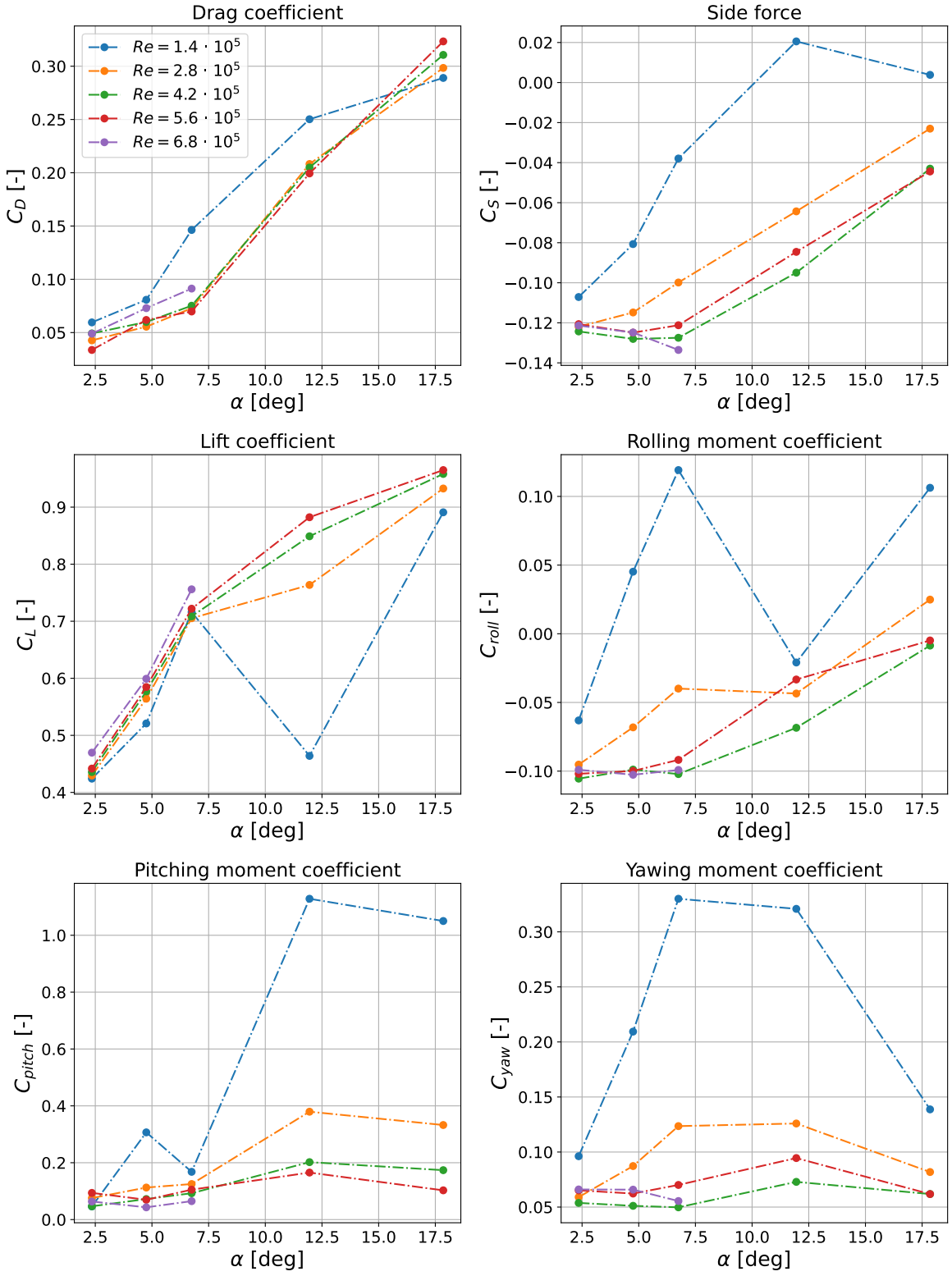

Figure A.22: Force and moment coefficient plots of the kite for $\beta = -6$ deg.

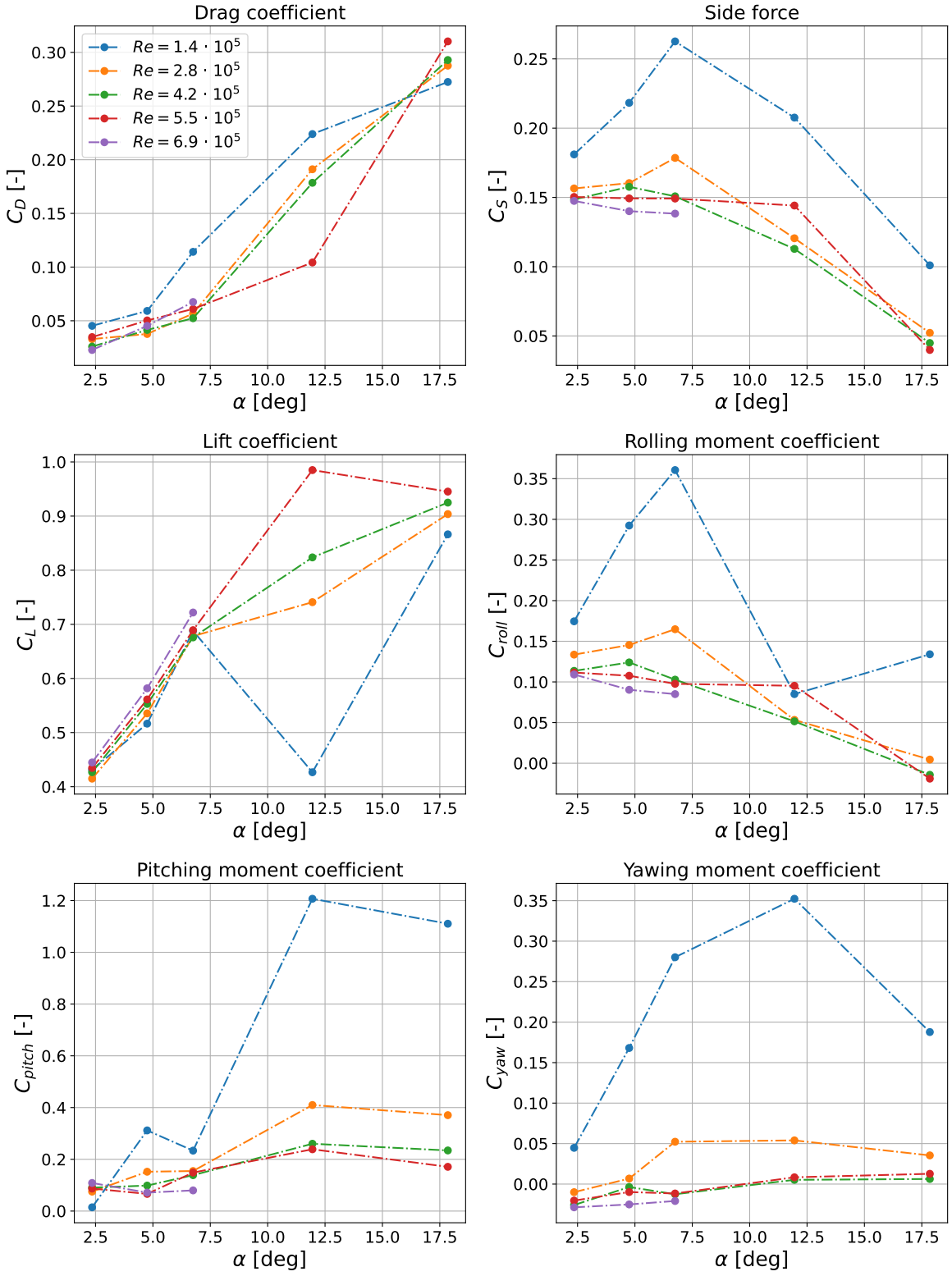

Figure A.23: Force and moment coefficient plots of the kite for $\beta = 8$ deg.

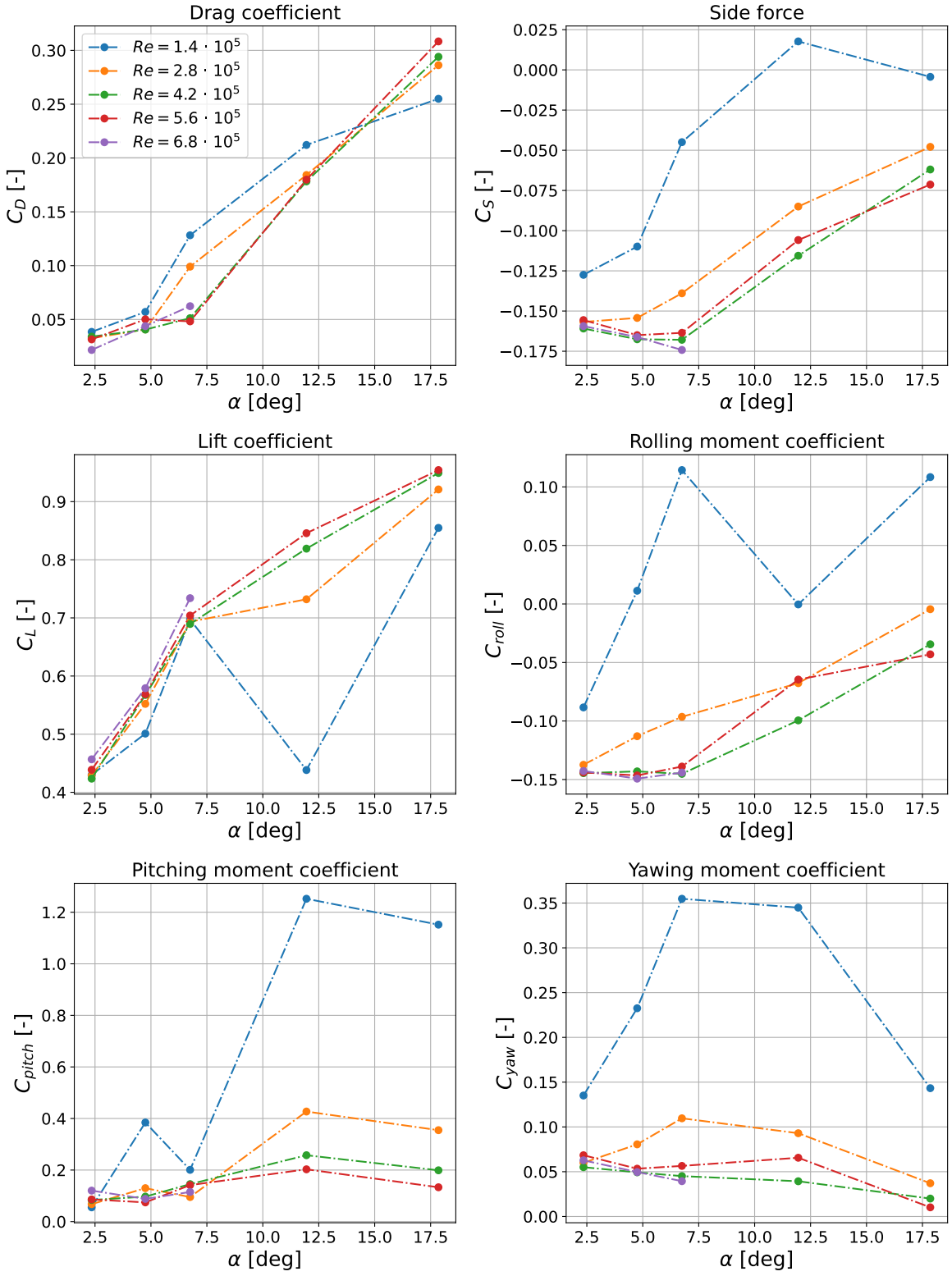

Figure A.24: Force and moment coefficient plots of the kite for $\beta = -8$ deg.

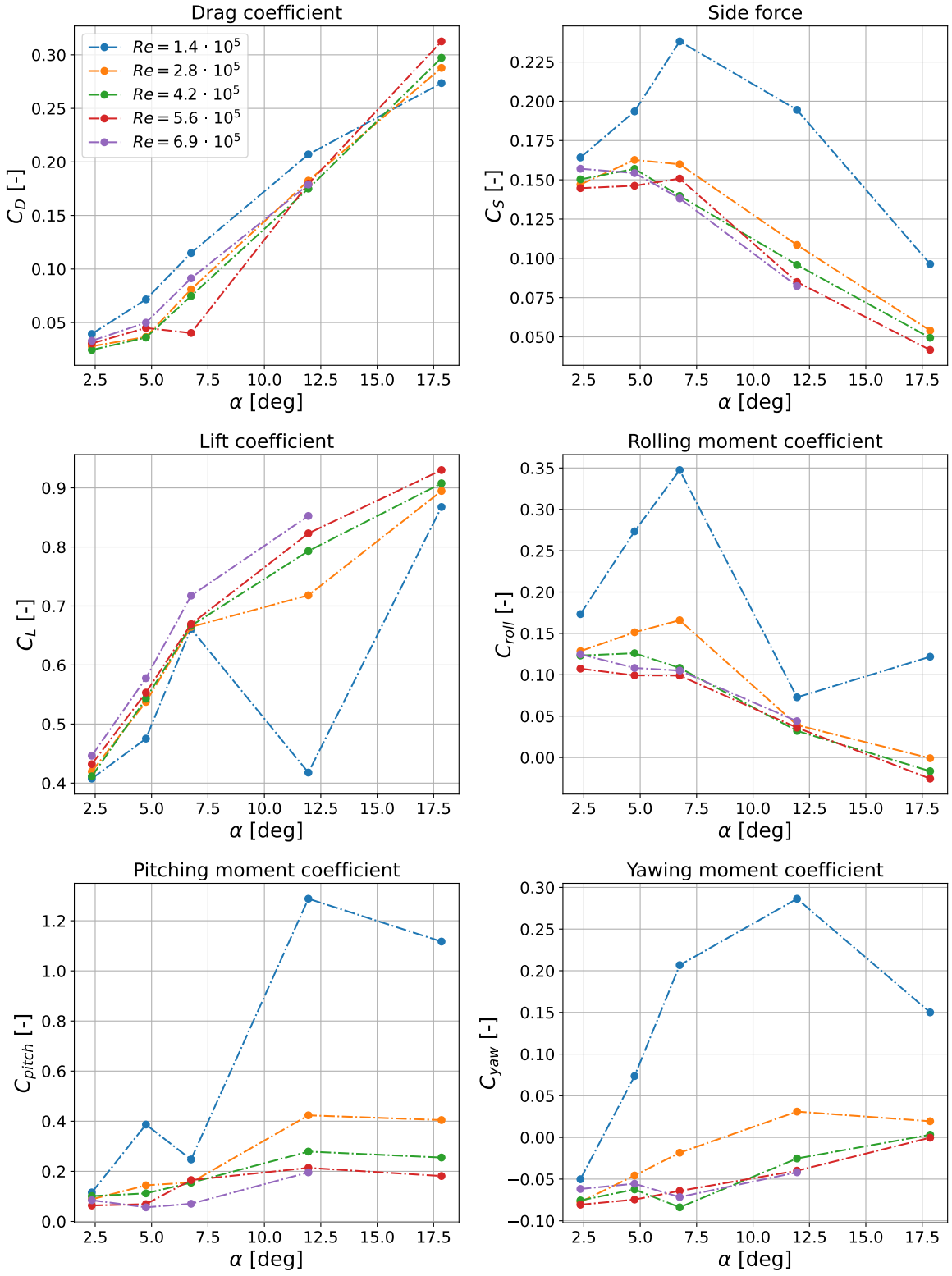

Figure A.25: Force and moment coefficient plots of the kite for $\beta = 10$ deg.

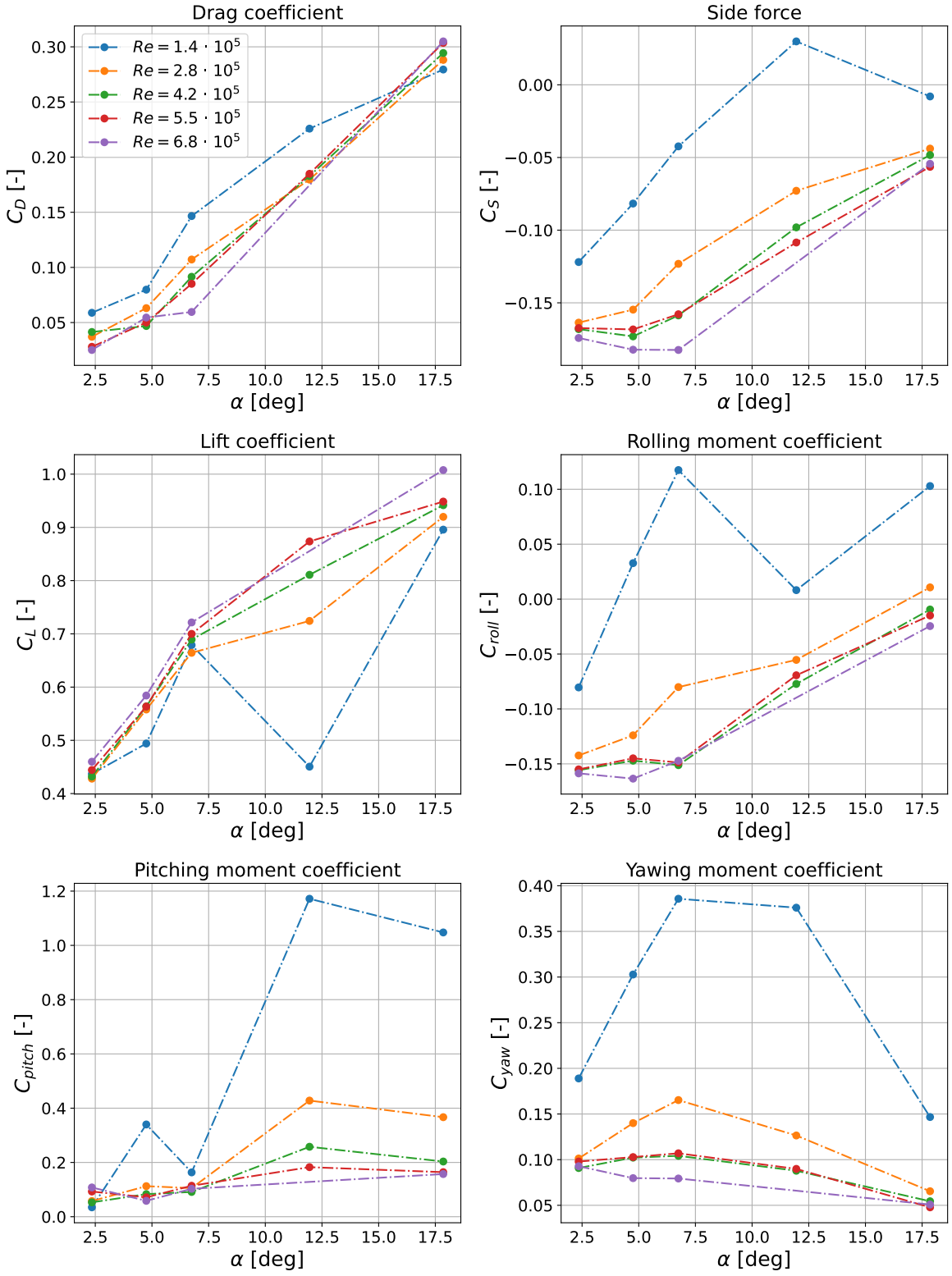

Figure A.26: Force and moment coefficient plots of the kite for $\beta = -10$ deg.

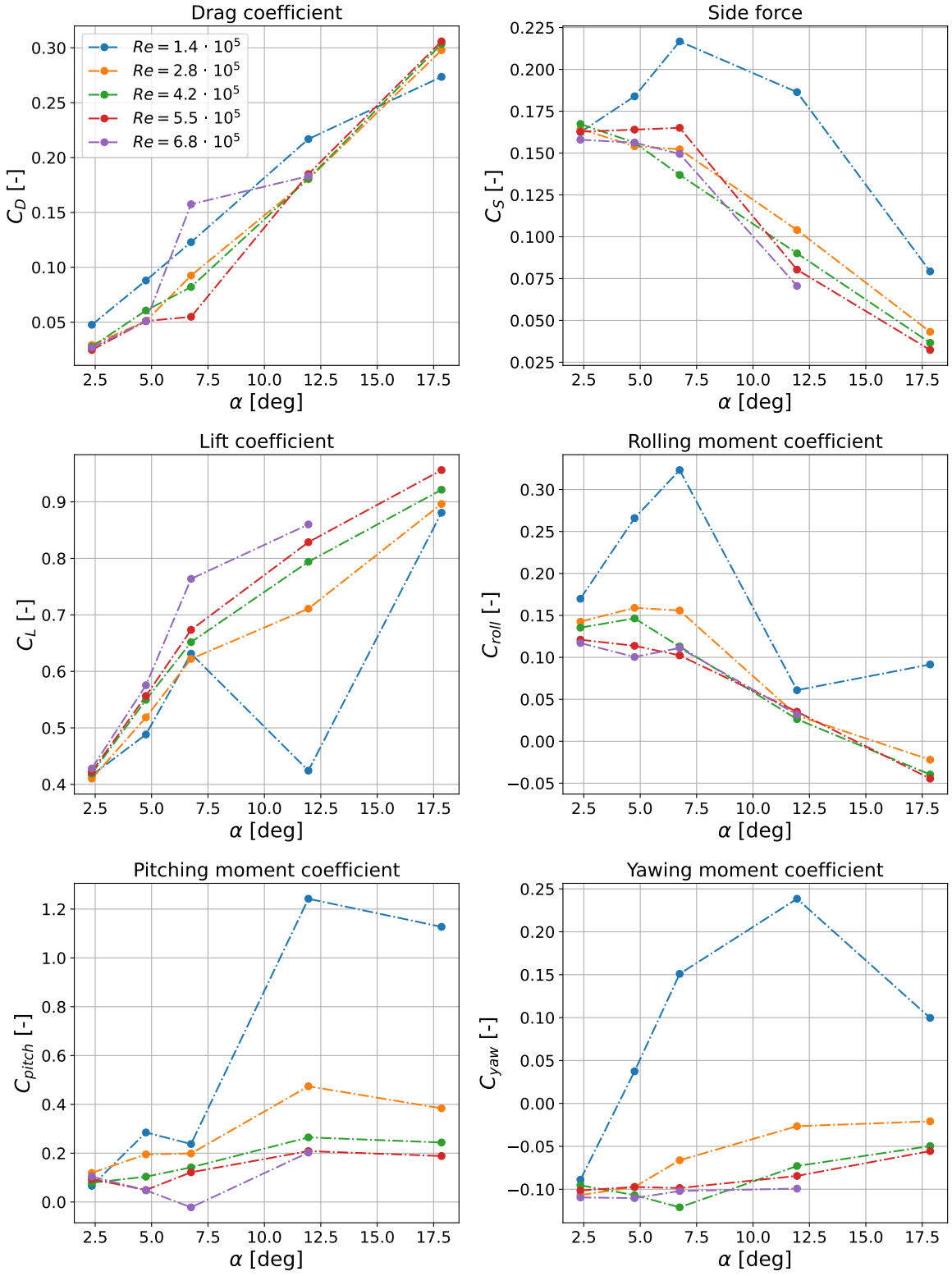

Figure A.27: Force and moment coefficient plots of the kite for $\beta = 12$ deg.

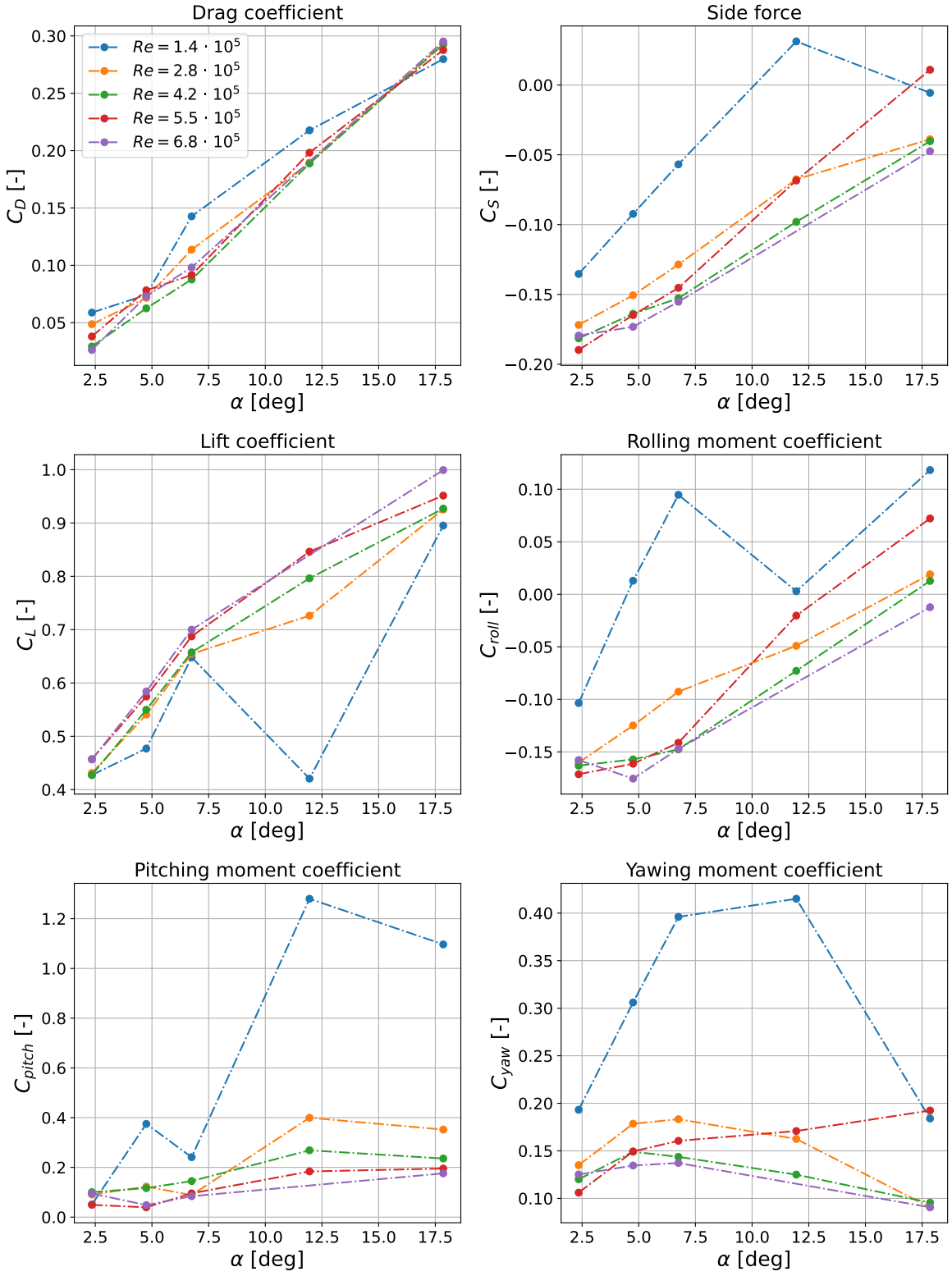

Figure A.28: Force and moment coefficient plots of the kite for $\beta = -12$ deg.

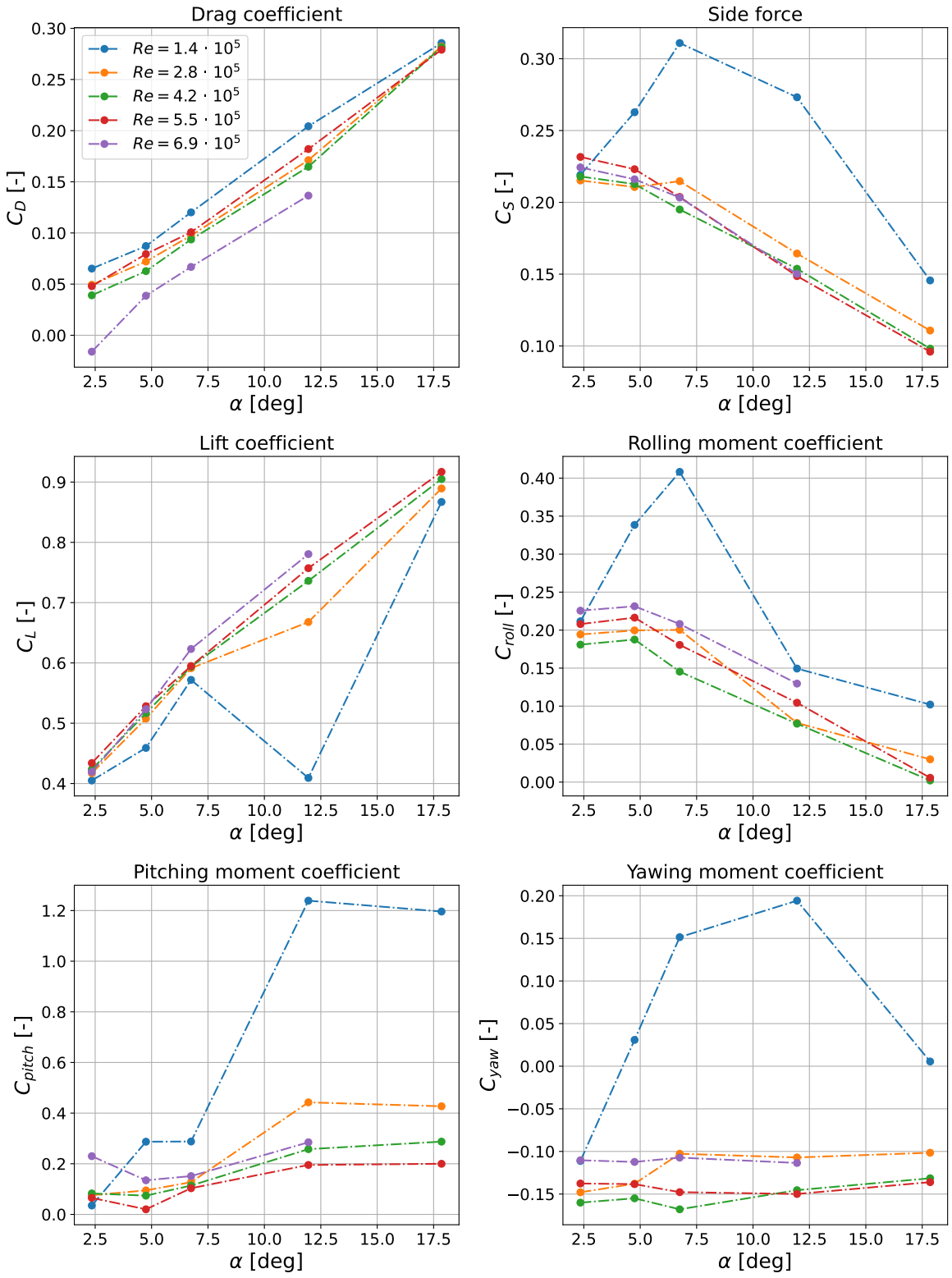

Figure A.29: Force and moment coefficient plots of the kite for $\beta = 20$ deg.

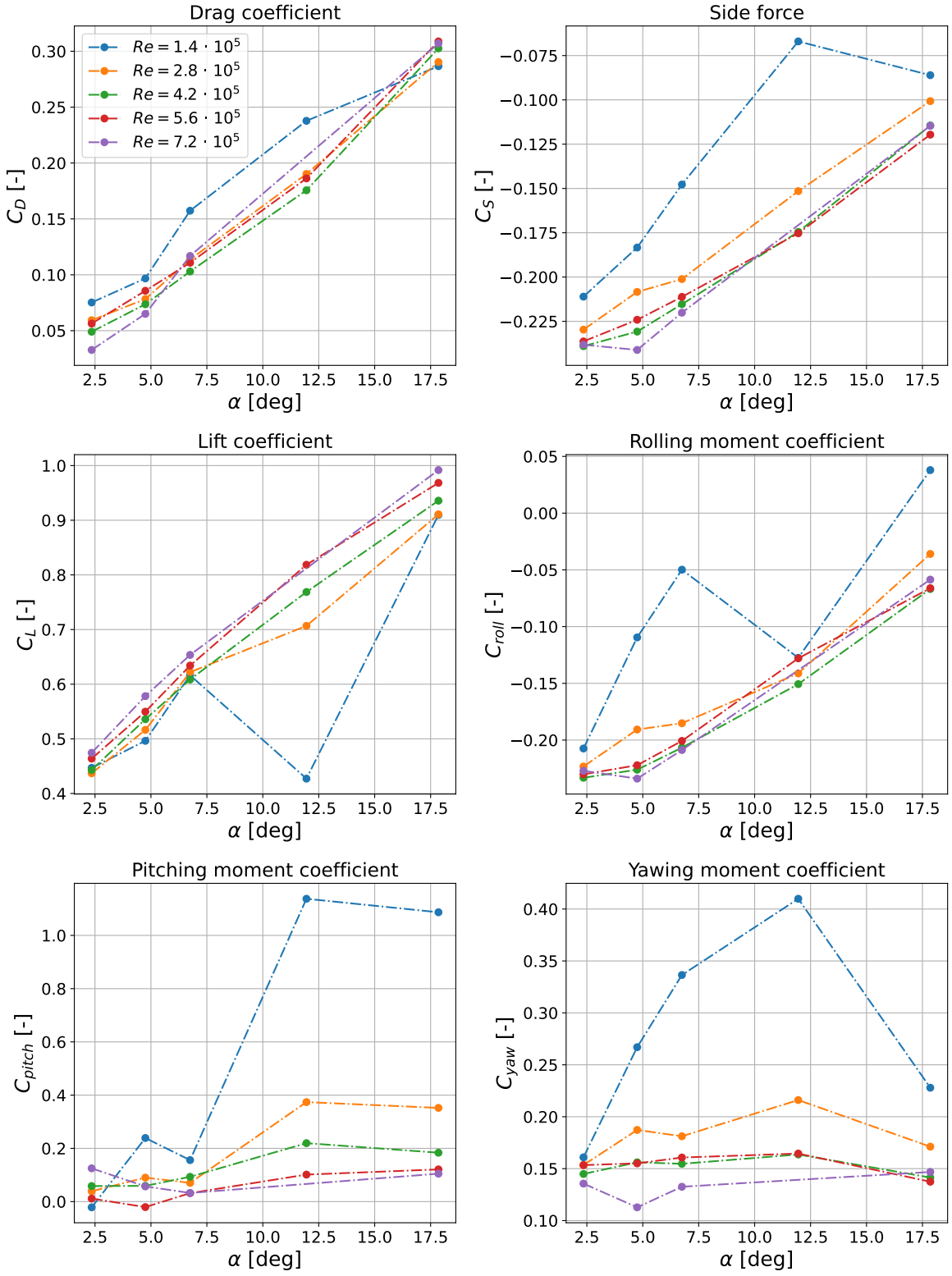

Figure A.30: Force and moment coefficient plots of the kite for $\beta = -20$ deg.

A.2.2. Plots versus β

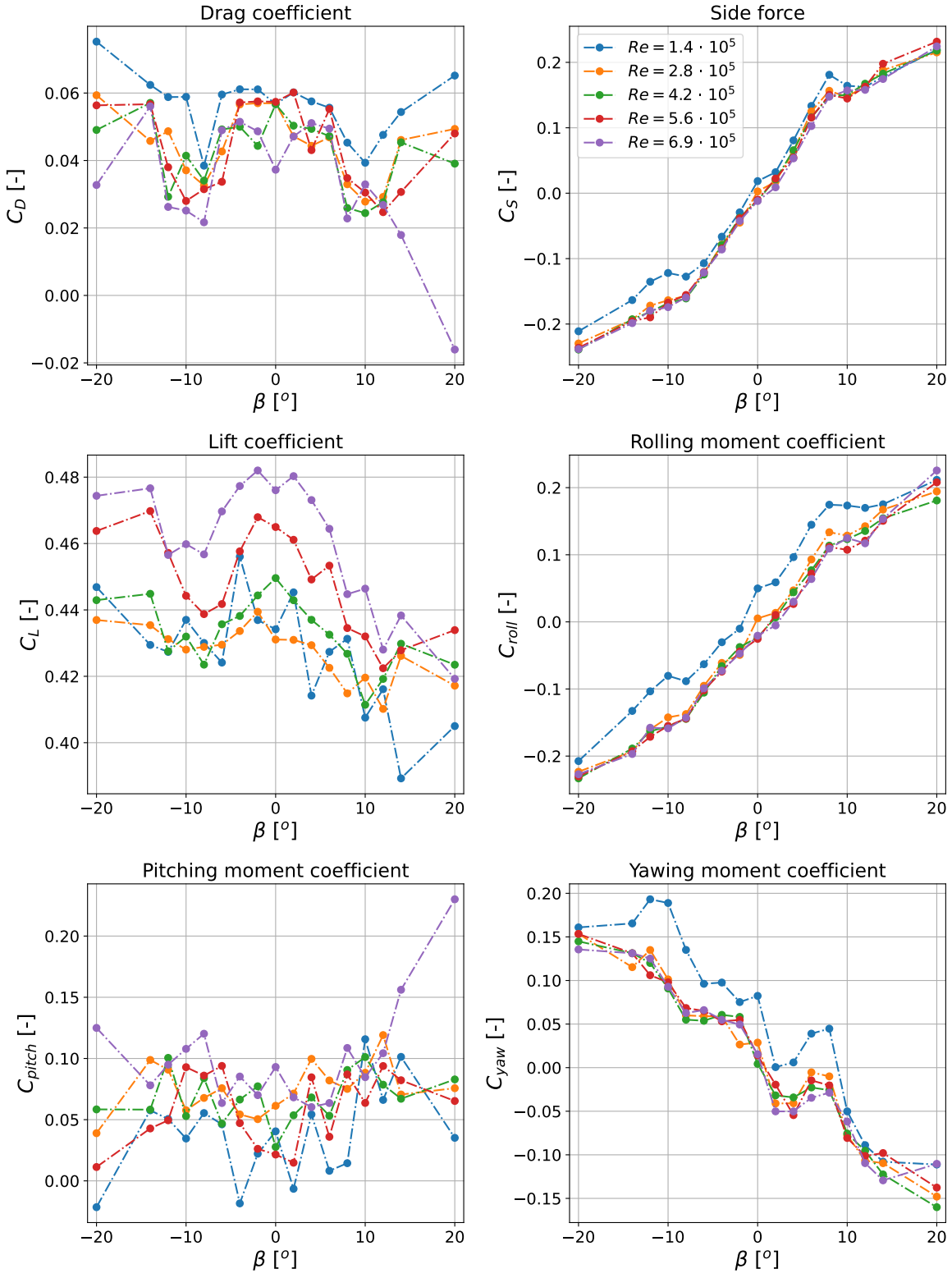

Figure A.31: Force and moment coefficient plots of the kite for $\beta = 2.35$ deg.

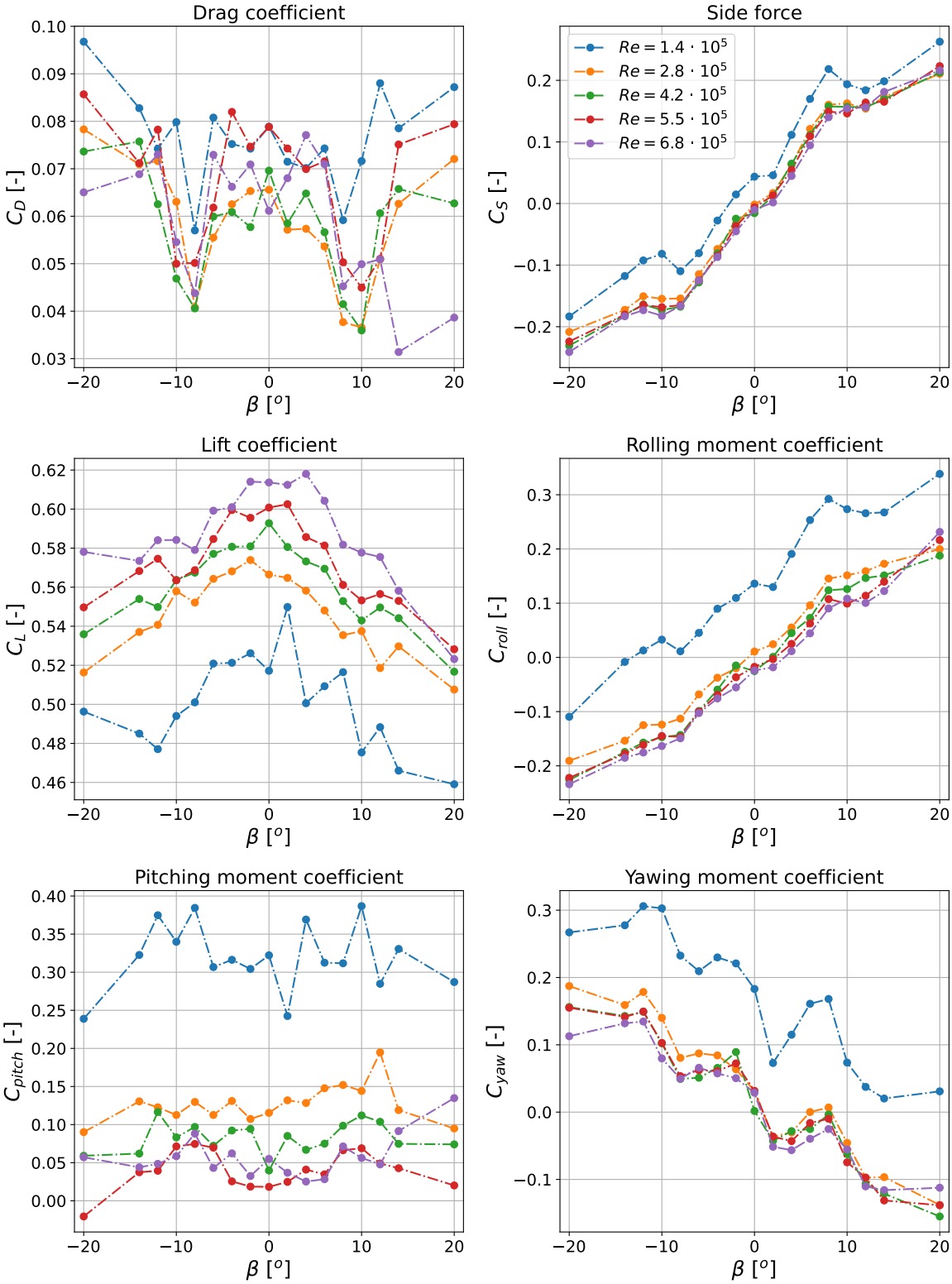

Figure A.32: Force and moment coefficient plots of the kite for $\alpha = 4.75$ deg.

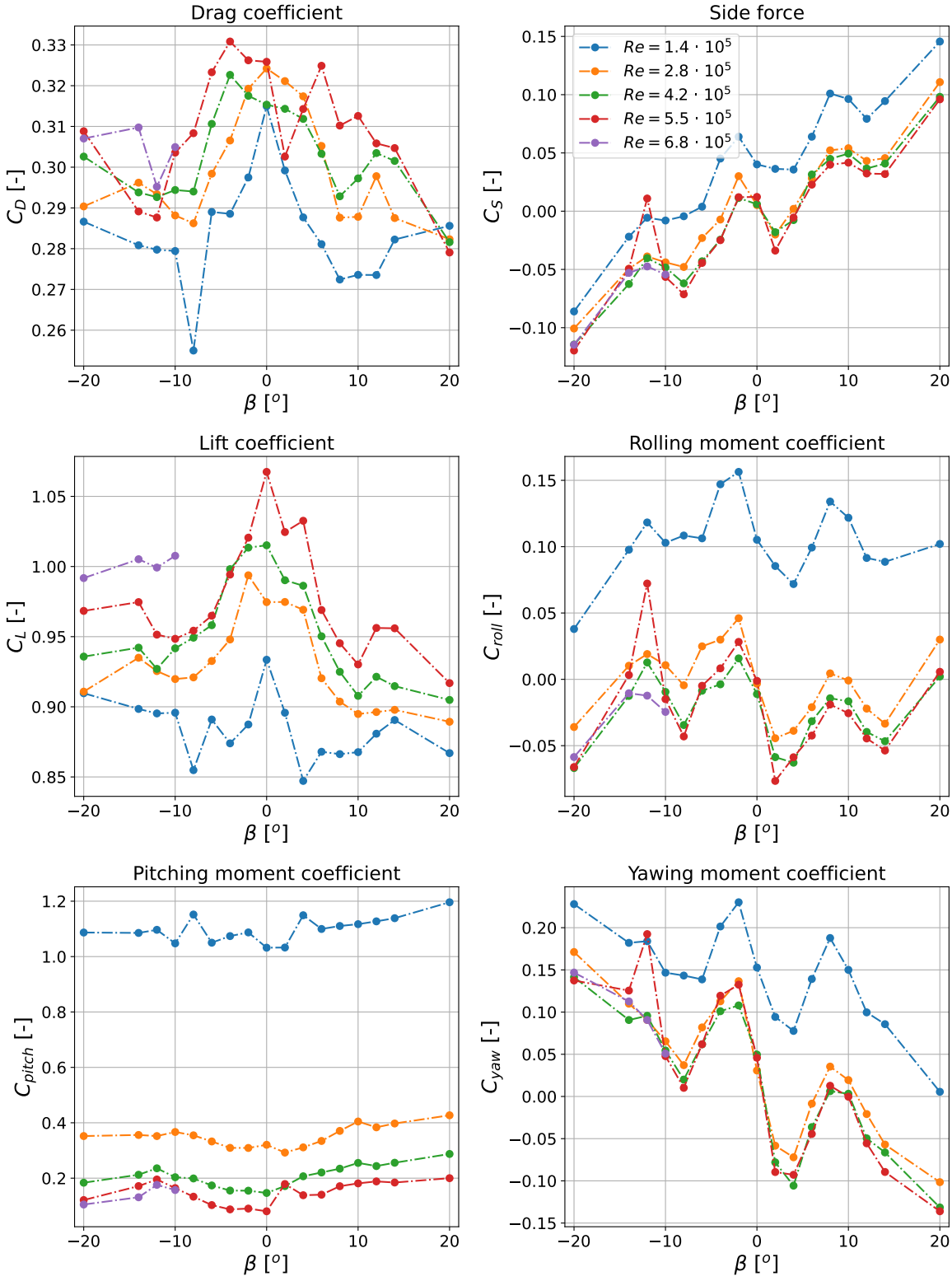

Figure A.33: Force and moment coefficient plots of the kite for $\alpha = 17.85$ deg.

A.3. Extra plots special cases

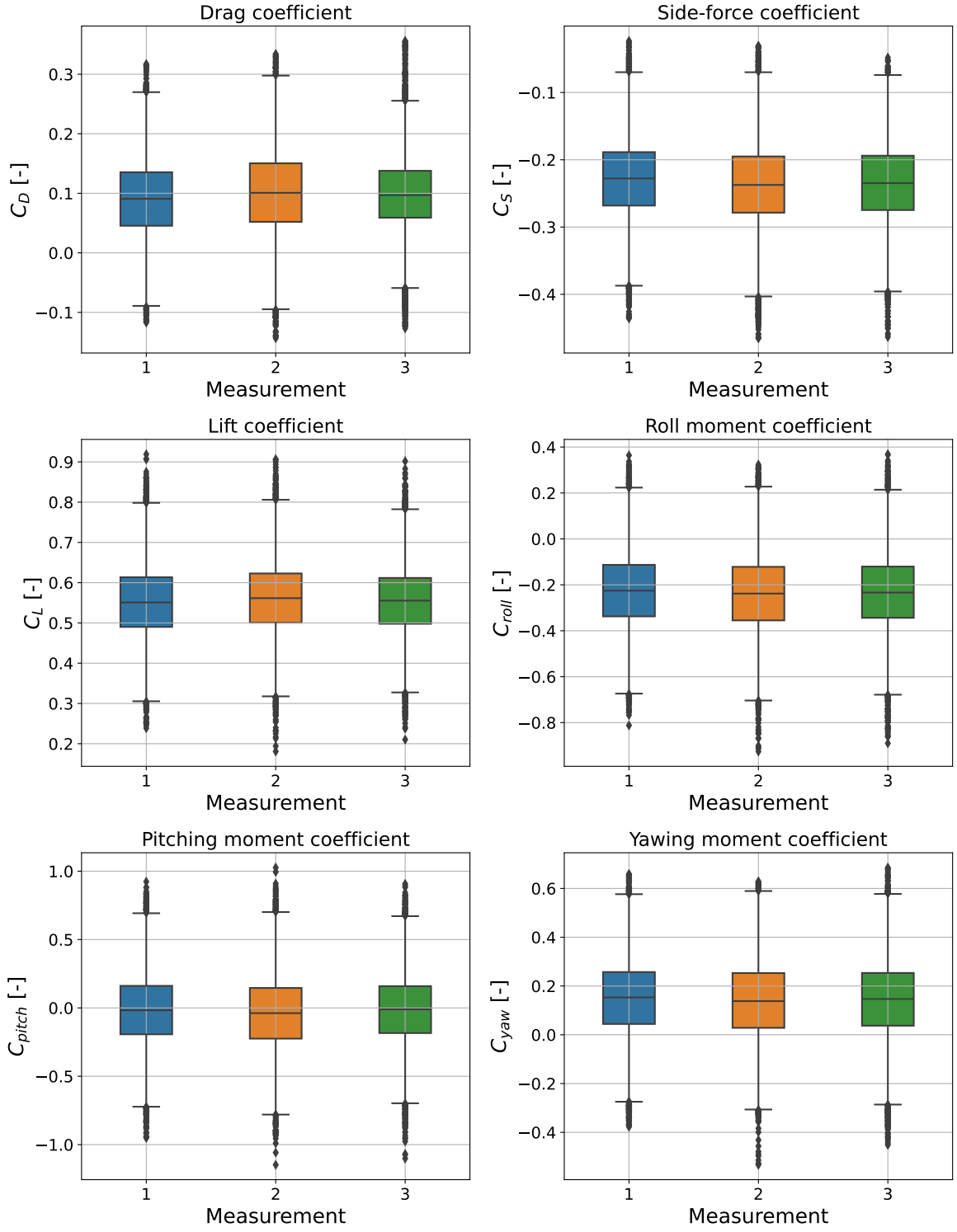

Figure A.34: Boxplots of force and moment coefficients for double measurements at $\alpha = 4.75$ deg, $\beta = -20$ deg, and wind speed of 20 m/s.

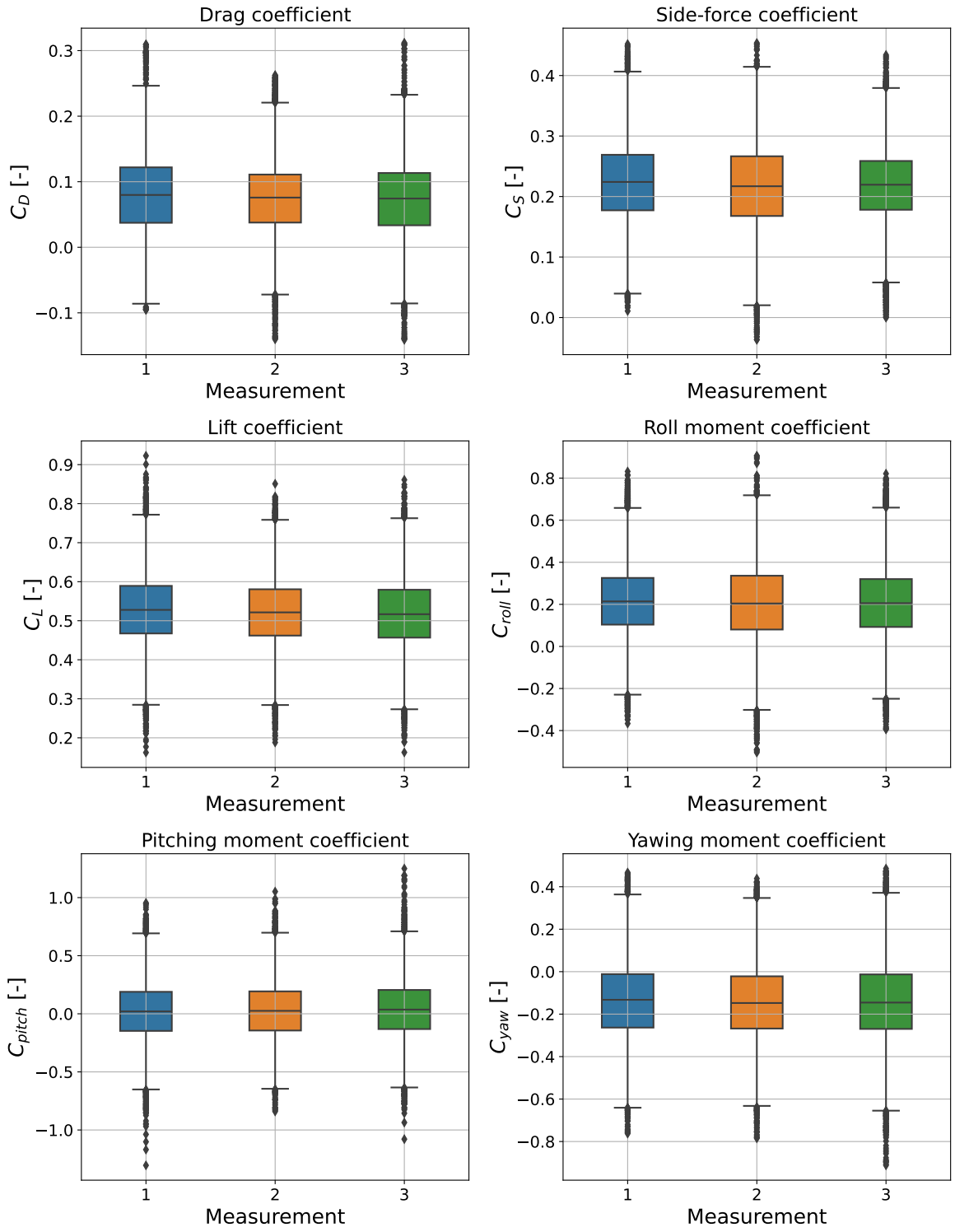

Figure A.35: Boxplots of force and moment coefficients for double measurements at $\alpha = 4.75$ deg, $\beta = 20$ deg, and wind speed of 20 m/s.